

A novel
Tissue-Equivalent Proportional Counter
Based on a
Gas Electron Multiplier

A novel
Tissue-Equivalent Proportional Counter
Based on a
Gas Electron Multiplier

Proefschrift

ter verkrijging van de graad van doctor
aan de Technische Universiteit Delft,
op gezag van de Rector Magnificus prof.dr.ir. J.T. Fokkema,
voorzitter van het College voor Promoties,
in het openbaar te verdedigen

op dinsdag 15 juni 2004 te 13:00 uur

door

Majid FARAHMAND

doctorandus in de natuurkunde
geboren te Isfahan, Iran

Dit proefschrift is goedgekeurd door de promotor:
Prof. dr. ir. C.W.E. van Eijk

Toegevoegd promotor: Dr. J. Zoetelief

Samenstelling promotiecommissie:

Rector Magnificus,	voorzitter
Prof. dr. ir. C.W.E. van Eijk,	Technische Universiteit Delft, promotor
Dr. J. Zoetelief,	Technische Universiteit Delft, toegevoegd promotor
Prof. dr. S. Vynckier,	Université Catholique de Louvain, Belgique
Prof. dr. H. Löhner,	Rijksuniversiteit Groningen
Prof. dr. ir. T.H.J.J. van der Hagen,	Technische Universiteit Delft
Prof. dr. G.J. Kearley,	Technische Universiteit Delft
Dr. A.J.J. Bos,	Technische Universiteit Delft

Published and distributed by: DUP Science

DUP Science is an imprint of
Delft University Press
P.O. Box 98
2600 MG Delft
The Netherlands
Telephone: +31 15 27 85 678
Telefax: +31 15 27 85 706
E-mail: info@library.tudelft.nl

ISBN 90-407-2488-1

Keywords: microdosimetry / nanodosimetry / tissue-equivalent proportional counter

Copyright © 2004 by M. Farahmand

All rights reserved. No part of the material protected by this copyright notice may be reproduced or utilized in any form or by any means, electronic or mechanical, including photocopying, recording or by any information storage and retrieval system, without written permission from the publisher: Delft University Press

Printed in the Netherlands

*In childhood we strove to go to school,
Our turn to teach, joyous as a rule
The end of the story is sad and cruel
From dust we came, and gone with winds cool.*

یکت چند کبود کی با سستا و شدم
یکت چند زاستادی خود شتا و شدم
پایان سخن شتو که مارا چه رسید
از خاک در آمدیم بر باد و شدم

Omar Khayam (1048 - 1123)

Aan Nelleke en Arman John

Table of Contents

1	GENERAL INTRODUCTION	1
1.1	INTRODUCTION	1
1.2	OUTLINE	7
	REFERENCES	9
2	EXPERIMENTAL MICRODOSIMETRY	11
2.1	MICRODOSIMETRY	12
2.1.1	EXPERIMENTAL MICRODOSIMETRY	13
2.1.2	MICRODOSIMETRIC QUANTITIES	13
2.2	PROPORTIONAL COUNTER IN MICRODOSIMETRY	16
2.2.1	BASIC PRINCIPLES OF PROPORTIONAL COUNTERS.....	16
	2.2.1.1 <i>Classification of particle tracks</i>	16
	2.2.1.2 <i>Site-size simulation</i>	17
2.3	REPRESENTATION OF MICRODOSIMETRIC DISTRIBUTIONS	20
2.4	APPLICATIONS OF EXPERIMENTAL MICRODOSIMETRY	21
2.4.1	RADIATION PROTECTION APPLICATIONS.....	21
2.4.2	RADIOTHERAPY APPLICATION	23
2.4.3	RADIOBIOLOGY.....	24
2.4.4	APPLICATIONS IN SPACE AND RADIATION EFFECTS ON MICROELECTRONICS.....	27
2.5	OTHER METHODS	27
2.5.1	VARIANCE-COVARIANCE METHOD.....	27
2.5.2	NANODOSIMETRY AND TRACK-NANODOSIMETRY.....	29
2.5.3	MICROSTRIP GAS COUNTERS (MSGC).....	30
2.5.4	SOLID STATE COUNTER	30
	REFERENCES	31
3	TISSUE-EQUIVALENT PROPORTIONAL COUNTER: PRINCIPLES OF OPERATION AND APPLICATION	35
3.1	THE COUNTER.....	36
3.1.1	GAS FILLED COUNTER	36
3.1.2	DETECTOR GEOMETRY CONSIDERATIONS.....	37
3.1.3	MATERIALS.....	39
3.2	GAS SYSTEM	40
3.2.1	FILLING GASES	40
3.2.2	GAS FLOW SYSTEM.....	41

3.3	ELECTRONICS.....	42
3.3.1	SIGNAL PROCESSING	42
3.3.2	ELECTRONICS AND SENSITIVITY	43
3.3.3	DATA COLLECTION AND PULSE PROCESSING	44
3.4	GAS AMPLIFICATION IN A PROPORTIONAL COUNTER.....	46
3.4.1	DIFFUSION EFFECTS	46
3.4.2	GAS MULTIPLICATION	47
3.4.3	AVERAGE ENERGY REQUIRED PER ION PAIR (W).....	49
3.4.4	ENERGY RESOLUTION	49
3.5	WALL EFFECTS.....	51
3.5.1	DELTA-RAY EFFECT	52
3.5.2	RE-ENTRY EFFECT	52
3.5.3	V-EFFECT	52
3.5.4	SCATTERING EFFECT.....	52
3.6	STATISTICAL VARIATION IN MICRODOSIMETRIC MEASUREMENTS	53
3.7	CALIBRATION METHODS	54
3.8	GAS ELECTRON MULTIPLIER (GEM).....	55
	REFERENCES	57
4	ANALITICAL CALCULATIONS OF NEUTRON MICRODOSIMETRIC DOSE DISTRIBUTION	59
4.1	CALCULATION OF MICRODOSIMETRIC DOSE DISTRIBUTION	60
4.2	CALCULATION OF MICRODOSIMETRIC DOSE DISTRIBUTION OF DIFFERENT PARTICLE TRACKS	61
4.3	CONTRIBUTION OF THE VARIOUS CHARGED PARTICLE TO THE MICROSCOPIC DOSE DISTRIBUTION	65
4.4	MICRODOSIMETRIC DOSE DISTRIBUTION FOR DIFFERENT NEUTRON ENERGIES	66
4.5	MICRODOSIMETRIC DOSE DISTRIBUTION FOR DIFFERENT SIMULATED SITE SIZE	68
4.6	CONCLUSIONS.....	69
	REFERENCES	70
5	HIGH-ENERGY NEUTRON MICRODOSIMETRY	71
5.1	HIGH-ENERGY NEUTRON SOURCES.....	71
5.1.1	QUASI-MONOENERGETIC NEUTRON SOURCE	72
5.1.2	SPALLATION PROCESS	73
5.2	NEUTRON TIME OF FLIGHT FACILITY AT CERN	74
5.3	CALCULATION OF INTERACTIONS IN COUNTERS USED FOR MICRODOSIMETRY.....	76
5.3.1	KERMA.....	78
5.3.2	MASS STOPPING POWER	80
5.3.3	PROTON FLUENCE	83
5.3.4	DISTRIBUTION FOR INTERVALS	84
5.3.5	EVENT DISTRIBUTION.....	86
5.4	MINI MULTI-ELEMENT TEPC(-GEM)	87
5.5	CONCLUSIONS.....	89
	REFERENCES	90
6	GAS ELECTRON MULTIPLIER (GEM) OPERATION WITH TISSUE-EQUIVALENT GASES AT VARIOUS PRESSURES	91
6.1	INTRODUCTION	91
6.2	EXPERIMENTAL SET-UP AND PROCEDURE.....	92

6.3	RESULTS AND DISCUSSION	93
6.4	CONCLUSION.....	98
	REFERENCES	99
7	DESIGN OF A NEW TISSUE-EQUIVALENT PROPORTIONAL COUNTER BASED ON A GAS ELECTRON MULTIPLIER	101
7.1	INTRODUCTION	101
7.2	DETECTOR DESIGN CONSIDERATIONS.....	102
	7.2.1 CALIBRATION CONSIDERATIONS	103
	7.2.2 EQUIPOTENTIAL LINE CALCULATIONS	103
7.3	DETECTOR DESCRIPTION	105
7.4	EXPERIMENTAL RESULTS	107
7.5	CONCLUSIONS.....	108
	REFERENCES	109
8	MICRODOSIMETRIC MEASUREMENTS WITH A TEPC BASED ON A GEM	111
8.1	INTRODUCTION	111
8.2	MOTIVATION.....	112
8.3	EXPERIMENTAL SETUP	113
8.4	NEUTRON MICRODOSIMETRIC MEASUREMENTS.....	115
	8.4.1 RESULTS	115
	8.4.2 CONCLUSIONS.....	117
8.5	X-RAY MICRODOSIMETRIC MEASUREMENTS	118
	8.5.1 CALIBRATION.....	118
	8.5.2 ELECTRIC POTENTIAL AND COLLECTION EFFICIENCY CALCULATIONS IN THE SENSITIVE VOLUME	121
	8.5.3 MICRODOSIMETRIC SPECTRA	124
	8.5.4 NANODOSIMETRIC SPECTRA.....	125
	8.5.5 CONCLUSIONS.....	126
	REFERENCES	127
9	DISCUSSION AND OUTLOOK	129
	SUMMARY	137
	SAMENVATTING	141
	DANKWOORD / ACKNOWLEDGEMENTS	145
	CURRICULUM VITAE	147
	LIST OF PUBLICATIONS	149

Chapter 1

General Introduction

1.1 Introduction

One essential characteristic of nature is the exchange of matter and energy between organisms and their environment. Radiation is a form of energy that has always been around in nature and human beings will be irradiated throughout life. In order to assess the impact of radiation exposure properly, it is essential to understand the mechanism of the interaction of radiation with living organisms.

The type of radiation and the radiosensitivity of tissues complicate the impact of radiation. The functions of living tissue are carried out by molecules, that is, combinations of different types of atoms united by chemical bonds. Some of these molecules can be quite large. The proper functioning of these molecules depends upon their composition and also their structure. Altering chemical bonds may change composition or structure. Ionizing radiation is powerful enough to achieve this.

In general, interaction of ionizing radiation with matter can be distinguished in two categories:

- 1) In the case of directly ionizing interactions of charged particles (e.g., electrons, protons, etc.) with matter, the energy is lost in a large number of relatively small interactions via the Coulomb forces causing ionizations and excitations of the molecules.
- 2) Indirectly produced ionizations arise from uncharged particles (e.g., neutrons) and from electromagnetic radiation (X rays and gamma rays) through the production of charged directly ionizing particles (so-called secondary charged particles) by various processes.

Biological effects of ionizing radiation result mainly from ionization and excitation of atoms and molecules in matter. In a living cell, these primary processes initiate a complex chain of events from chemical changes in some important bio-molecules through mutations to bio-functional changes such as transformation and cell death.

The cell is the basic unit of living organism. Within a cell, the deoxyribonucleic acid (DNA) molecules contain the information required for the synthesis of intracellular proteins, for cell reproduction and for organization of the tissues and organs. Ionizing radiation pushes an electron out of its orbit around an atomic nucleus, causing the formation of electric charges on atoms or molecules. If this electron comes from the DNA itself or from a neighboring molecule and directly strikes and disrupts the DNA molecule, the effect is called direct action. However, today it is estimated that about two-thirds of the damage caused by X-rays is due to indirect action. This occurs when the liberated electron does not directly hit the DNA, but instead hits an ordinary water molecule. This ionizes the water molecule, eventually producing what is known as a free radical. A free radical reacts very strongly with other molecules as it seeks to restore a stable configuration of electrons.

Passage of ionizing radiation can result in direct effect on DNA leading to single strand breaks (SSB), double strand breaks (DSB), associated base damage (BD), or clusters of these damage types. Because of their high ionization density, heavy charged particles can cause clusters of damage where many molecular bonds are broken in the tissue along their trajectory.

Although the absorbed dose due to exposure to radiation may be measured, another level of consideration must be made before the biological effects of this radiation can be predicted. The problem is that although two different types of charged particle may deposit the same average energy in an organ, living cells and tissues do not necessarily respond in the same way to these two different types of radiation. This distinction is made via the concept of Relative Biological Effectiveness (RBE) which is a measure of how effective a given type of particle is when compared to an absorbed dose of X-rays.

Technology developed in the past century has extensively altered human exposures to ionizing radiation. This has been most obvious in the development of radiation generating devices and the utilization of nuclear energy. But even air travel has had its impact on human exposure. Human exposure increases with advancing aircraft technology as a result of the higher flying altitudes reducing the protective cover provided by Earth's atmosphere from extraterrestrial radiations [1]. This increase in operating altitude is taken to a limit by human operations in space [2]. Complex radiation fields involving heavy charged particle (HCP), fast neutron and gamma/electron radiation fields are encountered in various types of radiobiological and medical applications, space, aircraft travel and nuclear reactors. HCP and neutrons are characterized as high linear energy transfer (LET) radiation, i.e. they produce an extremely dense lineal track of ionization and excitation events. Gamma rays and electrons, on the other hand, produce a more uniform distribution of ionization events and are considered to be low LET radiations. A LET of a few tens of $\text{keV}\mu\text{m}^{-1}$ is commonly considered the approximate dividing line between low and high LET radiation. It is generally accepted that the microscopic distribution of energy deposition in volumes of lineal cellular and sub-cellular dimensions is of critical significance in biological damage. In general,

microdosimetry concerns the nature of the energy depositions which occur in micro-volumes of the size of cellular and sub-cellular structures.

The basis of microdosimetry grew out of the study of radiation effects on living cells. Early attempts to understand cellular radiation effects recognized that knowledge of the energy distribution at a scale comparable to the structures affected by irradiation was essential [3].

In the 1920s Dessauer [4] and Crowther [5] developed the earliest forms of target theory which identified discrete energy transfers denoted as hits with individual ionization. The disregard of the spatial distribution of these events severely limited the predictive capability of this early work. The late 1940s saw the development of several important concepts, in particular the development of the concept of LET. Zirkle [6] provided the first definition of LET in 1952 although his work was closely linked to similar ideas introduced by Gray [7] and Lea [8]. ICRU report [9] defines LET as a measure of the loss of energy per unit distance along the path of a charged particle. However, there are some serious limitations of the LET concept in explaining relative biological effectiveness and the differences between radiation types.

Kellerer and Chmelevsky [10], have investigated the effects of these limitations and the ranges and energies over which they are important. There are several reasons for the limitations in the LET concept [11]. Firstly, the delta ray (energetic electron) energy distribution and its relationship to spatial dose distribution are not adequately considered. Particles with different velocities and charges can have the same LET but it is the particle velocity that largely determines the energy distribution of delta rays. In microscopic volumes, the delta-ray distribution may be a significant factor in the spatial distribution of energy, particularly at higher ion energies and small site sizes. Secondly, the limited range of charged particles relative to the finite target structure influences the energy deposition by two possible mechanisms; a change in LET through the site or the possibility of the track beginning or ending within the volume. Such effects are more predominant at lower ion energies and in sites with larger dimensions. Finally, LET, being a nonstochastic average quantity, does not account for the random fluctuations in energy deposition which become manifest as clustering of energy deposition and range straggling. The variance due to straggling may exceed the path length variations at high ion energies and small site sizes.

These limitations in LET lead to the formulation of a set of measurable stochastic quantities that provide the fundamental basis for the field of microdosimetry. The two principle quantities are *lineal energy* and *specific energy*. These quantities will be defined and discussed in section 2.1.2. It is the goal of experimental microdosimetry to measure these quantities in well-defined volumes.

Parallel to the theoretical development of radiation interaction with tissue there were two main experimental developments [12]. The first main experimental development included studies of visible chromosome aberrations in cells which demonstrated that ionizing radiation could induce exchanges of material between different, radiation damaged, chromosomes. This work was pioneered by Sax [13] and Lea and Catcheside [14] in the 1940s working on *Tradescantia* plant cells followed by Wolff [15] in the late 1950s and Neary [16] and coworkers in the 1960s. Analysis of the size of the affected chromosome structures under

different types of ionizing radiation suggested an interaction distance between pairs of damaged chromosomes of between 0.1 and 1 μm .

Clearly, the measurement of radiation quantities in sites of comparable size to the cell or even the chromosome interaction distance are required. Extreme importance was the development in the early 1950s of the low-pressure proportional counter, commonly called the Rossi counter after its pioneer [17]. This was the second main experimental development in microdosimetry and permits measurement of microdosimetric quantities at scales of the order of 1 μm . The operation and limitations of proportional counters will be described in chapter 3.

Intuitively, it would seem likely that there exists a link between microdosimetric experimental quantities and the observed effects of radiation on biological cells. The theory of dual radiation action (TDRA), first proposed by Kellerer and Rossi in 1972 [18], seeks to establish the link between experimental radiation physics and cellular radiobiology. This theory and the applicability of experimental microdosimetry to radiobiology, radiotherapy, radiation protection, and other applications are discussed briefly in section 2.4.

The principle operation of all radiation detectors is based on the interaction of the radiation with the sensitive medium of the detector [19]. Therefore, a change in the state of that medium is produced which can be, in most cases, measured. The detectors are classified as gaseous when the medium of interaction with radiation is a gas-filled chamber. The proportional counter belongs to the class of gaseous detectors which analyse individual ionisation events. Typical for these counters is phenomenon of gas multiplication which relies on the fact that the electric field within the counter is high enough to enable secondary ionisation, proportional to the amount of primary ionisation.

Proportional counters are applied to measure the absorbed dose in experimental microdosimetry which is the study and interpretation of single-event energy deposition at microscopic sites of tissue (chapter 2). The walls of the proportional counter used in microdosimetry are made of tissue-equivalent plastic and the filling gas has almost the same composition as human tissue to reach the equivalence to the human tissue. Therefore, these counters are called Tissue-Equivalent Proportional Counter (TEPC). The simulation of a microvolume is carried out by the reduction of the gas pressure (section 2.2.1).

A conventional TEPC is a proportional counter (PC) with a cavity containing a central anode wire and operated with a tissue-equivalent counting gas at low pressure to simulate tissue volumes of micrometer dimensions. The wall of the counter is commonly made of tissue-equivalent material and is used as cathode owing to the conductivity of the plastic. TEPCs are operated in pulse mode and the pulse-height spectrum is collected and converted to the parameter extensively used in microdosimetry, i.e. lineal energy, which is denoted by y . The lineal energy is defined as the quotient of the energy, ϵ_s , imparted to the matter in a volume by a single event and the mean chord length, \bar{l} , in that volume. Lineal energy is commonly presented in units of $\text{keV}\mu\text{m}^{-1}$. The shape of a microdosimetric spectrum contains quantitative information that can be used to predict the radiobiological effectiveness of radiation.

Microdosimetric data of high-energy neutrons are important to our understanding of dosimetry in radiation protection and radiotherapy such as the estimation of dose to aircraft

crews or the effect of secondary neutrons produced by high-energy accelerator facilities and in the treatment planning for cancer therapy at advanced proton and neutron therapy facilities. Modern neutron radiotherapy employs energies extending to 70 MeV. Secondary neutrons produced by advanced proton therapy facilities can have energies as high as 250 MeV [20]. The knowledge of neutron interactions and microdosimetric data for neutron energies between 20 and 50 MeV is clearly inferior to that for neutrons of lower energies and for photons. For neutron energies above 50 MeV microdosimetric data are very scarce. For several practical applications, in particular for radiation protection and clinical dosimetry, the knowledge of microdosimetric data in this energy range is insufficient. Therefore the neutron spallation source at CERN (European Organisation for Nuclear Research) has been planned to be used for measuring microdosimetric spectra of neutrons with energies up to 250 MeV. The problems involved in using this facility for microdosimetry, such as pile-up and not getting enough information in a reasonable period of time are discussed in chapter 5. Furthermore, possible solutions to these problems are given.

The scale of measurements in microdosimetry is typically at the micrometre level. At such small dimensions, the primary tool of experimental microdosimetry has been the low-pressure proportional counter. Although generally considered the best available detector, the currently used proportional gas counter has several shortcomings. These include a relatively large physical size which limits spatial resolution and increases sensitivity to pileup effects, inability to simulate smaller site sizes (nanometer), many difficulties in construction of a single and multi-element counter. Furthermore, the supply of presently available counters for routine practice is hampered by technical problems in the production of reliable detectors with predictable characteristics at comparatively little effort and hence low cost [21].

There are two trends which promote the development of TEPCs with a much smaller cavity. The first trend is the increasing application of neutron and proton therapy which has stimulated the need for further microdosimetric measurements to specify the beam quality in treatment fields. However, because of the high beam intensity of a therapeutic beam, the usual size of presently available TEPCs with a counter cavity diameter of a few centimetres cannot be employed due to pile-up of the electronic signals. Reducing the counter cavity size will reduce the pile-up effect. The second trend is an increased interest in the spectra of energy deposition by radiation in small (nanometer) sites, which are important for an improved understanding of the biological effects of densely ionising radiation. The usual size TEPCs cannot easily operate at pressures low enough to simulate some tens of nanometers. Reducing the counter cavity size will allow simulating such sites at a higher pressure.

In the past few years several groups have developed various types of mini TEPCs. Kliauga [22] measured single event distributions at simulated sizes below 300 nm with a single-wire mini TEPC with a diameter of 0.5 mm. Cesari et al. [23] reported microdosimetric measurements of a proton therapeutic beam with a mini TEPC of 1.0 mm diameter. Burmeister et al. [24] have applied a mini TEPC in high-flux mixed fields. All these mini TEPCs are based on the same principle namely miniaturising the dimensions of all components of a normal size TEPC. However, the construction of a central wire in a small cavity is extremely difficult and expensive. It becomes even more difficult in case of multi-element cavities applied to increase the counter sensitivity. These conditions justify our efforts to develop a new type of TEPC based on another principle of gas amplification using a Gas Electron Multiplier (GEM) [25].

The counting gases commonly used in dosimetry are methane-based [26] or propane-based [27] tissue-equivalent (TE) gases, referred to as TE-CH₄ and TE-C₃H₈ respectively. In microdosimetry the TEPC is operated at low pressure to simulate a microscopic tissue site. There is no information about GEM operation employing TE gases, neither at atmospheric pressure nor at low pressure. Therefore, for the first time results of GEMs operating under micro-TEPC conditions are presented and discussed (see chapter 6). In TE-CH₄, a maximum GEM gain of $1.5 \cdot 10^3$ has been reached while in TE-C₃H₈ this is $6 \cdot 10^3$. These maxima have been reached at different gas pressures depending on GEM structure and TE gas.

The design and construction of this novel type TEPC based on a Gas Electron Multiplier is described in chapter 7. The first pulse height measurements with this counter for both methane and propane based Tissue Equivalent (TE) gases are presented. These results show promising properties for application of this novel type TEPC in microdosimetric measurements.

Finally, the proper functioning of this novel counter is demonstrated with a 14 MeV monoenergetic neutron source and a californium (²⁵²Cf) source for a cylindrical counter cavity of equal diameter and height of 1.8 mm simulating 1.0 μm tissue site size. The pulse-height measurements at various low pressures for propane-based Tissue Equivalent (TE-C₃H₈) gas are presented. Furthermore, the first microdosimetric responses for low energy X-rays are presented for counter cavities of 1.8 mm, 1.0 mm and 0.5 mm diameter at various pressures, simulating tissue site sizes of 1.8 μm, 1.0 μm, 500 nm, 280 nm and 140 nm. Two independent calibration methods have been applied and are discussed.

1.2 Outline

The arrangement of this thesis is shown in detail in the Table of Contents and described briefly as follows:

- Chapter 1. Introduction and outline
- Chapter 2. Microdosimetry and some basic principles of the main device used in microdosimetry, i.e. proportional counter and the way in which the microdosimetric spectra are generally represented are explained. In addition, an introduction to the application of experimental microdosimetry is given. A few other commonly used experimental microdosimetry methods are briefly described.
- Chapter 3. The Tissue-Equivalent Proportional Counter (TEPC) and its principles are discussed. To perform correct microdosimetric measurements, gas system and electronics are fully described. Some basic principles of a proportional counter such as gas amplification, average energy required to produce an ion pair and energy resolution are debated. The distortion of microdosimetric spectra due to wall effects and the statistical variations in microdosimetry are discussed. The calibration methods are explained. Finally, the properties of the Gas Electron Multiplier (GEM) are discussed.
- Chapter 4. To obtain a clear understanding of the parameters that influence neutron microdosimetric spectra, analytical calculations have been carried out. The physical principles on which these calculations are based are explained. The different particle tracks have been calculated which is useful to distinguish between insiders, starters, stoppers and crossers. Knowledge of the contributions of different types of charged particles to the total lineal energy spectrum is also useful and is discussed. Changes in the shape of the microdosimetric spectra as a result of changing of the neutron energies are given. Finally, the influence of the simulated site sizes on the shape of the microdosimetric spectra is discussed.
- Chapter 5. Two types high-energy neutron source are considered (i.e. quasi-monoenergetic and spallation). The neutron spallation source at CERN (European Organisation for Nuclear Research) has been planned to be used for measuring microdosimetric spectra of neutrons with energies up to 250 MeV. The problems involved in using this facility for microdosimetry, such as pile-up and not getting enough information in a reasonable period of time are discussed. Furthermore, possible solutions to these problems are given. Finally, because of the impracticability of using a conventional Tissue Equivalent Proportional Counter (TEPC), a new type of TEPC based on Gas Electron Multiplier (GEM) is introduced.

- Chapter 6. The operation of two Gas Electron Multiplier (GEM) structures in both methane and propane based Tissue-Equivalent (TE) gases at different pressures varying from 0.1 to 1 atmosphere is studied. This work was motivated to explore the possibility of using a GEM for a new type of Tissue Equivalent Proportional Counter (TEPC). In methane based TE gas, a maximum safe GEM gain of $1.5 \cdot 10^3$ has been reached while in propane based TE gas this is $6 \cdot 10^3$. These maxima have been reached at different gas pressures depending on GEM structure and TE gas. Furthermore, we observed a decrease of the GEM gain in time before it becomes stable. Charge up/polarisation effects can explain this.
- Chapter 7. By employing a Gas Electron Multiplier (GEM) a new type of mini multi-element Tissue-Equivalent Proportional Counter (TEPC) has been designed and constructed. In this chapter the design of this novel counter is described. The first pulse height measurements with this counter for both methane and propane based Tissue Equivalent (TE) gases are presented. These results show promising properties for application of this novel type of TEPC in microdosimetric measurements.
- Chapter 8. The first microdosimetric measurements of the novel TEPC based on GEM exposed to a 14 MeV monoenergetic neutron beam and a californium (^{252}Cf) source for a counter cavity diameter of 1.8 mm simulating $1.0 \mu\text{m}$ tissue site size are presented. The measured spectra show excellent agreement with spectra from the literature. The specific advantages of the TEPC-GEM are discussed. It has been demonstrated that this counter for several cavity dimensions (as small as 0.5 mm of diameter) can be used very successfully to measure micro- and nanodosimetric spectra in various simulated tissue site sizes. Furthermore, the calibration methods of this type of TEPC are discussed.
- Chapter 9. Conclusions providing a summary of main results and suggested directions for further research.

References

- [1] Waters, M., Bloom, T.F. and Grajewski, B. *The NIOSH/FAA working women's health study: Evaluation of the cosmic-radiation exposures of flight attendants*. Health Phys. 79 (2000) 553.
- [2] Wilson, J.W. *Overview of radiation environments and human exposures*. Health Phys. 79 (2000) 470.
- [3] Bradley, P.D. *The development of a novel silicon microdosimeter for high LET radiation therapy*. Thesis, Department of Engineering Physics, University of Wollongong, (2000).
- [4] Dessauer, F. *Über einige Wirkungen von Strahlen*. I. Z. Phys. 12 (1922) 38.
- [5] Crowther, I. A. *Some considerations relative to the action of X-rays on tissue cells*. Proc. Roy. Soc. 96 (1924) 207.
- [6] Zirkle, R.E., Marchbank, D.F. and Kuck, K.D. *Exponential and sigmoid survival curves resulting from alpha and x-irradiation of Aspergillus spores*. J. Cell. Comp. Physiol. 39 (1952) 75.
- [7] Gray, L.H. *The distribution of the ions resulting from the irradiation of living cells*. Br. J. Radiol. Suppl. 1 (1947).
- [8] Lea, D.E. *Actions of Radiation on Living Cells*, 2nd ed. Cambridge: Cambridge, 1955.
- [9] International Commission on Radiation Units and Measurements. *Linear Energy Transfer*, (ICRU report: 16), Bethesda, Maryland, (1970).
- [10] Kellerer, A.M. and Chmelevsky, D. *Criteria for the applicability of LET*. Radiat. Res. 63 (1975) 226.
- [11] International Commission on Radiation Units and Measurements, *Microdosimetry* (ICRU report: 36), Bethesda, Maryland, (1983).
- [12] Goodhead, D.T. *An assessment of the role of microdosimetry in radiobiology*. Radiat. Res. 91 (1982) 45.
- [13] Sax, K. *Chromosome aberrations induced by X-rays*. J. Genetics 23 (1938) 494.
- [14] Lea, D.E. and Catcheside, D.G. *The mechanism of induction of radiation of chromosome aberrations in Tradescantia*. J. Genetics 44 (1942) 216.
- [15] Wolff, S. *Interpretation of induced chromosome breakage and rejoining*. Radiat. Res. Suppl. 1 (1959) 453.
- [16] Neary, G.J., Preston, R.J. and Savage, J.R.K. *Chromosome aberrations and the theory of RBE III. Evidence from experiments with soft X-rays, and a consideration of the effects of hard X rays*. International Journal of Radiation Biology and Related Studies. 12 (1967) 317.
- [17] Rossi, H.H. and Rosenzweig, W. *A device for the measurement of dose as a function of specific ionization*. Radiology 64 (1955) 404.
- [18] Kellerer, A.M. and Rossi, H.H. *The theory of dual radiation action*. Curr. Top. Radiat. Res. Q. 8 (1972) 85.
- [19] Kliauga, P., Waker, A.J. and Barthe, J. *Design of Tissue-Equivalent Proportional Counters*. Radiat. Prot. Dosim. 6 (1995) 309.
- [20] Chadwick, M.B., DeLuca Jr., P.M. and Haight, R.C. *Nuclear data needs for neutron therapy and radiation protection*. Radiat. Prot. Dosim. 70 (1997) 1.
- [21] Schuhmacher, H., *Tissue-equivalent proportional counters in radiation protection dosimetry: Expectation and present results*. Radiat. Prot. Dosim., 44 (1992) 199.
- [22] Kliauga, P. *Measurement of single event energy deposition spectra at 5 nm to 250 nm simulated site size*, Radiat. Prot. Dosim. 31 (1990) 119.
- [23] Cesari, V., Iborra, P.N., De Nardo, L., Querini, P., Conte, V., Colautti, P., Tornielli, G. and Chauvel, P. *Microdosimetric measurements of the Nice therapeutic proton beam*. Physica Medica, 17 (2001) 76.
- [24] Burmeister, J., Kota, C., Maughan R.L. and Waker, A.J. *Characterization of miniature tissue-equivalent proportional counters for neutron radiotherapy application*, Phys. Med. Biol. 47 (2002) 1633.
- [25] Sauli, F. *GEM: A new concept for electron amplification in gas detectors*. Nucl. Instr. And Meth. A 386 (1997) 531.
- [26] Rossi H.H. and Failla, G. *Neutron dosimetry*. Medical physics. Chicago: Year Book Publishers, inc. (1956) 603.
- [27] Srdoc, D. *Experimental technique of measurements of microscopic energy distribution in irradiated matter using Rossi counters*. Radiat. Res. 43 (1970) 302.

Chapter 2

Experimental Microdosimetry

Biological effects of ionizing radiation result mainly from ionization and excitation of atoms and molecules in matter. In a living cell these primary processes initiate a complex chain of events from chemical changes in some important bio-molecules through mutations to bio-functional changes such as transformation and cell death.

In this complex chain of events, studies of induction of visible chromosome aberrations in cells demonstrated that ionizing radiation could induce exchanges of material between and within chromosomes [1-4]. Analysis of the size of the affected chromosome structures suggested interaction distances of energy depositions at distances between 0.1 and 1 μm . This indicates that measurements of radiation quantities in sites of similar sizes are relevant. In general, microdosimetry concerns the nature of the energy depositions that occur in micro-volumes of the order of cellular and sub-cellular structures. Therefore, in the early 1950s the low-pressure proportional counter (section 2.2) has been developed which permits measurements of microdosimetric quantities (section 2.2.1) at scales of the order of 1 μm .

The origins of microdosimetry were intimately related to the radiobiological model known as the theory of dual radiation action (TDRA, section 2.4.3). One of the ways in which microdosimetry has evolved in the past decade has been its increasing application in practical fields such as health physics and medical physics. With this increased dissemination of microdosimetry to other fields, many new practitioners of microdosimetry are being engendered who may not always be familiar with the experimental techniques [5].

The outline of this chapter is: First, microdosimetry and its quantities will be explained (section 2.1). Then the proportional counters and some basic principles of proportional counters are discussed in sections 2.2. Furthermore, the way in which microdosimetric spectra should be graphically represented is discussed in section 2.3 while section 2.4 is dedicated to the applications of experimental microdosimetry. Finally, in section 2.5 current experimental methods are briefly reviewed.

2.1 Microdosimetry

Ionizing radiation is known to induce a wide variety of biological effects, including cell death, mutations, chromosome aberrations and carcinogenic transformations. Most effects of direct relevance to humans, whether from environmental, occupational, diagnostic, or therapeutic exposures are due to damage in individual cells. It is clear, that the microscopic patterns of interaction and energy deposition by ionizing radiation are crucial to any detailed understanding of the mechanisms by which these effects are induced.

Microdosimetry is the area that deals with the distributions of energy deposition events at the microscopic level and their correlation to the effects of radiation on biological targets. Microdosimetry is formally defined by Rossi and Zaider [6] as “the systematic study and quantification of the spatial and temporal distribution of absorbed energy in irradiated matter”.

The impact of radiation on living tissue is however complicated by the type of radiation and the variety of tissues. Radiations of different qualities have different degrees of effectiveness in producing effects in biological systems. When radiation is absorbed in biological material, the energy is deposited along the tracks of charged particles in a pattern that is characteristic of the type of radiation involved. The biological damage created by ionizing radiation is traceable to the chemical alteration of the biological molecules that are influenced by the ionizations or excitations caused by the radiation. The severity of these changes are directly related to the local rate of energy deposition along the particle track, known as the *Linear Energy Transfer* (LET) or *restricted linear electronic stopping power*. LET, L_{Δ} , is defined as the quotient of dE_{Δ} by dl , thus [7]

$$L_{\Delta} = \frac{dE_{\Delta}}{dl} \quad (2.1)$$

where dE_{Δ} is the energy lost by a charged particle due to electronic collisions in traversing a distance dl , minus the sum of the kinetic energies of all the electrons released with kinetic energies in excess of Δ . LET is commonly presented in units of $\text{keV}\mu\text{m}^{-1}$. It can also be expressed by

$$L_{\Delta} = S_{el} - \frac{dE_{kin,\Delta}}{dl} \quad (2.2)$$

where S_{el} is the linear electronic stopping power and $dE_{kin,\Delta}$ is the sum of the kinetic energies, greater than Δ , of all the electrons released by the charged particle traversing a distance dl . In the case of non-energy cutoff, L_{∞} ($\Delta = \infty$), the LET is equal to S_{el} and L_{∞} is replaced by L which is sometimes termed *unrestricted linear energy transfer*.

The densities of energy deposition along the track of the particles in tissue are roughly distinguished by LET. After exposure to X- or γ -rays, the ionization density would be quite low (low LET). After exposure to neutrons, protons, or alpha particles, the ionization along the tracks would occur much more frequently, producing a much denser pattern of ionizations

(high LET). These differences in density of ionizations are a major reason that neutrons and alpha particles produce more biological effect per unit of absorbed radiation dose than do more sparsely ionizing radiations such as X-rays, γ -rays, or electrons [8]. Other factors that contribute to these differences include the energy of the radiation used, the dose received and the temporal pattern in which it was received. Many scientific investigations have been conducted to study the difference in effectiveness of different types of radiation under different experimental conditions. Analysis of the Relative Biological Effectiveness, RBE, is a useful way to compare and contrast the results observed in these studies. RBE for a given test radiation, is calculated as the dose of a reference radiation D_{ref} , usually ortho-voltage (e.g. 250 kVp) X-rays or hard (e.g. ^{60}Co) γ -rays, required to produce the same level of *biological effect* as was seen with a test dose, D_T , of another type of radiation, e.g. neutrons. Thus:

$$RBE = \frac{D_{ref}}{D_T} \quad (2.3)$$

In microdosimetry there are concepts used which require further explanation for the reader who is not familiar with this technique. The site size concept involves the definition of volumes of interest called *sites* in which the energy absorbed by ionizing radiation is considered without regard to the microscopic distribution of energy within the site. *Regional microdosimetry* is concerned with measurements of energy deposition in sites and it is the principal purpose of experimental microdosimetry [6].

2.1.1 Experimental Microdosimetry

Microdosimetry is the systematic study and quantification of the spatial and temporal distributions of absorbed depositions of energy in irradiated matter [6]. Although microdosimetry can be utilized in the interpretation of a variety of radiation induced effects, its principal utility has been in the field of radiobiology. Experimental microdosimetry is the study and interpretation of single-event energy deposition spectra measured using low pressure proportional counters to simulate microscopic sites of tissue [9]. In experimental microdosimetry, pulses from single events are measured. They are proportional to the energy imparted in the counter gas. The pulse height distribution is converted to a distribution of dose in LET, and evaluated dose rate, or dose equivalent rate by different approximations of the measurement dependence on the quality factor (see section 2.4.1) and LET. However, the limitation in LET leads to the formulation of a set of measurable stochastic quantities that provide the fundamental basis for the field of experimental microdosimetry. The two principal quantities are *lineal energy* and *specific energy* which will be explained in the next section.

2.1.2 Microdosimetric quantities

The fundamental dosimetric quantity is the energy, ε , imparted to the matter in a volume¹. It is given by:

¹ ε is a stochastic quantity and the energy deposits over which the summation is performed may be due to one or more energy deposition events.

$$\varepsilon = \sum_i \varepsilon_i \quad (2.4)$$

where the summation is performed over all energy deposits, ε_i , in that volume.

The energy deposit, ε_i , is the energy deposited in a *single interaction*, i [7, 10, 11]:

$$\varepsilon_i = \varepsilon_{in} - \varepsilon_{out} + Q \quad (2.5)$$

where ε_{in} the kinetic energy of the incident ionizing particle, ε_{out} the sum of the kinetic energies of all ionizing particles leaving the interaction volume and Q includes the changes in the rest mass energy of the atom and all particles involved in the interaction.

In microdosimetry two principal quantities are determined: lineal energy, y , and specific energy, z , which are defined as follows.

The lineal energy, y , is the quotient of energy imparted, ε_s , to the matter in a volume by a *single event* and the mean chord length, \bar{l} , in that volume [7]:

$$y = \frac{\varepsilon_s}{\bar{l}} \quad (2.6)$$

Lineal energy is commonly presented in units of $\text{keV}\mu\text{m}^{-1}$. An important factor in the field of regional microdosimetry is the chord length distribution in a convex body. The mean chord length in a volume is the mean length of randomly oriented chords in that volume. Various types of randomness exist and the definition of \bar{l} typically refers to μ -randomness in which the body is exposed to a uniform, isotropic field of straight infinite lines [12]. According to a theorem by Cauchy [13], the mean chord length in a convex volume under μ -randomness is given by:

$$\bar{l} = \frac{4V}{S} \quad (2.7)$$

where V is the volume and S is the surface area of the body.

When particles interact with a given volume, they can release, with different probabilities, different quantities of energy, which generate a broad spectrum of the lineal energy. The frequency distribution of y is $f(y)$. The dose-distribution $d(y)$, is defined as the normalized distribution of the product $yf(y)$ and represents the relative contribution of the event y to the dose². This distribution is believed to be more meaningful to characterize the radiation action.

The relation between $f(y)$ and $d(y)$ is given by:

² Note: The use of the generally accepted notation may occasionally lead to confusion. E.g. $d(y)$ and dy are different!

$$d(y) = \frac{yf(y)}{\bar{y}_F} \quad (2.8)$$

The dose distribution relationship simply reflects the fact that higher lineal energies deposit a higher dose. In an irradiated medium the lineal energy is subject to a probability density distribution, $f(y)$. Characteristic parameters of the distribution are the frequency average lineal energy, \bar{y}_F , which is the first moment of $f(y)$ and the dose average lineal energy, \bar{y}_D , which is the second moment divided by the first moment:

$$\bar{y}_F = \int_0^{\infty} yf(y)dy \quad (2.9)$$

$$\bar{y}_D = \int_0^{\infty} yd(y)dy = \frac{1}{\bar{y}_F} \int_0^{\infty} y^2 f(y)dy \quad (2.10)$$

The second principal microdosimetric quantity is the specific energy (imparted), z , which is the quotient of the total energy imparted by ionizing radiation to matter of mass m , of a given volume.

$$z = \frac{\mathcal{E}}{m} \quad (2.11)$$

The special name for the unit of specific energy is gray (Gy) which is Jkg^{-1} in SI units. The frequency averaged specific energy, \bar{z}_F , is equal to the absorbed dose, D , and is given by:

$$\bar{z}_F = \int_0^{\infty} zf_1(z)dz \quad (2.12)$$

and the dose averaged specific energy is given by:

$$\bar{z}_D = \frac{1}{\bar{z}_F} \int_0^{\infty} z^2 f_1(z)dz \quad (2.13)$$

where $f_1(z)$ is the single-event microdosimetric spectrum and it is, by definition, the probability distribution of z under the condition that only single events took place.

Since the specific energy is due to the convolution of multiple events occurring in the mass m , it cannot be scaled from single-event quantities. However, the variance of z is both a function of the dose D and of y_D . Therefore it can be used to extract the mean value of the dose distribution, which is a single event parameter. The specific energy of a single event, z_1 , is the quotient of the energy imparted by a single ionizing particle to a mass, m , of a given volume and consequently it applies the macroscopic definition of absorbed dose (energy imparted to unit mass) to microscopic volumes. The specific energy is the stochastic analogue of the absorbed dose.

In general, the shape and the mean values of single-event spectra is by definition independent of the absorbed dose while on the contrary, multiple-event spectra and their averages are dose-dependent [14].

While the specific energy is the stochastic quantity analogue of the absorbed dose, the relation between the lineal energy and the somewhat similar non-stochastic quantity Linear Energy Transfer (LET) is not a simple analogy. For a given event, y and z , differ only by a numerical factor, which depends on the magnitude, shape and density of the given volume.

2.2 Proportional counter in microdosimetry

The Gas-filled low-pressure proportional counter is the principal instrument of microdosimetry. The method is based on the Bragg-Gray cavity principle [15]. The charge produced in small gas-filled cavities is generally considered to be a good measure for the absorbed dose of the surrounding material [16]. The problem of determining energy absorption in micrometer sized volumes in solids will be avoided by simulation of microscopic regions by geometrically similar gas volumes of equal effective dimensions (section 2.2.1). One of the principal advantages of the proportional counter is its sensitivity. It is a relatively simple device for detecting a few ionizations or even a single ionization, essentially independent of the location of the initial ionization in the chamber. Moreover, its relatively uniform internal amplification makes the proportional counter very useful. In chapter 3, we will focus on proportional counters used in microdosimetry, i.e. Tissue-Equivalent Proportional Counter (TEPC) in more detail. Here, we discuss some basic principles of proportional counters in microdosimetry.

2.2.1 Basic principles of proportional counters

2.2.1.1 Classification of particle tracks

The TEPC has excellent dosimetric properties as it forms a homogeneous Bragg-Gray cavity device and it offers tissue equivalency. Bragg-Gray cavity theory is one of the fundamentals of quantitative dosimetry [17]: the measurement of the ionization in a gas cavity yields the absorbed dose in the wall material surrounding the cavity. The wall thickness should be chosen so that for indirectly ionizing radiation Charged Particle Equilibrium (CPE) is obtained for the radiation of interest. It has to be at least as thick as the maximum range of the secondary charged particles but not too thick, to prevent reduction of the fluence as much as possible. CPE exists if any charged particle of a given type and energy leaving the sensitive volume is replaced by an identical particle of the same energy entering it, in terms of expectation values. For example, for 200 MeV neutrons, (with protons as secondary charged particles) this means a minimum thickness of about 23 cm (the maximum range of 200 MeV protons) Tissue-Equivalent plastic (Shonka A-150).

For the calculation and to understand the energy imparted [18-20], it is useful to distinguish between five classes of particle tracks (see Fig. 2.1) for each type of secondary charged particle depending on the location of their production with respect to the sensitive volume:

1. Particles originating in the volume may lose their entire energy in the volume (“insiders”).
2. Particles originating in the volume may leave the volume before losing all their energy (“starters”).
3. Particles originating outside the volume may enter the volume and stop within the volume (“stoppers”).
4. Particles originating outside the volume may cross the volume, depositing only part of their energy in the volume (“crossers”).
5. Particles originating outside the volume may not enter the volume in a straight line but by straggling or their delta rays (“touchers”).

One of the essential conditions of a Bragg-Gray device is that the cavity size should not modify the secondary charged particle spectrum produced by the interactions of the primary radiation field with the cavity wall material.

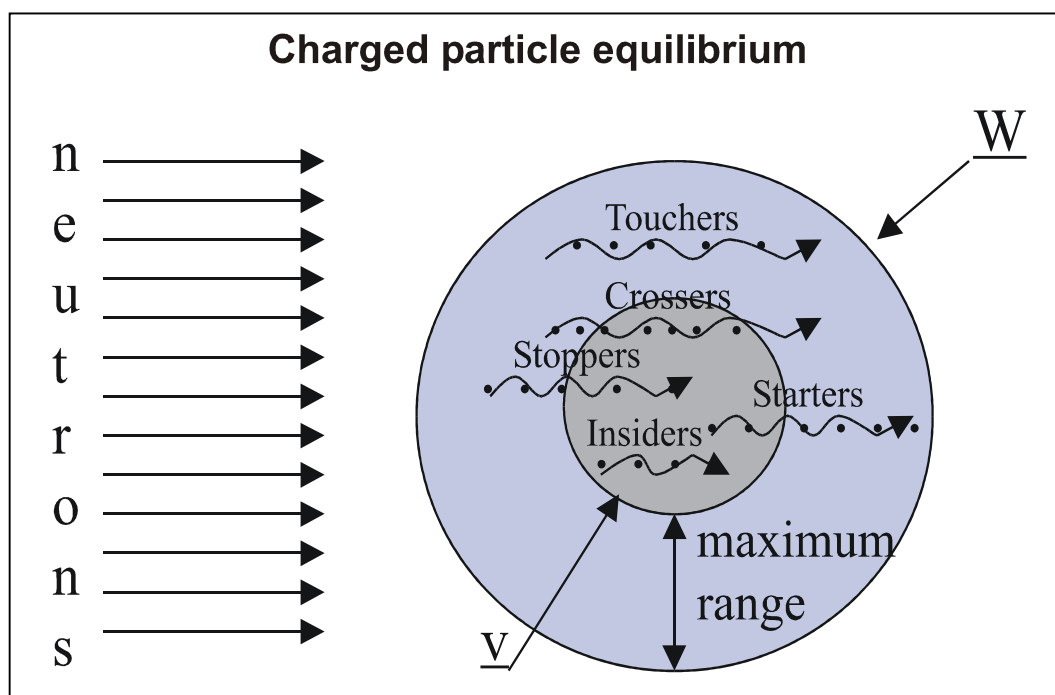


Figure 2.1: Classification of charged particle tracks with regard to their production with respect to the sensitive volume (V) and counter's wall (W).

2.2.1.2 Site-size simulation

For experimental microdosimetry the pressure of the filling gas has to be modified such that a charged particle crossing the counter volume deposits an identical amount of energy as the

same charged particle crossing a real tissue volume of microscopic diameter would do. The method of achieving this condition is illustrated by Fig. 2.2. Two spherical volumes, one of real medium (m) and the other of gas volume (g) are crossed by two identical particles.

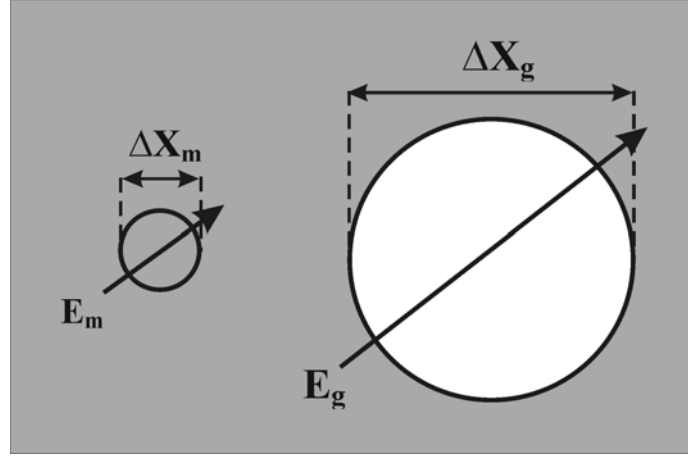


Figure 2.2: Microscopic tissue site size simulation using a tissue equivalent gas cavity.

The energy deposited by the particle in crossing the microscopic medium volume, E_m , is given by the product of the tissue mass stopping power, the tissue density and the path length across the medium volume [9], thus:

$$E_m = \left(\frac{1}{\rho} \frac{dE}{dx} \right)_m \rho_m \Delta X_m \quad (2.14)$$

The energy deposited by the particle in crossing the gas volume, E_g , is given in similar manner by:

$$E_g = \left(\frac{1}{\rho} \frac{dE}{dx} \right)_g \rho_g \Delta X_g \quad (2.15)$$

These two quantities must be equal if the energies deposited in medium and gas have to be the same.

$$\left(\frac{1}{\rho} \frac{dE}{dx} \right)_m \rho_m \Delta X_m = \left(\frac{1}{\rho} \frac{dE}{dx} \right)_g \rho_g \Delta X_g \quad (2.16)$$

When the mass stopping power of medium and used gas are the same, the condition required is thus:

$$\rho_m \Delta X_m = \rho_g \Delta X_g \quad (2.17)$$

If the product of the gas density and the gas cavity diameter is equal to the product of the tissue volume diameter and medium density, simulation of the microscopic medium volume is achieved.

In practice the simulation with the proportional counter is carried out by reducing the gas pressure (and so its density) so that an equality of the two products is reached. The relation between density and pressure can be obtained by using the ideal gas law:

$$p = \rho_g \frac{R \cdot T}{M} \quad (2.18)$$

Where p is the gas pressure, ρ_g is the gas density, R is the gas constant, T is the temperature and M is the molar mass of the gas. Using equations 2.17 and 2.18, the following expressions apply for a medium with ΔX_m and ρ_m :

$$p = \frac{\Delta X_m}{\Delta X_g} \cdot \rho_m \cdot \frac{R \cdot T}{M} \quad (2.19)$$

When gas mixtures are used, the molar mass M becomes a composition of the individual gas components. To carry out an accurate simulation of a microscopic volume of a biological tissue, it is inevitable that the employed gas and the wall of the counter are sufficiently tissue equivalent. The compositions of the gas and counter wall are explained in chapter 3. As an example, a 2.5 cm diameter sphere filled with propane based Tissue-Equivalent gas (see section 3.2.1) at 2.27 kPa (17 Torr) is equivalent to a 1 μm diameter sphere of unit density material. The absorbed dose is the same in both spheres but the number of charged particles per unit absorbed dose is multiplied by the square of the ratio of gas to tissue diameter $((\Delta X_g/\Delta X_m)^2)$.

In addition to decreasing the gas pressure, smaller sensitive volumes may be obtained by reduction of the simulating volume. Kliuga has reported reasonable spectral measurements obtained from an ultra-miniature cylindrical counter 0.5 mm in length and 0.5 mm in diameter operating at 560 Pa (4.2 Torr) and simulating a 5 nm diameter unit-density volume. The successful operation of such a counter is not well predicted by current theories of electron multiplication in gases. This may be more due to inadequacies of the theory rather than to experimental limitations. More research is required to understand the behavior and possible spectrum quality issues associated with such a counter.

Note, that apart from design restrictions a more fundamental limit [21, 22] on the minimum site size exists due to the fact that the unit of measurement is ionization and that excitation is not detectable. Single ionization in tissue equivalent gas is equivalent to a mean energy deposition of about 30 eV. At site diameters less than about 0.3 μm , errors in the conversion to energy may be quite large due to the small number of ionizations produced by individual low LET tracks with average energies below 30 eV.

2.3 Representation of microdosimetric distributions

Microdosimetric distributions can be represented in various ways. A question often encountered when microdosimetric spectra are presented graphically is what representation is the best to use. Because of a rather large range of values in most microdosimetric distributions, e.g. over eight orders of magnitude, the linear representation of $d(y)$ vs y is rarely employed. Instead, the representation of fundamental microdosimetric spectra is traditionally displayed as a log-linear plot with the ordinate multiplied by y such that the area under the curve delimited by two values of y is proportional to the fraction of events (for $f(y)$) or the fraction of dose (for $d(y)$) delivered by events in this range of lineal energy values. This can be illustrated by Fig. 2.3a where $d(y)$ over a wide range of interest is not visible.

One of the reasons showing spectra graphically is to be able to estimate from the plot the fraction of events that have lineal energy values in a given range of interest. Because this kind of information cannot be obtained directly from Fig. 2.3a, one employs a $yd(y)$ vs. y semi-log representation. This representation accommodates the wide lineal energy range often observed in microdosimetric spectra but requires further scaling to preserve the dose to area correspondence.

In this representation the ordinate must be multiplied by y because of the fact that:

$$\int_{y_1}^{y_2} d(y) dy = \int_{y_1}^{y_2} [yd(y)] d(\ln y) = \ln(10) \int_{y_1}^{y_2} [yd(y)] d(\log y) \quad (2.20)$$

and this integral is proportional to the dose deposited in the interval dy . The area delimited by any two values of y is proportional to the fractional number of events that have lineal energy in that range of y values.

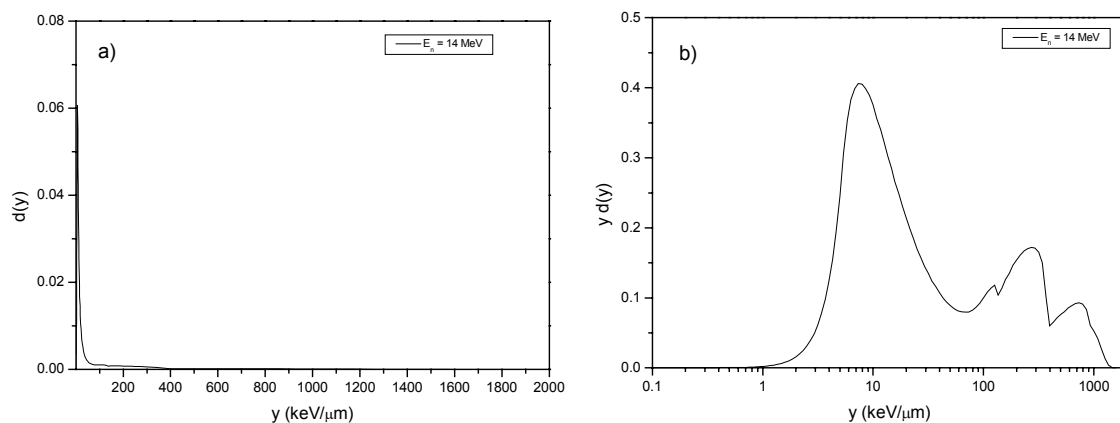


Figure 2.3: Calculated microdosimetric spectrum, $d(y)$, for energy deposited by 14 MeV neutrons in a 2 μm diameter volume. a) The dose distribution, $d(y)$, in linear presentation b) The dose distribution for the same spectrum in semi-log presentation. The ordinate is multiplied by y and in this semi-log representation the area under the curve restricted by any two values of y is proportional to the fraction of dose delivered by events with lineal energies in this range.

In Fig. 2.3b the same spectrum is shown in this new representation. The details are not longer obscured. This semi-log representation of $yd(y)$ vs. $\log(y)$ is the standard representation of a microdosimetric spectrum. When presenting spectra in semi-log form, care must be taken to perform correct normalization given a logarithmic histogram [11]. By definition, the distribution $d(y)$ is normalized to unity:

$$\int_0^{\infty} d(y) dy = 1 \quad (2.21)$$

This normalization should remain unchanged when plotted versus a logarithmic scale of y . Using equation (2.20) and (2.21), this means that:

$$\int_0^{\infty} yd(y)d(\ln y) \approx \frac{\ln 10}{B} \sum y_i d(y_i) = 1 \quad (2.22)$$

where the logarithmic scale of y is subdivided into B increments per decade such that the i th value of y is:

$$y_i = y_0 10^{i/B} \quad (2.23)$$

The approximation in equation (2.22) arises from the use of the relationship:

$$d(\log y) \approx \Delta(\log y) = \frac{1}{B} \quad (2.24)$$

where the difference between $d(\log y)$ and $\Delta(\log y)$ is negligible provided that B is large enough. In the plots used in this work $B = 60$ which was found to provide sufficient smoothing of the data, adequate display resolution and correct normalization.

2.4 Applications of experimental microdosimetry

Although the origins of microdosimetry were directly related to the models in the field of radiobiology, it can be used in the interpretation of a variety of radiation effects. Therefore, in the past decade experimental microdosimetry has been increasingly applied in practical fields such as radiation protection, radiotherapy, space dosimetry and radiation effects on microelectronics. In this section a brief introduction to the application of experimental microdosimetry is given.

2.4.1 Radiation protection applications

The recognition that different types and energies of ionizing radiation differ in effectiveness and that relative biological effectiveness (RBE, section 2.1) values are particularly large at low absorbed doses of principal importance to radiation protection, necessitated the

formulation of a quantity that weights absorbed doses by their biological effect. After earlier formulations the ICRU [14] defined the dose equivalent, H by:

$$H = Q \cdot D \quad (2.25)$$

where Q is the quality factor and D the absorbed dose. Q , like RBE, is a dimensionless quantity and H , therefore, has the same physical dimension as D in SI units, J kg^{-1} . To minimize confusion in cases where $Q = 1$, it was decided to admit different special names for the units of these quantities: D is expressed in gray (Gy) and H in sievert (Sv).

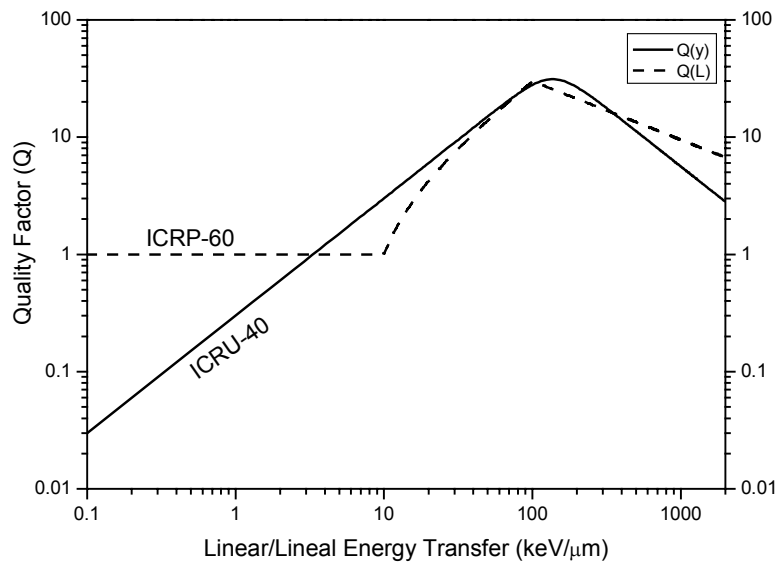


Figure 2.4: Different formulations of the quality factor. Quality factor, $Q(y)$, according to ICRU report 40 [24] (straight line) and according to ICRP 60 [23] (dashed line).

Radiation protection applications are primarily concerned with estimating the dose equivalent. For particles with a range of LET (L) the dose equivalent is defined as [6]:

$$H = \int_0^{\infty} Q(L)D(L)dL \quad (2.26)$$

Where the symbol $D(L)$ refers to the dose distribution as a function of LET and $Q(L)$ is a quality factor which weights the dose according to biological effect. Various forms of $Q(L)$ have been defined but the standard most recently adopted by ICRU and ICRP is the definition of $Q(L)$ presented in ICRP publication 60 [23], shown in Fig. 2.4.

$$Q(L) = \begin{cases} 1 & L < 10 \text{ keV}/\mu\text{m} \\ 0.32L - 2.2 & 10 < L < 100 \text{ keV}/\mu\text{m} \\ 300L^{-1/2} & L > 100 \text{ keV}/\mu\text{m} \end{cases} \quad (2.27)$$

In ICRU 40 [24], it was proposed that Q be based on lineal energy in 1 μm sites, i.e. $Q = Q(y)$. $Q(y)$ increases almost linearly to a maximum at $y \approx 150 \text{ keV}/\mu\text{m}$ and declines subsequently due to saturation. $Q(y)$ can be expressed by the formula [25]:

$$Q(y) = 0.3y \left[1 + \left(\frac{y}{137} \right)^5 \right]^{-0.4} \quad (2.28)$$

This is also illustrated in Fig. 2.4.

The main advantage in the choice of y rather than L is that it may be determined more accurately, and the selection of the site diameter of 1 μm permits relatively simple measurements. Note that the accuracy requirements are much less stringent in radiation protection compared to radiotherapy.

2.4.2 Radiotherapy application

For almost a century, ionizing radiation has been applied in the treatment of diseases, especially of cancer. The types of radiation initially employed were of relatively low LET (e.g. low energy X-rays and γ -rays from radium). However, modern therapy involves low LET and high LET radiation. For low LET radiation the differences in RBE are small while for high LET radiation the differences can be considerable. Therefore, microdosimetric methods are especially useful for high LET radiation therapy due to the requirement of quantitative specification of radiation quality. The high LET radiation therapies in which microdosimetric methods have been applied are Fast Neutron Therapy (FNT), Boron Neutron Capture Therapy (BNCT) and heavy ion therapy.

The benefit of high LET radiation therapy, compared to traditional radiation therapy, is based on two main considerations:

1. The high LET is important because of the oxygen effect: At low LET, the sensitivity of aerated cells is about three times greater than that of anoxic cells whilst at higher LET this difference is much less and the factor approaches 1 for LET values above 100 $\text{keV}/\mu\text{m}$ [6]. Tumors are generally poorly oxygenated and thus at higher LET a greater tumor dose may be delivered at the same normal tissue dose.
2. Except for neutrons (FNT), the spatial distribution of dose delivery is improved with high LET therapy. Due to the Bragg peak, the depth-dose profile of charged nuclear particles offers improved tumor to tissue absorbed doses. For BNCT, particular specificity may be gained due to the local deposition of high boron concentrations within a tumor.

For low LET radiation, absorbed dose is a good predictor of biological effects since the RBE does not vary significantly between X-rays, γ -rays or electrons in the energy range between about 1 to 50 MeV [26] and does not vary with position within the irradiated tissue. Thus, simple absorbed dose measurements suffice and microdosimetric studies are generally not needed for low LET radiation.

Empirical approaches have been developed based on calculating parameters from the microdosimetric spectrum $d(y)$ that correlate with RBE. The parameter \bar{y}_D is a measure of biological effectiveness under the conditions of low dose and minimal saturation effects. In an effort to improve the relationship between \bar{y}_D and observed biological effects, Kellerer and Rossi [27] proposed a saturation correction to account for the excessive ionization density of high lineal energy particles once cell death has occurred. The saturation corrected dose mean lineal energy y^* is given by:

$$y^* = \frac{\int_0^{\infty} y_{sat} y f(y) dy}{\int_0^{\infty} y f(y) dy} \quad (2.29)$$

where the saturation correction function y_{sat} is:

$$y_{sat} = \frac{y_0^2}{y} (1 - e^{-(y/y_0)^2}) \quad (2.30)$$

with $y_0 = 125 \text{ keV}/\mu\text{m}$.

Several studies in FNT beams have demonstrated that RBE values calculated from the saturation corrected dose mean lineal energy y^* are fairly well correlated with RBE data derived from radiobiological data [28-30]. Microdosimetric spectra have been extensively used to investigate radiation quality of neutron therapy facilities [31-33]. Several researchers have compared the radiation quality of neutron therapy facilities using microdosimetric measurements [34-36]. These results have shown that microdosimetric measurements, despite their empirical nature, are capable of discerning even subtle changes in the radiation field and provide insight into the interpretation of such changes.

2.4.3 Radiobiology

Radiation biology is concerned with targets that range in size over at least 10 orders of magnitude, between biomolecules and tissue of whole organisms. Most of the effects are ultimately due to DNA damage but in addition to their number the spatial distribution of the affected molecules is of importance in the causation of effects.

In 1972 Kellerer and Rossi formed the link between experimental microdosimetry, based on regional or site measurements, and radiobiology with the publication of the Theory of Dual Radiation Action (TDRA) [27]. The theory is based on a number of assumptions, including [37, 38]:

1. When a biological cell is exposed to ionizing radiation, the radiation produces sub-lesions within the cell and the number of sub-lesions is directly proportional to the energy imparted by the radiation.
2. A biological lesion is formed when sub-lesions combine with one another, possibly over relatively long distances on a sub-cellular scale.

3. Each lesion has a fixed probability of leading to a given biological effect.

Most importantly, the original theory was developed in a site model form compatible with TEPC measurement in simple spherical or cylindrical shapes. This leads to the final simplifying assumption:

4. All pairs of sub-lesions within a sensitive site have an equal probability of combining and zero probability outside the site.

Based on the assumption TDRA proposes that the mean number of lesions, $\varepsilon(D)$, after an absorbed dose D is:

$$\varepsilon(D) = k(\zeta D + D^2) \quad (2.31)$$

where k is a constant for a given biological system and ζ is the dose average of the specific energy (also written as z_D). The first term accounts for lesions formed by two sub-lesions that are produced in the same event (intra-track action) and the second term relates to the case of sub-lesions combining from two separate events (inter-track action).

The relative biological effectiveness (RBE see Equ. (2.3)) of high LET radiation H , relative to a low LET radiation L , is defined by:

$$R = \frac{D_L}{D_H} \quad (2.32)$$

where D_L and D_H are the absorbed doses of the two types of radiation causing equal effect. Utilizing equation (2.31) and equality of effect yields:

$$k(\zeta_H D_H + D_H^2) = k(\zeta_L D_L + D_L^2) \quad (2.33)$$

Substituting (2.33) into (2.32) gives:

$$R = \frac{1}{2D_H} \left[\sqrt{\zeta_L^2 + 4D_H(\zeta_H + D_H)} - \zeta_L \right] \quad (2.34)$$

The site model formulation of TDRA correctly predicts the inverse square root variation of RBE with dose (i.e. $\zeta_L \ll D_H \ll \zeta_H$, $R \approx \sqrt{\zeta_H/D_H}$). The domain in which the specific energy should be considered depends upon the average distance over which sub-lesions combine. Microdosimetric measurements of neutron beams employed in biological experiments indicate that the sites typically have a diameter of 0.2-2 μm [27, 37].

In the late seventies, it was recognized that the site model formulation of TDRA could not account for the effects of certain radiations such as soft X-rays [39, 40] or correlated pairs of charged particles [41, 42]. For instance, in a molecular ion beam experiment, it was found that if pairs of deuterons are separated by 90 nm the effect on the reproductive capability of

V79 cells was significantly different than for a single particle with twice the LET value. Yet the microdosimetric spectra for the two kinds of radiation are identical in volumes of the order of a few microns.

The TDRA was generalized by Kellerer and Rossi in 1978 with the introduction of the distance model formulation [43]. The generalized TDRA relaxed the site model assumption (4 above) and replaced it by:

4[#]. The probability $g(x)$ of sub-lesions combining is a function of their distance, x .

According to the distance model ζ in equation (2.31) becomes [6]:

$$\zeta = \int_0^{\infty} t(x)\gamma(x)dx \quad (2.35)$$

where $t(x)$ is a proximity function [6] specifying the spatial properties of the deposition of radiation energy and $\gamma(x)$ is the probability that two energy transfers separated by a distance x combine to form a lesion. The proximity function is a measure of the probability that the energy transfer points are separated by a distance x . On the other hand, the dose average specific energy is given by:

$$\bar{z}_D = \int_0^{\infty} t(x) \left[\frac{f_p(x)}{4\pi x^2 \rho} \right] dx \quad (2.36)$$

where $f_p(x)$ is the point pair distance distribution (ppdd) of the site where the specific energy is measured. Comparing the above two equations indicates that a measurement of \bar{z}_D yields the parameter ζ only if the microdosimeter and cell sensitive site have the same ppdd which is:

$$\gamma(x) = \frac{f_p(x)}{4\pi x^2 \rho} \quad (2.37)$$

Comparisons of experimentally determined $\gamma(x)$ with the function given by the right-hand side of the equation (2.37) indicate that the spherical TEPC is a poor representation of the sensitive geometry [42]. Finding a practically realizable detector structure that satisfies equation (2.37) may be difficult. However, Zaider and Rossi [44] have shown that any function $\gamma(x)$ may be represented as the algebraic superposition of ppdd's corresponding to spherical objects. Thus, the quantity ζ may be predicted from microdosimetric spectra measured in a series of spherical sites of different diameters. Implementations of these ideas suggest that 2-3 sites are sufficient. The site size required is very small of the order of tens of nanometers, which has consequently driven a demand for nanodosimetric detectors.

It has to be mentioned that the validity of the TDRA is under much debate with research actively being pursued in alternative radiobiological models such as Goodhead's repair model [37] and work by Zaider and Katz on track structure theory [45] (section 2.5.2).

2.4.4 Applications in Space and radiation effects on microelectronics

Aircrew and astronauts are exposed to evaluated levels of cosmic ionizing radiation of galactic and solar origin. Moreover, higher radiation levels in space naturally increase the biological risk in manned missions. To study the space environment, TEPCs have been flown on board of the space shuttle [46] and MIR space station [47]. The recorded microdosimetric spectra have been used to test radiation transport models and calculations [46]. The development and testing of such models may provide a system for predicting radiation quality during the spacecraft design phase. Microdosimetric measurements have similarly been performed in aircraft in order to quantify radiation effects on aircrew from secondary cosmic radiation [48, 49].

Radiation effects on electronics are more common at high altitude (avionics) and in space. The application of microdosimetry to radiation effects on microelectronics is a direct result of the current trend in the electronics industry towards manufacturing increasingly smaller devices. Consequently the amount of charge necessary for inducing a single-event upset (SEU) becomes correspondingly smaller [6]. In a manner similar to biological cell death, electronic memory cells may undergo state changes if sufficient energy is deposited in the sensitive region of the cell [50]. The sensitive region is localized around the depletion region of reverse-biased p-n junctions. The first evidence of SEU in memory cells was observed in 1975 by Binder [51] although the effect had been predicted in 1962 by Wallmark and Marcus [52]. Since then the effect has been extensively studied as testified by the large number of IEEE Nuclear Science journal publications devoted to SEU. Microdosimetric principles and techniques have been applied to several SEU problems based on the correlation of SEU and biological cell death [53-55, 6].

2.5 Other methods

For the sake of completeness, a few other commonly used experimental microdosimetry methods are briefly described in this section. Some methods are used to determine the microdosimetric parameters or to provide more detailed track information at small scale, other methods use site based detectors such as the TEPC but of a different concept. The interested reader may find in the literature [56, 57] recent useful reviews of detector developments that concentrate on neutron personal dosimeters.

2.5.1 Variance-Covariance method

Most of the systems measure pulses from single events, proportional to the energy imparted in the counter gas, convert the pulse height distribution to a distribution of dose in lineal energy, and evaluate dose rate, or dose equivalent rate by different approximations of the dependence of the quality factor on lineal energy.

An alternative technique for determination of the microdosimetric parameters is the variance method. In this case the electric charge proportional to the energy imparted over a specified time interval (including multiple events) is measured by an electrometer connected to the

TEPC. The fluctuations of the energy imparted in the counter are used to determine the dose average lineal energy or the dose average specific energy.

The variance technique is a method to study the single-event energy fluctuations without using single-pulse analysis. It started in the late 60's with a quite different approach. Their theoretical bases were elaborated by Kellerer [58] and experimentally developed by Bengtsson [59]. The aim of the variance technique is to extract from multi-event energy fluctuation some information about the single-event distribution.

The dose average energy imparted of single event, $\bar{\varepsilon}_{1,D}$, is the ratio of the second and first moment, $\overline{\varepsilon_1^2}$ and $\bar{\varepsilon}_1$, of the single-event distribution. Furthermore, it can be calculated using the first and the second moment, $\bar{\varepsilon}$ and $\overline{\varepsilon^2}$, of a multi-event distribution:

$$\bar{\varepsilon}_{1,D} = \frac{\overline{\varepsilon_1^2}}{\bar{\varepsilon}_1} = \frac{\overline{\varepsilon^2} - \bar{\varepsilon}^2}{\bar{\varepsilon}} = \left(\frac{\overline{\varepsilon^2}}{\bar{\varepsilon}^2} - 1 \right) \cdot \bar{\varepsilon} = V_{rel} \cdot \bar{\varepsilon} \quad (2.38)$$

The single-event dose-mean imparted energy is therefore equal to the product of the mean value of the multi-event imparted energy and the relative variance of the multi-event imparted energy, V_{rel} . Therefore this method is called variance method.

The variance method is, however, not applicable in time-varying fields since the variance of the beam invalidates the proportionality of the multi-event relative variance with the counter signal relative variance. In 1984 Kellerer and Rossi [60] proposed utilizing of a second detector, operating simultaneously with the first detector, to overcome this limitation. Utilizing two detectors, the relative variance of the signals of each detector and the relative covariance from the combination of the signals of the two detectors will be obtained. This has become known as the variance-covariance method. The variance-covariance method based on the determination of the fluctuation of the energy imparted in the tissue equivalent proportional counter provides a technique for determination of the dose averaged lineal energy \bar{y}_D and the dose equivalent. The dose averaged energy imparted of a single event is then:

$$\bar{\varepsilon}_{1,D} = (V_{rel} - C_{rel}) \cdot \bar{\varepsilon} \quad (2.39)$$

where V_{rel} is the relative variance of the response of both detectors and C_{rel} is the relative covariance of the response of the two detectors (detector A and B) and it is given by:

$$C_{AB} = \frac{\overline{\varepsilon_A \varepsilon_B}}{\bar{\varepsilon}_A \bar{\varepsilon}_B} - 1 \quad (2.40)$$

Equation (2.39) is applicable when the dose rate varies but the ratio of the dose rates for the two chambers is constant. The detectors are assumed to be uncoupled, i.e. the distance of the chambers must be large enough to ensure that the single particle does not impart energy, directly or indirectly, in both of them.

Equation (2.39) becomes:

$$\bar{\varepsilon}_{1,D} = \left(\frac{\overline{\varepsilon_A^2}}{\bar{\varepsilon}_A^2} - \frac{\overline{\varepsilon_A \varepsilon_B}}{\bar{\varepsilon}_A \bar{\varepsilon}_B} \right) \cdot \bar{\varepsilon}_A \quad (2.41)$$

for detector A , and it is similar for detector B .

Thus for the variance-covariance method simultaneous measurements in two detectors and two independent channels of signal processing are needed. They must contain low noise electronics with high resolution to allow the precise determination of the fluctuations of the energy deposition. Furthermore, while for the single event measurements the conventional and widely developed pulse height technique is applicable, the variance method requires high precision current measurements. Kyllönen et al. have used these methods to measure cosmic radiation on board of aircraft [61], in neutron beams between 71 keV and 180 MeV and in the cosmic radiation reference field (CERF) at CERN [62].

2.5.2 Nanodosimetry and Track-nanodosimetry

It is known that the biological effectiveness of radiation does not simply depend on the mean value of energy deposition, but on its stochastic distribution. The stochastic distribution of energy deposition in turn depends on the target size. There is general agreement about the main target size, which should be comparable to or smaller than the chromatin fiber thickness, that is about 25 nm [63]. However, the lateral extension of the ionization cloud surrounding the majority of charged particles used in radiobiological experiments are larger than the size of chromatin fiber thickness. It is therefore reasonable to believe that the ionization fluctuation, and hence the biological effectiveness, depends on the position of the site within the particle track. As a consequence, the track structure is believed to be very important to determine the quality of radiation.

The measurement of the ionization yield in nanometric volumes positioned at different distances from the particle track with the resolution of one ionization event is called track-nanodosimetry. De Nardo et al. [63] have constructed a 19 nm wall-less probe able to collect the electrons inside the interaction region and to transfer them to the single-electron counter. Another conceptually similar counter, but based on ion detection instead of electron detection, has been constructed [64, 65] which is able to measure the ionization distribution in a propane sensitive volume from 1 nm to about 20 nm. Furthermore, other experimental approaches to measure cluster distributions in nanometric sites, such as a gas Jet counter [66] based on ion detection and Optical Avalanche Chamber (OPAC) [67] based on a time projection chamber with optical readout, have proved able to measure properly ionisation distributions in nanometric sites. Moreover, a single grid, parallel-plate proportional counter [68] has been applied for use as a nano-dosimeter.

Low pressure cloud chambers have been employed in the study of track structures [69-71]. A three dimensional pattern of droplets created by individual ionization may be resolved and stereoscopically photographed [71]. Cloud chamber dosimetry provides rich detail on the location of individual ionization within the gas. However, it is a difficult process generally restricted to the research domain.

The three dimensional distribution of an individual ionization within a gas may also be determined using an optical ionization chamber as proposed by Turner [72]. The electrons in the particle track are made to oscillate rapidly by the application of an external, short duration, high-voltage electric field. The excited electrons produce additional ionization and electric excitation of the gas molecules in their immediate vicinity leading to abundant light emission (fluorescence) from the gas allowing the location of the electrons to be determined. Two digital cameras perpendicular to one another record the light emission. Turner et al. [72] predict a resolution of about 10 nm, based on a position uncertainty of about 1 mm at a gas pressure of 667 Pa (5 Torr). This may also prove a useful tool in the field of nanodosimetry as well as for track structure analysis.

Finally, it should be mentioned that nanodosimetry and track-nanodosimetry experimental data are scarce in literature. The availability of different experimental set-ups, to investigate the track structure at the nanometer level, is initiating the study of interaction mechanisms occurring in irradiated DNA.

2.5.3 Microstrip Gas Counters (MSGC)

The microstrip gas counter (MSGC) is a high rate and high spatial resolution device [73] which is similar to the multiwire proportional chamber (MWPC) except that the wires have been replaced by alternating anodes and cathodes of fine strips of metal formed on a substrate. The main advantage of MSGCs over MWPCs is the spacing between the centers of two neighboring anodes, which is 200 μm for MSGC and 500 μm or greater for MWPC. The high count rate and high spatial resolution (sub-millimeter readout spacing) are the principle features of MSGCs to experimental microdosimetry. Dubeau et al. [74, 75] have developed a device which combines MSGC with TEPC (chapter 3) design concepts. This device has been configured to simulate sub-micron tissue site sizes.

2.5.4 Solid state counter

As currently practiced, microdosimetric information on energy deposition comes almost entirely from either gas phase experiments (section 2.2) or gas phase analytical and Monte Carlo transport calculations of particle tracks [76-78]. The results scaled to the density of liquid water, are assumed to represent intracellular matter. The relationship between gas and tissue behavior and the manner of converting this information (gas to solid) is poorly understood. Furthermore, recent studies show that biological tissues should be treated as a solid state type of medium as opposed to the gas phase approximation [79]. Zaider et al. have shown significant phase effects in the estimation of microdosimetric parameters by theoretical calculations. Calculations of the energy deposition by 30 keV electrons in water vapor and condensed water sites ($d = 1 \mu\text{m}$) gave a 50% higher mean specific energy in condensed water relative to water vapor with equally large differences in the lineal energy spectra. Therefore, efforts were made to develop solid state microdosimetry. Bradley et al. [80, 38] have developed a silicon microdosimeter based on silicon. However, comparison of the silicon microdosimeter to a proportional counter shows that the silicon counter is still not a good alternative, despite of some benefits, due to the less well-defined sensitive volume, worse tissue equivalency, smaller radiation hardness and lower sensitivity at low energy. Currently, the investigations are going on to improve these shortcomings which could make

them feasible for a good alternative of proportional counters in many applications of microdosimetry. Moreover, these devices are developed not only because they may provide more accurate quality factors, but also because they are more practical for microdosimetry in routine health physics measurements.

References

- [1] Sax, K. *Chromosome aberrations induced by X-rays*. J. Genetics, 23 (1938) 494.
- [2] Lea, D.E. and Catchside, D.G. The mechanism of induction of radiation of chromosome aberrations in Tradescantia. J. Genetics, 44 (1942) 216.
- [3] Wolff, S. Interpretation of induced chromosome breakage and rejoining. Radiat. Res. 1 (1959) 453.
- [4] Neary, G.J., Preston, R.J. and Savage, J.R.K. *Chromosome aberrations and the theory of RBE III. Evidence from experiments with soft X-rays, and a consideration of the effects of hard X-rays*. Int. J. of Radiat. Biol., 12 (1967) 317.
- [5] Kliauga, P. Microdosimetry at middle age: some old experimental problems and new aspirations. Radiat. Res. 124 (1990) S5.
- [6] Rossi, H.H. and Zaider, M. *Microdosimetry and its applications*. Springer 1996.
- [7] International Commission on Radiation Units and Measurements, *Fundamental quantities and units for ionizing radiation*. (ICRU report; 60), Bethesda, Maryland, (1998).
- [8] Hall, E.J., Gross, W., Dvorak, R.F., Kellerer, A.M. and Rossi, H.H. Survival curves and age response functions for Chinese hamster cells exposed to X-rays or high LET alpha particles. Radiat. Res. 52 (1972) 88.
- [9] Waker, A.J. *Principal of Experimental Microdosimetry*. Radiat. Prot. Dosim. 61(4) (1995) 297.
- [10] International Commission on Radiation Units and Measurements, *Radiation Quantities and Units*. (ICRU report; 33), Bethesda, Maryland, (1980).
- [11] International Commission on Radiation Units and Measurements, *Microdosimetry*. (ICRU report; 36), Bethesda, Maryland, (1983).
- [12] Kellerer, A.M. Consideration on the random traversal of convex bodies and solutions for general cylinders. Radiat. Res. 47 (1971) 359.
- [13] Cauchy, A. *Memoire sur la rectification des courbes et la quadrature des surface courbe*. Oeuvres Completes. Vol. 2 (Gauthier-Villard, Paris) (1908).
- [14] International Commission on Radiation Units and Measurements, *Quantities and Units in Radiation Protection Dosimetry*. (ICRU report; 51), Bethesda, Maryland, (1993).
- [15] Fano, U. Note on the Bragg-Gray cavity principle for measuring energy dissipation. Radiat. Res. 1 (1954) 237.
- [16] International Commission on Radiation Units and Measurements, *Neutron Dosimetry for Biology and Medicine*. (ICRU report; 26), Washington, D.C., (1977).
- [17] Burlin, T.E. *A General Theory of Cavity Ionization*. Brit. J. Radiol. 39 (1966) 727.
- [18] Caswell, R.S. *Deposition of energy by neutrons in spherical cavities*. Radiat. Res. 27 (1966) 92.
- [19] Cruz, G.A.S., Palmer, M.R., Matatagui, E. and Zamenhof, R.G. *A theoretical model for event statistic in microdosimetry. I: Uniform distribution of heavy ion tracks*. Med. Phys. 28 (6) (2001) 988.
- [20] Cruz, G. A. S., Palmer, M. R., Matatagui, E. and Zamenhof, R. G. *A theoretical model for event statistic in microdosimetry. II: Nonuniform distribution of heavy ion tracks*. Med. Phys. 28 (6) (2001) 997.
- [21] Rossi, H. H. *Experimental limitations of microdosimetry*. Presented at Proceedings Second Symposium on Microdosimetry, Stresa, Italy. (1969) 303.
- [22] Kellerer, A.M. and Chmelevsky, D. *Concepts of Microdosimetry I Quantities*. Radiat. Environ. Biophys. 12 (1975) 61.
- [23] International Commission on Radiological Protection. *Recommendation of the International Commission on Radiological Protection*. (ICRP Publication 60). Oxford, Pergamon, 1990.
- [24] International Commission on Radiation Units and Measurements. *The quality factor in radiation protection*, (ICRU report; 40), Bethesda, Maryland, (1986).
- [25] Kellerer, A.M., and Hahn, K. *Considerations on a Revision of the Quality Factor*. Rad. Res. 114 (1988) 480.

- [26] Wambersie, A., Pichet, P. and Menzel, H.G. *The Role of Microdosimetry in Radiotherapy*. Radiat. Prot. Dosim. 31 (1990) 421.
- [27] Kellerer A.M. and Rossi, H. H. *The theory of dual radiation action*. Curr. Top. Radiat. Res. 8 (1972) 85.
- [28] Hall, E.J., Rossi, H. H., Kellerer, A. M., Goodman, L. and Marino, S. *Radiobiological studies with monoenergetic neutrons*. Radiat. Res. 54 (1973) 431.
- [29] Stinchcomb, T.G., Kuchnir, F.T., Myriantopoulos, L.C., Horton, J.L. and Roberts, W. K. *Correlation of microdosimetric measurements with the relative biological effectiveness from clinical experience for two neutron therapy beams*. Med. Phys. 13 (1986) 201.
- [30] Beach, J.L. and Milavickas, L.R. *Microdosimetric measurements of radiation quality variations in homogeneous phantoms irradiated by fast neutron beams*. Med. Phys. 9 (1982) 52.
- [31] Fidorra, J. and Booz, J. *Microdosimetric investigation on collimated fast-neutron beams for radiation therapy: I. Measurements of microdosimetric spectra and particle dose fractions in a water phantom for fast neutrons from 14 MeV deuterons on beryllium*. Phys. Med. Biol. 26 (1981) 27.
- [32] Fidorra, J. and Booz, J. *Microdosimetric investigation on collimated fast-neutron beams for radiation therapy: I. The problem of radiation quality and RBE*. Phys. Med. Biol. 26 (1981) 43.
- [33] Stafford, P.M., Horton, J.L. and Almond, P.R. *A microdosimetric characterization of a cyclotron-produced neutron beam*. Med. Phys. 14 (1987) 1015.
- [34] Pihet, P. *Etude microdosimétrique de fasiceaux de neutrons de haute energie. Applications dosimétriques et radiobiologiques*. Louvain: Catholic University Louvain, (1989).
- [35] Pihet, P., Menzel, H.G., Schmidt, R., Beauvain, M. and Wambersie, A. *Biological weighting function for RBE specification of neutron therapy beams. Intercomparison of 9 European centres*. Radiat. Prot. Dosim. 31 (1990) 437.
- [36] Gueulette, J., Menzel, H.G., Pihet, P. and Wambersie, A. *Specification of radiation quality in fast neutron therapy: Microdosimetric and radiobiological approach* in Fast neutrons and high-LET particles in cancer therapy, vol. 150, R. Engenhart-Cabillic and A. Wambersie, Eds., 1 ed. Berlin-Heidelberg: Springer-Verlag, 1998, pp. 31-53.
- [37] Goodhead, D.T. *An assessment of the role of microdosimetry in radiobiology*. Radiat. Res. 91 (1982) 45.
- [38] Bradley, P.D. *The development of a novel silicon microdosimeter for high LET radiation therapy*. Thesis, Department of Engineering Physics, University of Wollongong, (2000).
- [39] Cox, R., Thacker, J. and Goodhead, D.T. *Inactivation and mutation of cultured mammalian cells by aluminium characteristic ultrasoft x-rays II. Dose-responses of Chinese hamster and human diploid cells to aluminium x-rays and radiations of different LET*. International Journal of Radiation Biology and Related Studies. 31 (1997) 561.
- [40] Brenner, D.J. and Zaider, M. *Modification of the theory of dual radiation action for attenuated fields. II. Application to the analysis of soft x-ray results*. Radiat. Res. 99 (1984) 491.
- [41] Rossi, H.H. *Biophysical studies with spatially correlated ions. 1. Background and theoretical considerations*. Radiat. Res. 78 (1979) 185.
- [42] Kellerer, A.M., Lam, Y.P. and Rossi, H.H. *Biophysical studies with spatially correlated ions. 4. Analysis of cell survival data for diatomic deuterium*. Radiat. Res. 83 (1980) 522.
- [43] Kellerer, A.M. and Rossi, H.H. *A generalized formulation of dual radiation action*. Radiat. Res. 75 (1978) 471.
- [44] Zaider, M. and Rossi, H.H. *On the application of microdosimetry to radiobiology*. Radiat. Res. 113 (1988) 15.
- [45] Zaider, M. *Microdosimetry and Katz's track structure theory*. Radiat. Res. 124 (1990) 16.
- [46] Shinn, J.L., Bahdwar, G.D., Xapsos, M.A., Cucinotta, F.A. and Wilson, J.W. *An analysis of energy deposition in a tissue equivalent proportional counter onboard the space shuttle* Radiat. Meas. 30 (1999) 19.
- [47] Bottollier-Depois, J.F., Lebaron-Jacobs, L., Siegrist, M., Duvivier, E., Almarcha, B., Dachev, T.P., Semkova, J.V., Matviichuk, Y.N., Koleva, R.T., Tomav, B.T., Baynov, P.T., Petrov, V.M., Shurshakov, V.V., Begin, V. and Koslova, S. B. *Tissue equivalent detector data obtained recently on MIR space station. Comparison with solid state detector data*. Adv. Space Res. 18 (1996) 171.
- [48] Lindborg, L., Kyllonen, J.E., Beck, P., Bottollier-Depois, J.F., Gerdung, S., Grillmaier, R.E. and Schrewe, U. *The use of a TEPC for reference dosimetry*. Radiat. Prot. Dosim. 86 (1999) 285.
- [49] Dyer, C.S. and Truscott, P.R. *Cosmic radiation effects on avionics*. Radiat. Prot. Dosim. 86 (1999) 337.
- [50] Xapsos, M.A. *Microdosimetry theory for microelectronics applications*. Nucl. Instr. and Meth. B 184 (2001) 113.

- [51] Binder, D., Smith, E.C. and Holman, A.B. *Satellite anomalies from galactic cosmic rays*. IEEE Trans. Nucl. Sci. 22 (1975) 2675.
- [52] Wallmark, J.T. and Marcus, S.M. *Minimum size and maximum packing density of nonredundant semiconductor devices*. Proc. of IRE (1962) 286.
- [53] Bradford, J.N. *Single event error generation by 14 MeV neutrons reactions in silicon*. IEEE Trans. Nucl. Sci. 27 (1980) 1480.
- [54] Bradford, J.N. *Microvolume energy deposition from high energy proton silicon reactions*. IEEE Trans. Nucl. Sci. 29 (1982) 2085.
- [55] Farrell, G.E. and McNulty, P.J. *Microdosimetric aspects of proton-induced nuclear reactions in thin layers of silicon*. IEEE Trans. Nucl. Sci. 29 (1982) 2012.
- [56] Bartlett, D.T., Tanner, R.J. and Thomas, D.J. *Active neutron personal dosimeters – a review of current status*. Radiat. Prot. Dosim. 86 (1999) 107.
- [57] Barthe, J., Bordy, J.M. and Lahaye, T. *Electron neutron dosimeters: History and state of the art*. Radiat. Prot. Dosim. 70 (1997) 59.
- [58] Kellerer, A.M. *Mikrodosimetrie*. GSF-Bericht B-1 (1968).
- [59] Bengtsson, L.G. *Assessment of dose equivalent from fluctuation of energy depositions*. In: Proc. 2nd Symp. On Microdosimetry, EUR-4552 (Brussels: CEC) (1970) 375.
- [60] Kellerer, A.M. and Rossi, H.H. *On the determination of microdosimetric parameters in time-varying radiation fields: the variance-covariance method*. Radiat. Res. 97 (1984) 237.
- [61] Kyllönen, J.E., Lindberg, L. and Samuelson, G. *Cosmic radiation measurements on-board aircraft with the variance method*. Radiat. Prot. Dosim. 93 (2001) 197.
- [62] Kyllönen, J.E., Lindberg, L. and Samuelson, G. *The response of the sievert instrument in neutron beams up to 180 MeV*. Radiat. Prot. Dosim. 94 (2001) 227.
- [63] De Nardo, L., Alkaa, A., Khamphan, C., Conte, V., Colautti, P., Ségur, P. and Tornielli, G. *A detector for track-nanodosimetry*. Nucl. Instr. and Meth. A 484 (2002) 312.
- [64] Shchemelinin, S., Breskin, A., Chechik, R., Colautti, P. and Schulte, R.W.M. *First measurements of ionisation clusters on the DNA scale in a wall-less sensitive volume*. Radiat. Prot. Dosim. 82 (1999) 43.
- [65] Chechik, R. *Advances in Single-Charge Detectors and Their Applications*. IEEE Trans. Nucl. Sci. NS-47 (2000) 1404.
- [66] Pszona, S. *A new method for measuring ion clusters produced by charged particles in nanometre track sections of DNA size*. Nucl. Instr. and Meth. A 447 (2000) 601.
- [67] Titt, U. *A time projection chamber with optical readout for charged particle track structure imaging*. Nucl. Instr. and Meth. A 416 (1998) 85.
- [68] Tamboul, J.Y. *A proportional counter for measurement of the bio-effectiveness of ionising radiations at the DNA level*. Nucl. Instr. and Meth. B 184 (2001) 597.
- [69] Budd, T., Kwok, C. S., Marshall, M. and Lythe, S. *Microdosimetric properties of alpha-particle tracks measured in a low pressure cloud chamber*. Radiat. Res. 95 (1983) 217.
- [70] Budd, T. and Marshall, M. *Microdosimetric properties of electron tracks measured in a low pressure cloud chamber*. Radiat. Res. 93 (1983) 19.
- [71] Stonell, G.P., Marschall, M. and Simmons, J.A. *Track studies in water vapor using a low pressure cloud chamber I. Macroscopic measurements, II. Microdosimetric measurements*. Radiat. Res. 136 (1993) 341.
- [72] Turner, J.E., Hunter, S.R., Hamm, R.N., Wright, H.A., Hurst, G.S. and Gibson, W.A. *Development of an optical digital ionisation chamber*. Radiat. Prot. Dosim. 29 (1989) 9.
- [73] Oed, A. *Position-sensitive detector with microstrip anodes for electron multiplication with gases*. Nucl. Instr. and Meth. A 263 (1988) 351.
- [74] Dubeau, J., Waker, A.J., Bigger, M., Rayner, M.D., Sommerville, E.W. and Welch, S.E. *Dosimetric response to γ rays and neutrons of a tissue-equivalent microstrip gas counter*. Radiat. Prot. Dosim. 91 (2000) 391.
- [75] Dubeau, J., Dixit, M.S., Sommerville, E.W., Waker, A.J., Surette, R.A., Oakham, F.G. and Karlen, D. *Experimental microdosimetry with microstrip gas counter*. Presented at The proceedings of the twelfth symposium on microdosimetry: An interdisciplinary meeting on radiation quality, molecular mechanisms, cellular effects and health consequences of low level ionizing radiation, Keble College, Oxford, UK, 1996.
- [76] Coyne, J. J. and Caswell, R. S. *Neutron Energy Deposition on the Nanometer Scale*. Radiat. Prot. Dosim. 44 (1992) 49.
- [77] Caswell, R. S. and Coyne, J. J. *Interaction of Neutrons and Secondary Charged Particles with Tissue: Secondary Particles Spectra*. Radiat. Res. 52 (1972) 448.

- [78] Zaider, M. and Brenner, D. J. *Evaluation of a specific quality function for mutation induction in human fibroblasts*. Radiat. Prot. Dosim. 15 (1986) 79.
- [79] Zaider, M., Bardash, M.J. and Ladik, J. *Solid state microdosimetry*. Radiat. Prot. Dosim. 85 (1999) 443.
- [80] Bradley, P.D., Rosenfeld, A.B. and Zaider, M. *Solid state microdosimetry*. Nucl. Instr. and Meth. B 184 (2001) 135.

Chapter 3

Tissue-Equivalent Proportional Counter: Principles of Operation and Application

When radiation interacts with the sensitive medium of a detector a change in the state of that medium is produced which can be detected, and in most cases measured. This is the principle operation of all radiation detectors [1]. Some detectors provide a measurable parameter which yields information on the amount of energy which the radiation deposits within the medium. When the medium of interaction with radiation is a gas-filled chamber, the detectors are classified as gaseous. The proportional counter belongs to the class of gaseous detectors which analyse individual ionisation events. The essential characteristic of a proportional counter is its ability to amplify the ionisation from a single particle passage into a signal which is large enough to be distinct from electronic noise and consequently detectable. In a proportional counter charge amplification occurs, a process in which the relatively small number of ions produced by a single event is multiplied through secondary ionisation within the gas. The amplified signal is proportional to the primary signal.

Proportional counters are extensively used in experimental microdosimetry which is the study and interpretation of single-event energy deposition at microscopic sites of tissue (chapter 2). The equivalence to the human tissue is reached by employing Tissue-Equivalent (TE) materials. That is the reason for constructing the walls of the proportional counter out of a tissue-equivalent plastic and the filling gas has almost the same composition as human tissue. Therefore, these detectors are called Tissue-Equivalent Proportional Counter (TEPC). Simulation of a microvolume is carried out by the reduction of the gas pressure (section 2.2.1). The true versatility of microdosimetry as an experimental method was fully appreciated after the dual nature of the TEPC, i.e. it combines the functions of both a spectrometer and a dosimeter, was systematically investigated.

In this chapter, first the TEPCs and their principles will be discussed (section 3.1). The gas system and the electronics are explained in section 3.2 and 3.3, respectively. Some basic aspects of proportional counters such as gas amplification, average energy required per ion

pair and energy resolution are introduced in section 3.4. The distortion of microdosimetric spectra due to the wall effects are discussed in section 3.5 while section 3.6 is focused on the statistical variation in microdosimetry. The way in which the measured spectra are generally calibrated is explained in section 3.7. Finally, the properties of the Gas Electron Multiplier (GEM) are discussed in section 3.8.

3.1 The Counter

3.1.1 Gas filled counter

A proportional gas filled counter is a kind of ionisation chamber, filled with gas, to measure the charge of the ions of one sign created by the radiation. Typical for these detectors is the phenomenon of gas multiplication which relies on the fact that the electric field within the counter is high enough to enable secondary ionisation, proportional to the amount of primary ionisation. This will be discussed in more detail in section 3.4.

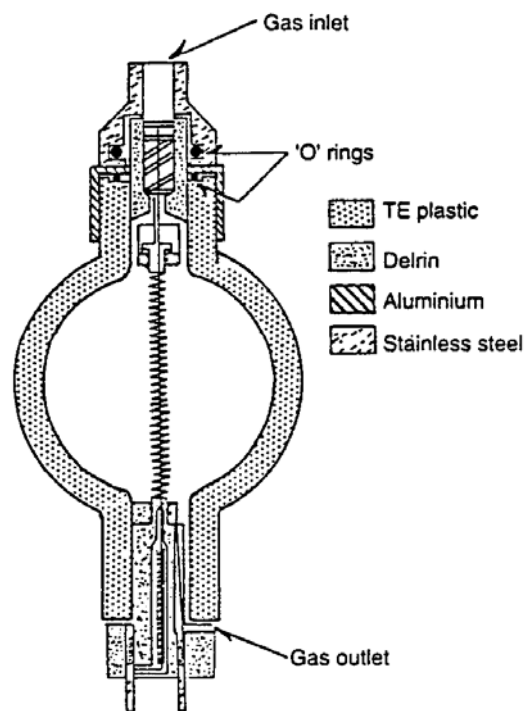


Figure 3.1: A typical spherical Tissue-Equivalent Proportional Counter (TEPC) with helix. This counter is often called “Rossi counter”[1].

To obtain information about the level of effect of radiation to human beings it is necessary to consider the absorbed dose D within the cell. Biological damage can lead to mutations or cell death, but it also can be repaired. Thus one has to simulate the dimensions of a cell or strictly speaking the dimensions of sub cellular targets like the cell nucleus (about 2 μm of diameter)

and the chromatin fibre (about 25 nm of diameter) consisting of DNA (about 2 nm of diameter). By using a proportional counter (PC), volumes are simulated which have the same range as cell structures. The simulation is performed by the reduction of the gas pressure which has been explained in section 2.2.1. The advantage of proportional counters is that the ionising particles, liberated by the radiation are multiplied in an electric field. This results in an amplified output signal proportional to the number of primary ionisation. The PC conventionally applied in microdosimetry (see chapter 2) has walls made of Tissue-Equivalent (TE) plastic (section 3.1.3) and is filled with TE gas (see section 3.2.1). Therefore the PCs used in microdosimetry called Tissue-Equivalent Proportional Counter (TEPC).

In general a TEPC consists of two electrodes: the wall of the counter is the cathode and the central wire the anode. Applying a helix around the anode provides a more uniform electric field along the anode. This type of counter is also known as Rossi counter due to the innovative design of Harold Rossi and his co-workers in mid-nineteen-fifties. A typical spherical TEPC (Rossi counter) with helix is shown in Fig. 3.1. Under the conditions for the Bragg-Gray principle (section 2.2.1) the absorbed dose to the TE material of the counter can be determined.

In summary, the TEPC belongs to the class of pulse detectors which analyse individual ionisation events. It is almost universally designed with a central anode surrounded by a cathode. In this configuration, the electric field becomes stronger in the vicinity of the anode. A positive potential applied to the anode causes electrons from ionising events to drift toward the anode. At a distance from the anode determined by the detector characteristics and applied voltage, these electrons will obtain a kinetic energy capable of ionisation of gas molecules between successive collisions. Moreover, the new electrons produced will also be capable of producing ionisation in the gas (section 3.4.2). The geometry of a TEPC is an important aspect which is discussed in the following section.

3.1.2 Detector geometry considerations

The choice of the detector geometry is the essential first step in the design of a TEPC. In general the intent of experimental microdosimetry is to model the energy deposited in volumes that are similar to critical tissue components such as cells or cell nuclei. Such components are frequently modeled as oblate spheroids or more simplistically as spheres. A spheroid is an ellipsoid with two axis of equal length and it is oblate if the third axis is smaller than the common axis length. The cells are usually randomly orientated unless they are in a flattened state characteristic of a tissue culture. Thus, even with a directional radiation source, the average response is that of a single cell in an isotropic field.

The microdosimetric measurements are generally performed using proportional counters having a spherical or cylindrical cavity. The spherical counter is preferred for two main reasons; the sphere is the only volume with an isotropic response and it has the lowest relative variance of chord lengths. Cylindrical counters have evolved due to their simpler design. Such counters do not have an isotropic response and simulation of an isotropic response, by the rotation of the counter under a constant fluence, is generally impractical.

Kellerer published an excellent paper [3] outlining the criteria for the equivalence of spherical and cylindrical proportional counters in microdosimetry.

Table 3.1: The chord length distribution and the mean chord length for various convex shapes.

SHAPE	CHORD LENGTH DISTRIBUTION	MEAN CHORD LENGTH
Sphere	$\frac{2l}{d^2}$, $0 \leq l \leq d$, l = chord length, d = diameter	$\frac{2d}{3}$, d = diameter
Cylinder	(see [2, 3, 4, 7, 8])	$\frac{d \cdot h}{(d/2) + h}$, d = diameter, h = height
Spheroid	$\frac{2l}{c_1 d^2} \left[c_2 + \frac{\sqrt{ 1-e^2 }}{4(e^{-2}-1)} \left\{ \sqrt{\frac{d^2}{l^2}-1} \left(\frac{d^3}{l^3} + \frac{3d}{2l} \right) + \frac{3}{2} c_i \left(\frac{d}{l} \right) \right\} \right]$ $c_i(x) = \begin{cases} \cos^{-1}(x) & \text{for } 0 \leq x \leq 1 \\ \cosh^{-1}(x) & \text{for } x > 1 \end{cases}$ $c_1 = \frac{1}{2} + \frac{e^2}{2\sqrt{ 1-e^2 }} c_i \left(\frac{1}{e} \right), \quad c_2 = \frac{1}{4e^2} + \frac{3}{4} c_1$ <p>e = elongation = smallest diameter/ largest diameter</p>	$\frac{8d \cdot e\sqrt{1-e^2}}{6\sqrt{1-e^2} + 3e^2 \log \left(\frac{1+\sqrt{1-e^2}}{1-\sqrt{1-e^2}} \right)}$ <p>e = elongation, d = main diameter</p>
Hemisphere	$\frac{2l}{3\pi^2} H(r-l) + \frac{1}{\pi r} c_1 + \frac{2r}{3\pi l^2} \left(c_1 + 2\frac{r}{l} \left(\cos^{-1} \left(\frac{l}{2r} \right) - \frac{\pi}{2} H(r-l) \right) \right)$ $c_1 = \sqrt{1 - \frac{l^2}{4\pi r^2}}$ <p>r = radius, l = chord length, H = step function</p>	$\frac{8r}{9}$ <p>r = radius</p>
Cube	$\frac{8}{3a\pi} \quad x=0$ $k(8x^3 - 3x^4) \quad 0 < x \leq 1$ $k(6\pi + 6x^4 - 1 - 8(2x^2 + 1)\sqrt{x^2 - 1}) \quad 1 < x \leq \sqrt{2}$ $k(6\pi + 3x^4 - 5 + 8(x^2 + 1)\sqrt{x^2 - 2} - 24Tan^{-1}(\sqrt{x^2 - 2})) \quad \sqrt{2} < x \leq \sqrt{3}$ $0 \quad x > \sqrt{3}$ <p>$x = l/a$, l = chord length, a = side length and $k = 1/(3a\pi x^3)$</p>	$\frac{2a}{3}$ <p>a = side length</p>

The lineal energy depends on the mean chord length of the collecting volume. The mean chord length may be calculated using the formula provided by Cauchy, which states that for any convex body, the mean chord length is equal to $4V/S$, where V is the volume and S is the surface area (see section 2.1.2). It is apparent from this formula that the mean chord length of a right cylinder (height equal to diameter) is the same as that of a sphere with the same

diameter d . However, the distribution of chord length is different. Moreover, the maximum chord length in such a cylinder is $d\sqrt{2}$, whereas in a sphere it is just d . The mean chord length and the chord length distribution for different collecting volume shapes are shown in Table 3.1. It can be seen that the chord length distributions differ significantly. The relative variance of chord lengths in spherical and cylindrical cavities may be found in Kellerer [2]. Although the relative variance of the sphere (0.125) is much less than that of the right cylinder (~ 0.25), the contribution of the variance in chord length distribution to the total relative variance is usually quite small [3]. The total relative variance involved in TEPC microdosimetry is generally dominated by straggling effects (section 3.6). The equivalence of spherical and right cylindrical detector volumes for microdosimetry has been further demonstrated elsewhere, both theoretically [4] and empirically [5]. Based on these criteria, the use of a right cylindrical detecting volume should have no significant effects on the single event spectrum.

3.1.3 Materials

Traditionally, proportional counters have been designed to simulate energy deposition in small tissue volumes. Tissue equivalence requires that the mass collision stopping powers of charged particles in the counter and the interaction cross section of the counter materials are identical to tissue. This requirement is fulfilled by utilizing materials with elemental compositions approaching that of standard muscle tissue as specified by ICRU [9]. Such a requirement conflicts somewhat with practical constraints such as electric conductivity, rigidity, and machining.

It is obvious that the high content of oxygen in tissue will not allow a truly tissue-equivalent material which is both mechanically stable and electrically conductive. This latter requirement can be achieved by substituting carbon for oxygen. As a consequence, differences in energy response due to the replacement of oxygen by carbon is expected. However, the differences in terms of energy response for photons are negligible since the atomic numbers of oxygen and carbon are similar [10]. These elements also possess very similar neutron cross sections from tens of keV to 10 MeV. For neutrons above 10 MeV the substitution of carbon for oxygen leads to poorer tissue equivalence due to differences in inelastic neutron interactions. However, to maintain tissue equivalence for fast neutrons, the hydrogen and nitrogen content must match that of tissue as close as possible.

Various plastics have been developed which meet the requirements of tissue-equivalence. The plastic formulation for use as a wall material was originally developed by Shonka and designated A-150 [11]. This conducting plastic is a mixture of calcium fluoride, polyethylene (for hydrogen), nylon (for nitrogen) and carbon (as a conductive replacement for oxygen). The elemental composition of muscle tissue [9], the muscle equivalent conductive plastic, A-150, and various insulating materials used in TEPCs, depending on their specific use, are listed in Table 3.2.

The wall of the TEPC used in this work is made of tissue-equivalent A-150 plastic and therefore also serves as the detector cathode. The insulating material is made of Rexolite®

1422 cross-linked polystyrene³. Rexolite was chosen due to its high volume resistivity ($\sim 10^{16}$ Ω cm), its low water absorption properties, and its relatively high heat capacity (allowing it to withstand bake-out temperatures). Furthermore, Rexolite has very good radiation stability. The density of Rexolite (1.05 g/cm^3) and its elemental composition are fairly tissue-equivalent.

Table 3.2: *The elemental composition of muscle tissue, TE plastic (A-150) and different insulator materials.*

	ICRU MUSCLE TISSUE	A-150 PLASTIC (TE)	KAPTON	REXOLITE	MYLAR	POLYET- HYLENE	TEFLON
H	10.1	10.2	2.6	9	4.2	14	---
C	11.1	76.8	69	91	62.5	86	24
N	2.6	3.6	7.4	---	---	---	---
O	76.2	5.9	21	---	33.3	---	---
F	---	1.7	---	---	---	---	76
Ca	---	1.8	---	---	---	---	---

3.2 Gas system

3.2.1 Filling gases

Generally, the choice of gas filling is very important, because it influences the gas gain and counting characteristics. The suitability of a tissue equivalent gas is determined by the quality of its elemental tissue composition, gas gain properties and homogeneity in the composition of gas and the wall. Among several gas mixtures that meet these requirements two types are predominantly used, i.e. a methane based mixture developed by Rossi and Failla [12] and a propane based mixture developed by Srdoc [13]. The propane mixture permits higher gas gains [14] and is more homogeneous with A-150 whilst the methane based mixture more closely models the ICRU [9] muscle tissue composition. The elemental composition (percent by weight) of these TE gases are presented in Table 3.3.

Table 3.3: *Elemental composition of the two main Tissue-Equivalent (TE) gas mixtures in percent by weight.*

GAS	H	C	N	O
Methane based TE gas	10.2	45.6	3.5	40.7
Propane based TE gas	10.3	56.9	3.5	29.3

³ C-LEC Plastics, Inc., 6800 New state road, Philadelphia, PA 19135-1532

The TE gases based on methane (64.4% CH₄, 32.5% CO₂, 3.1% N₂) and propane (55% C₃H₈, 39.6% CO₂, 5.4% N₂) are both available commercially. They may also be prepared by mixing the component gases according to partial pressure in a large volume from which they are led into the counter. Both propane and methane based tissue-equivalent gases are commonly used in mixed field dosimetry. The cavity will be filled to a low pressure with the counting gas in order to simulate a microscopic site in tissue. The site diameter simulated by the cavity is based on energy loss in the simulated site and may be calculated according to section 2.2.1.

The electron multiplication does not depend on the type or energy of incident radiation, but on the type of the gas and its pressure, as well as on the counter geometry and the applied voltage. Hence, a prerequisite for a gas is a sufficiently high gain. For working at a micro- and nano-metric level it is necessary, that the pressures have to be decreased. Decreasing the pressure, the quantity of the deposited energy gets lower and consequently the produced signal is more difficult to distinguish from the electronic noise. So, a high gain is necessary to reach good signals at low pressures. Other demands on a gas are the absence of polymerisation and a high drift velocity.

3.2.2 Gas flow system

Since gas and wall compositions are essential characteristics for a TEPC to ensure correct simulation of microscopic tissue volumes, one of the most important aspects of counter operation is the stability of the gas quality. Small decline in gas purity by contamination with electronegative gases, especially oxygen and water vapour, decreases the gas amplification significantly, while stopping power properties are not much affected. The sources of these gas impurities may be leakage and outgasing of plastic components or diffusion of gases trapped in metal parts. Outgasing problems are very difficult to avoid. Therefore, preferably a gas flow operation mode should be used which provides continuous cleaning of impurities caused by outgasing. The advantage of the gas flow mode is the continuous clearing of impurities liberated by outgasing. Using less reliable gas regulating devices resulting in a non-steady pressure may offset this benefit.

As mentioned above, the gas purity and stable pressure are important factors, which can greatly influence the stability of the gas gain and the reproduction of the measurements. Therefore a gas flow system is used for the measurements in this work which is schematically illustrated in Fig. 3.2.

A constant gas flow is made possible through a mass flow controller (MFC) (MKS Instruments, Inc., Andover, MA, U.S.A., type 1179 A) which controls the velocity of the gas flow into the system. When the TEPC is coupled to the system via a coupling valve (Swagelok, Ohio, U.S.A., Quick-Connects model SS-QC4-D-400) a throttling valve (MKS, type 248) which opening is automatically driven by a manometer (MKS, type 722A) to keep the pressure inside the TEPC constant. Under these conditions it appeared possible to make measurements with a constant pressure inside the TEPC. The vacuum is made with a low vacuum (L.V.) pump for the pre-vacuum and a high vacuum (H.V.) turbo pump. For the gas flow at low pressure, a separate L.V. pump is used. For safety reasons a magnet valve, connected to a gas alarm system, is applied in the gas system to shut down the gas supply in case of a leak in the gas flow system. The system was tested with a Helium leak detector.

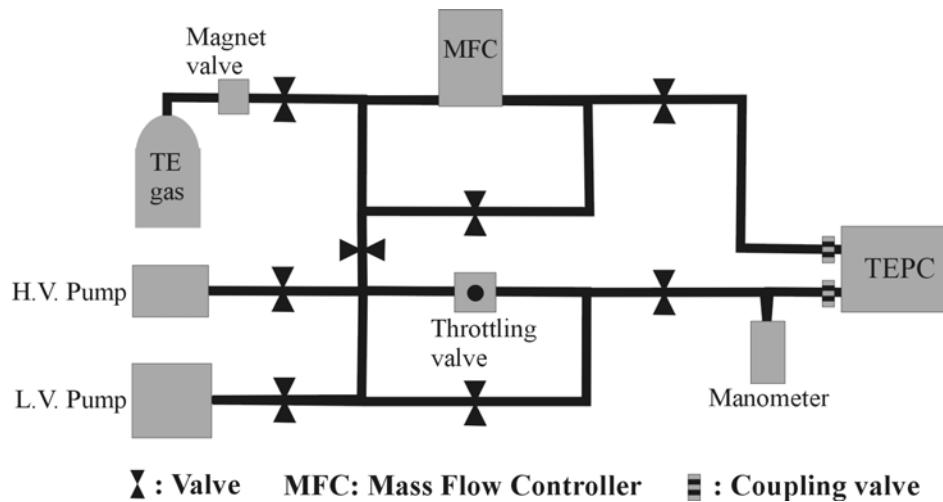


Figure 3.2: Schematic diagram of the gas flow system used with the Tissue-Equivalent Proportional Counter (TEPC). The Mass Flow Controller (MFC) allows a constant flow to the system and the throttling valve, that is controlled by a manometer, facilitates a constant pressure inside the TEPC. The vacuum is made with a high vacuum (H.V.) turbo pump. A low vacuum (L.V.) pump is applied for the gas flow.

3.3 Electronics

3.3.1 Signal processing

TEPCs are operated in the pulse mode to record each individual energy deposition event. The output pulse, which is proportional to the charge released in the cavity due to an event, from the anode wire is an electric charge. A low-noise charge-sensitive preamplifier (PA) integrates the charge on a feedback capacitor and delivers an output voltage with an amplitude proportional to the charge released by the counter and inversely proportional to the feedback capacitance [15, 16]. The pulses from the preamplifier are amplified and shaped in a linear amplifier (LA). The sharp increase of the signal which corresponds to the fast transport of electrons to the anode is followed by a slow increase due to the relatively slow movement of positive ions toward the cathode [17]. Therefore, shaping time constants must be long enough (typically up to several μs) to accommodate the relatively long time of pulses. The fast rise time of the signal can be used in specific applications, e.g. time-of-flight analysis.

The way in which the PA and the bias voltage are connected to the detector, can affect the detector system noise. There are two possibilities:

1. To hold the detector wall (cathode) at ground potential and apply positive high voltage to the wire (anode).

2. To apply negative high voltage to the detector wall and hold the anode at ground potential.

The second configuration has the advantage of eliminating the high voltage and blocking capacitor which reduces the total input capacitance somewhat. A disadvantage is that the cathode has to be insulated for high voltage and this can complicate the design and operation of the detector.

Due to the requirement to detect energy deposition events with lineal energies from 100 eV/ μm up to more than 1 MeV/ μm , depending of the radiation of interest, the PA should be designed to provide both linearity over 4-5 orders of magnitude and low noise characteristics. The preamplifier should be connected directly to the anode to reduce the input capacitance and thus to ensure low electronic noise. If it is not possible to couple the preamplifier directly to the anode, a cable connection as short as possible should be used. Since the range of pulse heights can exceed 10^5 it is frequently necessary to determine microdosimetric spectra in two or more regions. Employing logarithmic amplifiers or several linear amplifiers operated in parallel and at different gains will overcome this problem. A precision pulse generator should be used to test linearity and to determine precisely the amplifier gain ratios, taking into account the required dynamic range.

3.3.2 Electronics and Sensitivity

The principal limitation to useful electronic amplification is the preamplifier noise. In charge-sensitive preamplifiers, the noise is usually expressed in terms of Equivalent Noise Charge (ENC), which is the hypothetical charge at the preamp input that would cause the observed RMS (Root Mean Square) noise level at the output. Formally, the ENC is expressed in absolute unit of charge, or coulombs. However, it has become common to express it in units of electron charges. Modern preamplifiers typically have an ENC of 400 electrons although by integrating the preamplifier input FET into the counter design, ENC of ≤ 100 electrons is achievable [18]. The minimum detection threshold (or Lower Level Discriminator (LLD) setting) of the multi-channel analyzer should generally be set to about 5 times the ENC noise to eliminate the recording of noise counts [5]. This "rule of thumb" is applicable to proportional counters. However, a LLD up to 10 times the RMS noise may be required if a low count rate is expected near the LLD energy.

Thus, for a proportional counter the minimum detectable energy E_m is given by:

$$E_m \approx 5 \frac{e_{rms} W}{g} \quad (3.1)$$

where W (section 3.4.3) is the average energy required to generate an electron-ion pair, g is the gas avalanche gain and e_{rms} is the system electronic noise referred to the preamplifier input. Typical values are $W = 30$ eV, $g = 10^4$, and $e_{rms} = 400$ giving an $E_m = 6$ eV which is less than the ionization energy for a single ion pair. However, in order to measure a single ion pair at the anode, consideration must also be given to the distribution in charge collected from individual avalanches due to the distances covered between the ionizing collisions of electrons [19]. The spectrum for single electrons is well approximated by a Polya distribution

[5]. To ensure that all counts are registered the average signal for a single ion-pair should be about 10 times as large as E_m [20]. In summary, to measure the collection of a single ion pair at the anode, the preamplifier noise should be as low as possible and the gas gain should be high.

The output of the shaping amplifier should be monitored with an oscilloscope to ensure correct pulse shaping (pole-zero adjustment) and no evidence of signal pileup. The acquisition of the entire lineal energy spectra using a multi-channel analyzer may require two separate acquisitions with different amplifier gain settings due to the large dynamic range of the energy deposited. The two spectra may then be merged.

3.3.3 Data collection and pulse processing

The processing of each event from the detector to the lineal energy spectrum will be outlined in this section. The count rate is the basic limitation of dosimeters such as the proportional counter, which analyse individual events. Spectrum measurements are tending to distortion at very high-count rates. This distortion may be the result of space charge effects produced in the counter or pulse pile-up. A high count rate increases the probability that two or more separate ionising events occur close enough temporally to be added together (pulse pile-up) and mistakenly recorded as a single event. Furthermore, a pulse may arrive on the tail of a previous pulse, or at the time the input gate is opening or closing, causing the pulse height to be misrepresented. A summary of these phenomena is presented by Knoll [17].

As previously discussed, the time required for collection of the free electrons from gas multiplication is negligible with respect to that required for collection of the positive ions. Typical values for ion mobility in detector gases are of the order of $1-2 \times 10^{-4} \text{ m}^2 \text{ atm V}^{-1} \text{ s}^{-1}$ [17, 21]. Proportional counters with a cathode diameter around 1 cm, such as the Rossi counter (see section 3.1.1), have positive ion collection times of the order of a few hundred μs . This collection time seems somewhat prohibitive, as it appears to limit the count rate to a few thousand counts per second. However, the collection time given above is the time for full ion collection. The time required for the pulse to reach half of its maximum value is less than 1% of the total positive ion collection time in the TEPC. The majority of the pulse formation occurs within a small fraction of the collection time, significantly relaxing the count rate restrictions in the detecting volume.

The magnitude of an ionising event may be misrepresented if it occurs during the tail of a preceding event because electrons liberated by the new event will be travelling toward the anode as the positive ions from the preceding event are still migrating to the cathode. The effect of this phenomenon on the gas multiplication has been investigated by Wilkinson [22]. This investigation shows that no significant alterations in gas multiplication will occur until the count rate becomes so large that several new events occur during the migration time for positive ions from one event.

The pulse information from the counter is passed to the preamplifier. An Amptek charge sensitive preamplifier (Amptek Inc., MA, U.S.A., type A250F/NF) was employed. The preamplifier provides a conversion factor of 640 mV per 10^6 ion pairs. The high voltage is provided by a high voltage power supply (ORTEC, Oak Ridge, U.S.A., Model 710). The signal from the preamplifier is passed to a spectroscopy amplifier (ORTEC Model 855).

After amplification, the signal is sent to an analog to digital converter (ADC) (ORTEC Model AD413A). Two amplifier/ADC pairs are employed for each detector, allowing the collection of a more detailed spectrum. The amplifiers have gain settings of approximately 10 and 100. The high gain amplifier provides the low energy region of the lineal energy spectrum, while the low gain amplifier provides the high energy region. The two regions spanned by the amplifiers have a significant overlap to assure good agreement between the two spectra. The digital signal from the ADC is finally passed to a computer which produces histograms.

The decay time of the output pulse from the preamplifier is of the order of hundred microseconds and therefore must be reshaped in the spectroscopy amplifier to avoid pulse pile-up. The amplifier provides several pulse shaping times of 0.5, 1.5 or 3 μs . A short pulse length is desirable, as it allows a higher count rate without distortion of the spectrum. However, the shaping time of the amplifier must be longer than the rise time of the preamplifier pulse if the full amplitude of the pulse is to be maintained. The rise time of the preamplifier pulse corresponds to the ion collection time in the counter. If the shaping time of the amplifier is short compared to the preamplifier pulse rise time, the amplitude of the pulse will be decreased. This phenomenon is referred to as the ballistic deficit. If the charge collection time were the same for every pulse, the effect of the ballistic deficit would simply be to uniformly decrease the amplitude of all pulses. However, different events occur at different radii in the detector and therefore have different collection times. In this manner, the ballistic deficit can degrade the counter resolution. Kliuga has shown that the ballistic deficit has a significant effect on measurements made with a Rossi counter using amplifier shaping times less than 6 μs [23]. Since the distribution of radii in the miniature TEPCs is small and the charge collection time is short, large effects from the ballistic deficit are not anticipated for reasonably small shaping times

The ADC provides the conversion of the event from the shaped analog pulse delivered by the amplifier to the digital signal used for histogramming. This conversion requires a significant amount of time. The ADC deadtime consists of the linear gate time and the conversion time. The linear gate opens when the input rises above the input threshold and remains open until the input pulse falls below 90% of its maximum value. The conversion time is the time required to convert the analog pulse and increases with increasing pulse size. Each ADC was operated using a range of 8192 channels. The conversion time increases linearly with the channel number, ranging from roughly 2 μs for the lowest channels to roughly 12 μs for the highest. The greatest number of counts are observed in the lowest channels. Much of this signal is due to electronic noise in the system. The ADC is equipped with a lower level discriminator (LLD) to discard these pulses without converting them. The LLD is generally set based on the signal-to-noise ratio (gas gain) in the counter. Pulses arriving during the conversion process of another pulse will be rejected.

It may be concluded that the deadtime introduced during the processing of pulses is much larger than that in the counter itself. Since pulses occur with random frequency, the count rate capability of the system is much smaller. Large deadtimes introduce large uncertainties in the collected spectra. Therefore, a deadtime as small as possible is desired. Effects due to deadtime and pulse processing lead to significant inaccuracies in measurements made at high count rates. The system deadtime is defined as the fraction of the measurement time that the system is processing an event and therefore cannot accept a new event, and is dominated by the conversion time of the ADC. As previously mentioned, events occurring during this

system deadtime are discarded. A measurement of the deadtime is therefore required and a correction may be applied to the results. However, the deadtime should ideally be reduced to a minimum, as measurements obtained with large deadtimes suffer from larger uncertainties. This is at least partly a result of the fact that the clock pulses used to measure the deadtime are generally not the same shape or duration as the input pulses [17].

An investigation into the accuracy of the deadtime signal can be performed as follows. A pulser can be used to send random pulses simulating those that would arrive from the TEPC into the test input of the preamplifier. The number of counts of the pulser can be measured in a fast counter. A gaussian spectrum can be collected in the ADC, and the deadtime recorded. The corrected count rate will then be calculated using the number of counts in the spectrum and the measured deadtime. This measurement has to be performed for spectra in high and low channels of the ADC, as the conversion times are different for both. Another effect observed at high deadtimes is the misrepresentation of pulse amplitudes. Theoretically, all pulses observed in the spectrum should fall in the gaussian peak. However as the deadtime will increase, more counts are recorded outside the peak, indicating a misrepresentation of their true pulse height. The final investigation of the data acquisition system concerns the ADC linearity. Measurements can be made using the pulser to determine the linearity and offset of each ADC used.

3.4 Gas Amplification in a Proportional Counter

Charge transport in a gas takes place through the motion of electrons and ions. The passage of an ionising particle through a gas causes creation of ion pairs. When their energy is reduced to a few electron volts, electrons begin to drift through the gas under the influence of an applied electric field with a velocity that depends on the electric field strength, the gas pressure and the composition of the gas [1]. The positive ions formed also move under the influence of the electric field, in the opposite direction, although much more slowly than electrons. Electrons may be captured by positive ions during their motion in gas, a process called *recombination*. Another process of electron capture called *attachment* occurs in electronegative gases by neutral molecules forming a negative ion. The most important electronegative gas is oxygen. Therefore, it is important to avoid contamination of the counter gas with air.

3.4.1 Diffusion effects

Diffusion effects may produce incomplete charge collection if some of the electrons produced near the wall of a counter diffuse into the wall, or in the case of a wall-less type counter diffuse out of the collecting region. In the wall-less counter this may be compensated to some degree by reverse diffusion into the collecting volume, but in the walled counter this does not take place. The electron diffusion has to be concerned only, because diffusion of positive ions is of no practical importance in proportional counters. In absence of an electric field, diffusion of electrons will take place by random walk in a spherically symmetric pattern around the point of origin. When an electric field is applied, one can consider the entire diffusion pattern to drift through the gas along the direction of the field. An extensive treatment of electron diffusion is given in the literature [24, 25].

3.4.2 Gas multiplication

The process of signal amplification in a proportional counter through the process of Townsend avalanches near the anode wire is referred to as the gas multiplication, or gas gain. Many complete presentations of classical gas gain theory can be found in the literature [25-27]. Therefore, only a brief treatment of classical gas gain theory will be offered here. The gas multiplication process, which is generally based on the cascade of electrons, is expressed by the Townsend equation:

$$\frac{dn}{n} = \alpha dx \quad (3.2)$$

where α is the first Townsend coefficient and is defined as the mean number of secondary electrons produced by a free electron per centimetre of its path length, n is the number of electrons and x is the distance. It depends on the counting gas, the gas pressure and the field strength. Integrating Eq. (3.2) the exponential growth of the electron avalanche is expressed by:

$$G \equiv \frac{n(x)}{n_0} = \exp(\alpha x) \quad (3.3)$$

where G is the gas gain, $n(x)$ is the number of electrons at a given distance x and n_0 is the initial number of electrons. For a cylindrical counter, which has a radial electric field, one has to use cylindrical co-ordinates with the origin at the anode wire. Therefore, for a counter with an anode wire of radius r_a , the gas gain factor may be written as:

$$\ln G = \int_{r_a}^{r_c} \alpha(r) dr \quad (3.4)$$

where r_c is the critical radius. The critical radius is defined as the radius around the anode wire at which the reduced electric field, defined as the electric field strength over the counter pressure, becomes large enough to facilitate an electron avalanche.

Several frameworks exist for the derivation of general expressions of the gas gain factor based on physical characteristics of the proportional counter [28-31]. These are based on assumptions regarding the relationship between α and the electric field E . The Diethorn expression assumes linearity between α and E and may be represented as:

$$\ln G = \frac{V}{\ln(b/a)} \cdot \frac{\ln 2}{\Delta V} \left[\ln \frac{V}{pa \ln(b/a)} - \ln K \right] \quad (3.5)$$

where G = gas gain factor; V = anode voltage; a = anode radius; b = cathode radius;
 p = gas pressure; ΔV = potential difference between successive ionising events;
 K = minimum E/p (E = electric field) necessary for gas multiplication

Diethorn parameters for several commonly used counting gases may be found in Knoll [17]. Another popular representation is that offered by Campion. This formulation relies on the relation $\alpha/p = C \exp(-Dp/E)$, which has been observed to hold well in uniform fields. The Campion equation may be presented as:

$$\ln M = \frac{CV}{D \ln(b/a)} \left[\exp \frac{-aDp \ln(b/a)}{V} - \exp \frac{-rDp \ln(b/a)}{V} \right] \quad (3.6)$$

where C and D are constants empirically determined for the gas used [32]. The constants C and D have been empirically determined by Waker for propane-based TE gas [14].

An assessment of the effects of the counter gain characteristics on the entire microdosimetric spectrum must also be performed. Distortions of the lineal energy spectrum may arise from either the charge collection process inside the detecting volume or from effects of pulse processing external to the counter. The latter is discussed in section 3.3.2. Effects arising from charge collection in the detector will be discussed here. The avalanche process occurs in a small region around the anode wire referred to as the multiplication volume. A large number of electrons and positive ions are created in this region. The electrons are collected very quickly at the anode, while the slower moving positive ions drift outward toward the cathode. Large amounts of positive charge around the anode due to avalanches can considerably modify the local electric field and hence reduce the amplitude of the event pulse. This phenomenon is referred to as the space charge effect. Space charge effects can be classified into general and self-induced effects. General space charge effects result from the cumulative effect of many separate avalanches, and therefore become prevalent at high-count rates. Self-induced space charge effects arise when the gas gain is sufficiently high so that positive ions formed during a given avalanche can alter the field and reduce the number of electrons produced in further stage of the same avalanche [17]. Two general guidelines may be concluded from the definitions of general and self-induced space charge effects. These are that both the count rate and gas gain should be kept as low as possible in meeting the objectives of the desired measurement. Hendricks [33] has presented a framework for correcting for the loss in signal due to space charge effects, as well as recommendations for minimising these effects.

A further major complication is due to the fact that the motion of the electrons is not strictly radial. At low pressures they may circle the wire and undergo one or more further collisions before being absorbed in the wire which causes a higher multiplication [1]. Fig. 3.3 shows a calculated trajectory, in propane based TE gas-mixture, corresponding to an electron of initial energy 10 eV emitted at 100 μm from the anode at a pressure of $p = 573 \text{ Pa}$ (4.3 torr) [34]. When the pressure is high, the electron mean free path is short and electrons have no possibility of rotating around the anode wire between two collisions.

In general, a compromise must be made between two competing processes in the determination of the optimal voltage for a specific TEPC application. Achieving higher gas multiplication allows smaller energy depositions to be observed above the detector noise level. However, higher gas multiplication also introduces greater self-induced space charge effects. The effect of space charge on a specific event depends on factors that vary with each event, such as the geometry of the avalanche and the original ionisation, and charge produced in preceding events. This induces a non-linear distortion of the spectrum and a degradation of

counter resolution. The extreme low end of the lineal energy spectrum may be measured one time at high voltage for a given radiation field. Subsequent spectra are then measured at a lower voltage and the low end of the spectrum is matched to this spectrum and added on.

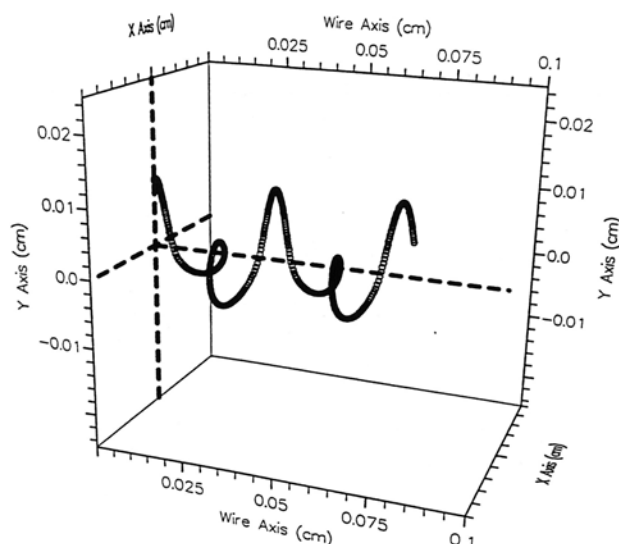


Figure 3.3: Typical helicoidal trajectory of electrons around the anode wire between two collisions at a pressure of $p = 573 \text{ Pa}$ (4.3 Torr), $V = 500 \text{ V}$ and counter geometry of $d_{\text{anode}} = 7 \mu\text{m}$, $d_{\text{cathode}} = 0.5 \text{ mm}$ [34].

3.4.3 Average energy required per ion pair (W)

The mean energy required for generating an electron-ion pair is defined as the W -value. The W -value is in principle a function of the type of gas involved, the type of radiation and its energy. Empirical observations, however, show that it is not a strong function of any of these variables and is a remarkably constant parameter for many gases and different types of radiation. For example, Goodman and Coyne [35] have shown that the W in a tissue equivalent methane gas mixture decreases from 32.8 to 31 eV as the energy of the neutrons increases from 0.1 to 20 MeV. W is largely constant for high velocities of particles but increases when the particle velocity becomes comparable to the orbital atomic electrons of the gas [8]. Thus, W increases with particle mass (for a given energy) and decreases with particle energy (for a given mass). The uncertainty in W limits the accuracy of the proportional counter in measuring the energy absorbed to around 5% [5].

3.4.4 Energy Resolution

The operation of the proportional counter is based on the proportional amplification of ionising events in the detector volume. However, a strict evaluation of the statistical fluctuations involved in the collection and gas amplification process is necessary to appropriately analyse the collected distribution of events.

Given microdosimetric events of equal magnitude, the proportional counter will measure a range of energies deposited due to various statistical fluctuations. The energy resolution (Full Width at Half Maximum (FWHM)) of a detector is defined as:

$$R_{FWHM} (\%) = 2.35 \frac{\sigma_E}{\bar{E}} \times 100 \quad (3.7)$$

where σ/\bar{E} is the relative standard deviation of the distribution of energy collected. The fluctuations contributing to the distribution can be divided in two classes:

1. *Theoretical resolution, R_{th}* : In proportional counter operation two inherent contributions to the ultimate theoretical resolution are largely unavoidable. Firstly, the number of ions produced when energy T is absorbed varies about a mean T/W according to a relationship proposed by Fano [36]. The relative variance V_f is given by:

$$V_f = \frac{W}{T} F \quad (3.8)$$

where F is the Fano factor which is typically 0.3 for TE gases [15]. Secondly, the previously mentioned statistics of gas amplification results in another contribution with a relative variance V_m given by:

$$V_m = \frac{W}{T} m \quad (3.9)$$

where m is a multiplication factor which is typically 0.6 for proportional counter [5]. Adding the relative variances gives the theoretical resolution, R_{th} :

$$R_{th} (\%) = 2.35 \sqrt{\frac{W}{T} [F + m]} \times 100 \quad (3.10)$$

2. *Instrumentation Resolution, R_{inst}* : Resolution is affected by imperfections in the counter design including preamplifier noise and variations in counter voltage, gas pressure and electric field uniformity. These contributions are typically less than 10% of the theoretical resolution [8]. Note that to determine the contribution of the preamplifier noise, e_{rms} must be divided by the number of electrons of the input of the preamplifier, i.e. $g \cdot (T/W)$, where g is the gas gain. Denoting non-preamplifier instrument resolution as R_{rest} , the instrumentation resolution may be expressed as:

$$R_{inst} (\%) = 2.35 \sqrt{\left(\frac{W}{T} \frac{e_{rms}}{g}\right)^2 + R_{rest}^2} \times 100 \quad (3.11)$$

Combining equation (3.10) and (3.11) gives the estimated resolution R_{PC} :

$$R_{PC}(\%) = \sqrt{R_{th}^2 + R_{inst}^2} = 2.35 \sqrt{\frac{W}{T} [F + m] + \left(\frac{W}{T} \frac{e_{rms}}{g} \right)^2} + R_{rest}^2 \times 100 \quad (3.12)$$

In summary, the dominant factor in the resolution is the gas multiplication variation. The instrumentation resolution is a minor contribution.

3.5 Wall effects

One of the principles of using a proportional counter in microdosimetry is the assumption that the spatial distribution of energy deposition in the gas-filled cavity is the same as in geometrically similar regions in the surrounding wall material when dimensions are inversely proportional to the density ratio (see section 2.2.1). However, the density difference between the cavity and the surrounding wall can lead to distortion of an experimental microdosimetric distribution even if the wall and the gas have the same atomic composition. These have been termed the *wall effects*. Wall effects are classified into four types [37, 38] and are described in the following subsection.

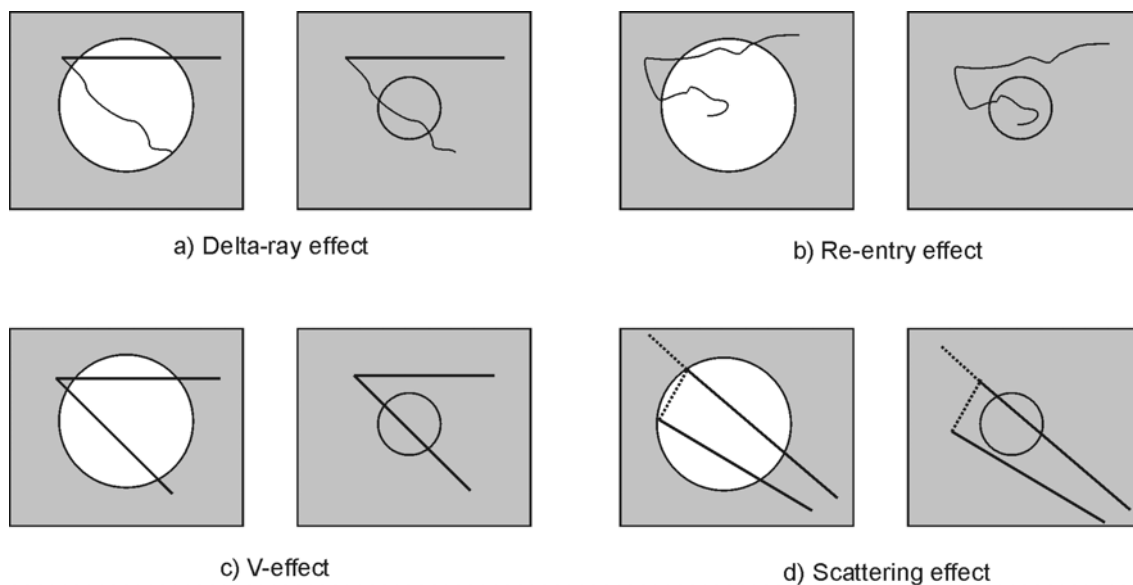


Figure 3.4: Schematic of the four types of wall effect in low pressure proportional counters. The twisting paths represent electron motion, straight lines heavier particles and dashed lines uncharged (neutron and photons) primary particles. High-density tissue material is symbolised by the shaded regions and the gas counter cavity represented by non shaded region. Each type of wall effect has two parts: the left indicates behaviour with a walled proportional gas counter and the right part shows this in equivalent real tissue. In all cases the wall effect leads to an increase in energy imparted by superposition of energy deposition events (left part) which would not occur simultaneously in a volume of uniform density (right part).

3.5.1 Delta-Ray Effect

The first type of wall effect is the delta-ray effect, illustrated in Fig. 3.4a. A primary particle enters the cavity along with one of its delta rays. However, the distance between the particles is such that only one particle would enter the real tissue volume in the case of uniform density. This effect is most significant for high-energy heavy charged particles and for high-energy electrons (delta ray and electron may have comparable energies). For heavy particles, the energy deposited by the delta ray is much less than the primary particles and hence \bar{y}_D is much less affected than \bar{y}_F . Kellerer [2, 39] estimated that for protons of energies above 5 MeV the frequency of double events is about 15% in 1 μm site sizes. For electron energies less than 1 MeV this frequency is less than 6% but the proportion increases at higher energies.

3.5.2 Re-entry Effect

The second type of wall effect is the re-entry effect, shown in Fig. 3.4b. An electron may re-enter the cavity after it has crossed it, due to its curved path. The points of exit and re-entrance can be far enough apart that the electron would not re-enter the actual high density microscopic volume. This effect is generally negligible for heavy particles but can be important for electrons, especially those that have an energy below about 1 MeV but a range that is more than the site diameter because they are the only particles with significant curvature of their paths. Kellerer [39] estimates that about 20% of all energy deposition events will be through double events due to the re-entry of the primary electrons.

3.5.3 V-Effect

The third type of wall effect is the V-effect. This effect occurs when the tracks of two heavy charge particles from an inelastic nuclear interaction form a V shaped pattern as illustrated in Fig. 3.4c. The V-effect is similar to the delta-ray effect except that the tracks are formed by two heavy charged particles. The two tracks make similar contributions and hence unlike the delta-ray effect \bar{y}_D as well as \bar{y}_F are substantially overestimated. It has been shown by Monte-Carlo calculations [38] that the V-effect is insignificant for neutrons up to 6 MeV but increases in importance above 10 MeV.

3.5.4 Scattering Effect

The fourth type of wall effect is the scattering effect. An uncharged primary particle may undergo interaction producing charged particles which are close enough so that both charged particles may enter the cavity as shown in Fig. 3.4d. In the real microscopic region, the two particles may be sufficiently spaced so that only one of the particles would enter the actual microscopic region. This effect is not well investigated although it may be considered important for neutrons and photons that undergo multiple scattering.

The wall effect has motivated the development of *wall-less counters*. There are two approaches to the essential compromises which must be realised, as closely as possible, for

design of wall-less counters [15, 40, 41]. The first approach makes use of electric field lines, surrounded by small field shaping electrodes, to define the collecting boundary. The main disadvantages of the field defined counter are the poor boundary definition due to slight variations in the field strength and the extreme care required in the set up adjustment. A second approach is to describe the boundary using a fine material grid such that the amount of solid at the boundary is small. Although such a counter has a well defined boundary and is relatively easy to use. It has the disadvantage of not being truly wall-less. Finally, for all wall-less counters particular care should be taken to ensure that the container in which the counter is placed does not disturb charged particle equilibrium [39].

3.6 Statistical variation in microdosimetric measurements

The application of a proportional counter for microdosimetry is explained by its ability to obtain spectra of energy depositions arising from single individual particle passages. The shape of the pulse height distribution obtained by a TEPC is influenced by several random processes. Analysis by Kellerer [42] and Rossi [5] uses the concept of relative variance to quantify the relative significance of various processes. The relative variance (V) of a probability distribution, $f(x)$, is a measure for the width of the distribution and is defined as:

$$V = \frac{\sigma^2}{m_1^2} = \frac{m_2}{m_1^2} - 1 \quad (3.13)$$

where σ^2 is the variance and m_1 and m_2 are the first and second moments of $f(x)$.

The total relative variance (V_{Tot}) of the measured pulse height distribution is the sum of the relative variances of several statistical factors each characterized by a probability distribution. For a single event spectrum, the following main distributions are evident [8]:

- i) The distribution of *path lengths* traversed through the site. (V_t)
- ii) The distribution of *particle LET*. (V_L)
- iii) The distribution of the *number of collisions*. (V_c)
- iv) The distribution of *energy imparted in individual collisions*. (V_e)
- v) The distribution of the *fraction of energy retained in the site* (not escaping as delta radiation). (V_d)
- vi) The distribution of the *number of ion pairs* formed by particles of the same energy (the Fano factor). (V_f)
- vii) The distribution due to *measurement electronic noise and other measurement phenomena*. (V_m)

The most common geometry for microdosimetric measurements is a spherical volume using a proportional counter. This is the only geometry with an isotropic response. Furthermore, of all geometries the relative variance due to the varying path lengths (V_t) is considered to be the smallest for a spherical volume (although this is unproven) [2]. Rossi [5] notes that for many geometries $V_t \ll V_{Tot}$ consequently non-spherical counters in particular of cylindrical shape may be used without significantly affecting the measurement.

Most microdosimetric applications involve multi-particle complex radiation fields with varying LET. The relative LET variance (V_L) varies considerably from about 0.3 for Co γ radiation to greater than 0.8 for high energy (> 2 MeV) neutrons [5]. It is a significant contribution to the total variance in neutron measurements.

Factors (iii-v) are three aspects of range and energy straggling. They are best characterized by experimental measurements with monoenergetic sources since they are very geometry and radiation type dependent. Monte-Carlo simulations are also useful for quantify straggling effects.

Distributions (vi and vii) are features of the particular measurement system used. The number of ion pairs formed in the gas for a given energy deposited is subject to variation. Not all of the energy deposited in the gas will always be converted into ion pairs. If the partitioning of energy between ionization and excitation were completely uncorrelated the process would be described by Poisson statistics. However, some correlation exists and Fano [36] introduced an empirical correction (F) to the Poisson relation to give the experimentally observed variance.

$$V_f = \frac{F}{n} \quad (3.14)$$

where F = Fano factor and n is the average number of electron ion pairs. Electronic noise (V_m) is particularly important for determining the low energy threshold of the system.

The total relative variance of a microdosimetric spectrum is [5]:

$$V_{Tot} = V_L + V_t + V_s + V_f + V_m \quad (3.15)$$

where V_s is the total relative variance due to straggling. In microdosimetry, depending on the type of radiation, LET or straggling variance will predominate, but the terms due to measurement variations (V_f and V_m) are generally considered small compared with these. Ideally in a TEPC, one would like to minimize the variation due to path length variations (V_t). This is particularly important for a non-isotropic radiation incident on a non-spherical detector.

3.7 Calibration methods

The calibration of TEPCs used for microdosimetry comprises the conversion of pulse height into lineal energy. The calibration is generally performed using one or both of two methods. One is calibration based on an internal alpha source and the other is calibration based on

features of the lineal energy spectrum. The Rossi counter (see section 3.1.1) is generally constructed with an internal alpha emitter which may be used to calibrate the energy deposition spectrum of the counter. This adds an additional complexity to the design and construction of the counter. The calibration based on features of the lineal energy spectrum is generally performed by analysing the *proton edge* which represents the maximum energy that can be deposited by a recoil proton and is characterised by a sharp cut off at the upper end of the proton peak. The calculated proton edge for 1.0 and 0.5 μm simulated site diameters are 146 and 150 keV/ μm , respectively [43]. Empirical determination of this point serves to calibrate the entire lineal energy spectrum. However, this assumes that the amount of energy required to produce an ion pair is constant for all charged particles depositing the absorbed dose. This assumption is not valid, necessitating the application of correction factors to account for differences in W-values between different particle types and for changes in W-values as a function of charged particle energy. The W-value correction factors have been adopted from calculations by Kota et al. [44]. The proton edge is commonly chosen as the mid-point of the final linear segment of the proton recoil portion of the lineal energy spectrum [45, 46]. This methodology of proton edge determination has been employed in the present study. Due to difficulties in the alpha particle calibration technique, calibration based on features of the lineal energy spectrum have proven to be the more reliable and accurate method [23]. Kliauga has estimated an uncertainty of 2-3% in the determination of the proton edge [23]. Complete reviews of the calibration process and its associated uncertainties have been presented by Pihet [47] and Dietze [48].

3.8 Gas Electron Multiplier (GEM)

Methods for obtaining large, stable proportional gains in gaseous detectors are a continuing subject of investigation in the detector's community. In the last few years a variety of micro-pattern detectors has invaded the scene of charged particle tracking replacing the traditional Multi-Wire Proportional Chambers (see chapter 2.5.3) with their higher rate. Since the Micro-Strip Gas Chamber (MSGC) was introduced in 1987 [49], a large amount of effort has been invested in the new field of gas avalanche micro-pattern detectors. Improvements in and variations of the original MSGC design have led to better detector performance. Another innovative device has been introduced in 1997, Gas Electron Multiplier (GEM) [50].

The basic concept of the GEM consists of a compact array of small apertures in metal-coated, 50 μm thick, Kapton foil. The apertures, of 50-100 μm in diameter, are typically spaced (pitched) by 100-200 μm using the photo-lithographic process. The schematic diagram and electric fields of the GEM illustrated in Fig. 3.5. With the application of suitable potentials, electrons released by ionisation in the upper gas layer (conversion and drift gap) drift into the open channels of the GEM (amplification region), where they multiply in an avalanche in the high field and transfer to the second gap (transfer gap). Signals are induced on the pick-up strips by the electron swarm leaving the GEM, with an amplitude corresponding to the total drifting charge. Due to its design, positive ion feed back into the drift region is reduced as compared to that of a wire chamber [51]. The GEM geometry has a unique advantage in that the multiplication region is separated from the readout electrodes, which are usually very vulnerable to damage from sparking in the case of gas avalanche micro-pattern detectors [52] (e.g. MSGC, Micro-Gap Chamber, etc.).

A GEM can be used as single GEM detector, by cascading several GEMs [53, 54], or as a preamplifier in a multiple structure [53, 54]. The latter configurations permit to reach large overall gains in a harsh radiation environment. In addition, there are advantages resulting from the signal formation by electron collection in the GEM, in contrast to positive ion collection in many other systems, leading to a faster signal and no signal cancellation due to positive ion drift from adjacent electrodes. The GEM has the unique property of having a good efficiency for collecting photoelectrons and focussing them into the apertures (defined as *transfer* or *transmission efficiency*) [55, 56]. In applications where a relatively large number of primary electrons are deposited within the gas volume preceding the GEM, e.g. microdosimetric measurements, the transfer efficiency would effect the pulse-height resolution. The GEM transfer efficiency is a crucial issue, particularly when detecting single photons or electrons. It depends on the given GEM geometry, the electric field above and across the GEM and on the gas type composition and pressure.

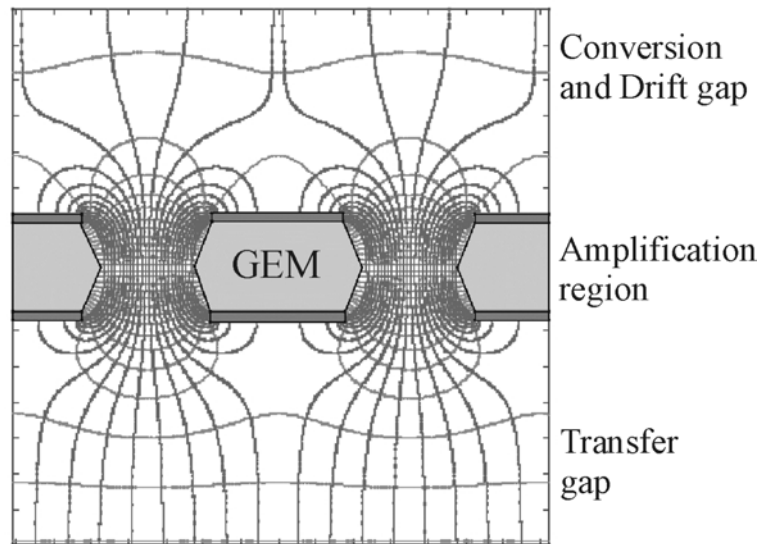


Figure 3.5: *schematic cross-section and electric fields of the Gas Electron Multiplier (GEM) for two apertures. The conversion and drift gap, the amplification region and transfer region are indicated. The electrons multiply in an avalanche in the high field region of the GEM apertures.*

In addition to GEM transfer efficiency there are still other considerations to ensure optimal GEM operation. In particular, a substantial fraction of avalanche electrons may be drawn to the bottom GEM electrode instead of to the collection plane, and therefore would not contribute to the readout signal, resulting in an *effective* GEM gain that is less than the absolute GEM gain. This can be optimised by proper choice of the field configuration and geometry. Another issue is that the conventional GEM design has a conically shaped hole in the insulating substrate (Kapton) as can be seen in Fig 3.5. In the case of this device, a gain variation with time is observed [57]. This gain shift is presumably due to the charging by avalanche ions (or electrons) of the GEM Kapton insulator. For comparison, a laser drilled GEM on 125 μm -thick polyimide foil with nearly straight walls (8° wall inclination) has been made [57]. Cho et al. [57] have reported that this exhibited a very stable gain.

References

- [1] Kliauga, P., Waker, A. J. and Barthe, J. *Design of Tissue-Equivalent Proportional Counters*. Radiat. Prot. Dosim. 6 (1995) 309.
- [2] Kellerer, A.M. *Considerations on the random traversal of convex bodies and solutions for general cylinders*. Radiat. Res. 47 (1971) 359.
- [3] Kellerer, A.M. *Criteria for the equivalence of spherical and cylindrical proportional counters in microdosimetry*. Radiat. Res. 86 (1981) 277.
- [4] Mader, U. *Chord length distributions for circular cylinders*. Radiat. Res. 82 (1980) 454.
- [5] Rossi, H. H. and Zaider, M. *Microdosimetry and Its Applications*. Springer-Verlag, Berlin, (1996).
- [6] Eickel, R. and Booz, J. *The influence of the counter wall and the counter shape on the spectral energy deposition in small volumes by ^{60}Co gamma-rays and 200 kV x-rays*. Rad. Env. Biophys. 13 (1976) 145.
- [7] Kellerer, A.M. *Chord length distributions and related quantities for spheroids*. Radiat. Res. 98 (1984) 425.
- [8] Bradley, P.D. *The development of a novel silicon microdosimeter for high LET radiation therapy*. Thesis, Department of Engineering Physics, University of Wollongong, (2000).
- [9] International Commission on Radiation Units and Measurements, *Tissue Substitutes in Radiation Dosimetry and Measurement (ICRU report 44)*. Bethesda, Md., U.S.A. ICRU, 1989.
- [10] Braby, L.A., Johnson, G.W. and Barthe, J. *Practical consideration in the design and construction of tissue-equivalent proportional counter*. Radiat. Prot. Dosim. 61 (1995) 351.
- [11] Shonka, R.F., Rose, J.E. and Faila, G. *Conducting plastic equivalent to tissue, air and polystyrene*. In: Proc Second United Nations Conference on Peaceful Uses of Atomic Energy (United Nations, New York). 21 (1958) 184.
- [12] Rossi, H.H. and Failla, G. *Tissue equivalent ionization chambers*. Nucleonics, 14 (1956) 32.
- [13] Srdoc, D. *Experimental technique of measurement of microscopic energy distribution in irradiated matter using Rossi Counters*. Radiat. Res. 43 (1970) 302.
- [14] Waker, A.J. *Gas gain characteristics of some walled proportional counters used in microdosimetry*. in Proc. 8th Symp. on Microdosimetry, Booz, J., Ebert, H. G., (eds.). CEC, Luxembourg (1981) 1017.
- [15] International Commission on Radiation Units and Measurements, *Microdosimetry (ICRU report 36)*. Bethesda, Maryland, U.S.A. ICRU, 1983.
- [16] Gerdung, S., Pihet, P., Grindborg, J.E., Roos, H., Schrewe, U.J. and Schuhmacher, H. *Operation and application of tissue-equivalent proportional counter*. Radiat. Prot. Dosim. 61 (1995) 381.
- [17] Knoll, G.F. *Radiation detection and measurement*. 3th Ed. (Wiley, New York, 1999).
- [18] Radeka, V. *Low-Noise Techniques in Detectors*. Ann. Rev. Nucl. Part. Sci. 38 (1988) 217.
- [19] Srdoc, D. and Krajer-Bronic, I. *Statistical fluctuations in the ionization yield for low energy photons absorbed in polyatomic gases*. J. Phys. B: Atm. Molec. Phys. 20 (1987) 4473.
- [20] Srdoc, D. *Experimental technique of measurement of microscopic energy distribution in irradiated matter using Rossi Counters*. Radiat. Res. 43 (1970) 302.
- [21] Sauli, F. *Principles of operation of multiwire proportional and drift chambers*. European Organization for Nuclear Research (CERN), Geneva, CERN 77-09 (1977).
- [22] Wilkinson, D.H. *Ionization chambers and counters*. University Press, Cambridge. (1950).
- [23] Kliauga, P. *Microdosimetry at middle age: Some old experimental problems and new aspirations*. Radiat. Res. 124 (1990) S5.
- [24] Townsend, J. *Electrons in gases*. Hutchinson, London. (1947).
- [25] Loeb, L. *Basic processes of gaseous electronics*. Univ. of Cal. Press, Berkeley and Cambridge Univ. Press, London. (1955).
- [26] Rose, M.E. and Korff, S.A. *An investigation of the properties of proportional counters. I*. Phys. Rev. 59 (1941) 850.
- [27] Von Engel, A. *Ionized Gases*. 2nd Ed., Oxford University Press, Oxford. (1965).
- [28] Diethorn, W. *A methane proportional counter system for natural radiocarbon measurements*. NYO-6628 (1956).
- [29] Williams, A. and Sara, I. *Parameters affecting the resolution of a proportional counter*. Int. J. Appl. Rad. and Iso. 13 (1962) 229.
- [30] Champion, P.J. *The operation of proportional counters at low pressures for microdosimetry*. Phys. Med. Biol. 16 (1971) 611.

- [31] Bambynek, W. *On selected problems in the field of proportional counters*. Nucl. Instr. Meth. 112 (1973) 103.
- [32] Champion, P.J. *Some comments on the operation of proportional counters*. in Proc. Third Symp. on Microdosimetry, Ebert, H. G. (ed.) EUR 4452 (CEC, Brussels, 1972).
- [33] Hendricks, R.W. *Space charge effects in proportional counters*. Rev. Sci. Instr. 40 (1969) 1216.
- [34] Ségur, P., Olko, P. and Colautti, P. *Numerical modelling of tissue-equivalent proportional counters*. Radiat. Prot. Dosim. 6 (1995) 323.
- [35] Goodman L.J. and Coyne, J.J. *Wn and neutron kerma for methane-based tissue equivalent gas*. Radiat. Res. 82 (1980) 13.
- [36] Fano, U. *Ionization yield of radiations. II. The fluctuations of the number of ions*. Phys. Rev. 42 (1947) 26.
- [37] Kellerer, A.M. *An assessment of wall effects in microdosimetric measurements*. Radiat. Res. 47 (1971) 377.
- [38] Oldenburg, U. and Booz, J. *Wall effects of spherical counter*. Proceedings of the second symposium on microdosimetry. Report No. EUR 4452, (1970) 269.
- [39] Kellerer, A.M. *Event simultaneity in cavities. Theory of the distortions of energy deposition in proportional counters*. Radiat. Res. 48 (1971) 216.
- [40] Glass, W.A. and Braby, L.A. *A wall-less detector for measuring energy deposition spectra*. Radiat. Res. 39 (1969) 230.
- [41] Glass, W.A. and Gross, W.A. *Wall-less detectors in microdosimetry*. in *Topics in Radiation Dosimetry, Radiation Dosimetry Supplement 1*, vol. 1, F. J. Attix, Ed. New York: Academic Press. (1972) 221.
- [42] Kellerer, A.M. *Analysis of patterns of energy distribution*. (Euratom eport, EUR4522, d-e-f) presented at Second symposium on microdosimetry, Brussels. (1970).
- [43] Burmeister, J., Kota, C., Maughan, R.L., Waker, A.J. *Miniature tissue-equivalent proportional counters for BNCT and BNCEFNT dosimetry*. Med. Phys. 2 (2001) 1911.
- [44] Kota, C. and Maughan, R.L. *Use of low pressure tissue equivalent proportional counters for dosimetry in BNCT and BNCEFNT*. Med. Phys. 27 (2000) 535.
- [45] Pihet, P. and Menzel, H.G. *Atomic data required in accurate measurements of KERMA for neutrons with low pressure proportional counters*. in *Atomic and Molecular Data for Radiotherapy*, IAEA, Vienna. (1989).
- [46] Waker, A. J. *Experimental uncertainties in microdosimetric measurements and an examination of the performance of three commercially produced proportional counters*. Nucl. Instr. Meth., A 234 (1985) 354.
- [47] Pihet, P., Gerdung, S., Grillmaier, R.E., Kunz, A. and Menzel, H.G. *Critical assessment of calibration techniques for low pressure proportional counters used in radiation dosimetry*. Radiat. Prot. Dosim. 44 (1992) 115.
- [48] Dietze, G., Menzel, H.G. and Bühler, G. *Calibration of tissue-equivalent proportional counters used as radiation protection doseimeters*. Radiat. Prot. Dosim. 9 (1984) 245.
- [49] Oed, A. *Position-sensitive detector with microstrip anode for electron multiplication with gases*. Nucl. Instr. Meth., A 263 (1988) 351.
- [50] Sauli, F. *GEM: A new concept for electron amplification in gas detectors*. Nucl. Instr. Meth., A 386 (1997) 531.
- [51] Sauli, F. *GEM readout of the time projection chamber*. Internal report, CERN-EP-TA1 (1999).
- [52] Van den Berg, F.D. *Gas-filled micro-patterned radiation detectors*. Thesis, Department of Radiation Technology Group of the Interfaculty Reactor Institute, Delft University of Technology, (2000).
- [53] Bachmann, S., Bressan, A., Ropelewski, L., Sauli, F. and Mörmann, D. *Recent progress in GEM manufacturing and operation*. Nucl. Instr. and Meth. A 433 (1999) 464.
- [54] Chechik, R., Breskin, A., Garty, G., Mattout, J., Sauli, F. and Shefer, E. *First results on the GEM operated at low gas pressures*. Nucl. Instr. and Meth. A 419 (1998) 423.
- [55] Chechik, R., Breskin, A., Garty, G., Shefer, E., Singh, B.K. and Shchemelinin, S. *Advances in single-charged detectors and their applications*. IEEE Trans. Nucl. Sci. 47 (2000) 1404.
- [56] Richter, C., Breskin, A., Chechik, R., Mormann, D., Garty, G. and Sharma, A. *On the efficient electron transfer through GEM*. Nucl. Instr. and Meth. A 478 (2002) 538.
- [57] Cho, H.S., Kadyk, J., Han, S.H., Hong, W.S., Perez-Mendez, V., Wenzel, W., Pitts, K., Martin, M.D. and Hutchins, J.B. *GEM: Performance and aging tests*. IEEE Trans. Nucl. Sci. 46 (1999) 306

Chapter 4

Analytical calculations of neutron microdosimetric dose distributions

Neutrons do not carry a net electric charge and as a result they do not interact with atomic electrons in passing through matter. In other words, they do not directly cause ionization and are not continuously slowed down. They interact with atomic nuclei, but only through the nuclear force which has an extremely short range. Therefore they must score an almost direct hit on a nucleus before an interaction occurs. Since atomic nuclei are so much smaller than atoms, the probability of an energetic neutron hitting a nucleus is very low and neutrons can traverse great thickness of material before being stopped. Neutrons therefore cause ionization indirectly through protons and recoiling nuclei which are products of various reactions of neutrons with atomic nuclei (i.e. elastic scattering, inelastic scattering, capture and spallation). These particles are all much heavier than the electrons which generate the ionization in γ -ray interactions. The heavier particles generate ionization more densely along their path, and therefore have a higher linear energy transfer (LET) [1]. As a result energetic neutrons are more effective at producing damage than X- or γ -rays for the same amount of ionization per unit mass of tissue. Damage to living tissue is due to the ionization produced by the charged subatomic particles resulting from nuclear reactions.

To gain a clear understanding of the parameters influencing neutron microdosimetric spectra, analytical calculations have been carried out. The physics on which these calculations are based is explained in section 4.1. In section 4.2 particle tracks have been calculated which are useful to distinguish between insiders, starters, stoppers and crossers. The knowledge of the contribution of different types of charged particles to the total lineal energy spectrum is also useful and is discussed in section 4.3. The changes of the shape of the microdosimetric spectra as a result of changing of the neutron energies are given in section 4.4. Finally in section 4.5 the influence of the simulation site size on the shape of the microdosimetric spectra is discussed.

4.1 Calculation of microdosimetric dose distribution

The calculations of microdosimetric spectra have been carried out by an analytical method. This method has the advantage, above the Monte Carlo method, that the calculations are less time consuming and, in contrast to Monte Carlo method, it is not necessary to find a good balance between precision and expense.

Analytical calculations of dose distribution, $d(y)$, for micrometer sized sensitive sites have been performed for neutrons. Two groups, Caswell and Coyn [2-6] and Dennis and Edwards [7] carried out the development of the analytical method. One of the basic assumptions of the method is that charged particle equilibrium has been established in the medium (see section 2.2.1). Furthermore, these calculations are based on the assumption that the energy deposition in the sensitive volume crossed by a neutron-induced ion can be calculated from the Continuous Slowing Down Approximation (CSDA). In this approximation it is assumed that ions traverse the sensitive volume along straight lines and that the kinetic energy of the ions changes continuously i.e. in a non-stochastic manner along its path.

With this approximation, and with the assumption of charged particle equilibrium, the slowing-down spectrum $\phi(E)$ of a particular type of charged particle can be obtained from the corresponding initial spectrum by the equation

$$\phi(E) = \frac{1}{S(E)} \int_E^{E_{\max}} n(E') dE' \quad (4.1)$$

Where E_{\max} is the maximum energy of charged particles of a given type, $S(E)$ their linear collision stopping power at the energy, E , and $n(E')$ their initial spectrum produced in the medium such as counter wall (number of particles set in motion per unit of energy and volume).

The CSDA can be used to calculate energy deposition of heavy charged particles in the sensitive volume if straggling and delta ray effects are neglected (i.e. the touchers are not included in the calculation). For neutron-generated protons and heavy ions of energies below 1 MeV/u in TE material, straggling can be neglected in calculations for site sizes above 1 μm [8].

For these calculations the important useful functions are the chord length distribution that results from the random transversal of a convex body. In this context, two different kinds of randomness are relevant [9]:

- 1) Mean free path randomness (μ -randomness). A chord of a convex body is defined by a point in Euclidian space and a direction. The point and the direction are from independent uniform distributions. This randomness results if the convex body is exposed to a uniform isotropic field of straight infinite tracks. The probability density (see Table 3.1) for μ -randomness, $f_{\mu}(l)$, for a sphere of diameter d is presented by

$$f_{\mu}(l)dl = \frac{2l}{d^2} dl \quad 0 \leq l \leq d \quad (4.2)$$

where l is the chord length.

- 2) Internal source randomness (i-randomness). A segment is defined by a point in the interior of a convex body and a direction. The point and the direction are from independent uniform distributions. This i-randomness is what one obtains if the interior of the body is a uniform source of straight particle tracks. The probability density for i-randomness, $f_i(l)$, for a sphere of diameter d is given by

$$f_i(l)dl = \frac{3}{2d} \left(1 - \frac{l^2}{d^2}\right) dl \quad 0 \leq l \leq d \quad (4.3)$$

Furthermore, the probability densities for μ -randomness and i-randomness are related by

$$f_i(l) = \frac{1}{\bar{l}_\mu} \int_0^\infty f_\mu(x) dx \quad (4.4)$$

where \bar{l}_μ is the mean chord length for μ -randomness.

4.2 Calculation of microdosimetric dose distribution of different particle tracks

For the calculation of energy imparted, it is useful to distinguish the classes of particle tracks (see section 2.2.1) for each type of particle. The particle tracks can be classified into two groups. The first group consists of particles originating outside sensitive volume (stoppers and crossers) where μ -randomness has to be applied for the calculation. The second group consists of particles originating inside the sensitive volume (starters and insiders) where i-randomness has to be applied for the calculation.

The number of stoppers and crossers is determined by the slowing-down spectra (or differential fluence spectra) at the surface of the sensitive volume, $\phi(E)$, and the chord length distribution, $f_\mu(l)$. The number of the stoppers given energy imparted, ε , between E and $E + dE$ is given by

$$n_{STP}(\varepsilon)d\varepsilon = A \left\{ \phi(E) \int_{R(E)}^{l_{max}} f_\mu(l) dl \right\} d\varepsilon \quad (4.5)$$

where $A = V/\bar{l}$ (V is the volume and \bar{l} is the mean chord length), $R(E)$ is the range of a stopper of energy E ($E = \varepsilon$ by definition), and l_{max} is the maximum chord length. The maximum energy loss for stoppers is the energy, ε_{max} , such that $R(\varepsilon_{max}) = d$.

The crossers enter the volume with all energies from ε to the maximum possible energy, ε_{max} . The number of crossers giving energy imparted between ε and $\varepsilon + d\varepsilon$ is given by

$$n_{CR}(\varepsilon)d\varepsilon = A \left\{ \int_{\varepsilon}^{\varepsilon_{max}} \phi(E) f_{\mu}(l) \frac{dl}{dE} dE \right\} d\varepsilon \quad (4.6)$$

where l equals $R(E) - R(E - \varepsilon)$ and $f_{\mu}(l) = 0$ for $l > l_{max}$. The term $dl/dE = 1/S(E - \varepsilon)$, is the inverse of the stopping power of the particle as it leaves the sensitive volume.

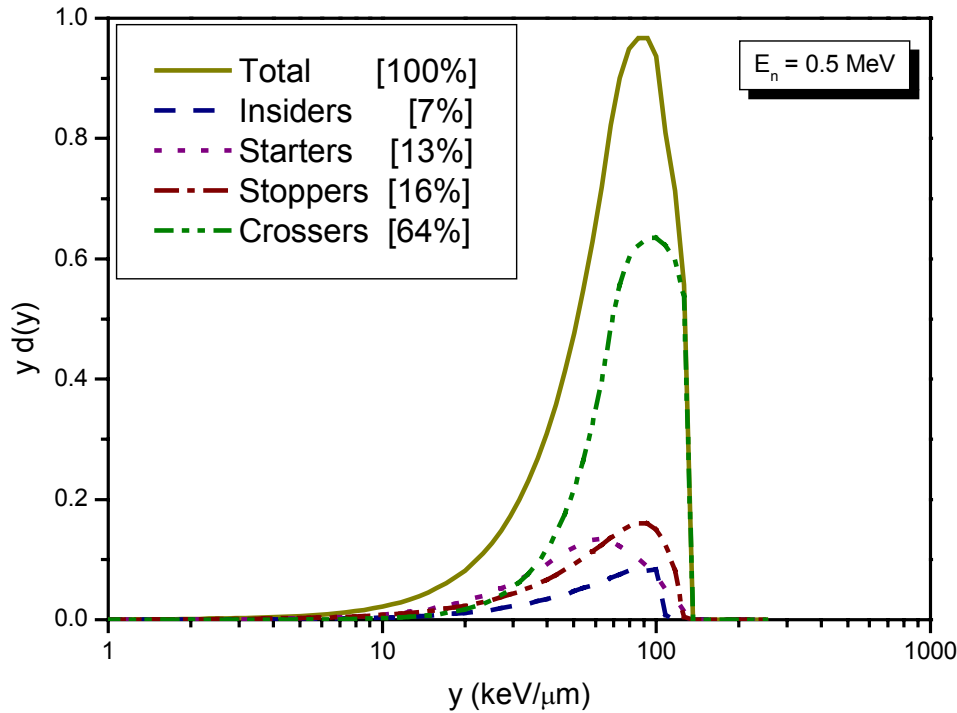


Figure 4.1: Analytical calculation of $yd(y)$ of 0.5 MeV neutrons in TE plastic (A-150), and propane-based TE gas ($2\mu\text{m}$ simulated diameter). Contributions of insiders, starters, stoppers and crossers to the total dose distribution are given.

The number of insiders and stoppers is determined by the initial spectrum of particles produced in the sensitive volume, $n(E)$, and the chord-length distribution, $f_i(l)$. The number of insiders with energy imparted between ε and $\varepsilon + d\varepsilon$ is given by the expression

$$n_{INS}(\varepsilon)d\varepsilon = \rho A \left\{ n(\varepsilon) \bar{l}_{\mu} \int_{R(E)}^d f_i(l) dl \right\} d\varepsilon \quad (4.7)$$

where $R(E)$ is the range of a particle of energy, E ($E = \varepsilon$ by definition), and \bar{l}_{μ} is the average chord length. The starters can start with any energy from $E = \varepsilon$ to E_{max} , the maximum

possible energy of the particle, and their number with energy imparted between ε and $\varepsilon + d\varepsilon$ is given by

$$n_{STR}(\varepsilon)d\varepsilon = \rho A \left\{ \bar{l}_\mu \int_{E=\varepsilon}^{E_{\max}} n(E) f_i(l) \frac{dl}{dE} dE \right\} d\varepsilon \quad (4.8)$$

where l must equal $R(E) - R(E - \varepsilon)$, \bar{l}_μ is the average chord length for μ -randomness and dl/dE is the inverse of the stopping power.

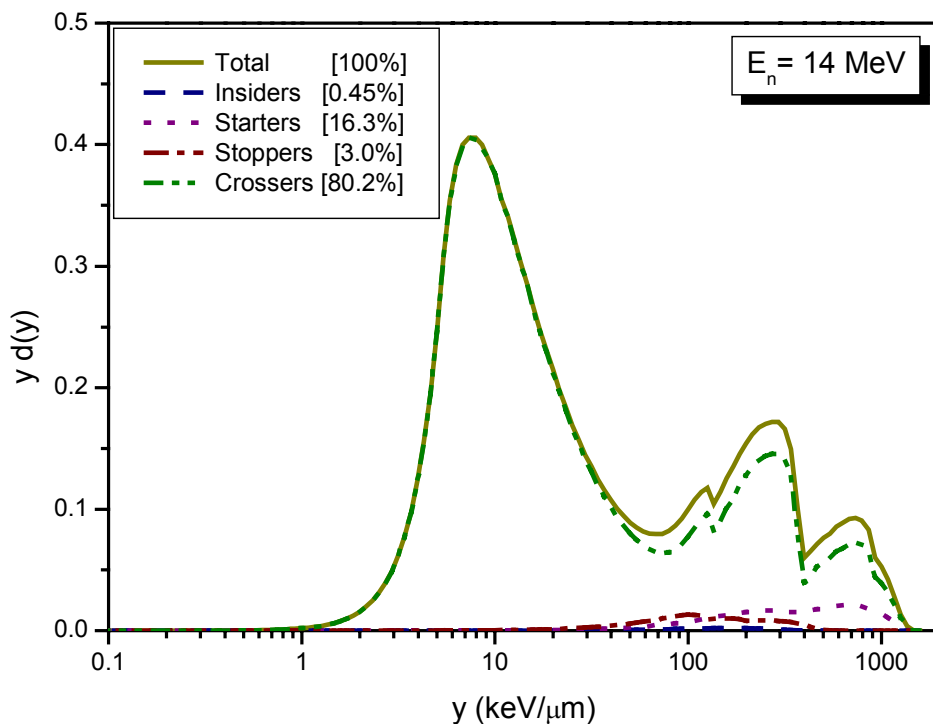


Figure 4.2: Analytical calculation of $yd(y)$ of 14 MeV neutrons in Tissue-Equivalent plastic (A-150), and propane-based TE gas ($2\mu\text{m}$ simulated diameter). Contributions of insiders, starters, stoppers and crossers to the total dose distribution are given. The contribution of insiders is negligible small.

The single event distribution of energy imparted in the volumes is given by the equation

$$f_1(\varepsilon) = \frac{n_{INS} + n_{STR} + n_{STP} + n_{CR}}{n} \quad (4.9)$$

where n is given by

$$n = \int_0^{\varepsilon_{\max}} \{n_{INS}(\varepsilon) + n_{STR}(\varepsilon) + n_{STP}(\varepsilon) + n_{CR}(\varepsilon)\} d\varepsilon \quad (4.10)$$

From $f_1(\epsilon)$, it is easy to calculate the different microdosimetric distributions (see section 2.3).

The dose fraction per logarithmic interval of lineal energy for different particle tracks for mono-energetic neutrons of 0.5 MeV and 14 MeV is illustrated in Figs. 4.1 and 4.2 respectively. The calculations have been performed for A-150 Tissue-Equivalent (TE) plastic as a wall material and propane-based TE gas as a counting gas for 2 μm sensitive volume. The analytical code by Caswell et al. has been used for these calculations to evaluate energy imparted to small spheres, based on the cross section data of the Evaluated Nuclear Data File Version B (ENDF/B-V, Brookhaven National Laboratory, Upton, New York) [10]. The contribution in terms of percentage of insiders, starters, stoppers and crossers to the total dose distribution is given in the graph. The largest contribution is coming from the crossers as it was expected since the range of the most secondary particles is much larger than the 2 μm sensitive volume size. As the neutron energy increases and the range of the secondary particles increases, the contribution of insiders decreases while the contribution of crossers increases.

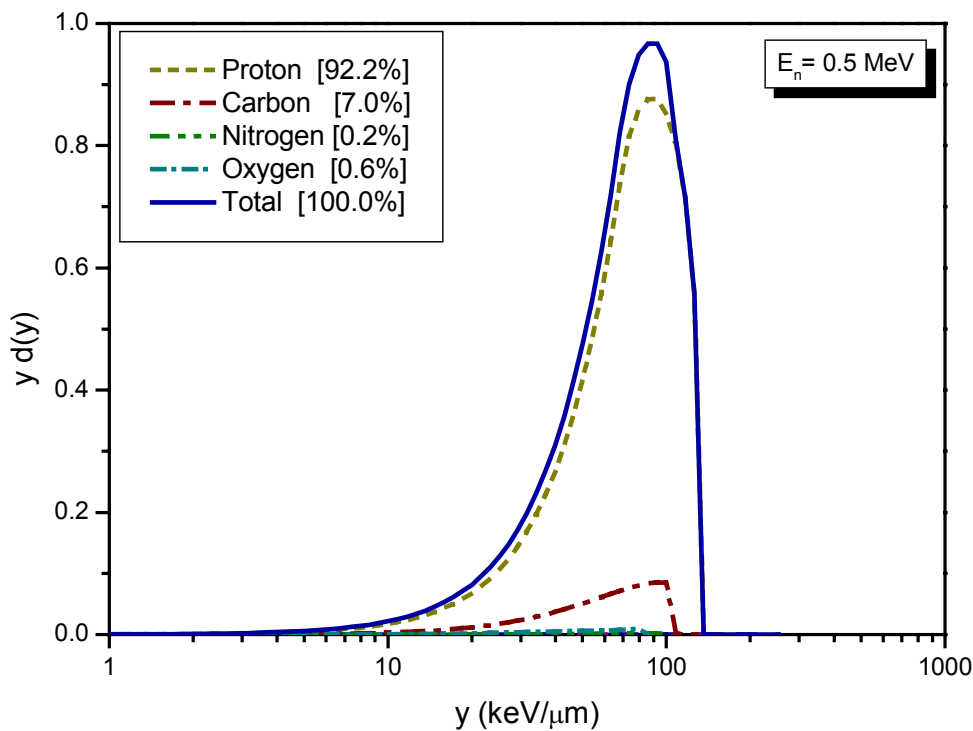


Figure 4.3: Analytical calculation of $yd(y)$ of 0.5 MeV neutrons in TE plastic (A-150), and propane-based TE gas (2 μm simulated diameter). Contributions of protons, carbon, nitrogen and oxygen recoils to the total dose distribution are given. Protons contribute more than 92% to the total spectrum.

4.3 Contribution of the various charged particle to the microscopic dose distribution

The human body is composed largely of water which contains many hydrogen nuclei. Elastic scattering of the neutrons with the hydrogen nuclei will cause the protons to recoil violently. Similarly elastic collisions of neutrons with carbon, oxygen or other heavier nuclei will cause these to recoil. Because the mass of protons and the other recoiling nuclei is much larger than that of electrons, they generate a much denser ion path resulting in more damage to the tissue. Once neutrons have been slowed down by elastic collisions to thermal energy, 0.025 eV, they are readily captured. So, the ionization in hydrogenous matter (e.g. tissue) exposed to neutrons is mainly produced by recoil protons, heavy recoil nuclei and products of nuclear reactions. These secondary particles are produced by elastic scattering, inelastic scattering, and capture processes. Because a large fraction of a neutron's energy can be transferred to the proton of a hydrogen atom, protons dominate the energy deposition in those biological materials, which have relatively high hydrogen content.

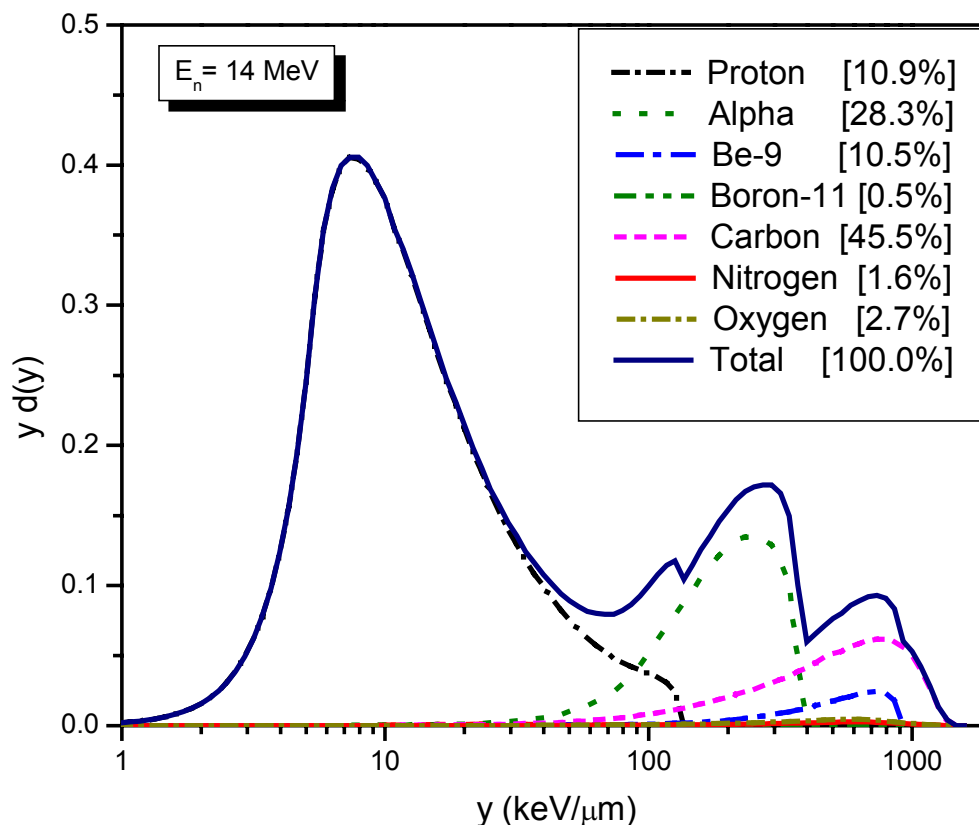


Figure 4.4: Analytical calculation of $yd(y)$ of 14 MeV neutrons in TE plastic (A-150), and propane-based TE gas ($2\mu\text{m}$ simulated diameter). Contributions of the secondary charged particles to the total dose distribution are indicated.

In order to analyze the microdosimetric spectra and their differences, the contribution of different particles to the total spectrum can be evaluated separately in these calculations. The

calculations of microdosimetric dose distribution for different particle contribution have been performed for neutron energies of 0.5, 14 and 20 MeV and are shown in Figs. 4.3, 4.4 and 4.5. For monoenergetic neutrons of 0.5 MeV of energy protons contribute more than 90% to the total spectrum. As the neutron energy increases the contribution of protons decreases while the contribution of heavy particles increases. This is illustrated in Figs. 4.4 and 4.5 where the contribution of protons has been reduced to 11% and 7.5 % for neutron energies of 14 and 20 MeV, respectively while the contribution of other particles has been increased compared to the spectrum with neutron energy of 0.5 MeV.

Notice that because tissue-equivalent plastic tends to have a carbon-to-oxygen ratio larger than tissue, the microdosimetric spectra can be somewhat distorted in a TE counter for neutron energies at which the contribution of carbon and oxygen becomes significant.

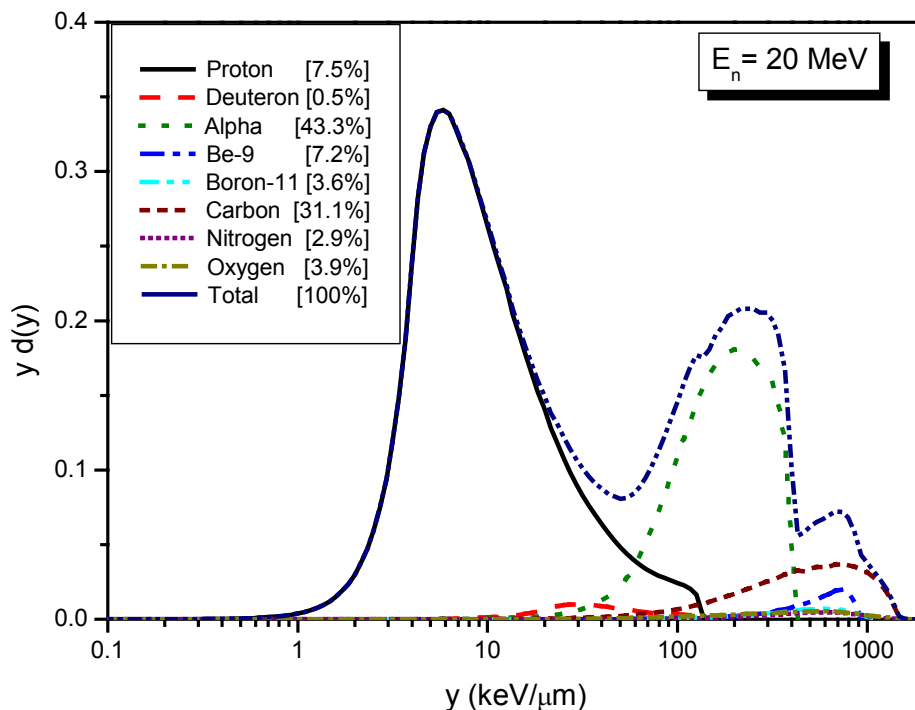


Figure 4.5: Analytical calculation of $yd(y)$ of 20 MeV neutrons in TE plastic (A-150), and propane-based TE gas ($2\mu\text{m}$ simulated diameter). Contributions of the secondary charged particles to the total dose distribution are indicated.

4.4 Microdosimetric dose distribution for different neutron energies

The way in which neutrons interact with matter depends to a large extent on their energies. Moreover, the relative importance of the different interaction modes is dependent on neutron energy and the elemental composition of the absorbing medium. Therefore, the neutron

energy has a substantial influence on the shape of the microdosimetric spectra. As the neutron interaction with tissue depends on the neutron energy, the produced secondary charged particles will be different and hence the shape of microdosimetric spectra will be different. The change of the lineal energy spectrum of neutrons with different energy at a given site diameter, $d = 2 \mu\text{m}$, is demonstrated in Fig. 4.6. The calculations have been done for A-150 plastic TE as a wall material and propane-based TE gas as a counting gas. As long as the neutron energy is low enough that the maximum range of the protons is less than the site size, increasing of the neutron energy from 0.1 MeV to 0.5 MeV causes the proton peak maximum to extend to higher values of lineal energy. This is due to the fact that by increasing the neutron energy and hence the average proton energy the amount of deposited energy inside the same site increases leading to a higher lineal energy value. When the energy is large enough that the range of protons becomes larger than the site size (above 0.5 MeV), increasing the neutron energy (and hence the average proton energy) causes the proton peak maximum to extend to lower values of lineal energy. This shift in position of the proton peak maximum expresses the fact that with increasing neutron energy the average recoil proton energy will be higher and the average proton stopping power will be lower. This decrease in stopping power will lead to lower values of lineal energy.

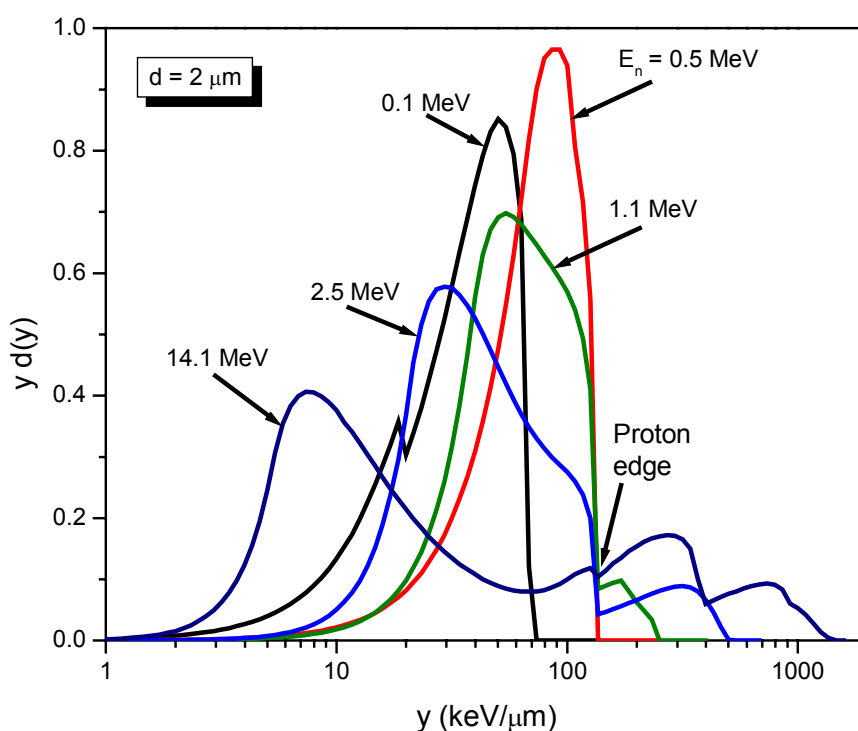


Figure 4.6: Calculated event-size (site size $2 \mu\text{m}$) spectra showing the dose fraction per logarithmic interval of lineal energy for different neutron energies. Dose distribution, $y d(y)$, changes by changing the neutron energy.

The upper end of the proton peak is characterized by a sharp cut off known as the *proton edge* and this represents the maximum energy that can be deposited by a recoil proton. Imparted energy is the integral of the stopping power along the path length, therefore a

maximum value will be obtained for recoil protons that have a residual range that matches the sensitive volume diameter. For a 2 μm simulated site size the lineal energy value of the proton edge is 136 $\text{keV}/\mu\text{m}$. Beyond the proton edge at $y = 136 \text{ keV}/\mu\text{m}$ the contribution of alpha particles and heavy recoil ions of carbon, nitrogen and oxygen is evident and increases in importance with increasing neutron energy.

4.5 Microdosimetric dose distribution for different simulated site size

Another parameter, which has influence on the shape of the microdosimetric spectra, is simulated site size. An increase of simulated site size causes narrowing of the distribution because of reduction of straggling [11]. The change of the lineal energy spectrum for different simulated site sizes, at a given neutron energy ($E_n = 2.5 \text{ MeV}$), is shown in Fig. 4.7. The spectra shift to lower lineal energy values as the site size increases, accompanied by a broadening of the spectral distribution. This can be explained as follows: The initial proton recoil flux, having an approximately rectangular spectrum [12], is intercepted by spheres of different dimensions. For a sphere diameter equivalent to 1 μm or less of tissue, most of the recoil protons cross the sphere, producing a relatively sharp peak in microdosimetric

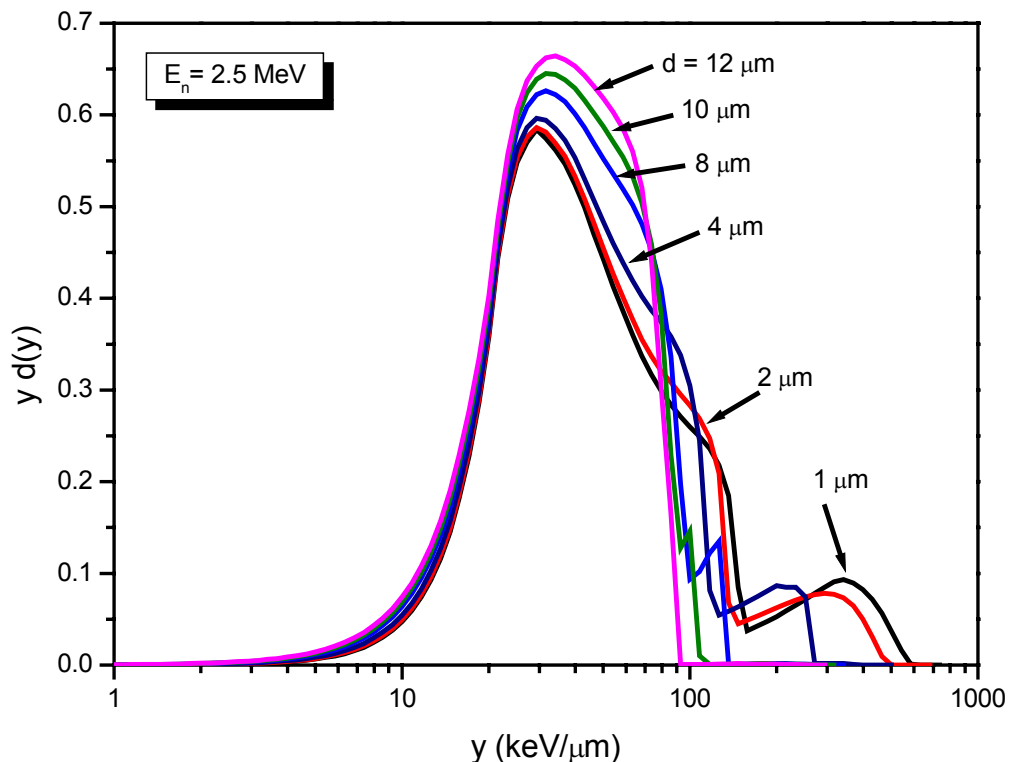


Figure 4.7: Calculated event-size spectra showing the dose fraction per logarithmic interval of lineal energy for different simulated site sizes. Dose distribution, $yd(y)$, changes by changing the simulated diameters.

spectrum. As the sphere's diameter increases above 1 μm , an increasing fraction of protons deposit their energy within the sphere. A further increase in diameter is not accompanied by more energy deposition, and therefore the whole spectrum is shifted toward lower y values. Moreover, the proton edge shifts downward because at the larger sizes the maximum energy that protons can expend in the sensitive volume is less than the product of the maximum LET and the diameter [13]. The contribution of heavy recoils is entirely within the proton spectrum if $d = 12 \mu\text{m}$. At this diameter $y_{\text{max}} \approx 90 \text{ keV}/\mu\text{m}$ and the maximum energy deposited by traversing protons, $(2d/3)y_{\text{max}} = 720 \text{ keV}$, is more than that deposited by maximum energy recoils even if these originate and terminate in the gas volume ($E_{\text{carbon}} \approx 0.28 \times 2.5 \text{ MeV} = 700 \text{ keV}$, see Eq. 5.7).

4.6 Conclusions

We have calculated the microdosimetric spectra of neutrons applying an analytical method. Calculations were performed for interactions of neutrons, with different energies, with tissue and tissue equivalent material at micrometer level. It has been shown that the contribution of different particle tracks (insiders, starters, stoppers and crossers) changes as the neutron energy or the simulated site size vary. The largest contribution, to the dose distribution, is originating from the crossers as long as the ranges of the secondary particles are much larger than the simulated site size. Furthermore, the contribution of insiders decreases with increasing of neutron energy.

Two parameters, neutron energy and simulated site size, which have a significant influence on the shape of microdosimetric spectra are extensively discussed. Increasing the neutron energy causes the proton peak maximum to extend to higher values of linear energy as long as the maximum range of protons is less than the site size. Increasing the neutron energies, for a situation that the maximum range of protons is larger than the site size, causes the proton peak maximum to shift to lower values of linear energy. As the neutron energy increases, the contribution of heavy particles increases which causes more densely ionization along their path. These heavy particles have a higher linear energy transfer (LET) and therefore they cause more biological damages to living tissue. Increasing the simulated site size causes narrowing of the dose distribution and a shift of the spectrum to lower lineal energy values.

These calculations give understanding of the influence of the various parameters influencing the microdosimetric spectra and can be used to compare with the measured microdosimetric spectra. However, in the case of measured spectra utilizing a proportional counter there are two stochastic factors which can make the shape of microdosimetric spectra slightly different from calculated spectra: 1) Fano-fluctuations, i.e. the number of ions produced per unit energy deposition and 2) multiplication statistic. Furthermore, the neutron sources are usually contaminated by γ -rays that can also effect the shape of spectra.

References

- [1] ICRU. *Microdosimetry*. Report 36 (Bethesda, MD: ICRU Publications) (1983).
- [2] Caswell, R. S. *Deposition of Energy by Neutrons in Spherical Cavities*. Radiat. Res. **27**, 92-107 (1966).
- [3] Caswell, R. S. and Coyne, J. J. *Interaction of Neutrons and Secondary Charged Particles with Tissue: Secondary Particles Spectra*. Radiat. Res. **52**, 448-470 (1972).
- [4] Caswell, R. S., Coyne, J. J. and Randolph, M. L. *Kerma Factor for Neutron Energies below 30 MeV*. Radiat. Res. **83**, 217-254 (1980).
- [5] Coyne, J. J. and Caswell, R. S. *Microdosimetric Energy Deposition Spectra and their Averages for Bin-Averaged and Energy-Distributed Neutron Spectra*. In: Proc. Seventh Symp. On Microdosimetry, Oxford, 1981, EUR 7141 (London: Harwood) p.689 (1981).
- [6] Coyne, J. J. and Caswell, R. S. *Neutron Energy Deposition on the Nanometer Scale*. Radiat. Prot. Dosim. **44**, 49-52 (1992).
- [7] Edwards, A. A. and Dennis, J. A. *The Calculations of Charged Particle Fluence and LET Spectra for the Irradiation of Biologically Significant Materials by Neutrons*. Phys. Med. Biol. **20**, 395-409 (1975).
- [8] Kellerer, A. M. and Chmelevsky, D. *Criteria for the Applicability of LET*. Radiat. Res. **63**, 226-234 (1975).
- [9] Kellerer, A. M. Consideration on the random traversal of convex bodies and solutions for general cylinders. Radiat. Res. **47**, 359-365 (1971).
- [10] Buhler, G., Menzel, H.G., Schuhmacher, H. and Dietze, G. *Neutron interaction data in carbon derived from measured and calculated ionisation yield spectra*. Radiat. Prot. Dosim. **13**, 13-17 (1985).
- [11] Srdoc, D., Goodman, L.J., Marino, S.A., Mills, R.E., Zaider, M., Rossi, H.H. *Microdosimetry of monoenergetic neutron radiation*. Seventh symposium on microdosimetry, London: Harward academic publishers, pp. 765-774 (1981).
- [12] Srdoc, D. and Marino, S.A. *Microdosimetry of monoenergetic neutrons*. Radiat. Res. **146**, 466-474 (1996).
- [13] Rossi, H. H. and Zaider, M. *Microdosimetry and its applications*. Springer 1996.

Chapter 5

High-Energy Neutron Microdosimetry

Microdosimetric data of high-energy neutrons are important to our understanding of dosimetry in radiation protection and radiotherapy e.g. for the estimation of dose to aircraft crews or the effect of secondary neutrons produced by high-energy accelerator facilities, and in the treatment planning for cancer therapy at advanced proton and neutron therapy facilities. Modern neutron radiotherapy employs energies extending to 70 MeV. Secondary neutrons produced by advanced proton therapy facilities can have energies as high as 250 MeV [1].

The knowledge of neutron interactions and microdosimetric data for neutron energies between 20 and 50 MeV is clearly inferior to that for neutrons of lower energies and for photons. For neutron energies above 50 MeV microdosimetric data are very scarce. For several practical applications, in particular for radiation protection and clinical dosimetry, the knowledge of microdosimetric data in this energy range is insufficient.

In this chapter, we will first have a look at two different high-energy neutron sources (i.e. quasi-monoenergetic and spallation). The neutron spallation source at CERN (European Organisation for Nuclear Research) has been planned to be used for measuring microdosimetric spectra of neutrons with energies up to 250 MeV. We will discuss the problems involved in using this facility for microdosimetry, such as pile-up and not getting enough information in a reasonable period of time. Furthermore, possible solutions to these problems are given. Finally, because of the impracticability of using a conventional Tissue Equivalent Proportional Counter (TEPC), a new type of TEPC based on Gas Electron Multiplier (GEM) is introduced.

5.1 High-energy neutron sources

A neutron is one of the fundamental particles that make up matter. In the universe, neutrons are abundant, making up more than half of all visible matter. But, for research on physical

and biological materials, neutron facilities of the right brightness are in short supply. In general, neutrons can be produced from a reactor (fission) or by bombarding matter with energetic particles (spallation or specific reactions).

Bombardment neutron sources have several features that are impossible or difficult to realise in reactors:

- 1) They can deliver an extremely wide range of neutron energies, from the GeV range all the way down to micro-eV, or even lower.
- 2) Neutrons can be generated with virtually any time structure from nanosecond pulses to practically continuously.
- 3) The flux levels obtainable during the pulses can exceed those of controlled fission-based sources by several orders of magnitude.

In addition to spallation, a favourable reaction to produce high-energy neutrons is ${}^7\text{Li}(p,n){}^7\text{Be}$ reaction. Both methods are discussed in the following.

5.1.1 Quasi-monoenergetic neutron source

High-energy, quasi-monoenergetic neutrons, can be generated by proton bombardment of a ${}^7\text{Li}$ -enriched target through the ${}^7\text{Li}(p,n){}^7\text{Be}$ reaction, such as at the Uppsala cyclotron, at the

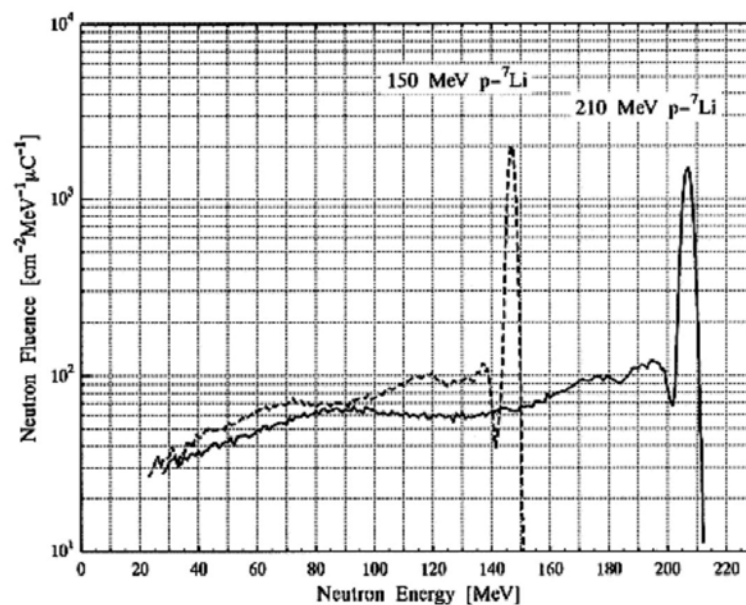


Figure 5.1: Energy spectra of quasi-monoenergetic neutrons from ${}^7\text{Li}$ target bombardment by 150 MeV and 210 MeV protons [2, 5]. Each neutron spectrum has a sharp monoenergetic peak at an energy of 3 to 4 MeV lower than the associated proton energy and a small amount of continuous lower energy.

Paul Scherrer Institute (PSI) and at RIKEN (The Institute of Physical and Chemical Research) in Japan. Since the ${}^7\text{Li}(p,n)$ reaction, which leads to the ground (0 MeV) and the first excited (0.429 MeV) states of ${}^7\text{Be}$ nuclei, has been measured well over the energy range up to 800 MeV, the ${}^7\text{Li}(p,n){}^7\text{Be}$ (g.s. + 0.429 MeV) is a convenient reaction for neutron sources. The p- ${}^7\text{Li}$ neutrons give a sharp dominant monoenergetic peak with a small amount of continuous lower energy neutrons. The neutron energy spectra from ${}^7\text{Li}$ target bombardment by 150 and 210 MeV protons are illustrated in Fig. 5.1 [2-5]. This figure clearly shows that each neutron spectrum has a sharp monoenergetic peak at an energy of 3 to 4 MeV below each proton energy and a small amount of continuous lower energy neutrons. Using this technique, neutrons have been generated up to 210 MeV of energy.

5.1.2 Spallation process

The bombardment of heavy metal targets by an intense beam of protons for neutron production, which is called spallation, has become an established technique for the production of high intensity fluxes of neutrons. When a fast particle, such as a high-energy proton, bombards a heavy atomic nucleus, some neutrons are "spalled," or knocked out, in a nuclear reaction. Other neutrons are "boiled off" as the bombarded nucleus heats up. For every proton hitting the nucleus, 20 to 700 neutrons (depending on proton energy) are liberated.

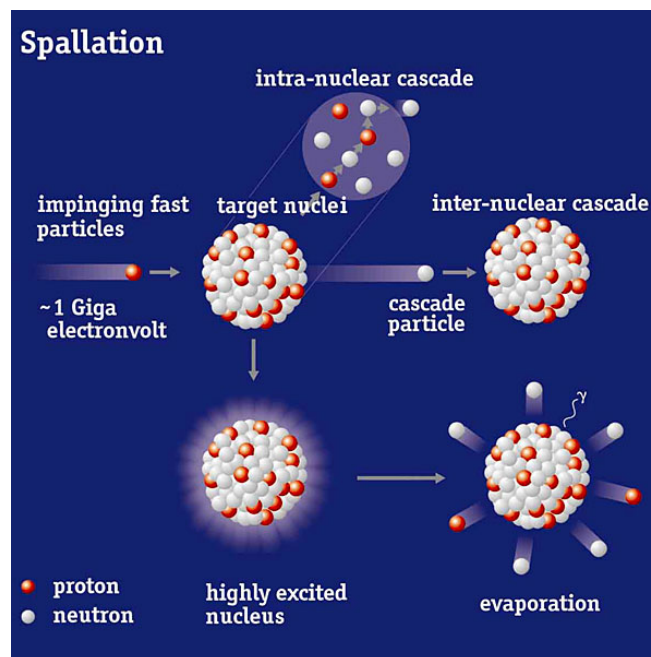


Figure 5.2: *The spallation process (ESS web site). An energetic proton interacts with a target nucleus. A few energetic particles are produced, leaving the nucleus in a highly excited state. The nucleus returns to the ground state by emission of neutrons, protons, deuterons, tritons and alpha particles (evaporation). The energetic particles go on to interact with other target nuclei producing more excited nuclei, and hence neutrons (nuclear cascade).*

Spallation neutron sources exploit the thermal excitation of heavy nuclei by energetic (GeV) protons and the subsequent decay of these nuclei by evaporation of mainly neutrons with energies of a few MeV. Only a small fraction of the proton's kinetic energy is dissipated into thermal excitation energy while a larger fraction is carried off during the initial intra-nuclear cascade (INC) by energetic (hundreds of MeV) particles (mainly nucleons). These pre-equilibrium particles in turn initiate, in a thick target, secondary reactions (inter-nuclear cascade) producing additional neutrons [6, 7].

A schematic of a spallation process is shown in Fig. 5.2 (ESS web site). The processes can be described by means of high-energy transport codes which are widely used to design pulsed Spallation Neutron Sources such as the European Spallation Source (ESS). Spallation neutron sources generally produce a wide range of neutron energies with the highest neutron energy approaching that of the incident charged particle beam. If the incident beam is pulsed, time-of-flight techniques can be used to determine the energy of the neutrons.

Each pulse contains neutrons of various energies, so neutrons of different energies can be separated by letting them travel down a path of a few hundred meters. The high-energy neutrons reach the sample ahead in time of the medium-energy neutrons, and the lowest-energy neutrons take the longest time to arrive at the sample. So the energy of an individual neutron is easily determined by its "time of flight" to the sample.

5.2 Neutron Time Of Flight facility at CERN

Most of the world's neutron sources were built decades ago, and although the use and demand for neutrons have increased throughout the years, few new sources have been built. But now at CERN the construction of a new, accelerator-based neutron source, neutron Time Of Flight (n_TOF) facility has been finished. It provides intense pulsed neutron beams for scientific research. In this facility the spallation mechanism, which is a remarkably powerful source of neutrons, is used.

The general layout of the n_TOF experiment is shown in Fig. 5.3 [8]. After the protons are accelerated by a linear accelerator (LINAC), they enter a single Booster ring as a single bunch. The single bunch in the single Booster ring is accelerated and injected into the Proton Synchrotron (PS) at 1.4 GeV. The bunch is injected and accelerated by means of the Radio Frequency (RF) source. Finally, proton bunches of 24 GeV are extracted and led onto a lead spallation target. The neutrons produced by spallation are canalised to an experimental area located 200 m downstream through a vacuum pipe making use of the existing TT2A tunnel. The CERN PS accelerator is capable of accelerating 3×10^{13} ppp (protons per pulse).

In a lead spallation target, one 24 GeV proton may produce as many as 760 neutrons, resulting in as many as 2×10^{16} neutrons in each pulse. This source can be concentrated in short time (7 ns width) pulses with a repetition time of 14.4 s. The distributions of neutrons and charged particles as a function of their arrival time and their energy at 200 m are shown in Fig. 5.4 [9].

A dipole magnet has been used in the beam transfer line to sweep away the charged particles that contaminate the neutron beam. The neutron beam of n_TOF will have a maximum spatial spread of 2 cm radius (4 cm diameter) at 184.5 m (sample position) and reaches 4 cm radius at the place where the beam hits the tunnel floor. The beam profile at different distances [10] is shown in Fig. 5.5.

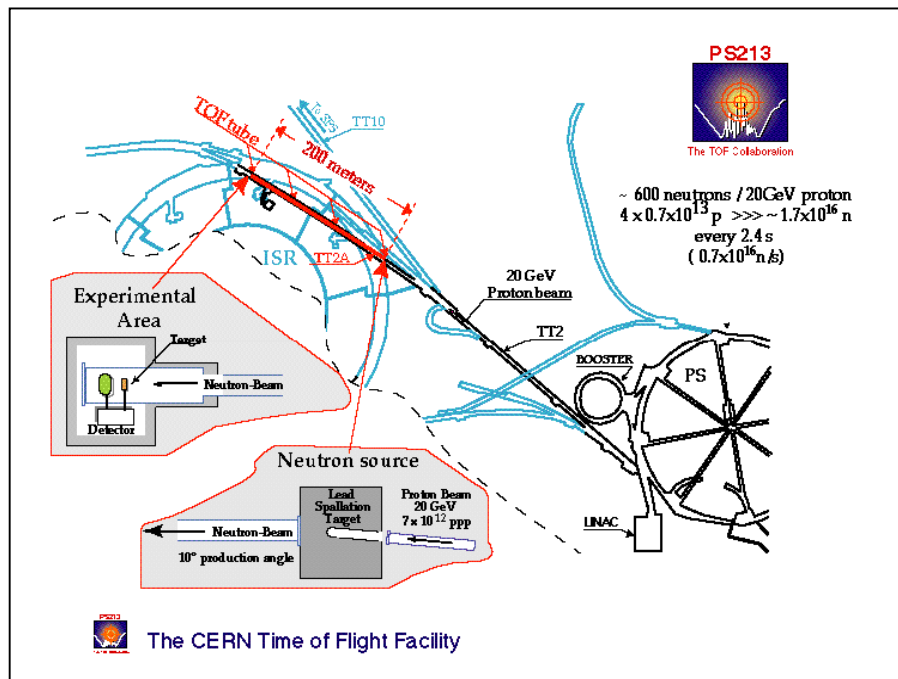


Figure 5.3: General layout of the n_TOF experiment [8]. Protons for the PS are extracted via the TT2 transfer line and hit a lead target. About 200 m from the lead target, at the end of the TOF tunnel (TT2A), neutrons are detected.

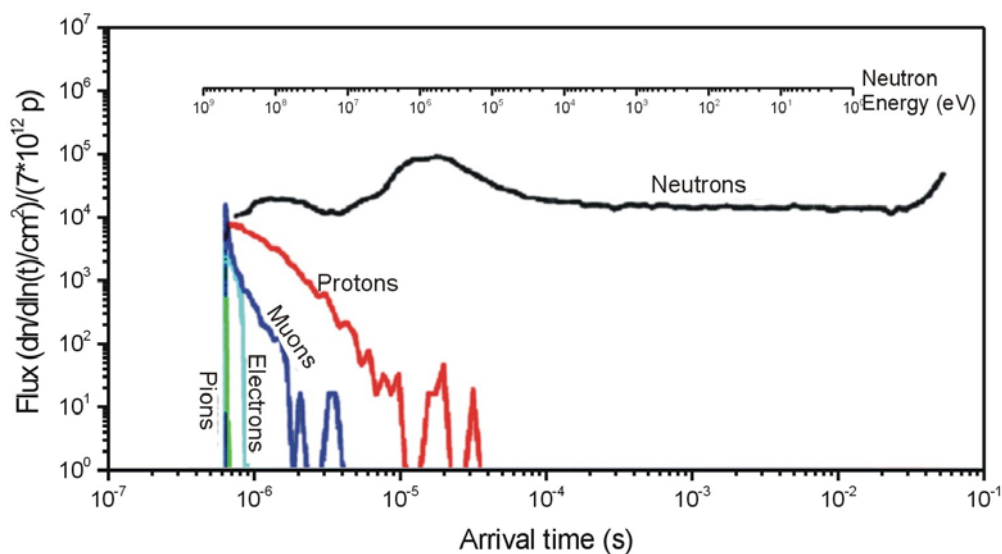


Figure 5.4: Fluxes of neutrons and the charged secondary particles produced by the spallation process as a function of their arrival time at 200 m. In the upper part, the energy is also shown [8, 9].

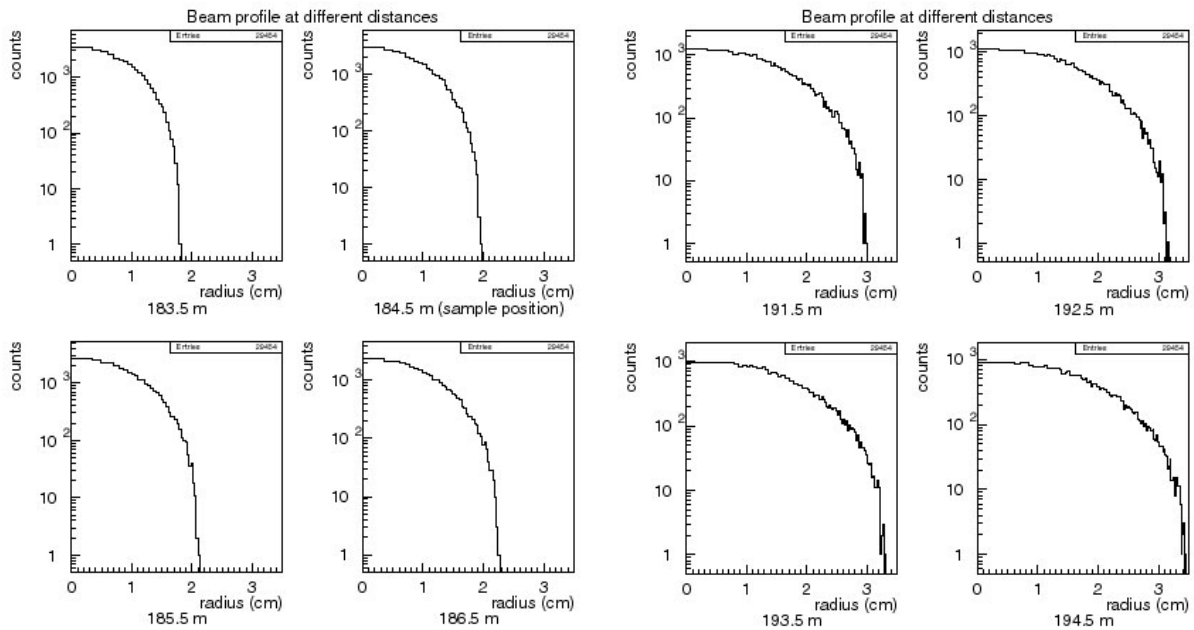


Figure 5.5: The beam profile on n_TOF at different distances from the spallation target [10]. The neutron beam has a maximum spread of 2 cm radius at sample position (184.5 m) and reaches 4 cm at the place where the beam hits the tunnel floor.

5.3 Calculation of interaction in counters used in microdosimetric

The microdosimetric measurements of high-energy neutrons were planned to be performed at the n_TOF facility at CERN. At the n_TOF facility, the acquisition of microdosimetric data is complicated by the low duty cycle and high instantaneous flux that may cause pile-up which results in spectral distortions. This problem has severely hindered previous efforts to collect microdosimetric data at therapy facilities at which high flux sources are applied [11]. To minimise pile-up and dead time problems, either the instantaneous flux should be kept low or the size of the counter cavity has to be decreased to ensure proper measurement of single event data. Since modification to the neutron flux of the n_TOF facility is difficult if not possible, the only possibility for acquisition of microdosimetric data from this facility will be the proper choice of the counter cavity size. To choose the counter cavity size, the Secondary Charged Particle (SCP) fluxes, which originate from the interaction of the n -TOF beam with the counter material, has to be estimated. A method has been developed which appears to be fast and reliable to estimate the order of SCP fluxes. This method will be explained in more detail.

The starting point for this method is the flux of the neutrons at n_TOF facility as a function of their arrival time at 200 m downstream where the detector can be placed (see Fig. 5.4). In the

energy region between 50 MeV and 250 MeV, the flux per logarithm of time is almost constant. The neutron flux can be separated into individual time intervals. Then the neutron fluence per interval i , $\Phi_{n,i}$, can be given as (see Fig. 5.4):

$$\Phi_{n,i}(\text{cm}^{-2}) = 3 \cdot 10^4 \times \ln\left(\frac{t_i + \Delta t}{t_i}\right) \quad (5.1)$$

where t_i represents the time of arrival of neutrons having a certain energy at each interval and Δt the time interval corresponding to a certain energy width. The arrival time, at 200 m from the spallation target, of neutrons as a function of their relativistic kinetic energy, E_{kin} , can be written as:

$$t_{\text{arrival}}(s) = \frac{x}{v} = \frac{200}{c \times \sqrt{1 - \frac{1}{\left(\frac{E_{\text{kin}}}{m_0 c^2} + 1\right)^2}}} \quad (5.2)$$

where x represents the neutron travel distance, v and m_0 the neutrons velocity and rest mass and c the light velocity.

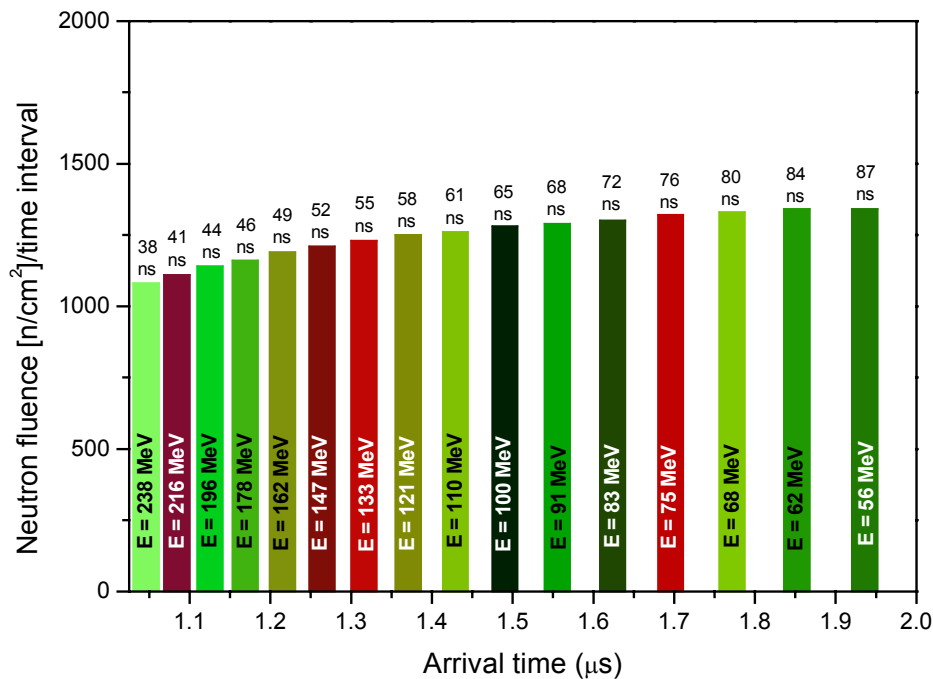


Figure 5.6: The calculated neutron fluence per time interval as a function of neutron arrival time at 200 m from the spallation target. Each interval corresponds to an average neutron energy which is indicated at each interval. The corresponding time intervals are also indicated at the top of each interval.

For a neutron energy width of 10% for each interval which corresponds to a certain time interval Δt , the neutron flux can be calculated by substituting Eqs. 5.2 into 5.1. The calculated neutron fluence per time interval as a function of their arrival time is illustrated in Fig. 5.6. Each interval corresponds to an average neutron energy as indicated. At the top of each column the time interval, Δt , is also shown. This calculation has been shown for neutron energies down to 50 MeV because the 50-250 MeV interval is the most interesting region for our purpose.

The number of SCP per unit area, which will be created by neutrons with an energy E_n , can be estimated from:

$$n_{SCP} = \left(\frac{K_{(E_n)}}{(S/\rho)_{(\bar{E}_{SCP})}} \right) \quad (5.3)$$

where K is the Kinetic Energy Released per Unit Mass (kerma) and (S/ρ) is the mass stopping power of the SCP. These quantities are explained in the next section.

5.3.1 Kerma

The kerma, K , is a quantity closely related to absorbed dose, D , which describes the transfer of energy from indirectly ionizing radiation (photons or neutrons) into kinetic energy of charged particles. Kerma is a basic quantity for neutron dosimetry and for studies on neutron-induced damage. The ratio of K and neutron fluence, Φ_n (the number of neutrons per unit area), is called fluence-to-kerma conversion coefficient, k_Φ (in short, kerma coefficient).

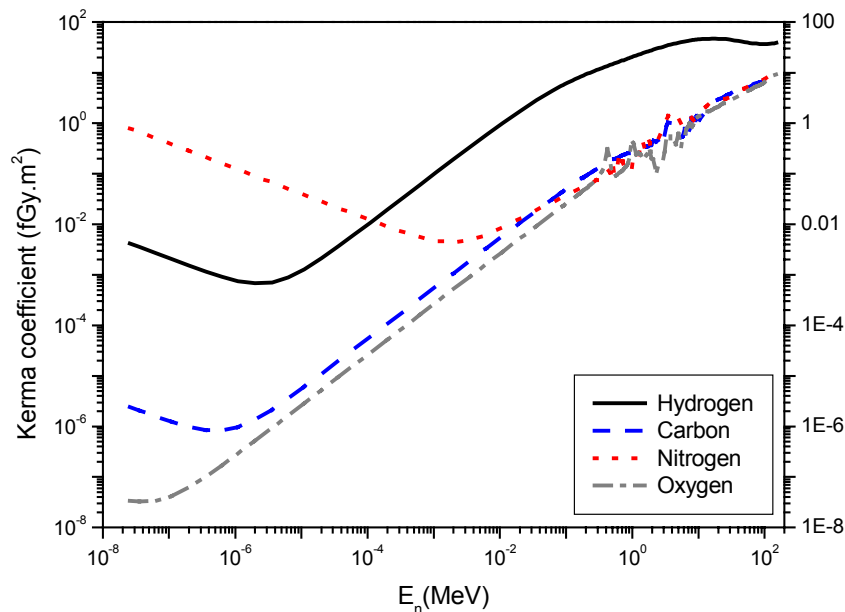


Figure 5.7: The kerma coefficient as a function of neutron energy for the most important components of tissue (e.g. hydrogen, carbon, nitrogen and oxygen) [14] up to neutron energy of 150 MeV. At higher neutron energies, heavy recoils become significant.

The kerma coefficient for neutron interactions with single elements is given by [12]:

$$k_{\Phi}(E_n) = \frac{K}{\Phi_n} = N \sum_j \bar{\varepsilon}_j(E_n) \sigma_j(E_n) \quad (5.4)$$

where $\bar{\varepsilon}_j$ is the average energy of projectile j expressed in MeV and σ_j the production cross section of projectile j expressed in barns. The coefficient $N = 9.64853 \cdot 10^{-15} / M_A$, where M_A is the atomic mass of the target in units of u, converts the kerma coefficient from units of MeV·b to S.I. units of fGy·m².

Ionisation in hydrogenous matter (e.g. tissue) exposed to neutrons is mainly produced by recoil protons, heavy recoil nuclei and products of nuclear reactions. These secondary particles are produced by elastic scattering, inelastic scattering, capture processes (important for thermal neutrons), and spallation (significant at neutron energies above 100 MeV [13]). Because an incident neutron can transfer up to its entire energy in a single collision with a hydrogen nucleus (see Eq. 5.7), protons dominate the energy deposition in all biological materials that have relatively high hydrogen content, e.g. muscle. Heavy ion recoils may, however, become significant at higher neutron energies as it is shown in Fig. 5.7 [14]. Fig. 5.7 shows the kerma coefficient as a function of neutron energy for the most important components of tissue and TE materials (e.g. hydrogen, carbon, nitrogen and oxygen) up to a neutron energy of 150 MeV.

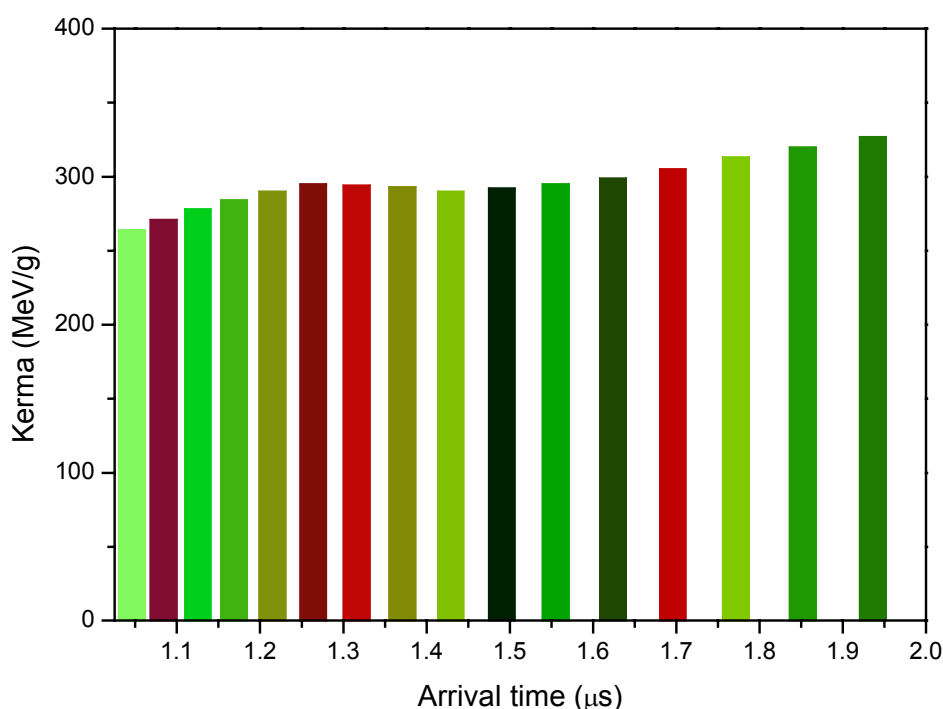


Figure 5.8: The calculated hydrogen kerma for each interval. In this calculation used for neutron energies > 150 MeV the kerma coefficient at 150 MeV was used.

The kerma for each component of tissue can be calculated according to:

$$K_{comp}[eV/g] = f_{comp} \times k_{\phi}[Gy \cdot m^2] \times \Phi_n[cm^{-2}] \times \left(\frac{10}{1.6 \cdot 10^{-19}} \right) \quad (5.5)$$

where f_{comp} is the fraction of an elemental component of tissue, k_{ϕ} the kerma coefficient and Φ_n the neutron fluence. Fig. 5.8 illustrates the calculated hydrogen kerma for each time interval of the n-TOF facility using the neutron flux, shown in Fig. 5.6, and Eq. 5.5. For neutron energies above 150 MeV, the kerma coefficient at 150 MeV neutron energy has been used since these data are not yet available. Moreover, we do not expect major differences of kerma coefficient values between 150 and 250 MeV.

5.3.2 Mass Stopping Power

Neutrons cannot interact with matter by means of the Coulomb force since they carry no charge. When a neutron does undergo interaction, it is with a nucleus of the absorbing material which generally occurs via elastic scattering, inelastic scattering, capture and spallation. The relative importance of the different interaction modes is dependent on the neutron energy and the elemental composition of the absorbing medium. According to ICRU report [13], the normal (muscle-equivalent) tissue composition in elements of H, C, N, O, and others in percent by weight is 10.2, 12.3, 3.5, 72.9 and 1.2, respectively.

In the inelastic scatter process, neutrons undergo capture and reemission. The scattering nucleus may be left in an excited state. The excited nucleus will decay to its ground state within a short interval of time, emitting gamma rays [15]. These reactions are possible only when the neutron energy is greater than a certain threshold energy. The energy transferred to a recoil nucleus, E_R , left in an excited state with mean energy $\overline{E^*}$ above the ground state is given by the formula [16]:

$$E_R = \frac{2AE_n}{(1+A)^2} - \frac{\overline{E^*}}{(1+A)} - \frac{2AE_n}{(1+A)^2} \left[1 - \frac{(A+1)\overline{E^*}}{AE_n} \right]^{1/2} \cos\theta_{cm} \quad (5.6)$$

where A represents the atomic mass of the target nucleus, E_n is the incoming neutron kinetic energy (laboratory system), E_R is recoil nucleus kinetic energy (laboratory system) and θ_{cm} is scattering angle of the neutron in the center of mass system. Important inelastic reactions in tissue are those with carbon, nitrogen and oxygen.

The kinetic energy transferred from a neutron to a nucleus in an elastic collision can be treated mathematically as a special case of inelastic collision for $\overline{E^*} \equiv 0$. It is clear that the energy given to the recoil nucleus is only determined by the scattering angle with a distribution in which the recoil energies are distributed between the minimum of zero ($\theta_{cm} \cong 0^\circ$) and the maximum possible recoil energy ($\theta_{cm} \cong -180^\circ$) equal to:

$$E_R = \frac{4A}{(1+A)^2} E_n \quad (5.7)$$

This means that the maximum energy of a proton, a carbon, a nitrogen or an oxygen recoil resulting from a collision of 1 MeV neutrons is 1, 0.28, 0.25 and 0.22 MeV, respectively.

For fast neutrons with energies up to 10 MeV, hydrogen is by far the most important target nucleus. For neutrons with energies higher than 10 MeV, other target nuclei become significant too. For single scattering in hydrogen, the fraction of the incoming neutron energy that is transferred to the recoil proton can range from anywhere between zero and the full neutron energy (see Eq. 5.7). Because all scattering angles are possible, a continuum of possible recoil energies between these minimum and maximum values should be expected. The average proton energy is one-half of the neutron energy if the scattering process is isotropic in the center-of-mass-coordinate system. However, there are some complicating factors which are beyond this estimation that can distort this simple rectangular response.

For charged particles in a given absorber the linear stopping power, S , is simply defined as the ratio of the differential energy, dE , for that particle within the material and the corresponding differential path length, dx :

$$S = -\frac{dE}{dx} \quad (5.8)$$

A particle passing through matter interacts with electrons and with nuclei, possibly also with the medium as a whole (Cherenkov radiation, coherent bremsstrahlung). A light projectile colliding with a heavy target particle will be deflected (Multiple Scattering), but will lose little energy unless the collision is inelastic. A heavy projectile colliding with a light target will lose energy without being appreciably deflected.

Except when the projectile is highly relativistic, excitation and ionisation are the main electromagnetic contribution to the energy loss for charged particles. The mean energy loss (the stopping power) due to excitation and ionisation for heavy charged particles is given by the Bethe-Bloch formula [17]:

$$-\frac{dE}{dx} = \frac{4\pi e^4 z^2}{m_0 v^2} NB \quad (5.9)$$

where

$$B \equiv Z \left[\ln \frac{2m_0 v^2}{I} - \ln \left(1 - \frac{v^2}{c^2} \right) - \frac{v^2}{c^2} - \frac{C}{Z} - \frac{\delta}{2} \right]$$

In these expressions, the particle has atomic number z and velocity v , the electron has rest mass m_0 and charge e and the absorber has atom number density N of atomic number Z . The parameter I is interpreted as the mean atomic excitation potential incorporating all excitation and ionisation processes. The parameters C and δ are the shell correction and the density correction term, respectively. Expression B is known as the stopping number (atomic number scaled for stopping). As particles are non-relativistic, only the first term in B is significant. From these equations, it can be seen that the specific energy loss is greatest for high density, high Z absorbers and also for ions in higher charge states.

For non relativistic charged particles ($v \ll c$), the general behaviour of the stopping power can be derived from the behaviour of the multiplicative factor of Eq. 5.9 since the expression for B varies slowly with particle energy. Therefore, the stopping power varies as $1/v^2$, or inversely with particle energy, and z^2 . Thus for particles of the same velocity, the one with the highest charge will have the largest specific energy lost.

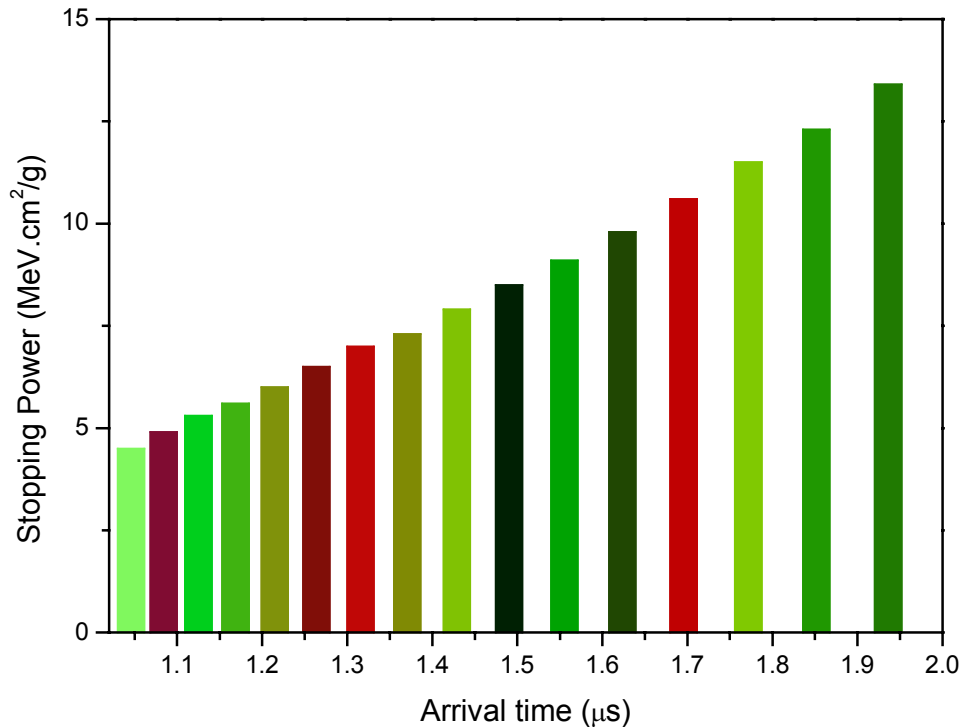


Figure 5.9: The mass stopping power as a function of neutron arrival time of the n_{TOF} facility. For each interval the average proton energy is calculated and the corresponding mass stopping power in A-150 TE plastic [18] is shown.

The linear stopping power of a material normalised for the density of the material is defined as the mass stopping power. It should be noticed that the Linear Energy Transfer (LET) is similar to the stopping power except that it does not include effects such as Bremsstrahlung and delta ray. The difference between LET and S is that LET is local energy deposition only while S is concerned with the total energy lost by the particle.

The mass stopping power of protons in A-150 TE plastic for each time interval is shown in Fig. 5.9. For each interval, the average proton energy is calculated and the mass stopping power of protons in A-150 TE plastic [18] corresponding to that interval is illustrated. It should be kept in mind that as the proton energy decreases, the mass stopping power will increase until a certain energy (depending on the particle) below which it will decrease.

5.3.3 Proton fluence

The number of protons per unit of area can be estimated applying Eq. 5.3 for protons. The kerma (section 5.3.1) and mass stopping power (section 5.3.2) of protons for each interval have been calculated. By simply dividing the kerma by the mass stopping power for each interval, the number of protons can be estimated for each interval. The calculated average number of protons per mm^2 for each time interval is illustrated in Fig. 5.10.

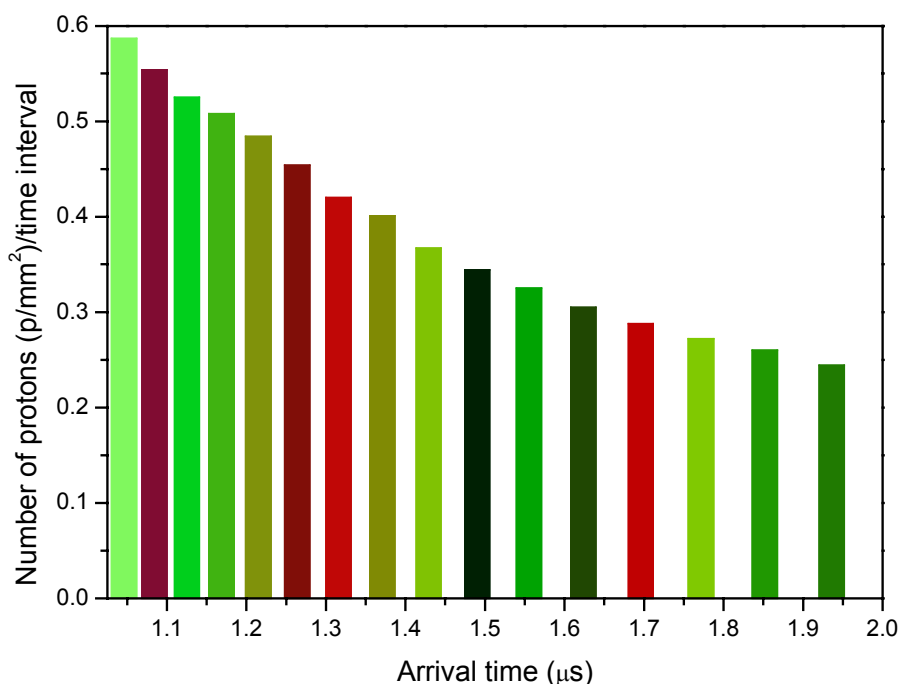


Figure 5.10: The estimated number of protons per mm^2 for each interval as a function of neutron arrival time of the n_TOF facility.

The number of protons has also been calculated by using the Monte Carlo code FLUKA [19] which is a general purpose transport code. This calculation has been performed for mono-energetic neutrons with energies of 150, 200 and 250 MeV after passing different thicknesses of TE material. The normalised neutron and proton fluences, as a function of thickness of TE material, are presented in Table 1. The TE material thickness, at which charged particle equilibrium is obtained for the applied neutron energy, and the corresponding neutron and proton fluences are shown bold in Table 1. A comparison has been made between the calculated proton fluence using FLUKA and the estimated proton fluence using stopping power and kerma (see Table 2). The order of magnitude of the proton fluence calculated using FLUKA corresponds well with the proton fluence estimation. Therefore, we conclude that the proton fluence estimation using kerma and mass stopping power are trustworthy.

From these results, it becomes clear that in order to prevent pile-up effect a counter which has a sensitive-volume diameter in the order of a millimetre is required. Thus, a usual counter which has a sensitive volume diameter of few centimetres, is not applicable in the n_TOF facility for microdosimetric measurements due to pile-up effect.

Table 1: The normalised neutron and proton fluences are shown as a function of thickness of A-150 TE material for three mono-energetic neutron energies (viz. 150, 200, 250 MeV) using the Monte Carlo code FLUKA. The TE material thickness, at which the charged particle equilibrium is obtained for the applied neutron energies, and corresponding neutron and proton fluences are shown bold.

D (cm)	Neutron Energy (MeV)					
	150		200		250	
	ϕ_n (n/cm ²)	ϕ_p (p/cm ²)	ϕ_n (n/cm ²)	ϕ_p (p/cm ²)	ϕ_n (n/cm ²)	ϕ_p (p/cm ²)
1	1.00	0.74E-2	1.00	0.71E-2	1.00	0.77E-2
2.5	0.96	0.15E-1	0.98	0.13E-1	0.98	0.15E-1
3.5	0.96	0.17E-1	0.97	0.18E-1	0.98	0.20E-1
5	0.95	0.21E-1	0.97	0.22E-1	0.95	0.25E-1
8	0.92	0.25E-1	0.94	0.33E-1	0.94	0.37E-1
15	0.88	0.40E-1	0.87	0.47E-1	0.87	0.55E-1
25	0.82	0.52E-1	0.81	0.70E-1	0.81	0.83E-1
35	0.75	0.47E-1	0.75	0.84E-1	0.79	0.96E-1
50	0.68	0.48E-1	0.69	0.67E-1	0.65	0.11E0

Table 2: Comparison of the calculated proton fluences using the Monte Carlo code FLUKA and the method using stopping power (S) and kerma for three mono-energetic neutron energies under the conditions of charged particle equilibrium.

	Neutron Energy (MeV)		
	150	200	250
Neutron fluence of n_TOF ϕ_n (n/mm ²)	12	11	10
Proton fluence using FLUKA ϕ_p (p/mm ²)	0.5	0.8	1.0
Proton fluence using S and kerma ϕ_p (p/mm ²)	0.5	0.5	0.6

5.3.4 Distribution for intervals

To select events that are attributed only to neutrons of a particular energy, a detector with good timing characteristics has to be applied in the n_TOF facility. The drift length in the cavity of the counter and hence the electron drift velocity in applied gases determine the time response of the detector. The fast rise time signal produced by free electrons is very small compared to the signal resulting from the drift of positive ions towards the cathode. In standard TEPC, the avalanche consisting of 10^4 - 10^7 (by a gain of about 1000) ion pairs is formed in a narrow zone around the anode wire and it is the drift of the positive ion cloud in the strong field near the anode that produces the electric signal proportional to the total number of charges in the avalanche. The time intervals separating random events are of interest for these measurements.

In order to derive a distribution function to describe the time interval between successive random events, first we assume that an event has occurred at time $t = t_0$. To find the differential probability that the next event will take place within a differential time Δt_i after a time interval of length t , two independent conditions have to be considered.

- 1) No event occurs within the time interval from t_0 to t .
- 2) An event takes place in the next differential time increment Δt_i .

The overall probability will then be given by the product of the probabilities characterising the two processes [16]:

$$\begin{array}{l} \text{Probability of next} \\ \text{event taking place} \\ \text{in } \Delta t_i \text{ after delay of } t \end{array} = \begin{array}{l} \text{Probability} \\ \text{of an event} \\ \text{during } \Delta t_i \end{array} \times \begin{array}{l} \text{Probability of no} \\ \text{events during time} \\ \text{from } t_0 \text{ to } t \end{array}$$

$$I(t) = \frac{N_i}{\Delta t_i} \times \exp\left(-\frac{N_i}{\Delta t_i}(t-t_0)\right) \quad (5.10)$$

where N_i represents the total number of protons in interval Δt_i .

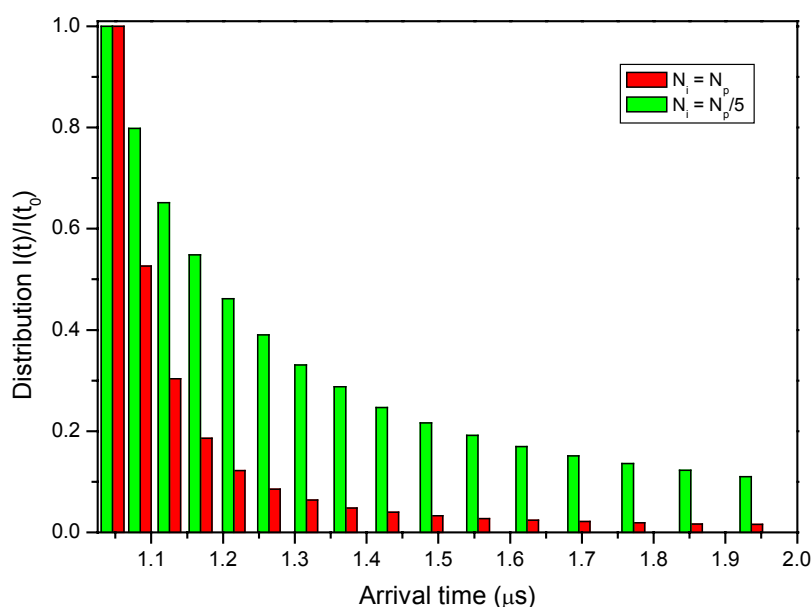


Figure 5.11: *The relative distribution for intervals between contiguous random events as a function of neutron arrival time in the n_TOF facility. It is shown for the calculated number of protons (section 5.4.3) and for the case that the number of protons has been decreased by a factor of five.*

The distribution function for intervals between contiguous random events is shown in Fig. 5.11. Because the distribution function depends on the total number of protons, the

distribution has been shown for the number of protons calculated in the previous section as well as for the case that the number of protons has been lowered by a factor of five. It can be seen that decreasing the total number of protons causes an increase of the probability of having the first interaction in other intervals than the first interval.

5.3.5 Event distribution

Employing the calculated distribution function for microdosimetric measurements at the n_TOF facility and considering the fact that for each interval (spectrum) between 10^5 - 10^6 events are needed for good statistics, the event distribution as a function of neutron arrival time has been calculated for 16 intervals with a total of $16 \cdot 10^6$ events. This seems to be the minimum required total number of events. It is illustrated in Fig. 5.12. The event distribution is shown for the total number of calculated protons (section 5.3.3) and for the case of one-fifth of the calculated number of protons.

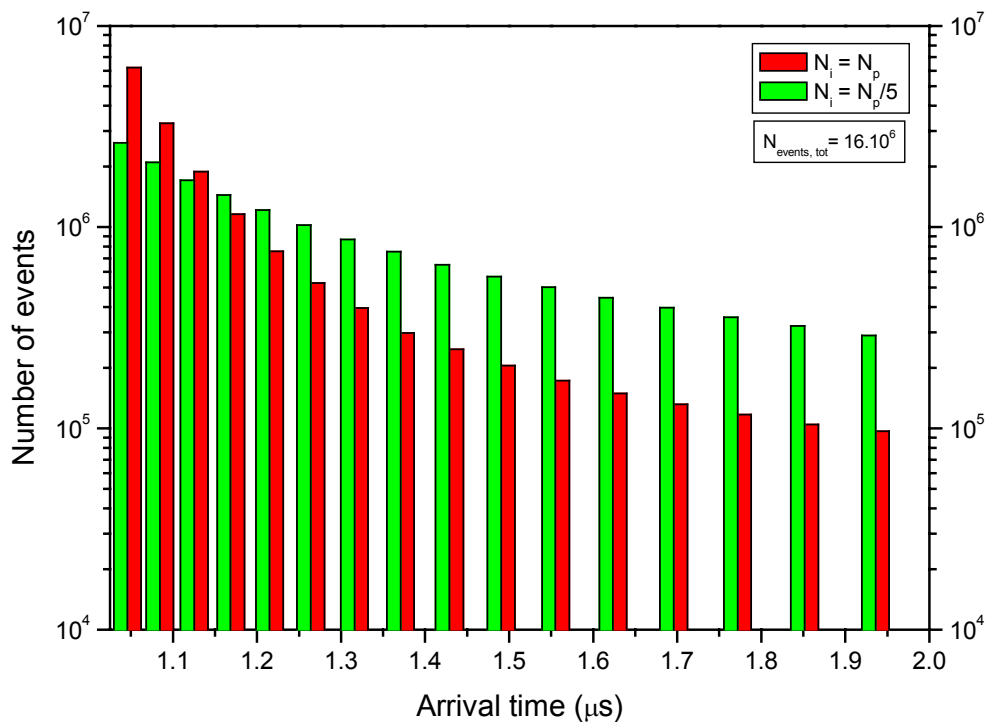


Figure 5.12: The event distribution is shown the total number of calculated protons and for one-fifth of this number.

Considering the repetition time of 14.4 s (section 5.2) of the n_TOF neutron source and the possibility of measuring one event per pulse, the total required time to measure $16 \cdot 10^6$ events becomes more than 7 years, which is not realistic. A multi-element counter has been proposed to reduce the measuring time. By using a multi-element counter of 12×12 the measuring time will be decreased by a factor of 144 which implies a measuring time of 19 days. Though much shorter this is still quite long.

There are other problems regarding performing microdosimetric measurements at the n_TOF facility. However, these will not be discussed here (e.g. the size of the beam (section 5.2), the prompt gamma flash [9]) since the main goal of the research was modified, developing a novel counter (section 5.4).

We have seen that we meet some difficulties in performing microdosimetric measurements at the n_TOF facility. The most important are the pile-up effect and long measuring times. The solution to minimising pile-up has been found in reducing the counter sensitive volume diameter. To collect enough data in a relatively short time a multi-element counter has been proposed. Therefore, rather than performing measurements at n_TOF we concentrated on the development of a mini multi-element counter.

5.4 Mini multi-element TEPC(-GEM)

In the past few years several groups have developed various types of mini TEPCs. Kliauga [20] measured single event distributions with a single-wire mini TEPC of 0.5 mm of diameter which simulates sizes below 300 nm.

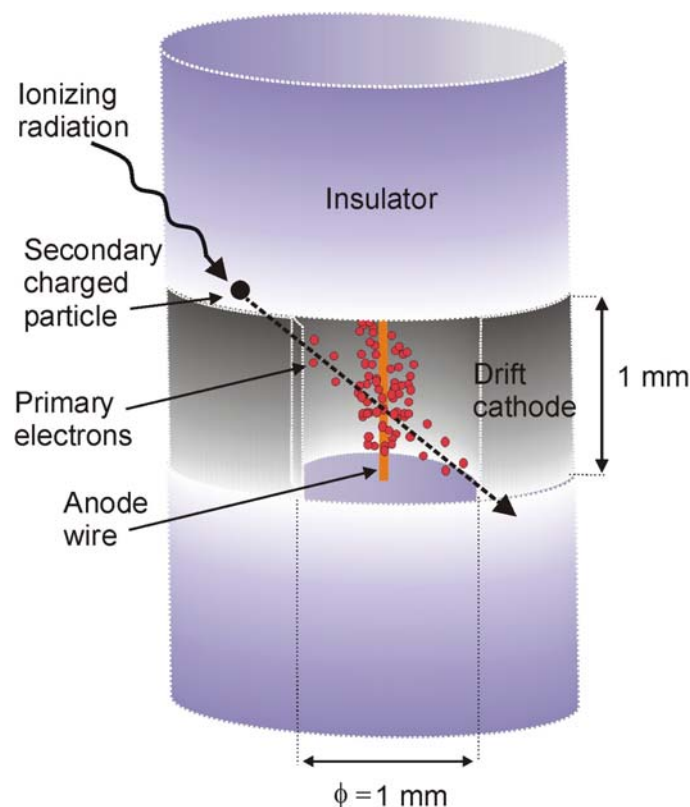


Figure 5.13: A schematic 3D view of the usual mini TEPC. The drift cathode, the insulator and the gas are of tissue-equivalent material. As the ionising radiation interacts with the counter wall, a secondary charged particle is created. This may pass through the counter sensitive volume (see text).

Cesari et al. [21] reported microdosimetric measurements of a proton therapeutic beam with a mini TEPC of 1.0 mm diameter. Burmeister et al. [22] applied a mini TEPC in high-flux mixed fields. However, all these mini TEPCs are designed based on the same principle of the traditional TEPC. In other words, this has been done by miniaturising the dimensions of all components of a usual TEPC, i.e. a proportional counter (PC) with a cavity with a central anode wire operating with a tissue-equivalent counting gas.

A schematic 3D view of a usual mini TEPC is shown in Fig. 5.13. The drift cathode, the insulator and the gas are of tissue-equivalent material. As the ionizing radiation interacts with the counter wall, a secondary charged particle is created which may pass through the counter sensitive volume (SV). This secondary particle will produce a number of ion pairs in the gas inside the cavity. The electrons drift toward the anode wire. In a narrow zone around the anode wire where the electric field is strong enough, multiplication will occur. Employing a helix (common in usual TEPCs) is not possible in mini TEPC due to the lack of space. Therefore, the central anode wire of a mini TEPC has to be centered precisely to ensure an isotropic electric field. Construction of a central wire in a small cavity is not an easy task. This becomes even more difficult for a mini multi-elemental counter. This situation motivated us to think of an alternative TEPC that avoids these difficulties. The use of a central anode wire can be eliminated by using a Gas Electron Multiplier (GEM) (section 3.8). This simplifies the counter construction considerably.

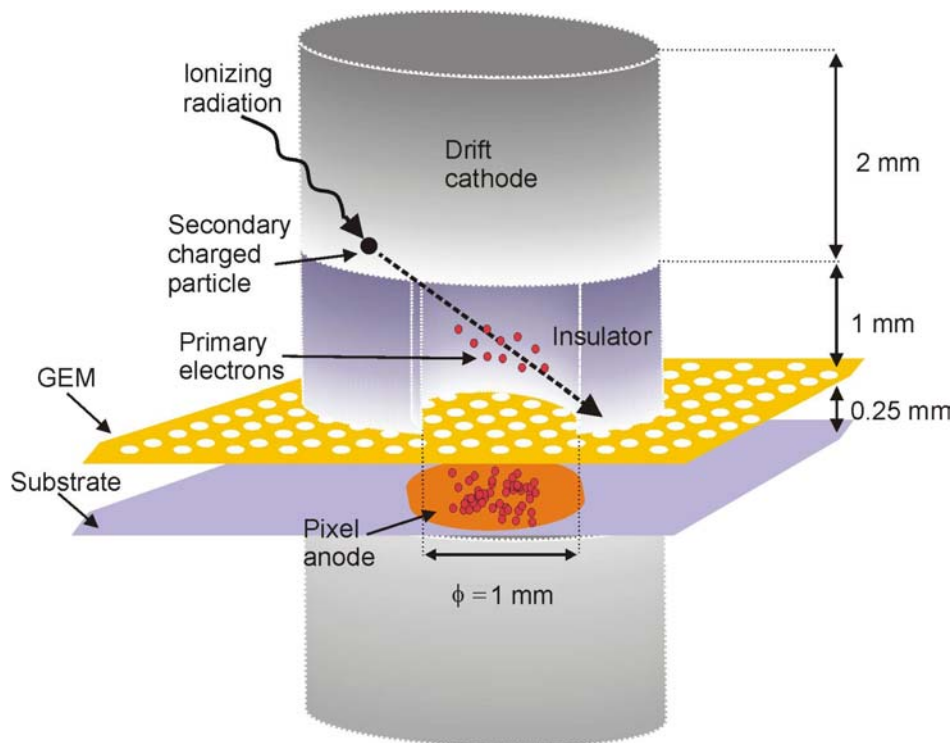


Figure 5.14: Schematic 3D view of a TEPC-GEM. The drift cathode, the insulator and the gas are of tissue-equivalent material. The sensitive volume is the volume inside the insulator. The GEM, gas amplification inside the holes and the pixel-anode are indicated.

A Schematic 3D view of TEPC-GEM is shown in Fig. 5.14. The drift cathode, the insulator and the gas are of tissue-equivalent material. The SV is the volume inside the insulator. The GEM with gas amplification inside the holes and pixel-anode are indicated. Application of a GEM simplifies the construction of (i) a miniature counter with a small sensitive volume to reduce pile-up effects and (ii) multi-element counter configurations to increase the sensitivity of the TEPC to measure very low radiation field intensities. Furthermore, the possibility of performing microdosimetric measurements (e.g. nanodosimetry, personal and space dosimetry) will be expanded utilizing this novel design.

5.5 Conclusions

In this chapter we have discussed and explained two different high-energy neutron sources, based on the ${}^7\text{Li}(p,n){}^7\text{Be}$ reaction and the spallation process. Both neutron sources are based on the release of neutrons from matter by bombardment with energetic particles. For microdosimetric measurements of high-energetic neutrons we have focused on the n_TOF facility at CERN, which is based on the spallation process, since this neutron source was available to use. Some possible difficulties utilising this neutron source for extracting microdosimetric data have been discussed.

The high neutron flux density of n-TOF causes the problem of pile-up which can be reduced by decreasing the counter size. A calculation has been performed to estimate the proper counter size based on kerma and mass stopping power from which the number of secondary charge particles can be estimated. This calculation appears to be a fast, reliable method to estimate the fluence of secondary charged particles. The Monte Carlo code FLUKA has also been used to calculate the fluence of secondary charged particles. The results of the Monte Carlo calculation and the calculation utilising kerma and mass stopping power agree well. Therefore, we can conclude that the proton fluence estimation using kerma and mass stopping power is trustworthy.

The calculations have shown that a mini TEPC, which has a sensitive volume diameter of 1 mm, will be needed to reduce the pile-up effect properly. Furthermore, the n-TOF facility has a large neutron pulse repetition time of 14.4 s which gives the problem of not getting enough information in reasonable measuring time. Therefore, a multi-TEPC has been proposed.

Since the construction of traditional mini multi-element TEPC based on a central anode wire is difficult, a novel TEPC design based on the Gas Electron Multiplier (GEM) has been introduced. This new design will not only simplify the construction of mini multi-element counters but it will also expand the possibility of performing microdosimetry measurements (e.g. nanodosimetry, personal and space dosimetry) in a relatively easy manner.

To investigate the possibility of using a TEPC based on a GEM, the operation of GEMs employing Tissue-Equivalent gases has to be studied. This will be described in the next chapter.

References

- [1] Chadwick, M. B., DeLuca Jr., P. M. and Haight, R. C. *Nuclear data needs for neutron therapy and radiation protection*. Radiat. Prot. Dosim. 70 (1997) 1.
- [2] Nakao, N., Uwamino, Y., Nakamura, T., Shibata, T., Nakanishi, N., Takada, M., Kim, E. and Kurosawa, T. *Development of a quasi-monoenergetic neutron field using the ${}^7\text{Li}(p, n){}^7\text{Be}$ reaction in the 70-210 MeV energy range at RIKEN*. Nucl. Instr. and Meth. A 420 (1999) 218.
- [3] Schuhmacher, H., Brede, H.J., Dangendorf, V., Kuhfuss, M., Meulders, J.P., Newhauser, W.D. and Nolte, R. *Quasi-monoenergetic neutron beams with energies from 25 to 70 MeV*. Nucl. Instr. and Meth. A 421 (1999) 284.
- [4] Nakane, Y. and Sakamoto, Y. *Measurements of absorbed dose distribution in a plastic phantom irradiated by 40- and 65-MeV quasi-monoenergetic neutrons*. Nucl. Instr. and Meth. A 459 (2001) 552.
- [5] Nakao, N., Nakashima, H., Nakamura, T., Tanaka, Sh., Tanaka, Su., Shin, K., Baba, M., Sakamoto, Y. and Nakane, Y. *Transmission through shields of quasi-monoenergetic neutron generated by 43- and 68-MeV protons- I and - II*, Nucl. Sci. Eng., 124 (1996) 228.
- [6] Broome, T. *High power targets for spallation sources*, Rutherford Appleton Laboratory, Chilton, Didcot, Oxon., UK (1996).
- [7] Fischer, W.E. *Application of spallation neutron sources*, Paul Scherrer Institute, Villigen, Switzerland (2002).
- [8] Proposal for a neutron time of flight facility. CERN/SPSC 99-8, SPSC/P 310, 17th March 1999.
- [9] Neutron TOF Facility (PS 213), Technical Design Report. CERN/INTC/2000-004, 11 February 2000.
- [10] n_TOF Technical Report, Private communication. 2000.
- [11] Langen, K.M., Binns, P.J., Lennox, A.J., Kroc, T.K. and DeLuca Jr, P.M. *Pileup correction of microdosimetric spectra*. Nucl. Instr. and Meth. A 484 (2002) 595.
- [12] Bühler, G., Menzel, H.G., Schuhmacher, H. and Dietze, G. *Neutron interaction data in carbon derived from measured and calculated ionisation yield spectra*. Radiat. Prot. Dosim. 13 (1985) 13.
- [13] ICRU Report 36, *Microdosimetry*, International Commission on Radiation Units and Measurements (1983).
- [14] ICRU Report 63, *Nuclear Data for Neutron and Proton Radiotherapy and for Radiation Protection*, International Commission on Radiation Units and Measurements (2000).
- [15] Hogeweg, B. *Microdosimetric measurements and some applications in radiobiology and radiation protection*. Ph.D. thesis, TNO Rijswijk, The Netherlands (1978).
- [16] Bach, R.L. and Caswell, R.S. *Energy transfer to matter by neutrons*. Radiat. Res. 35 (1968) 1.
- [17] Knoll, G.F. *Radiation detection and measurements*, John Wiley & Sons, New York (2000).
- [18] ICRU Report 49, *Stopping Power and Ranges for Protons and Alpha Particles*, International Commission on Radiation Units and Measurements (1993).
- [19] Aarnio, P.A., Fassò, A., Ferrari, A., Moehring, H.-J., Ranft, J., Sala, P.R., Stevenson, G.R., Zazula, J.M. *FLUKA: hadronic benchmarks and applications*, Proc. MC93 Int. Conf. on Monte Carlo Simulation in High Energy and Nuclear Physics, Tallahassee (Florida), 22-26 February 1993. Ed. by P. Dragovitsch, S.L. Linn, M. Burbank, World Scientific, Singapore (1994) 88.
- [20] Kliauga, P. *Measurement of single event energy deposition spectra at 5 nm to 250 nm simulated site size*, Radiat. Prot. Dosim. 31 (1990) 119.
- [21] Cesari, V., Iborra, P. N., De Nardo, L., Querini, P., Conte, V., Colautti, P., Tornielli, G. and Chauvel, P. *Microdosimetric measurements of the Nice therapeutic proton beam*. PHYSICA MEDICA 17 Suppl. 3, (2001) 76.
- [22] Burmeister, J., Kota, C., Maughan, R.L. and Waker, A. J. *Characterization of miniature tissue-equivalent proportional counters for neutron radiotherapy application*, Phys. Med. Biol. 47 (2002) 1633.

Chapter 6

Gas Electron Multiplier (GEM) operation with tissue-equivalent gases at various pressures

We have studied the operation of two different Gas Electron Multiplier (GEM) structures in both methane and propane based Tissue-Equivalent (TE) gases at different pressures varying from 0.1 to 1 atmosphere. This work was motivated to explore the possibility of using a GEM for a new type of Tissue Equivalent Proportional Counter (TEPC). In methane based TE gas, a maximum GEM gain of $1.5 \cdot 10^3$ has been reached while in propane based TE gas this is $6 \cdot 10^3$. These maxima have been reached at different gas pressures depending on GEM structure and TE gas. Furthermore, we observed a decrease of the GEM gain in time before it becomes stable. Charge up/polarisation effects can explain this.

6.1 Introduction

In experimental microdosimetry the effects of ionising radiation on biological targets are studied by investigating the statistical distribution of energy-deposition events at a microscopic level employing a Tissue-Equivalent Proportional Counter (TEPC) [1]. A traditional TEPC is a proportional counter (PC) with a central anode wire operated with a tissue-equivalent counting gas. A new type of TEPC is in the making [2] based on a Gas Electron Multiplier (GEM) [3]. Application of a GEM simplifies the design of (i) the miniature counter which has a sensitive volume of 1 mm^3 or even less to reduce pile-up effects and (ii) multi-counter configurations to increase the sensitivity of the TEPC to measure very low radiation field intensities.

The counting gases commonly used in dosimetry are methane based [4] or propane based [5] tissue-equivalent (TE) gases, referred to as TE-CH₄ and TE-C₃H₈ respectively. The components (percentage by partial pressure) of the former are 64.4% CH₄, 32.5% CO₂, and 3.1% N₂ and of TE-C₃H₈ these are 55% C₃H₈, 39.6% CO₂, and 5.4% N₂. In microdosimetry

the TEPC is operated at low pressure to simulate a microscopic tissue site. There is no information about GEM operation employing TE gases, neither at atmospheric pressure nor at low pressure. In this chapter we present for the first time results of GEMs operating under micro-TEPC conditions.

6.2 Experimental set-up and procedure

The experimental set-up consisting of a drift cathode, a GEM and a charge-collecting electrode (anode) is shown schematically in Fig. 6.1. A GEM consists of a 50 μm thick Kapton foil metalized with 5 μm copper on both sides. In the foil a hexagonal matrix of holes has been made (see section 3.8). We used two GEMs: in one GEM the holes have an outer diameter at the surface of 80 μm , an inner diameter of 60 μm at the centre of the foil and a pitch distance of 140 μm (140/80 GEM), in the other GEM these values are respectively 60, 50 and 90 μm (90/60 GEM). The active area of the GEMs is $5 \times 5 \text{ cm}^2$. The GEMs were produced at the CERN printed circuits workshop.

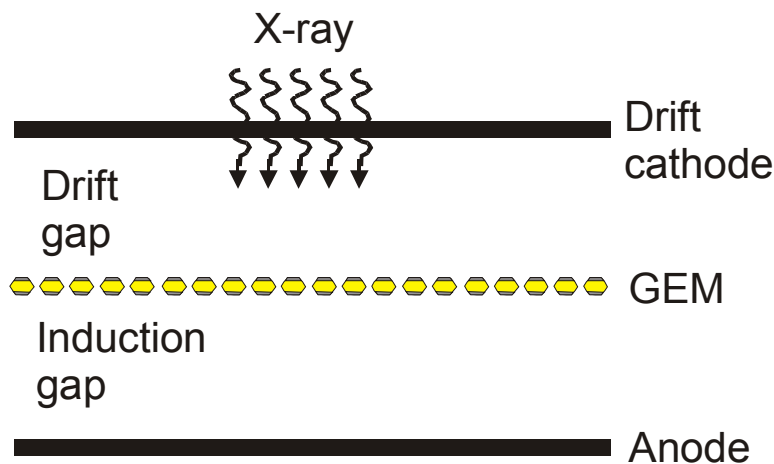


Figure 6.1: Schematic of the experimental set-up.

The gain measurements were made in pulse mode employing an X-ray tube with chromium anode, having its K_{α} peak at 5.4 keV. The W values, i.e. the average energy needed to generate an electron-ion pair, for TE- CH_4 and TE- C_3H_8 are 31.2 eV and 27.0 eV respectively [6] resulting in an average number of ionisation electrons in the drift gap of 173 and 200 respectively. The signal was read out with a charge-sensitive preamplifier. In both GEMs and gases, typical electric fields in the drift gap were $E_D = 1 - 2 \text{ kV/cm}$ and in the induction gap $E_I = 4.5 - 5.5 \text{ kV/cm}$.

6.3 Results and discussion

Figures 6.2 and 6.3 show the GEM gains as a function of the voltage across the GEM electrodes measured in TE-CH₄ gas in the pressure range 0.2-1 atm for the two GEM types. The end points of the lines at the top of the figures correspond to the maximum safe gain at which no discharge is observed. One can see that the gain-voltage dependence is exponential. For both GEM structures a maximum safe gain of $1.5 \cdot 10^3$ has been obtained, for the 140/80 GEM at ~ 0.35 atm, and for the 90/60 GEM at ~ 0.5 atm.

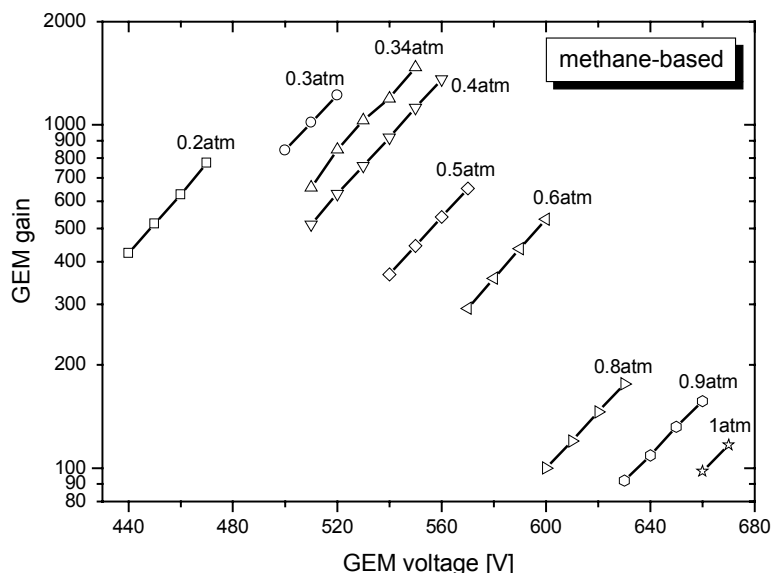


Figure 6.2: GEM gains measured in TE-CH₄ at various pressures in the range 0.2-1 atm, as a function of voltage across the 140/80 GEM.

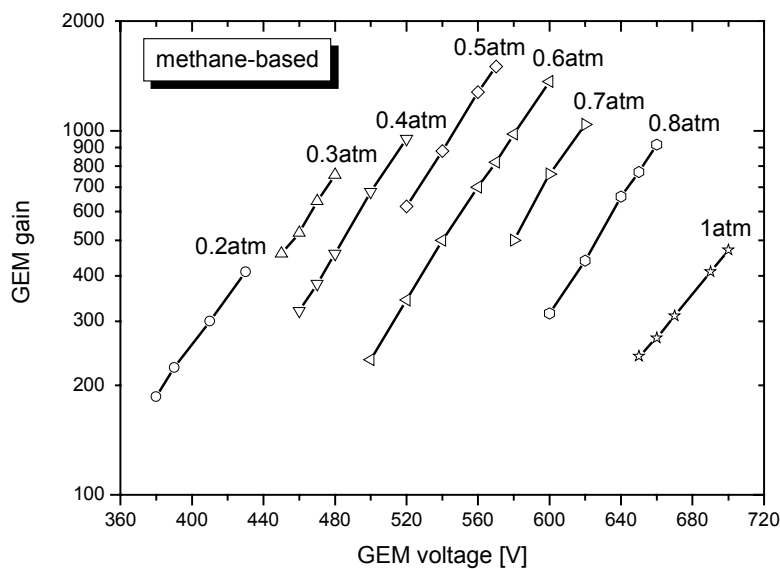


Figure 6.3: GEM gains measured in TE-CH₄ at various pressures in the range 0.2-1 atm, as a function of voltage across the 90/60 GEM.

Up to 0.4 atm the maximum safe gain is higher for the 140/80 GEM while at pressures above 0.4 atm the 90/60 GEM has a higher maximum safe gain. Notice that for pressures up to 0.4 atm the maximum applicable voltage across the GEM electrodes is lower for the 90/60 GEM. From 0.4 to 0.8 atm the maximum voltage is almost the same for both GEMs and at pressures > 0.8 atm the 90/60 GEM allows higher voltages across its electrodes.

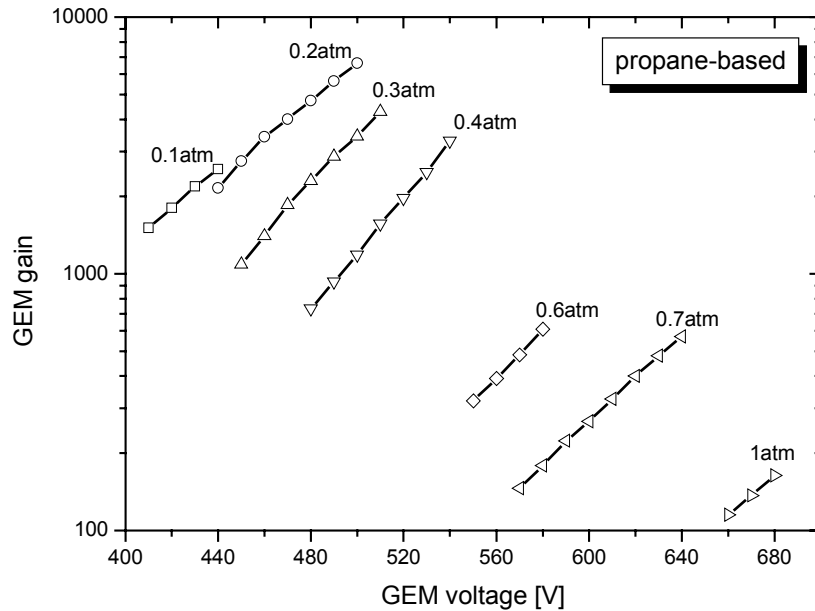


Figure 6.4: GEM gains measured in $TE-C_3H_8$ at various pressures in the range 0.1-1 atm, as a function of voltage across the 140/80 GEM.

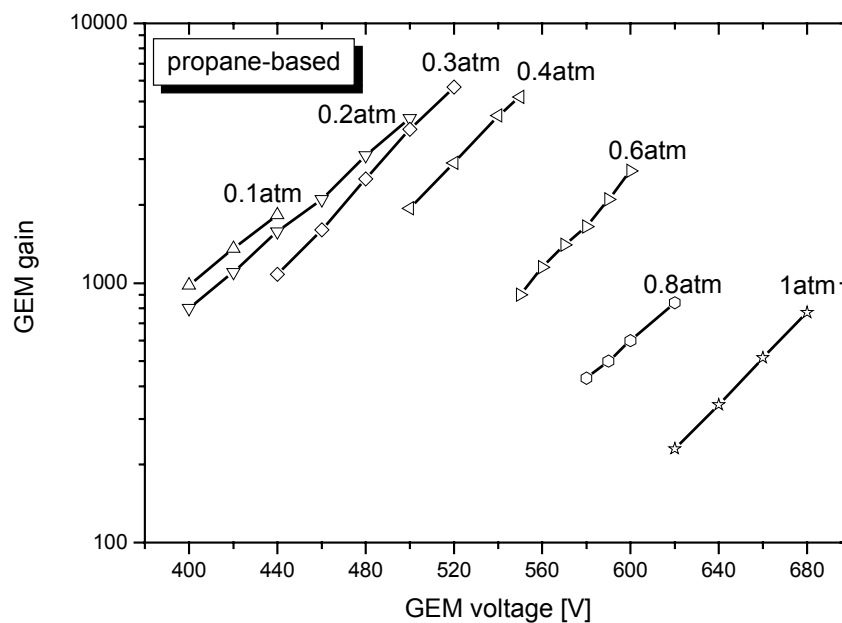


Figure 6.5: GEM gains measured in $TE-C_3H_8$ at various pressures in the range 0.1-1 atm, as a function of voltage across the 90/60 GEM.

Figures 6.4 and 6.5 show the GEM gains as a function of the voltage across the GEM electrodes for the two GEM geometries measured in TE-C₃H₈ gas in the pressure range 0.1-1 atm. A maximum safe gain of more than $6 \cdot 10^3$ has been obtained for both GEMs. For the 140/80 GEM the maximum safe gain is reached at ~ 0.2 atm while for 90/60 GEM the maximum safe gain is obtained at ~ 0.3 atm. The maximum safe gains are higher for the 140/80 GEM at pressures < 0.3 atm while at pressures > 0.3 atm the 90/60 GEM has higher maximum safe gains.

Notice that the maximum applicable voltages across the GEM electrodes are almost the same for both GEM structures over the whole pressure range. Furthermore, the maximum safe gain of GEMs operating in TE-C₃H₈ is higher than the maximum safe gain of GEMs operating in TE-CH₄.

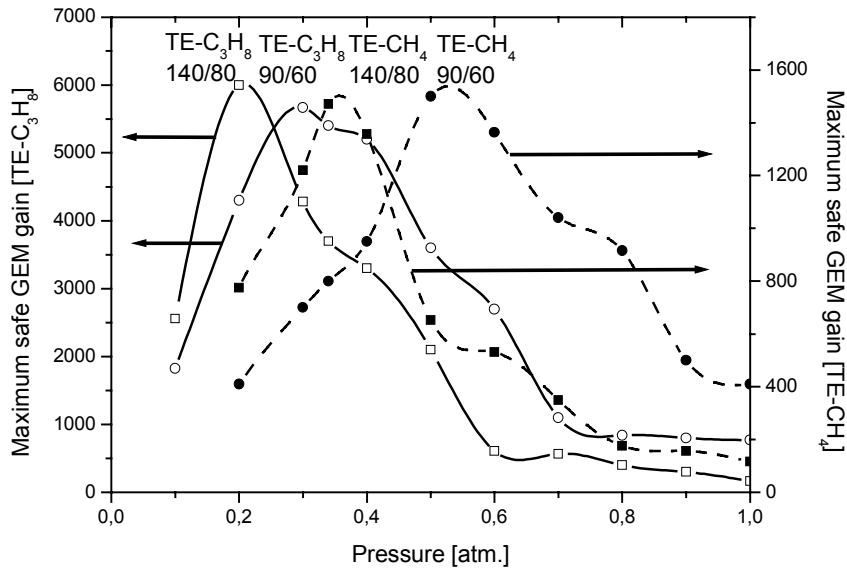


Figure 6.6: Maximum safe gains as a function of gas pressure. The solid lines and dashed lines represent the measured maximum safe GEM gains in TE-C₃H₈ and TE-CH₄ respectively. The circles and squares refer to 90/60 and 140/80 GEMs respectively.

The main features observed for both gases and GEMs are that the maximum gain increases when increasing the gas pressure till a certain pressure where it reaches a maximum and then it decreases when further increasing the gas pressure. This is summarised in Fig. 6.6. We can explain these phenomena by the differences in the ionisation mean free path for the two gases and the differences in GEM structure.

We distinguish between the distance along the direction of the electric field between two non-ionising collision events, λ_{coll} , and the distance along the direction of the electric field between two ionisation events, λ_{ion} . The first ionisation coefficient (first Townsend coefficient) can be written as [7]:

$$\alpha = \frac{1}{\lambda_{coll}} \exp(-\lambda_{ion}/\lambda_{coll}) \quad (6.1)$$

Where $\lambda_{coll} \leq \lambda_{ion}$.

We notice that λ_{ion} is depending on the effective ionisation potential and the electric field and therefore we expect λ_{ion} to be approximately independent of the gas pressure while λ_{coll} is depending on the number of gas molecules per cm^3 and therefore pressure dependence.

By lowering the gas pressure at constant electric field the probability of non-ionising collision events will decrease which means λ_{coll} will increase and at the same time $\lambda_{\text{ion}}/\lambda_{\text{coll}}$ will decrease. Consequently the first ionisation coefficient (α) will increase (see (6.1)) and so does the gain. So for the same voltage across the GEM, at lower pressure the gain will be higher. The maximum will be reached when λ_{coll} becomes as large as λ_{ion} . This can be seen in Fig. 6.6.

However, below a certain gas pressure the distance between ionising collisions becomes so large that in the volume of the GEM aperture in which the electric field is high enough to have multiplication, the number of ionisation collisions will decrease and consequently the gain will decrease as well.

This feature depends on a) the dimension of the GEM aperture and b) the gas properties.

Using those results of Fig. 6.6 where the gas properties are the same but the GEM structures are not (curves with same line styles) a comparison can be made of the ratio of the volumes, V , of the GEM holes (in μm^3), taking into account the hole shapes (section 6.2), and the inverse ratios of the pressures, P , at which the maximum gain is reached:

$$\frac{V_{140/80}}{V_{90/60}} = \frac{1.5 \cdot 10^5}{1.0 \cdot 10^5} \approx \left(\frac{P_{90/60, \text{max}}}{P_{140/80, \text{max}}} \right)_{\text{gas}} \approx \left(\frac{0.30}{0.20} \right)_{\text{TE-C}_3\text{H}_8} \approx \left(\frac{0.52}{0.35} \right)_{\text{TE-CH}_4} \quad (6.2)$$

This relation approximately holds. It can be used to predict the behaviour (the pressure at which the maximum gains will be reached) of GEMs with another aperture structure.

To see the dependence of the gas properties another comparison can be made. Using the ratio of the gas mass density and the inverse ratio of the gas pressures at which the maximum gain has been obtained from the curves in Fig. 6.6 for which the volumes of the holes are constant but the gas properties are different (curves with same symbols) it follows:

$$\frac{\rho_{\text{TE-CH}_4}}{\rho_{\text{TE-C}_3\text{H}_8}} = \frac{1.06}{1.83} \approx \left(\frac{P_{\text{TE-C}_3\text{H}_8, \text{max}}}{P_{\text{TE-CH}_4, \text{max}}} \right)_{\text{GEM structure}} \approx \left(\frac{0.30}{0.52} \right)_{90/60} \approx \left(\frac{0.20}{0.35} \right)_{140/80} \quad (6.3)$$

This relation approximately holds too. It can be used to prophesy the behaviour of GEMs with other gases.

Since the minimum detection threshold should generally be set to about five times the RMS noise to eliminate the recording of noise counts [1] the minimum required gain can be given by:

$$G_{\text{min}} \approx 5 \frac{e_{\text{rms}} W}{E_{\text{min}}} \quad (6.4)$$

Where e_{rms} is the system electronic noise and E_{min} is the minimum required detectable energy. In our counter design this will be corresponding to a minimum gain of 700.

From Fig. 6.2 we see that for the 140/80 GEM operated in TE-CH₄ this requirement can be met in the pressure range $0.2 \text{ atm} < P_g < 0.4 \text{ atm}$, which corresponds to a counter diameter range $4.5 \text{ mm} > d_g > 2 \text{ mm}$ to simulate a $1 \mu\text{m}$ tissue site. In case of the 90/60 GEM operated in TE-CH₄ (see Fig. 6.3) the pressure range $0.3 \text{ atm} < P_g < 0.8 \text{ atm}$ meets the demand which implies a counter diameter on the range $3 \text{ mm} > d_g > 1 \text{ mm}$ to simulate $1 \mu\text{m}$ tissue site. This means that for a TEPC, operating in TE-CH₄, with a diameter as small as 1 mm the 90/60 GEM is employable. For a counter diameter less than 1 mm operating in TE-CH₄ gas the GEM structure that has smaller aperture, compared to 90/60 GEM, is needed. On the contrary to simulate a tissue site smaller than $1 \mu\text{m}$ with a 1 mm TEPC (operating at pressure lower than 0.1 atm) a GEM structure which has bigger aperture structure (bigger holes or/and thicker kapton insulator), compared to 140/80 GEM, is required.

For the 140/80 GEM operated in TE-C₃H₈ (see Fig. 6.4) the pressure range $0.1 \text{ atm} < P_g < 0.4 \text{ atm}$, which corresponds to a counter diameter $5 \text{ mm} > d_g > 1.3 \text{ mm}$, fulfils the requirement. The operation of the 90/60 GEM in TE-C₃H₈ in the pressure range $0.1 \text{ atm} < P_g < 1 \text{ atm}$ meets the requirement as shown in Fig. 6.5. This pressure range corresponds to a counter diameter range $5 \text{ mm} > d_g > 0.5 \text{ mm}$ to simulate a $1 \mu\text{m}$ tissue site.

In our set up we could not perform gain measurements at pressures below 0.2 atm and 0.1 atm in TE-CH₄ and TE-C₃H₈, respectively. This is due to the limitation of the dimension of the employed conversion gas volume, which is smaller than the range of a photoelectron with a kinetic energy of 5.4 keV in this pressure range.

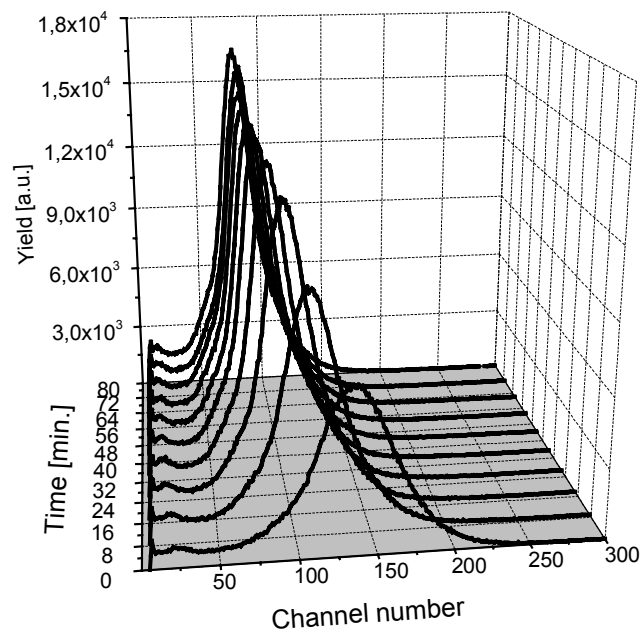


Figure 6.7: Pulse-height spectra of 5.4 keV X-ray measured for 90/60 GEM operated in TE-C₃H₈ at 0.4 atm. The 5.4 keV photopeak position moves from channel number ~135 to ~80.

When studying the GEM characteristics we observed a decrease of the GEM gain in time. In Fig. 6.7 the energy spectra in TE-C₃H₈ at 0.4 atm measured every 8 minutes are shown. This conduct can be explained by charge up/polarisation effects. By starting the measurements at a certain voltage across the GEM part of the ions created inside the GEM holes during the multiplication will attach to the Kapton insulator of the GEM. This will affect (decrease) the electric field across a GEM and decreases the gain. After some time (depending on the number of interaction per time unit) an equilibrium is reached in which a maximum amount of ions has been attached to the insulator and the electric field across the GEM will become constant and so does the GEM gain. This behaviour is pressure dependent. At low pressure the gain is decreased by a factor 1.7, while at high pressure by a factor of 1.2.

Once the GEM gain becomes stable, it remains stable as long as the voltage across the GEM the pressure and the count rate remain unchanged. This is measured for more than one day.

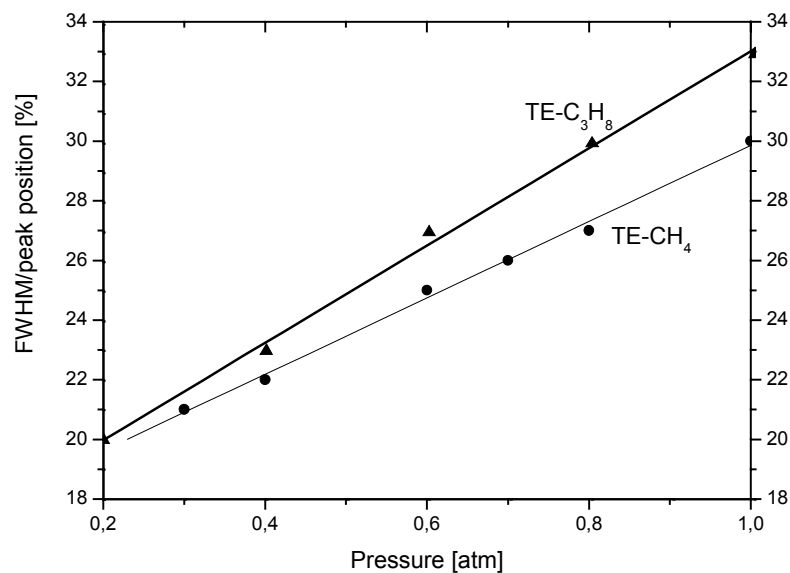


Figure 6.8: Energy resolution as a function of pressure for both TE gases. The energy resolution increases as the pressure increases. At higher pressure TE-CH₄ has a better energy resolution compared to TE-C₃H₈.

Furthermore we observed the energy resolution dependency of the 5.4 keV peak on pressure. The energy resolution as a function of pressure for both TE gases is shown in Fig. 6.8. The energy resolution increases linearly with increasing pressure. At lower pressure both TE gases have almost the same energy resolution. As the pressure increases, the line width increases for both gases while at the same time that for TE-C₃H₈ becomes worse than that for TE-CH₄.

6.4 Conclusion

We have studied the operation of two GEM structures, of pitch/outer diameter 140/80 μm and 90/60 μm, in both methane and propane based tissue-equivalent gases at various pressures.

This has been done to investigate the feasibility of GEM application in a new type of TEPC with a GEM instead of a central electric field detector.

In TE-CH₄ a maximum safe gain of $1.5 \cdot 10^3$ has been obtained while in TE-C₃H₈ a maximum safe gain of $6 \cdot 10^3$ has been reached for both GEM structures. These maxima have been obtained at different pressures depending on GEM structure and gas properties. We have derived empirical relations which can be used to predict the maximum-safe-gain variation of GEMs operating with the same gas as a function of their structure and to predict this variation for a certain GEM as a function of counting gas.

We observed that sufficiently high GEM gains, for both GEM structures and both TE gases, can be obtained for different pressure ranges. We advise the use of TE-C₃H₈ above TE-CH₄ because of its relatively higher gain for the whole pressure range.

For the 90/60 GEM the pressure range with high gains is broader than for 140/90 GEM. However for applications at relatively low pressure it is better to use the GEM with larger holes (140/90 GEM) while for applications at relatively higher pressure we recommend to use a GEM with relatively smaller GEM aperture (90/60 GEM).

The charge up/polarisation effect of the GEM is a cause for concern. Fortunately this effect becomes stable after some time and once it is stable it does remain stable. This effect will be investigated in more detail for our application.

We also observed that the energy resolution becomes better by lowering the pressure. Since in microdosimetry the counters have to operate at low pressure we will benefit for this phenomenon.

References

- [1] H. H. Rossi and M. Zaider, *Microdosimetry and Its Applications*. Springer-Verlag Berlin Heidelberg 1996.
- [2] M. Farahmand, A.J.J. Bos, J. Huizenga, L. De Nardo and C.W.E. van Eijk, *Nucl. Instr. And Meth. A* 509 (2003) 262.
- [3] F. Sauli, *Nucl. Instr. And Meth. A* 386 (1997) 53.
- [4] H.H. Rossi and G. Failla, *Neutrons dosimetry. Medical physics*. Chicago: Year Book Publishers, inc., pp. 603-607 (1956).
- [5] D. Srdoc, *Experimental technique of measurements of microscopic energy distribution in irradiated matter using Rossi counters*. *Radiat. Res.* 43 (1970) 302.
- [6] I. Krajcar Bronic, D. Srdoc and B. Obelic, *The mean energy required to form an ion pair for low-energy photons and electrons in polyatomic gases*. *Radiat. Res.* 115 (1988) 213.
- [7] P. Segur, P. Olko and P. Colautti, *Numerical Modelling of Tissue-equivalent Proportional Counters*. *Radiat. Prot. Dosim.* 61 (1995) 323.

Chapter 7

Design of a new Tissue-Equivalent Proportional Counter based on a Gas Electron Multiplier

By employing a Gas Electron Multiplier (GEM) a new type of mini multi-element Tissue-Equivalent Proportional Counter (TEPC) has been designed and constructed. In this chapter, we describe the design of this novel counter. The first pulse height measurements with this counter for both methane and propane based Tissue Equivalent (TE) gases are presented. These results show promising properties for application of this novel type TEPC in microdosimetric measurements.

7.1 Introduction

In experimental microdosimetry the effects of ionising radiation on biological targets are studied by investigating the statistical distribution of energy-deposition events at a microscopic level employing a Tissue-Equivalent Proportional Counter (TEPC) [1].

In high dose-rate radiation fields, such as found in clinical application of linear accelerators [2], a normal size TEPC cannot be employed because of pile-up of the electronic signals [3]. On the other hand, for the purpose of radiation protection it is desirable to use counters which have enough sensitivity to measure low dose rates. The physical dimensions of a TEPC are an important instrument-design parameter in reducing the effects of dead time and spectrum distortion due to pulse pile-up. In the past few years several groups have developed various types of mini TEPCs [4,5,6]. This is usually done by miniaturising the dimensions of all components of a conventional TEPC. A conventional TEPC is a proportional counter (PC) with a cavity with a central anode wire operating with a tissue-equivalent counting gas. Construction of a central wire in a small cavity is not an easy task. Here we describe a new type of TEPC based on a Gas Electron Multiplier (GEM) [7]. A schematic of a TEPC-GEM is shown in Fig. 7.1. Application of a GEM simplifies the construction of (i) a miniature

counter with a small sensitive volume (SV) to reduce pile-up effects and (ii) multi-element counter configurations to increase the sensitivity of the TEPC to measure very low radiation field intensities.

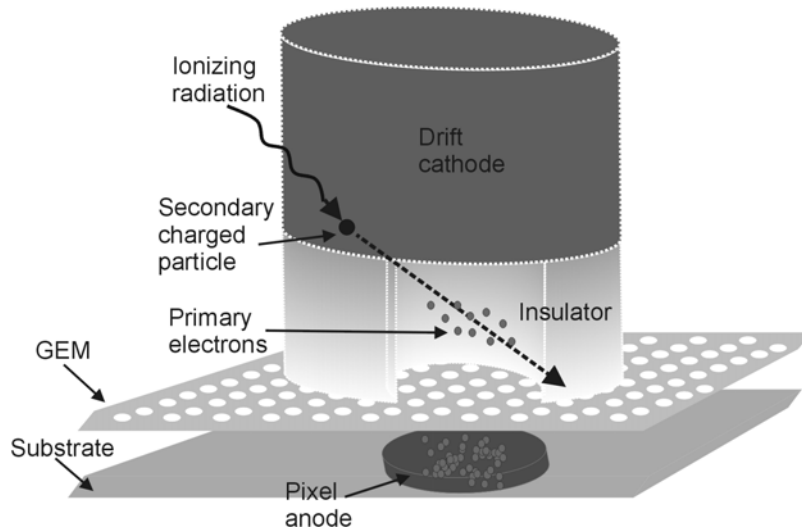


Figure 7.1: Schematic 3D view of TEPC-GEM. The drift cathode, the insulator and the gas are of tissue-equivalent material. The Sensitive Volume (SV) is the volume inside the insulator. GEM with gas amplification inside the holes and pixel-anode are indicated.

In an earlier study (see chapter 6), GEM operation in methane based and propane based TE gases has been investigated [8]. The GEM gain has been measured over a wide gas-pressure range. Adequate gas gain has been achieved to allow lineal energy, y with unity $\text{keV}/\mu\text{m}$, spectrum measurements for simulated site sizes of 1.5 to $0.4 \mu\text{m}$ for methane based TE gas and 3.5 to $0.3 \mu\text{m}$ for propane based TE gas.

7.2 Detector design considerations

The first step in designing a low-pressure proportional counter is the choice of the detector geometry. Cylindrical geometry rather than spherical geometry was chosen which results in considerable simplification of the construction of a counter with smaller dimensions. In experimental microdosimetry the measurements are generally performed with a spherical cavity. However, the mean chord length of a right cylinder (height equal to diameter d) is the same as that of a sphere of diameter d , namely $2d/3$. The chord length distribution differs slightly, but this difference does not significantly influence the single event spectrum [9,10].

The present counter has been designed with small dimensions so that it can be used for conventional microdosimetry in intense pulsed radiation fields to measure the microdosimetric spectrum, for instance in the beam of a clinical linear accelerator.

Furthermore, the counter is designed as mini multi-element counter to be used for applications in which a high sensitivity to neutron radiation is required.

Another step in the counter design is the choice of the polarity of the voltage. The way in which the preamplifier and the bias voltage are connected to the detector can affect the detector system noise [11]. It was chosen to apply negative high voltage to the detector wall and hold the anode at ground potential. This configuration has the advantage of eliminating the signal resistor and blocking capacitor which reduce the detector capacitance. It also eliminates high voltage on the anode feedthrough which may cause noise. The disadvantage is that the cathode has to be insulated for high voltage and this can complicate the design and operation of the detector.

The gas purity is an important factor which can strongly influence the stability of the gas gain and the reproduction of the measurements. To ensure the gas purity and to keep the gases as clean as possible it was decided to work with a continuous flow gas supply system.

7.2.1 Calibration considerations

The calibration of TEPCs used for microdosimetry comprises the conversion of pulse height into lineal energy. The calibration is generally performed by means of low-energy characteristic X-rays from an external source or by an internal alpha source or by using the proton edge of the lineal energy spectrum. However, for multi-element mini counters, the use of characteristic X-rays or an alpha source becomes entirely impracticable due to their weak penetration and not being fully stopped in the gas. A calibration method that is in principle suitable for a multi-element proportional counter relies on addition of a small amount of ^{37}Ar to the TE gas [12]. Application of this method is, however, not practical since ^{37}Ar has to be produced by neutron activation of ^{36}Ar .

For our multi-element counter we have chosen to use characteristic X-rays as a calibration source. This has the advantage that the photon energy is well known. However, it is necessary that the range of the photoelectrons is significantly less than the counter diameter (the number of Compton electrons is negligible). The photoelectrons are ejected predominately sideways at low photon energy [13]. Taking this into account, an extra cavity with larger dimensions than the mini-counter sensitive volumes was constructed to make sure that the photoelectrons will be fully stopped in the gas. The extra cavity operates only for calibration purpose; it is gas-connected to the actual mini-counter SVs. This extra-cavity method offers also a practical way to control the stability of gas gain during the measurements.

7.2.2 Equipotential line calculations

To define more accurately the drift, multiplication and induction regions, equipotential lines have been calculated using a two-dimensional model for the actual dimensions of 1.8 mm height and 1.8 mm diameter of the SV, a GEM with 80 μm hole diameters and a pitch distance of 140 μm , and the distance of 250 μm in the region between the GEM and the pixel-anode (see Fig. 7.2). For these calculations the FlexPDETM software⁴ has been used. It

⁴ FlexPDETM, Finite Element Software, PDESolutions Inc.

solves the Laplace equation with a general Galerking finite-element algorithm. Fig. 7.2a displays the equipotential lines of one counter cavity. The upper part of the figure represents the cathode surface which is held at negative high voltage and the lower part represents the anode which is held at ground potential. A total potential difference of 680 V has been employed. The applied electric fields in the drift gap, across the GEM and in the induction gap are typical electric fields which have been applied during the operation of the GEM with TE gases [8]. Field lines are normal to the equipotential lines. In Fig. 7.2b a close up of the equipotential lines across the GEM are shown where a potential difference of 500 V is applied. Figure 7.2c presents a close up of the equipotential lines in the induction region with a 120 V potential difference. These results show that the drift, multiplication and induction region can be well defined.

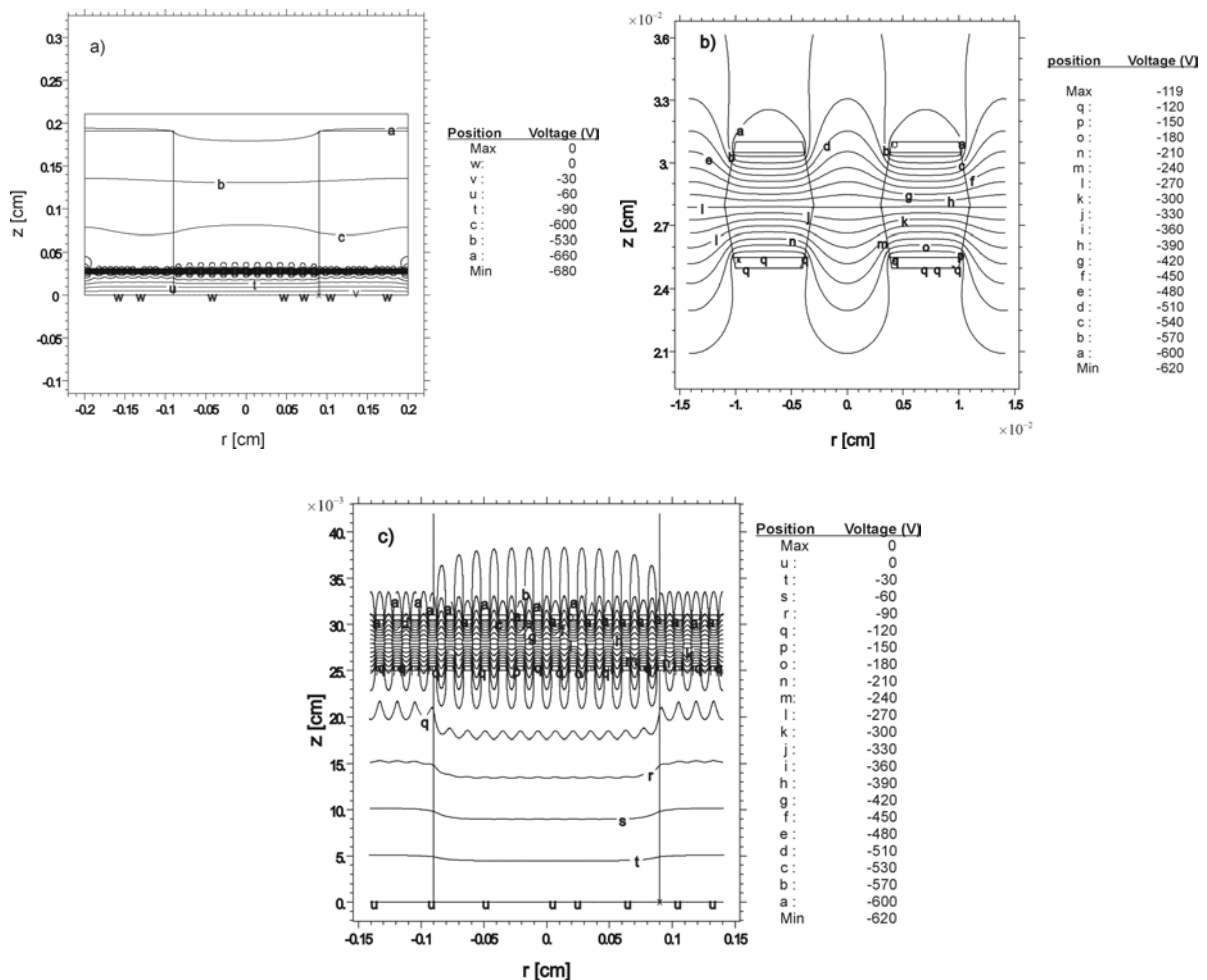


Figure 7.2: Equipotential line plots for a TEPC-GEM in the region a) of one counter cavity where a total potential difference of 680 V has been applied. The cathode (upper part) is held at negative voltage and the anode (lower part) is held at ground potential. b) across the GEM where a potential difference of 500 V is employed. c) in the induction region with a potential difference of 120 V.

7.3 Detector description

Our prototype cylindrical multi-element proportional counter, based on the GEM, has been designed and constructed with five SVs of 4.6 mm^3 . A cross section is shown schematically in Fig. 7.3. Five SVs, of which two are shown, are being used for the microdosimetric measurements. Two additional cavities of 1.4 mm^3 and 0.4 mm^3 have been added (not shown in Fig. 7.3) to study the minimum cavity dimensions applicable in this new design. Furthermore, the two X-ray calibration cavities are shown.

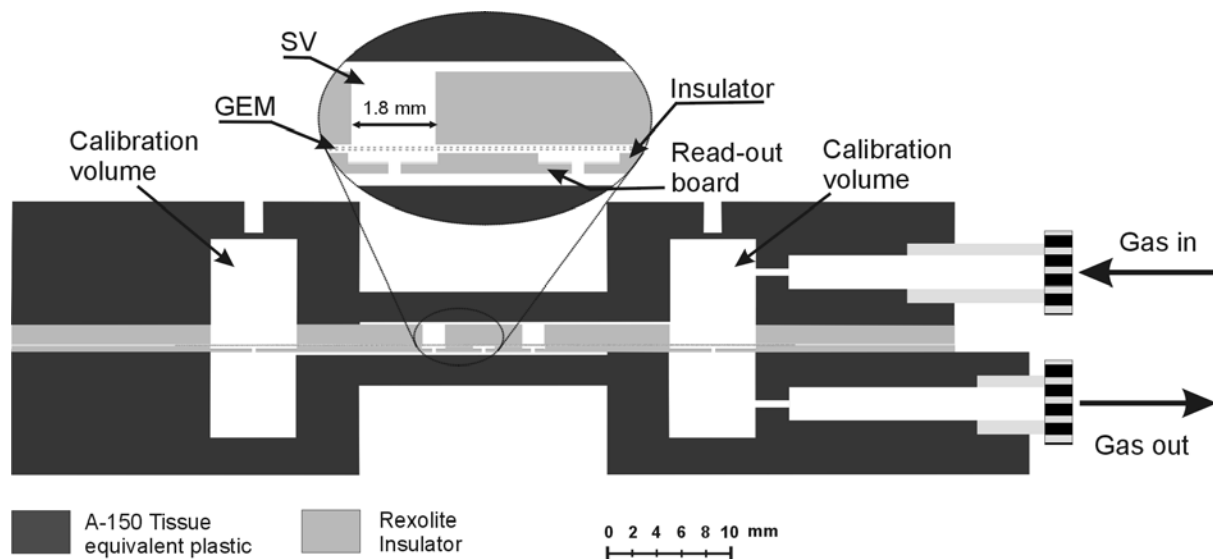


Figure 7.3: Cross-section view of the prototype TEPC-GEM. Read-out board, insulator, GEM and SVs are sandwiched between two layers of A-150 TE plastic. In this cross section only two of the five SVs can be seen. The hollow tubes, holes in the read-out pixels and the space above SVs and below the read-out board are for the gas flow. At the position of calibration volumes the upper wall has been thinned. The upper A-150 wall which functions as a cathode is held at negative high voltage. The anodes are held at ground potential.

The TEPC-GEM prototype consists of:

- Read-out board with anode pixels: $250 \mu\text{m}$ thick Rexolite[®] with a $17 \mu\text{m}$ copper-clad; nine pixels of 2.1 mm diameter with a pitch of 4 mm and two square pixels of $9 \times 9 \text{ mm}^2$.
- Insulator: a $250 \mu\text{m}$ thick Rexolite spacer insulator between the anodes and GEM with in total seven holes of 1.8 mm , one of 1 mm , one of 0.5 mm diameter with a pitch of 4 mm and two square apertures of $7 \times 7 \text{ mm}^2$.
- GEM: with an active area of $5 \times 5 \text{ cm}^2$ which consists of a $50 \mu\text{m}$ Kapton foil metalized with $5 \mu\text{m}$ copper on both sides. A hexagonal matrix of holes with a diameter of $80 \mu\text{m}$ and a pitch distance of $140 \mu\text{m}$ has been made in this foil.

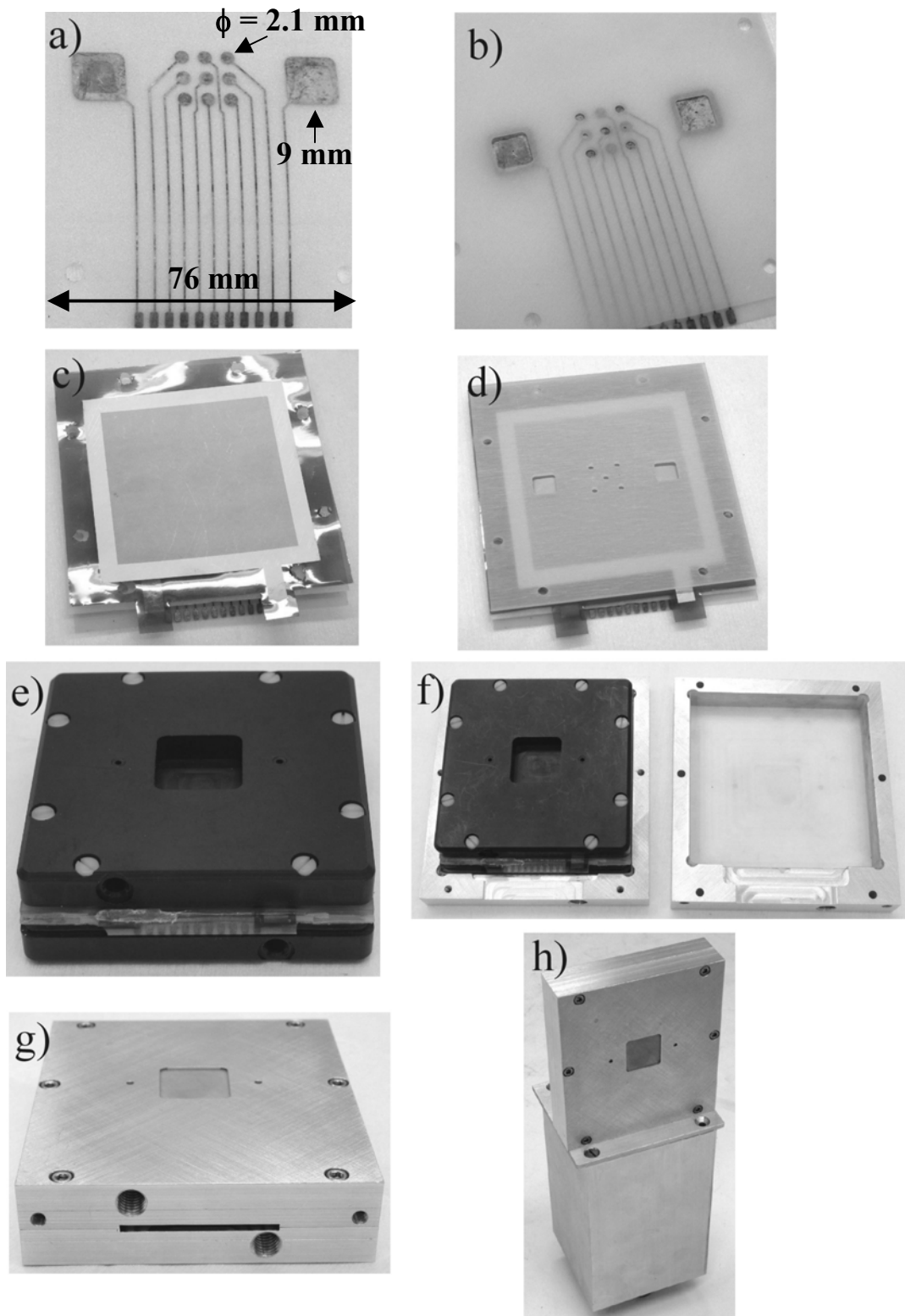


Figure 7.4: The photographs of counter components a) read-out board with anode pixels b) spacer insulator c) GEM d) sensitive volumes e) A-150 plastic counter walls f) the aluminium counter box g) the gas and electronics feed-through of TEPC-GEM h) complete counter with the electronics box.

- Sensitive volumes: Rexolite of 1.6 mm thickness with five holes of 1.8 mm, one of 1 mm, one of 0.5 mm diameter with a pitch of 4 mm and 2 square apertures of 7×7 mm².

All these layers are sandwiched between two layers, as counter walls, of A-150 plastic. The upper A-150 layer wall functions as drift cathode. These walls have a thickness of 2.5 mm at the position of the sensitive volumes. The photographs of counter components are shown in Fig. 7.4. At the position of the calibration volumes the upper wall has been thinned to 0.4 mm to minimise the attenuation of the low energy X-rays. The dimensions of the SVs are 1.8 mm diameter by 1.8 mm height, with a circular cross-section. To investigate the signal that is generated in the dead space between the GEM and the read-out board, two pixels have been included above which no SVs are present. The counter can operate in gas flow mode as well as in sealed mode. To allow gas flow through the read-out board, holes of 0.3 mm have been made in the read-out pixels. Also a space of 0.2 mm above the SVs and below the read-out board has been saved for gas flow. The upper A-150 wall which is used as drift cathode, is isolated from the lower A-150 wall by using non-conductive screws.

7.4 Experimental results

For calibration purposes a cavity which has larger dimensions than the SVs has been used. Pulse height spectra were obtained employing an X-ray tube with chromium anode, having its K_{α} peak at 5.4 keV. The range of a 5.4 keV photoelectron in methane and propane based TE gases are 0.78 mm and 0.45 mm [14] at standard pressure.

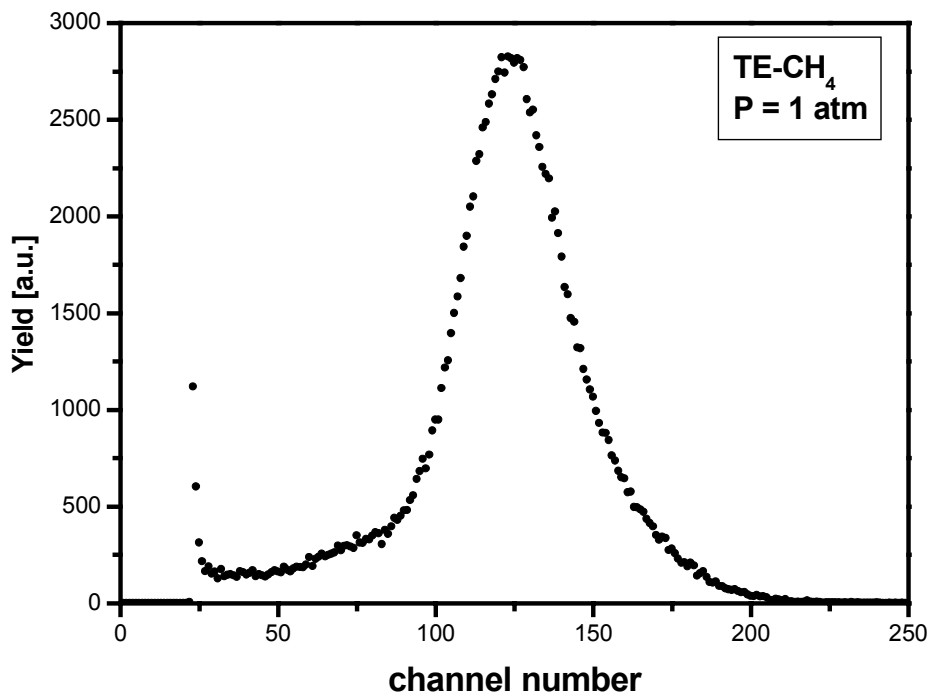


Figure 7.5: Pulse-height spectrum of 5.4 keV X-ray measured with the new TEPC-GEM counter using TE-CH₄ at a pressure of 1 atm. The channel numbers correspond with photoelectron energies.

Fig. 7.5 shows the energy spectrum measured with the TEPC-GEM counter using methane based TE gas (TE-CH₄) at a pressure of 1 atm. The 5.4 keV photopeak position is used for the conversion into lineal energy. At energy lower than the photopeak it can be seen that the number of photoelectrons that lose only part of their energy in the counter is small. In Fig. 7.6 the energy spectrum measured with the TEPC-GEM using propane based TE gas (TE-C₃H₈) at a pressure of 1 atm is displayed. The number of photoelectrons that are not fully stopped in the gas is also small. It appears that it is even smaller than in case of TE-CH₄, which can be explained by the fact that the range of the 5.4 keV photoelectrons in TE-CH₄ is a factor of 1.7 larger than that in TE-C₃H₈.

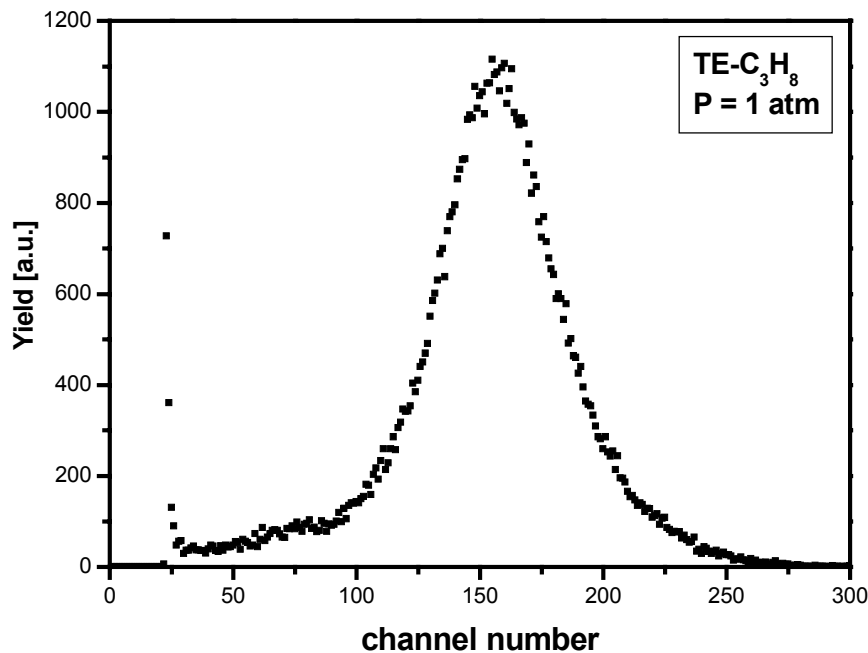


Figure 7.6: Pulse-height spectrum of 5.4 keV X-ray measured with the new TEPC-GEM counter using TE-C₃H₈ at a pressure of 1 atm. The channel numbers correspond with photoelectron energies.

7.5 Conclusions

We have designed and constructed a new type of TEPC based on a GEM instead of a conventional central anode wire TEPC. This has been done to simplify the construction of a mini, multi-element TEPC which is essential for applications in many fields where experimental microdosimetry is required. For our design right cylindrical geometry was chosen because of simplification of the construction. A continuous flow system was chosen to ensure the gas purity. Furthermore, it was chosen to hold the anode at ground potential and to apply negative high voltage to the detector wall (drift cathode).

For the calibration of TEPC-GEM, characteristic X-rays (5.4 keV) were employed. The first pulse-height calibration measurements have been performed successfully using both methane and propane based TE gases. These results show that in principle this new type of TEPC can be used for microdosimetric measurements.

The next step will be to compare the microdosimetric spectra measured with TEPC-GEM to microdosimetric spectra measured with conventional and mini TEPCs.

References

- [1] H. H. Rossi and M. Zaider, *Microdosimetry and Its Applications*. Springer Verlag Berlin Heidelberg 1996.
- [2] J. Burmeister, C. Kota and R.L. Maughan. *Nucl. Instr. And Meth. A* 422 (1999) 606.
- [3] K.M. Langen, P.J. Binns, A.J. Lennox, T.K. Kroc and P.M. DeLuca Jr. *Nucl. Instr. And Meth. A* 484 (2002) 595.
- [4] J. Burmeister, C. Kota, R.L. Maughan and A. J. Waker. *Phys. Med. Biol.* 47 (2002) 1633.
- [5] P. Kliauga, *Radiat. Prot. Dosim.* 31 (1990) 119.
- [6] P. Kliauga, A.J. Waker and J. Barthe, *Radiat. Prot. Dosim.* 61 (1995) 309.
- [7] F. Sauli, *Nucl. Instr. And Meth. A* 386 (1997) 53.
- [8] M. Farahmand, A.J.J. Bos and C.W.E. van Eijk, *Nucl. Instr. And Meth. A* 506 (2003)160.
- [9] R. Eickel, J. Booz, *Rad. Envir. Biophys.* 13 (1976) 145.
- [10] A. Kellerer, *Rad. Res.* 86 (1981) 277.
- [11] L. A. Braby, G. W. Johnson and J. Barthe. *Radiat. Prot. Dosim.* 61 (1995) 381.
- [12] E. Anachkova, A. M. Kellerer and H. Roos. *Rad. Envir. Biophys.* 33 (1994) 353.
- [13] R. D. Evans, *The Atomic Nucleus*. McGraw-Hill book company, Inc. 1955.
- [14] E. Waibel and B. Grosswendt, *Phys. Med. Biol.* 37 (1992) 1127.

Chapter 8

Microdosimetric Measurements with a TEPC based on a GEM

A multi-element Tissue-Equivalent Proportional Counter (TEPC), based on a Gas Electron Multiplier (GEM) has been applied to perform microdosimetric measurements with a 14 MeV monoenergetic neutron beam, a californium (^{252}Cf) source and for low energy X-rays. This counter has been designed having small dimensions with the aim to be used for microdosimetric measurements in intense, pulsed, radiation fields. It is shown that small site sizes (nanometres) can be simulated employing this counter, at relatively high pressure. To increase the sensitivity the counter is designed as mini multi-element counter. The first microdosimetric measurements of this novel counter exposed to a 14 MeV monoenergetic neutron beam and a californium source for a counter cavity diameter of 1.8 mm simulating 1.0 μm tissue site size are presented. The measured spectra show an excellent agreement with spectra from the literature. The first pulse-height measurements at low pressures with this counter for propane based Tissue Equivalent (TE) gas are demonstrated. Furthermore, it has been demonstrated that this counter for several cavity dimensions (as small as 0.5 mm of diameter) can be very successfully used to measure micro- and nanodosimetric spectra in various simulated tissue site sizes. The specific advantages and the calibration methods of this type of TEPC are discussed.

8.1 Introduction

Ionising radiation causes a wide variety of effects in biological targets. These effects cannot only be determined by the specification of absorbed dose. The effectiveness of a given absorbed dose can be modified by several factors, one of which is the distribution of energy deposition events along the ionising-particle path on a microscopic scale. In experimental microdosimetry the effects of ionising radiation on biological targets are studied by investigating the statistical distribution of energy deposition events at the microscopic level

employing a Tissue-Equivalent Proportional Counter (TEPC) [1]. A TEPC is usually a proportional counter (PC) with a cavity containing a central anode wire and operated with a tissue-equivalent counting gas at low pressure to simulate tissue volumes of micrometer dimensions. The wall of the counter is commonly made of tissue-equivalent material (mainly Shonka plastic A-150) and is used as cathode owing to the conductivity of the plastic.

TEPCs are operated in pulse mode and the pulse-height spectrum is collected and converted to the parameter extensively used in microdosimetry 'lineal energy', which is denoted by y . The lineal energy is the quotient of energy imparted, ϵ_s , to the matter in a volume by a single event and the mean chord length, \bar{l} , in that volume (see section 2.1.2). Lineal energy is commonly presented in units of $\text{keV}\mu\text{m}^{-1}$. The shape of a microdosimetric spectrum contains quantitative information that can be used to predict the radiobiological effectiveness of radiation [1, 2].

In chapter 6, the GEM [3] operation in methane- and propane-based TE gases has been investigated and the design and construction of the novel type TEPC based on GEM have been described [4] in chapter 7. In this chapter, the proper functioning of this novel counter is demonstrated with a 14 MeV monoenergetic neutron source and a californium (^{252}Cf) source for a cylindrical counter cavity of equal diameter and height of 1.8 mm simulating 1.0 μm tissue site size. The first pulse-height measurements at various low pressures for propane-based Tissue Equivalent (TE- C_3H_8) gas [5] are represented. Furthermore, the first microdosimetric responses for low energy X-rays are presented for counter cavities of 1.8 mm, 1.0 mm and 0.5 mm diameter at various pressures, simulating tissue site sizes of 1.8 μm , 1.0 μm , 500 nm, 280 nm and 140 nm. Two independent calibration methods have been applied and will be discussed.

8.2 Motivation

In experimental microdosimetry there are some conditions in which the normal size of TEPCs with a counter cavity of a few centimetres in diameter are not applicable. For instance at high dose-rates such as found in clinical application of high flux therapy beams [6], a normal size of TEPC cannot be employed because of pile-up of the electronic signals [7]. The physical dimensions of a TEPC are an important instrument-design parameter in reducing the effects of dead time and spectrum distortion due to pulse pile-up. To cope with a high intensity beam a miniature TEPC can be used. Another reason to reduce the physical dimensions of a TEPC is the increased interest in the spectra of energy deposition in small site sizes [8], which are important for an improved understanding of the biological effects of densely ionising radiation. It is well known that TEPCs of usual size will not operate at pressures low enough to simulate some tens of nanometres. Reducing the counter cavity size will allow measurements simulating some tens of nanometres at relatively high pressure.

In the past few years several groups have developed various types of mini TEPCs [9]-[12]. This is usually done by miniaturising the dimensions of all components of a usual TEPC. However, the construction of a central wire in a small cavity is extremely difficult and expensive. It becomes even more difficult in the case multi-element cavities are applied to increase the counter sensitivity. Furthermore, the supply of presently available counters for routine practice is hampered by technical problems in the production of reliable detectors

with predictable characteristics at comparatively little effort and hence low cost [13]. These drawbacks justify our efforts to develop a new type of TEPC based on Gas Electron Multiplier (GEM). A GEM consists of a 50 μm thick Kapton foil metalised with 5 μm copper on both sides [3]. In the foil a hexagonal matrix of holes has been made. By applying an adequate voltage across the GEM electrodes, the primary electrons produced in the counter gas will have enough kinetic energy to ionise the gas particles in the GEM holes (multiplication). The counter will be referred to as TEPC-GEM. In this type of counter no central anode wire is needed, which makes the construction much easier. The TEPC-GEM lends itself easily to a multi-element counter which increases the sensitivity of the counter.

8.3 Experimental setup

A multi-element TEPC was constructed based on a GEM. A cross section of the TEPC-GEM is shown schematically in Fig. 7.3. Read-out board, insulator, GEM and cylindrical Sensitive Volumes (SVs) are sandwiched between two layers of 2.5 mm tissue equivalent Shonka A-150 plastic. The insulators are made of Rexolite[®]. In Fig. 7.3 only two of the five SVs can be seen. The tubes, holes in the read-out pixels and the space above SVs and below the read-out board allow for gas flow of the system. At the position of the calibration volumes the upper wall has been thinned over a small area. The upper A-150 wall which functions as cathode is held at negative high voltage and is insulated from the covering aluminium counter encapsulation box with a thin Rexolite layer of 0.25 mm thickness. The anodes are held at ground potential. More details of the design and the construction of this counter can be found in chapter 7. The five cylindrical SVs have dimensions of 1.8 mm diameter and 1.8 mm height. Two additional SVs of 1.0 mm and 0.5 mm diameter, both having a height of 1.8 mm, have been added to study the behaviour of a counter at smaller cavity dimensions.

The GEM used in this study consisted of holes with a diameter of 60 μm at the surface and a centre to centre distance of 90 μm . The active area of the GEM arrangement is $5 \times 5 \text{ cm}^2$. The GEMs were produced at the CERN printed-circuit workshop. Typical electric fields in the drift gap (the gap between cathode and upper GEM surface) were $E_D = 0.4 - 0.7 \text{ kV}\cdot\text{cm}^{-1}$, and in the induction gap (the gap between lower GEM surface and anode) $E_I = 4.5 - 5.5 \text{ kV}\cdot\text{cm}^{-1}$. Applied voltages across the GEM electrodes were $V_{\text{GEM}} = 430 \text{ V}$, 470 V and 520 V. These values are well below the maximum voltage across the GEM electrodes at which discharge is observed [14].

Table 8.1: *The components (percent by partial pressure) of propane based tissue-equivalent gas that has been during this work and that according to the literature [5].*

	C_3H_8	CO_2	N_2
This work	55.1	39.3	5.6
ICRU-26	55.0	39.6	5.4

The counter is filled with propane based Tissue-Equivalent ($\text{TE-C}_3\text{H}_8$) gas. The gas components (percent by partial pressure) used in this work and those from literature [5] are shown in Table 8.1. In order to remove impurities from the gas, typically formed by out-gassing of the detector materials, a gas flow system with a flow rate of $10 - 20 \text{ ml}\cdot\text{min}^{-1}$ at STP conditions (0°C and 1013 hPa) is applied.

The neutron microdosimetric measurements were performed utilising two neutron sources: 1) An encapsulated californium source (^{252}Cf) with an activity of 10 MBq . Such a source produces a mix of fission neutrons having energies of the order of 1 MeV . 2) A neutron generator (MF-physics, Model A-711) that produces neutrons using the deuterium tritium reaction ($^3\text{H}(\text{d},\text{n})^4\text{He}$). This generator produces a continuous current of neutrons with energy of 14 MeV and an almost isotropic neutron yield of $1\cdot 10^{11} \text{ n}\cdot\text{s}^{-1}$.

The X-ray microdosimetric measurements were made employing an X-ray tube with chromium anode, having its K_α peak at 5.4 keV and an applied maximum voltage of 8.5 kV . The X-ray experimental set-up is shown in Fig. 8.1.

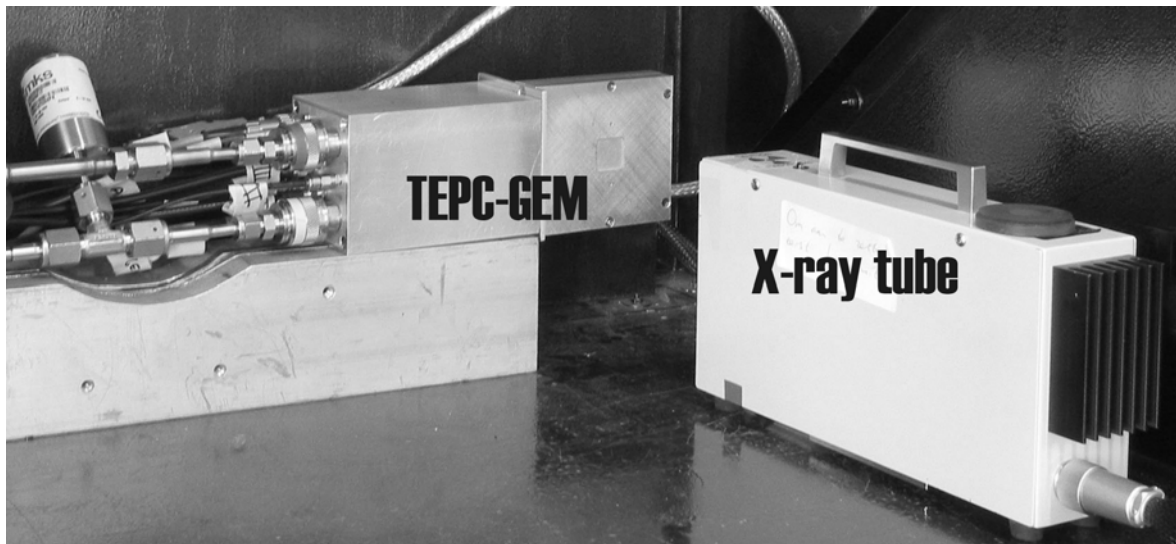


Figure 8.1: *The X-ray microdosimetric measurement set-up. The X-ray tube with a chromium anode with a maximum voltage of 8.5 kV is applied.*

The pulses provided by TEPC-GEM were processed with a charge-sensitive preamplifier (AMPTEK A250F/NF) of low-noise ($200 \text{ electrons RMS}$). This preamplifier extended the measurements down to energy depositions of several ion pairs per event. A linear spectroscopy amplifier (LA) provided additional gain and pulse shaping. A shaping time of $0.5 \mu\text{s}$ was applied for these measurements. The unipolar output of the LA fed an analogue-to-digital converter (ADC) module in a CAMAC-based data acquisition system. A computer connected with the CAMAC system provided real-time display and long-term data storage. The stability and performance of the electronics were tested using a precision pulse generator connected to the test input of the preamplifier.

8.4 Neutron microdosimetric measurements

8.4.1 Results

The most common presentations of the microdosimetric data are the dose-distribution, $d(y)$, as a function of $\log(y)$ and $yd(y)$ as a function of $\log(y)$ (see section 2.3). We chose the latter representation, in which the area delimited by any two values of the lineal energy, y , is equal to the fraction of dose delivered in that interval. The measured microdosimetric spectrum for 14 MeV neutrons is shown in Fig. 8.2 for the TEPC-GEM operating at a pressure of 31 kPa. This configuration simulates 1.0 μm diameter of condensed phase tissue. For 14 MeV neutrons, the proton peak lies at around 10 keV/ μm and the high-energy tail splits into distinct peaks, belonging to alpha particles and heavy recoil ions of carbon, nitrogen and oxygen [15] which are indicated in Fig. 8.2. Events from the individual ion types are not

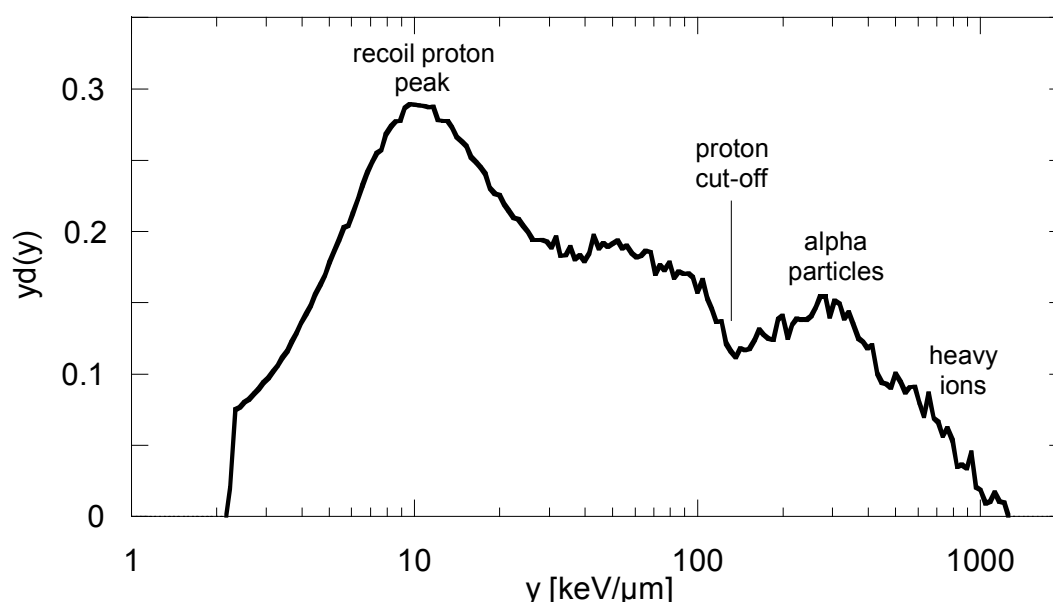


Figure 8.2: Microdosimetric spectrum for a 1- μm site size for 14-MeV neutrons measured by the TEPC-GEM with a cylindrical counter cavity of 1.8 mm in diameter and 1.8 mm in height. The contributions of recoil protons, alpha particles and heavy ions to the total spectrum are indicated. The proton cut-off known as ‘proton edge’ has been marked.

resolved from one another and there is considerable overlap of the event sizes from various particle types. Furthermore, a sharp proton cut-off (also indicated in Fig. 8.2) known as the ‘proton edge’ represents the maximum energy that can be deposited by a recoil proton (see section 3.7). This edge has been used to perform the calibration. Empirical determination of this point serves to calibrate the entire lineal energy spectrum. The proton edge is chosen as the mid-point of the final linear segment of the proton recoil portion of the lineal energy spectrum. The difference of the shape of the $yd(y)$ as a function of y spectra for the total

spectrum and the spectrum corrected for the signal generated in the induction region was not significant and the spectra were essentially identical. This means that the contribution of signals from the induction region to the spectrum is negligible.

The measured microdosimetric spectrum shown in Fig. 8.2 is not corrected for the contribution of γ -rays present in the radiation field. We expect mainly a contribution of the γ -ray energy deposition below $1\text{ keV}/\mu\text{m}$. Moreover, a small contribution in the region between 1 and $15\text{ keV}/\mu\text{m}$ is expected. The spectrum shows a very good agreement with the microdosimetric spectra found in the literature [15, 16].

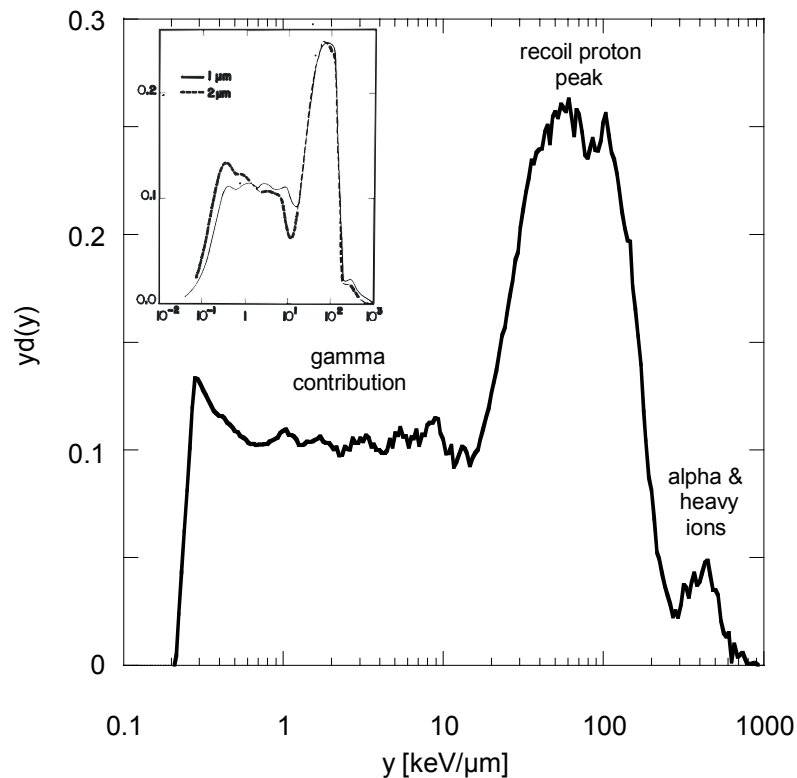


Figure 8.3: *Microdosimetric spectrum for a $1\text{-}\mu\text{m}$ site size in the field of encapsulated ^{252}Cf source measured by the TEPC-GEM for a cylindrical counter cavity of 1.8 mm in diameter and 1.8 mm in height. The gamma component, the proton peak, and the contributions of alpha and heavy ions to the total spectrum are indicated. The inset shows the same spectrum measured before by TEPC [16].*

The microdosimetric spectrum for an encapsulated californium (^{252}Cf) source has also been measured for the same counter cavity and gas pressure as above. It is shown in Fig. 8.3. The ^{252}Cf source produces a mixed γ/n field. The fission neutrons have energies of the order of 1 MeV (mean energy of 2.3 MeV). The spectrum can be divided into three regions: First, the region up to a y value of about $10\text{ keV}/\mu\text{m}$ due to the contribution of gamma rays to the spectrum; then, the region up to about $150\text{ keV}/\mu\text{m}$ produced by proton recoils in elastic scattering; finally, the region for y values larger than $150\text{ keV}/\mu\text{m}$ belonging to the contribution of α particles and heavy ion recoils. These regions overlap, but the main features are indicated in Fig. 8.3. The low activity of the ^{252}Cf source used and hence the small

number of collected counts has led to a relatively high counting uncertainty. The spectrum shows a very good agreement with the microdosimetric spectra found in the literature [16, 17] which confirms the feasibility of utilising a TEPC-GEM for microdosimetric measurements.

8.4.2 Conclusions

A new type of mini multi-element Tissue-Equivalent Proportional Counter (TEPC) based on a Gas Electron Multiplier (GEM) has been designed and constructed. Application of a GEM simplifies the construction of a miniature counter with a small Sensitive Volume (SV). A small SV reduces pile-up effects and makes it possible, in the future, also to perform nanodosimetric measurements. We have measured the microdosimetric response of this novel counter to a 14 MeV neutron source and a ^{252}Cf source. The spectra have been compared with the microdosimetric spectra measured by others with the presently available TEPC. Excellent agreement was found. Therefore, we can conclude that the TEPC-GEM is a good alternative for presently used TEPCs to perform microdosimetric measurements. Because of the relatively simple design and construction the TEPC-GEM is not only cheap and easy to produce but also its components (sensitive volume, wall materials) are very easy to adapt to the needs. Furthermore, the counter lends itself for a multi-element counter system that increases the sensitivity considerably and will broaden the applications of the counter in the fields of personal and space dosimetry. In future work, the possibility of using the TEPC-GEM for smaller site sizes (nanodosimetry) will be investigated.

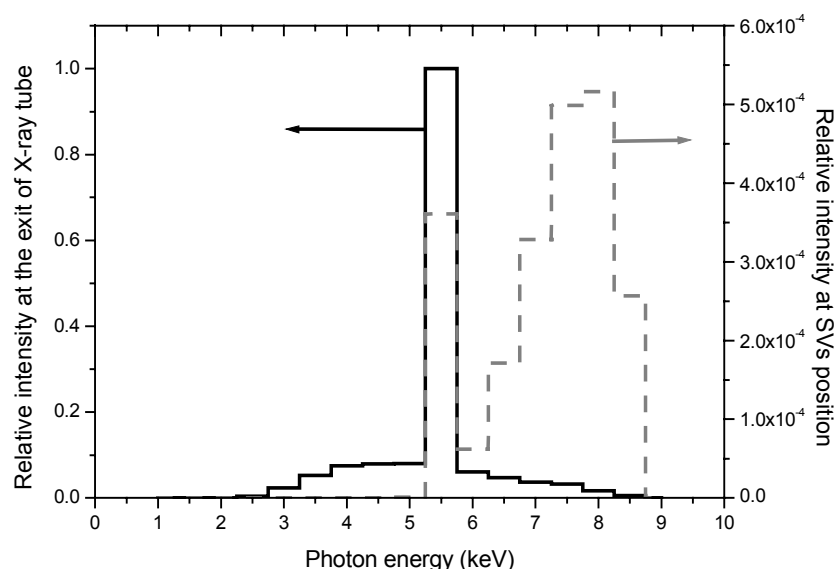


Figure 8.4: The calculated energy spectrum of an X-ray tube with a chromium anode with an applied maximum voltage of 8.5 kV. The solid curve represents the energy spectrum at the exit of the X-ray tube while the dashed curve represents the energy spectrum of the X-ray tube after passing the counter wall i.e. at the position of a sensitive volume.

8.5 X-ray microdosimetric measurements

The multi-element TEPC-GEM has been also applied to perform microdosimetric measurements for low energy X-rays. The details of the experimental set-up are described in section 8.3. Because the proton edge calibration method (see section 3.7) is not applicable for these measurements, other calibration methods are applied which are discussed in the following.

8.5.1 Calibration

A calibration is based on the electron edge. This method can be used as long as the maximum energy that can be deposited into the SV is known. For the present microdosimetric measurements, an X-ray tube with a chromium anode operated at a maximum voltage of 8.5 kV is applied. The calculated energy spectra of the X-ray source at the exit of the X-ray tube and after passing the counter wall, i.e. at the position of the SVs, are shown in Fig. 8.4. It is also seen that at the SVs the relative contribution of higher energy photons is higher. The

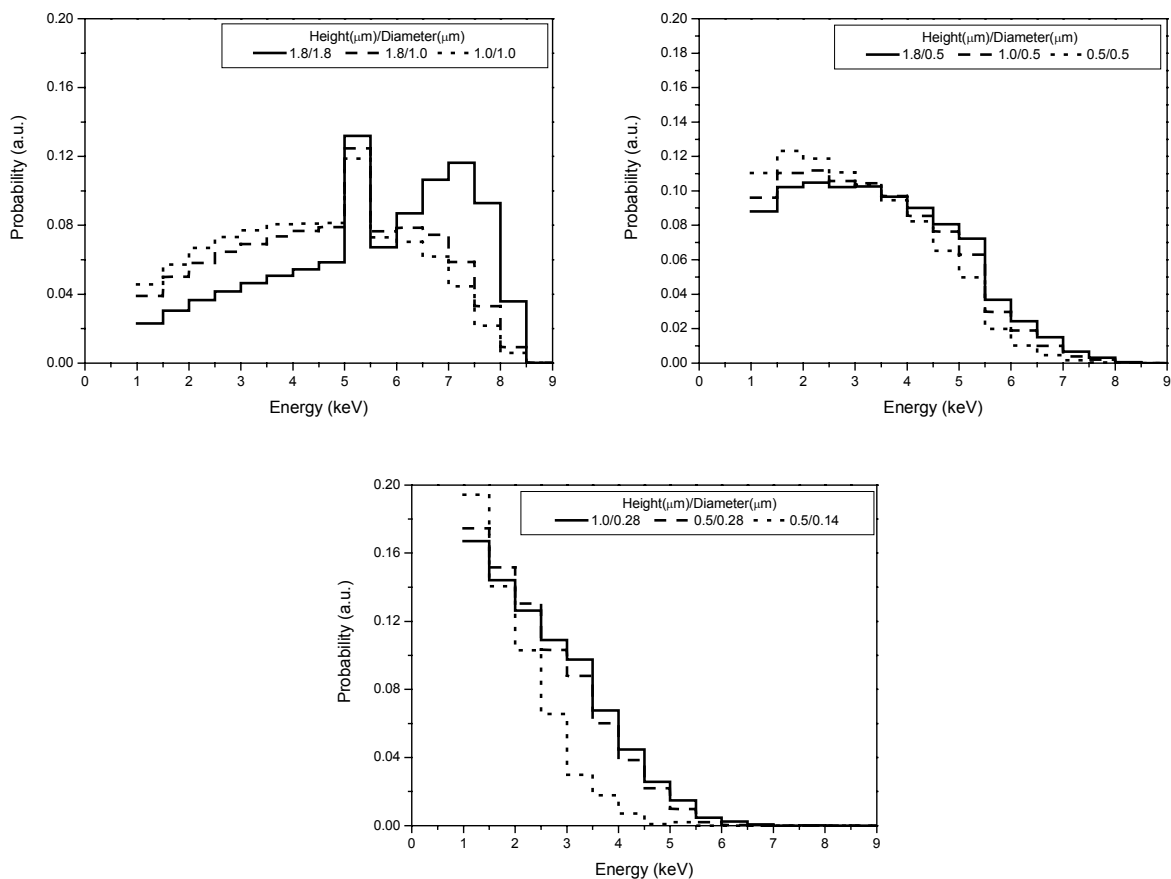


Figure 8.5: The calculated energy deposition spectra of the X-ray source in tissue equivalent material for various cylindrical dimensions. The 8.5 keV photoelectrons can deposit all their energy in three largest diameter site sizes while in the other sites the maximum energy deposition is lower than the maximum photoelectron energies.

energy deposition spectra in tissue equivalent material (Shonka A-150) for various cylindrical dimensions have been calculated applying the calculated X-ray energy spectrum at SV positions and MCNP4C [18] software. The results are shown in Fig. 8.5. Photoelectrons of 8.5 keV can deposit all their energy in the three simulated site sizes with relatively large diameter while in the other sites the maximum energy deposition is lower. The 8.5 keV photoelectrons can deposit all their energy into a tissue volume as small as 1 μm of diameter. For smaller dimensions, however, the maximum energy that can be deposited is smaller. Knowing the maximum energy deposition in each SV from the calculations, the edges in the microdosimetric spectra have been used to calibrate the measured spectra. A measured microdosimetric spectrum (raw data) for a counter cavity of both 1.8 mm diameter and height, simulating 1 μm tissue, is illustrated in Fig. 8.6. The electron edge is also indicated.

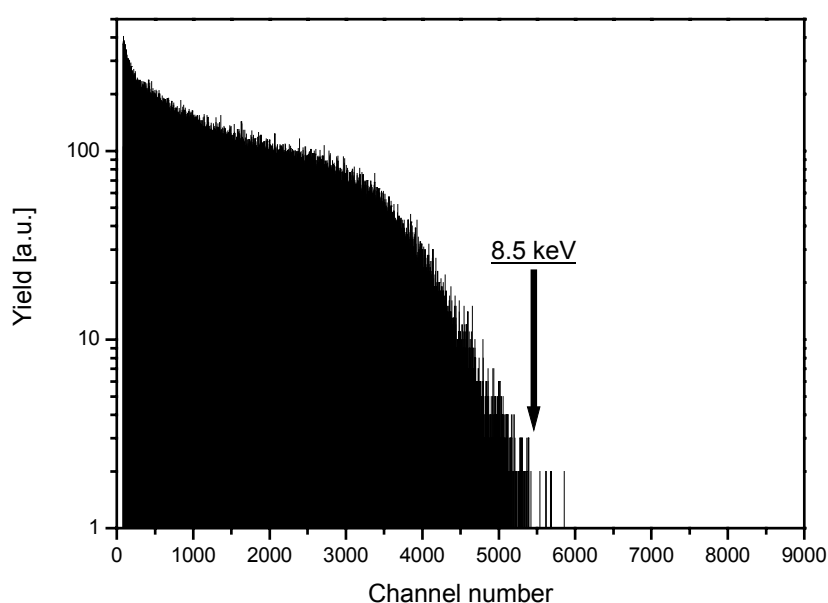


Figure 8.6: A measured pulse-height (raw data of microdosimetric spectrum), with a counter cavity of equal diameter and height of 1.8 mm simulating 1 μm diameter of tissue, of an X-ray tube as radiation source with an applied maximum voltage of 8.5 kV. The electron edge used for calibration is indicated with an arrow.

An other calibration method is used based on the pulse-height spectra recorded in the calibration volumes. The calibration cavities with larger dimensions than the mini-counter SVs (see Fig. 7.3) have been used to make sure that the photoelectrons will fully stop in the gas. Pulse height spectra were obtained employing the chromium K_{α} X-ray peak at 5.4 keV. Fig. 8.7a shows the recorded spectrum using TE- C_3H_8 at a pressure of 30 kPa. The 5.4 keV photopeak position is used for conversion into lineal energy. At energies lower than the photopeak it can be seen that the number of photoelectrons that lose only part of their energy in the counter is small. In Fig. 8.7b and Fig. 8.7c the energy spectra are shown measured with TE- C_3H_8 at pressures of 20 kPa and 10 kPa. The number of photoelectrons that are not fully stopped in the gas has become more significant at reduced the pressure. This can be explained by the fact that the range of the 5.4 keV photoelectrons at pressures of 20 kPa and 10 kPa is respectively 1.5 and 3 times that at a pressure of 30 kPa.

This second calibration method agrees with the previously described one for the relatively large SV (1.8 mm) simulating 1.8 μm . But as the size of the SV or the site size simulation, i.e. the gas pressure, decreases the calibration value (energy/channel) becomes lower than found with the electron edge method. This difference can become as large as almost a factor two in case of a SV of 0.5 mm in diameter simulating a tissue volume of less than 500 nm in diameter. To understand this behaviour charge collection efficiency calculations have been performed.

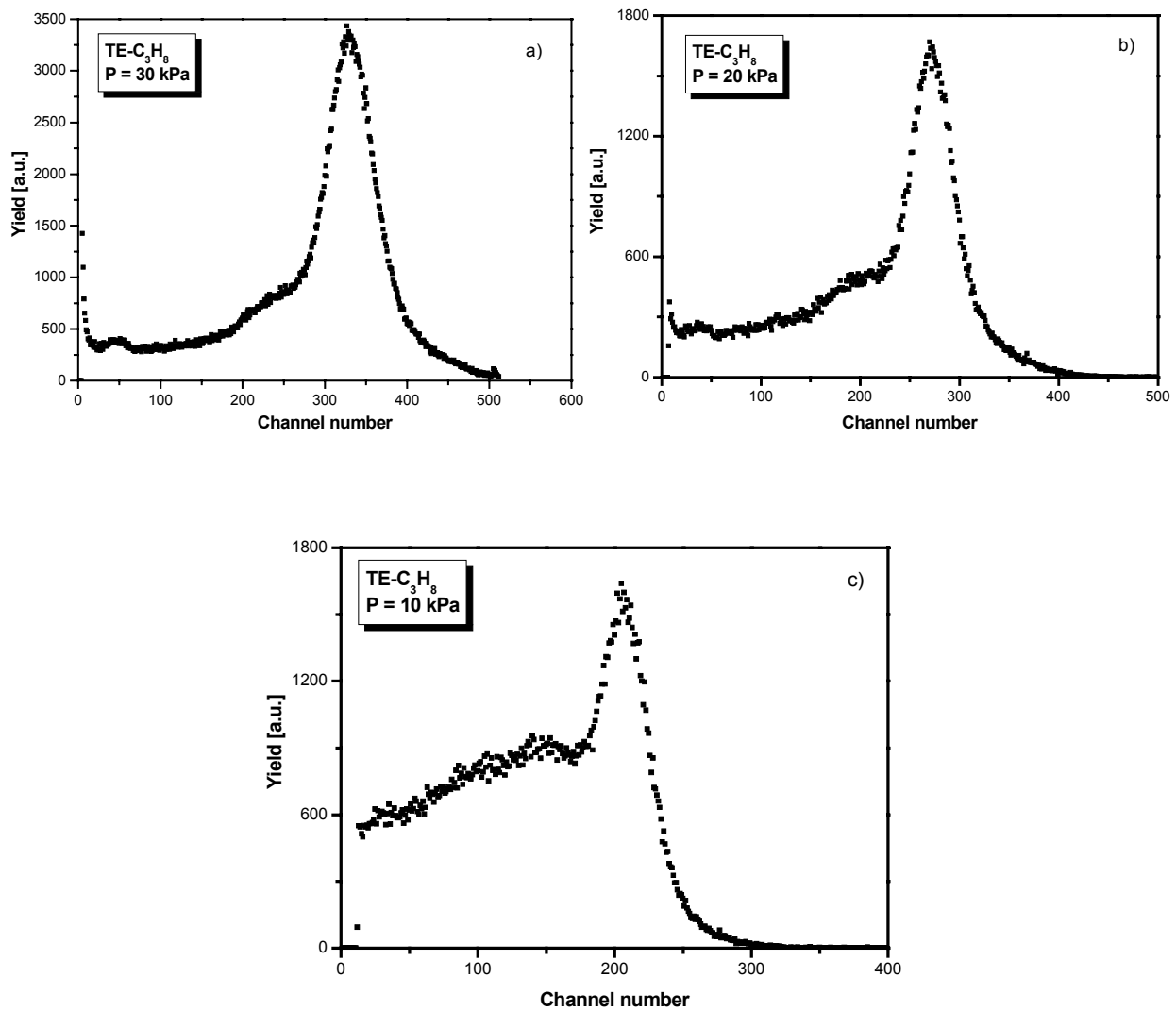


Figure 8.7: Pulse-height spectrum of 5.4 keV X-rays measured with the novel TEPC-GEM counter in the calibration volume using propane-based tissue-equivalent gas (TE-C₃H₈) at a pressure of a) 30 kPa b) 20 kPa c) 10 kPa. The 5.4 keV photopeak position is used for the conversion into lineal energy. The number of photoelectrons that is not fully stopped in the gas becomes more significant by reducing the pressure.

8.5.2 Electric potential and collection efficiency calculations in the sensitive volume

To calculate the electric potential in the drift volume, i.e. the SV of the detector, the Laplace equation was solved with the 3D version of the general purpose partial differential equation solver FlexPDETM (see section 7.2.2). It uses the finite-element method for the solution of boundary and initial value problems.

Our version of FlexPDE does not have full control over the mesh density in a fully 3D space: cell layers are created with a thickness compatible with the dimension of the cells in the XY plane. Besides, where thick layers adjoin thin layers, there is a gradual change to the thin-layer dimension in the cells of the thick layer. Due to the small dimension of the GEM hole in the GEM plane (XY plane) and its small depth, a huge number of cells are required to appropriately calculate the electric potential. Consequently, we performed only 3D calculations to a maximum distance of 0.7 mm from the GEM plane (towards the cathode).

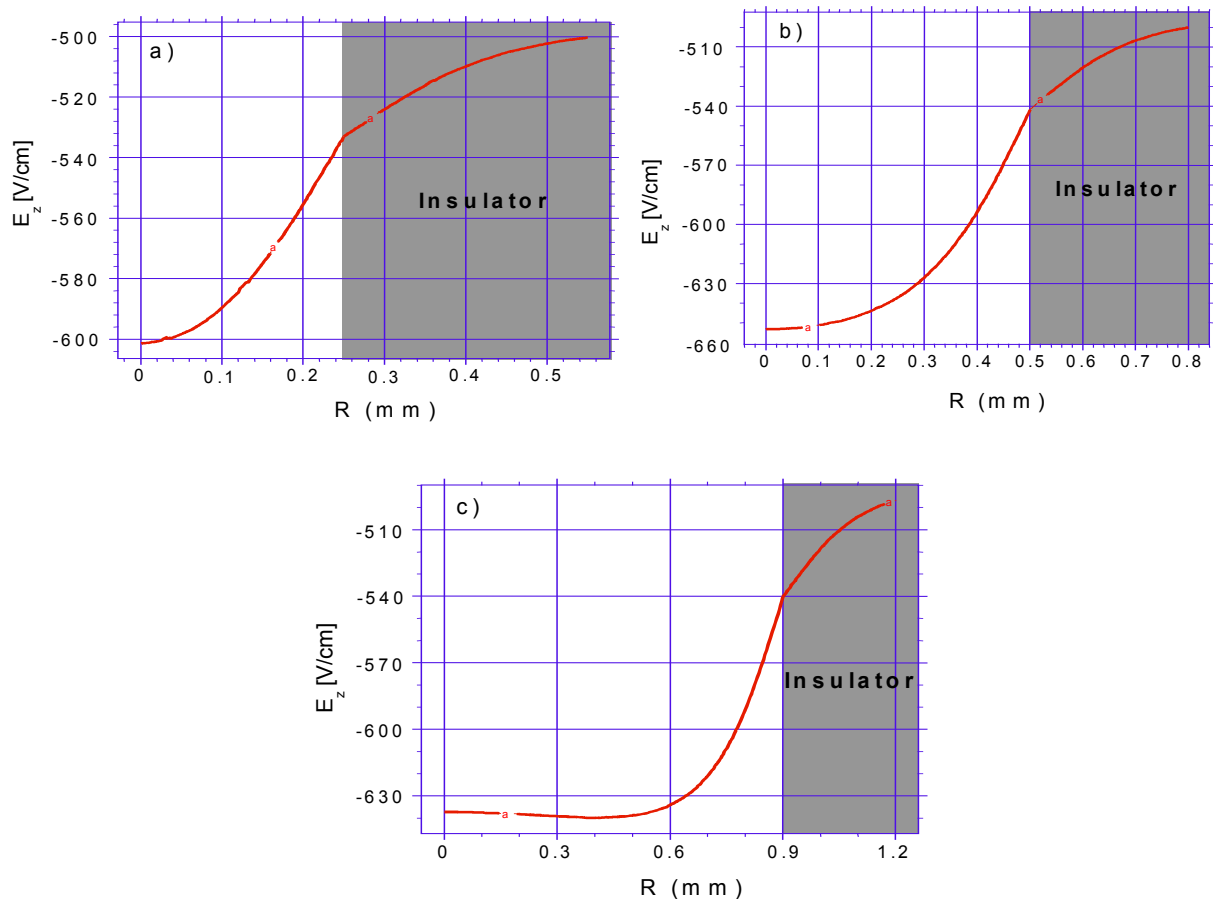


Figure 8.8: The calculated z-component of the electric field at a distance of 0.5 mm from the cathode for a sensitive volume of a) 0.25 mm b) 0.5 mm c) 0.9 mm of radius. The electric fields are different for the different diameters due to the influence of the dielectric material surrounding the sensitive volume.

These calculations show that the electric potential around a single GEM hole can be considered to have a cylindrical symmetry. Calculations show that equipotential lines of a 3D simulation are very similar to the equipotential lines calculated considering a single GEM hole with cylindrical symmetry. Therefore, we used the cylindrical approximation for the electric field calculation in the drift region for our counter with a drift distance of 1.8 mm. Calculation of the electric field of a single GEM hole in the SV shows that the z-component of the electric field in the drift region volume is uniform in most of this region. The z-component of the electric field starts to show a small non-uniformity at a distance of 0.3 mm from the GEM, but it is only at a distance of 0.1 mm from the GEM plane that this non-uniformity becomes really evident. For this reason, the electric potential in the SV can be approximated by using a plane anode instead of the GEM plane. Therefore, to evaluate the electric fields in the SVs (in the presence of a dielectric) of our detector, we have used a simple cylindrical geometry, putting a plane anode (at a distance of 1.8 mm from the cathode) instead of the GEM plane. The voltage applied to the anode was chosen such that the same z-component of the electric field was obtained as in most of the SV with a single GEM hole. The electric field calculations for these volumes show that the electric fields, for the same z-plane, are different for different diameters of the SVs due to the influence of the dielectric material surrounding the SV. In Fig. 8.8a-8.8c the z- component of the electric field at a distance of 0.5 mm from the cathode for SVs of 0.5, 1.0 and 1.8 mm diameter are shown, respectively. The z-component of the electric field is different for different SVs. Closer to the GEM this effect is smaller, further away it is larger.

Using this approximation, the collection efficiency of initially generated electrons in the SV was calculated with a Monte Carlo code [19]. The software FlexPDETM was used to provide to the Monte Carlo code both the electric field inside the counter and the boundaries of the domain in matrix form. Details about the code can be found elsewhere [19].

Table 8.2: *The calculated charge collection efficiency for sensitive volumes of 1.8, 1.0 and 0.5 mm diameter, all having a height of 1.8 mm, at a pressure of 31 kPa for a uniform initial electron distribution ($E_{initial} = 2$ eV).*

	CALIBRATION VOLUME	SENSITIVE VOLUMES (SVs)		
Height (mm)	9.0	1.8	1.8	1.8
Diameter (mm)	8.0	1.8	1.0	0.5
Efficiency (%)	100	85	79	69

The charge collection efficiency was calculated for a uniform initial electron distribution ($E_{initial} = 2$ eV) for three SVs of diameter 1.8, 1.0, 0.5 mm with equal height of 1.8 mm. Moreover, TE-C₃H₈ gas at a pressure of 31 kPa is used which simulates an 1.8 mm gas cavity height to a site size of 1 μ m condensed phase tissue. The results are shown in Table 8.2. The efficiency of the calibration volume is assumed to be 100% considering its large dimensions.

Because the efficiency loss happens close to the cathode and close to the dielectric, we expect the lowest efficiency for a SV of 0.5 mm diameter, which is in agreement with the results shown in Table 8.2. These differences in efficiency loss explain the failure of the pulse height calibration method. The differences become larger with smaller SV dimensions. It has to be mentioned that these calculations do not include the GEM transparency. But the electric field close to the GEM is a function of drift gap and the drift gap is equal (1.8 mm) for three considered SVs, the efficiency values should scale for the same factor. Furthermore, the GEM transparency can be different for a drift gap of 9 mm (calibration) and 1.8 mm (SV) as the electric fields are different close to the GEM as it is shown in Fig. 8.9a and 8.9b. However, we do not expect major differences since the electric field differences close to the GEM are not large.

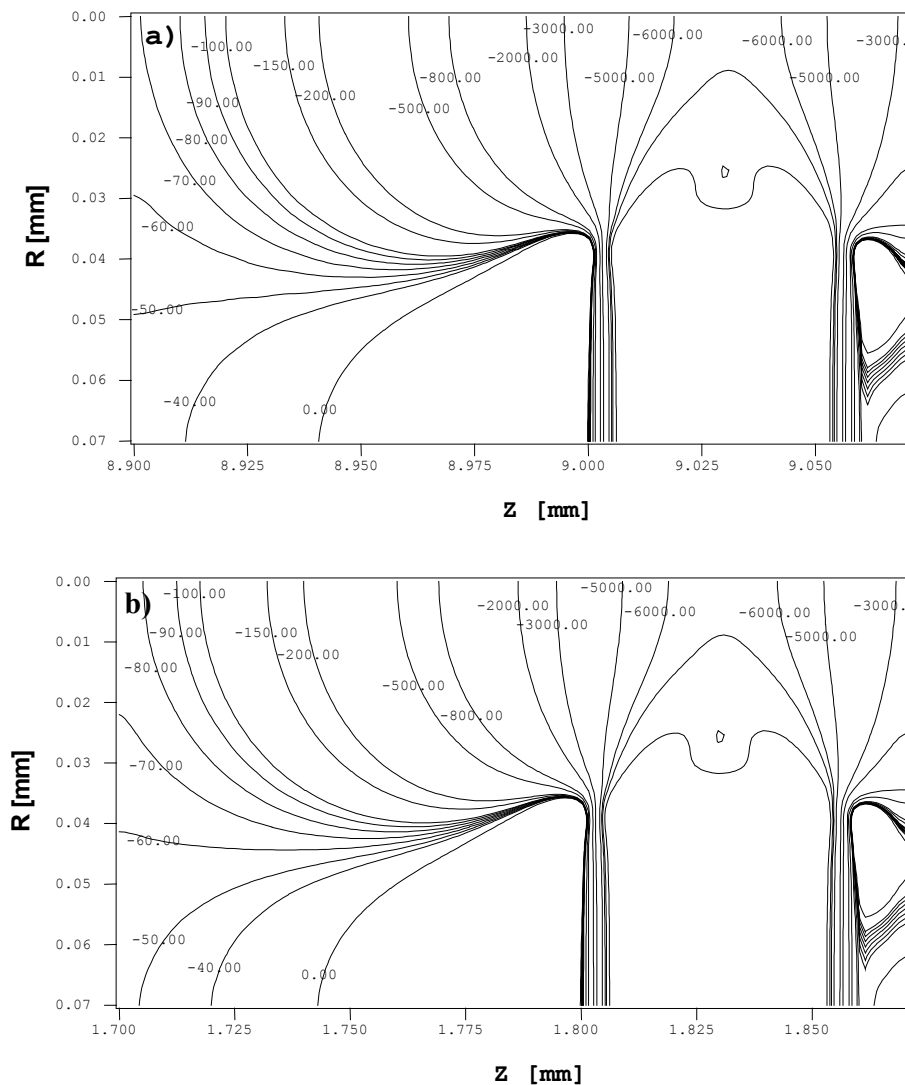


Figure 8.9: The calculated z-component of the electric fields (V/mm) close to the GEM (pitch/diameter of 140/80 μm) for drift gap of a) 9 mm and b) 1.8 mm. The differences in electric fields are small for these two configurations.

8.5.3 Microdosimetric spectra

Microdosimetric spectra from TEPC-GEM measurements can be determined according to well-prescribed methods [16], [20]. In this work, these spectra were processed to a single lineal energy distribution of 60 intervals per decade resulting in microdosimetric spectra in lineal energy y . A spectrum was measured every five minutes to observe the gain stability. No change in gain has been observed during these measurements. A total of more than 10^5 counts has been collected for each spectrum during a period of 1 to 1.5 h to keep the counting error small. Fig. 8.10 shows the processed microdosimetric spectra obtained from TEPC-GEM measurements for the counter cavity of 1.8 mm in diameter and 1.8 mm in height at 56 kPa, 31 kPa and 16 kPa pressures of TE-C₃H₈. At these pressures the gas mass in the cavity simulates 1.8 μm , 1.0 μm and 0.5 μm diameter of condensed phase tissue respectively.

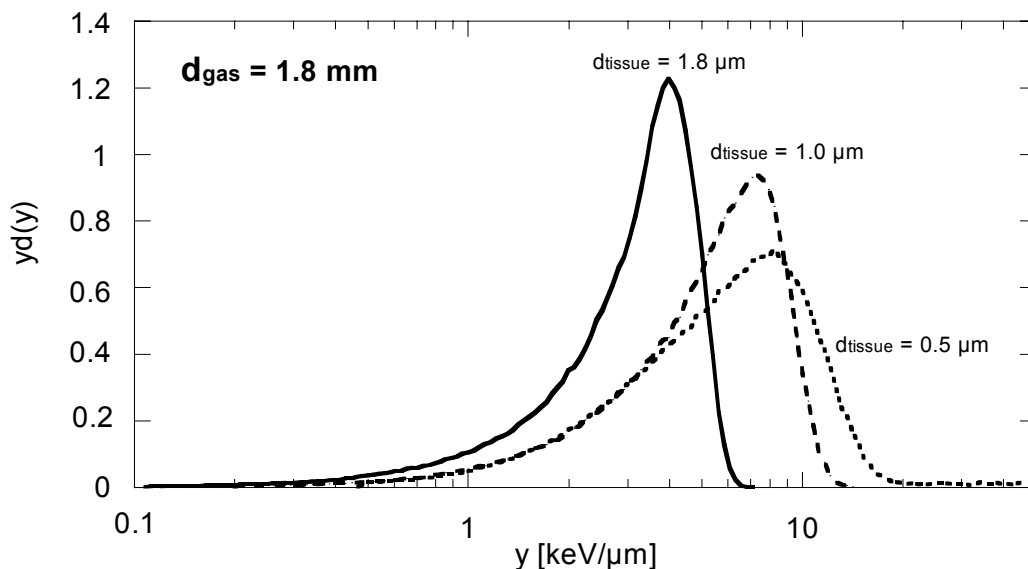


Figure 8.10: The processed microdosimetric spectra of 8.5 kV X-rays obtained from a TEPC-GEM for a counter cavity of 1.8 mm in diameter and 1.8 mm in height at 56 kPa, 31 kPa and 16 kPa which simulates tissue volumes of 1.8 μm , 1.0 μm and 0.5 μm in diameter respectively.

Increasing the site diameter causes narrowing of the dose distribution and downward shifting of the spectrum edge. Narrowing of the dose distribution can be explained by the fact that by increasing the site diameter, the numbers of insiders and stoppers increase while the number of crossers decreases. The downward shifting of the spectrum edge can be explained by the fact that the same amount of energy is imparted in the larger volume with larger mean chord length causing lowering of the maximum lineal energy.

Microdosimetric spectra also have been measured using the cavities having different diameters and these data are compared to study the behaviour of TEPC-GEM with smaller cavity dimensions. Fig. 8.11 illustrates the microdosimetric measurements simulating 0.5 μm tissue utilising cavities of 1.8 mm, 1.0 mm and 0.5 mm in diameter at pressures of 16 kPa, 28

kPa and 56 kPa respectively. Note that all three cavities have the same height of 1.8 mm. The shapes of these three spectra are almost the same, which indicates the possibility of operating

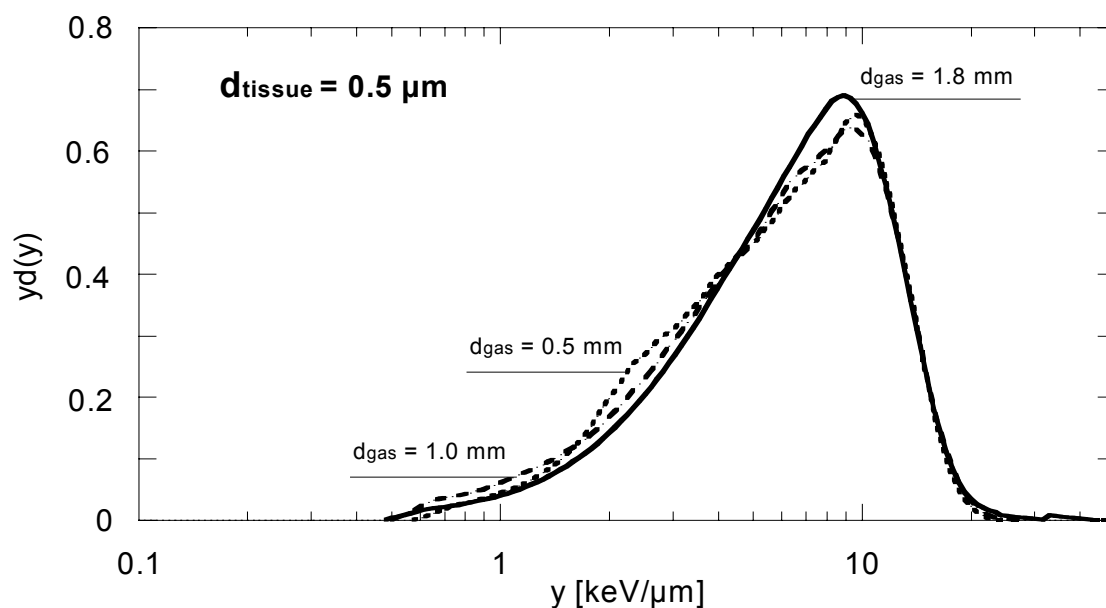


Figure 8.11: *The processed microdosimetric spectra of 8.5 kV X-rays obtained from TEPC-GEM simulating tissue volume of $0.5 \mu\text{m}$ in diameter for counter cavities of 1.8 mm, 1.0 mm and 0.5 mm of diameter. All three cavities have the same height of 1.8 mm.*

this counter with a cavity diameter as small as 0.5 mm. Furthermore, a small difference in the spectral shape and a shift of the maximum peak to higher y value can be observed as the cavity diameter reduces. This can be explained by the fact that the heights of all three cavities are the same but the diameters differ. Therefore the chord length distribution of each cavity is different and because of this, the maximum peak of y -spectra distributions is slightly different. However, the photoelectrons are ejected predominantly sideways at this low photon energy and so the effect of simulated height differences is not considerable as can be derived from Fig. 8.11.

8.5.4 Nanodosimetric spectra

The TEPC-GEM is applied to operate at a pressure of 16 kPa TE- C_3H_8 gas for a counter cavity diameter of 1 mm which simulates a tissue diameter of 280 nm. This tissue site size has also been simulated by measuring with a counter cavity of 0.5 mm of diameter at a pressure of 31 kPa. The results, shown in Fig. 8.12, are very similar. Small differences can be explained by differences in chord length distribution (see discussion above). Figure 8.12 shows also the spectrum measured with the cavity of 0.5 mm diameter at a pressure of 16 kPa which simulates 140 nm tissue size. These results show the shape which could be expected and therefore confirm the proper operation of this counter for nanodosimetry. In an earlier study (unpublished) the successful GEM operation with TE- C_3H_8 gas at a pressure of 5 kPa has been demonstrated. At this pressure the SV of 0.5 mm of diameter simulates 45 nm

condensed phase tissue. Even this pressure is not the limitation of GEM operation. However, the linearity at low pressure has to be investigated especially when applying small cavities.

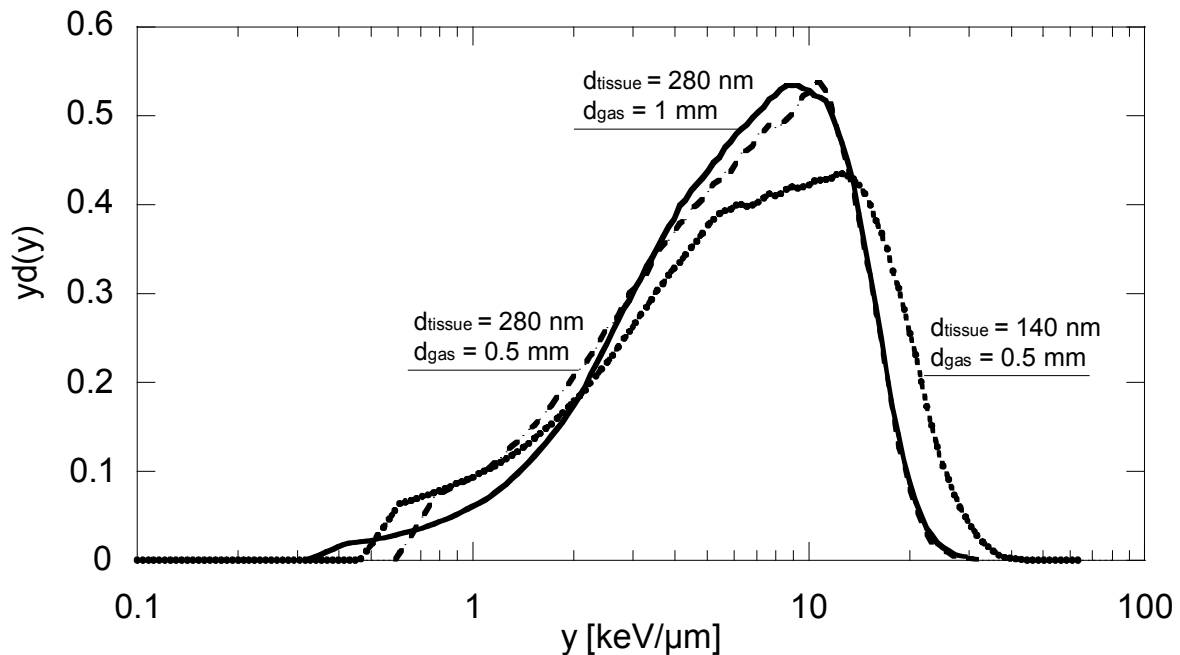


Figure 8.12: The processed microdosimetric spectra of 8.5 kV X-rays obtained from TEPC-GEM simulating tissue volumes of 280 nm and 140 nm of diameter with counter cavities of 1.0 mm and 0.5 mm of diameter.

8.5.5 Conclusions

The first microdosimetric spectra have been measured using the novel TEPC-GEM and X-rays. This has been demonstrated for a cylindrical counter cavity of 1.8 mm in diameter and 1.8 mm in height simulating 1.8 μm , 1.0 μm and 0.5 μm sites, depending on the gas pressure. The applied calibration method is based on using the electron edge of the measured microdosimetric spectra.

We have measured the first pulse height spectra at low pressure, employing the TEPC-GEM and X-rays. It was tried to use the 5.4 keV photopeak of this spectrum for calibration of microdosimetric spectra in terms of lineal energy. We have shown that this method does not work in a proper way due to incomplete charge collection in the counter cavity. It has been shown that the collection efficiency of electrons is decreasing when the diameter of the SV is reduced due to the influence of the dielectric material surrounding the SVs which disturb the z-component of the electric field.

The TEPC-GEM has many advantages compared to the usual TEPCs such as, simple in construction, robust and stable in operation, and suitable both as mini-single and multi-element counter. Moreover, the components (SV, GEM and wall material) are easy to modify.

From the excellent results of the TEPC-GEM obtained in this work and the earlier microdosimetric measurements (see section 8.4), applying various neutron sources, [21] we conclude that the TEPC-GEM is a promising counter to perform microdosimetric measurements for simulating micrometer site sizes. We were also able to measure a microdosimetric spectrum, applying TEPC-GEM with a cylindrical counter cavity as small as 0.5 mm in diameter. This spectrum has been compared to the spectra measured with larger counter cavity sizes (1.0 mm and 1.8 mm) simulating the same tissue site size. These spectra correspond very well which indicates the possibility of using this counter with a cavity as small as 0.5 mm in diameter. Finally, we have measured a microdosimetric spectrum using the 0.5 mm cavity simulating tissue size of 140 nm of diameter. This seems, however, not the minimum site size that can be simulated. In future work the minimum dimension will be investigated.

In general it can be concluded that this small counter cavity opens new possibilities in application for high intensity radiation field as well as in nanodosimetry.

At the end we like to mention that the present prototype TEPC-GEM is designed with seven cavities (with different dimensions) which are considered as single TEPCs in this work. In applications in which high sensitivity is important such as personal, space and aircraft dosimetry the counter cavities can easily be coupled to a multi-element TEPC.

References

- [1] H. H. Rossi and M. Zaider, "Microdosimetry and Its Applications," Springer Verlag Berlin Heidelberg 1996.
- [2] T. Loncoln, V. Cosgrove, J.M. Denis, J. Gueulette, A. Mazal, H.G. Menzel, P. Pihet and R. Sabattier, "Radiobiological effectiveness of radiation beams with broad LET spectra: microdosimetric analysis using biological weighting functions," *Radiat. Prot. Dosim.* vol. 52, pp. 347-352, 1994.
- [3] F. Sauli, "GEM: A new concept for electron amplification in gas detectors," *Nucl. Instr. And Meth. A*, vol. 386, pp. 531-534, 1997.
- [4] M. Farahmand, A. J. J. Bos, J. Huizenga, L. De Nardo and C. W. E. van Eijk, "Design of a new tissue-equivalent proportional counter based on a gas electron multiplier," *Nucl. Instr. And Meth. A*, vol. 509, pp. 262-267, 2003.
- [5] International Commission on Radiation Units and Measurements, "Neutron Dosimetry for Biology and Medicine," (ICRU report; 26). Washington, D.C., 1977.
- [6] J. Burmeister, C. Kota and R.L. Maughan, "Paired miniature tissue-equivalent proportional counters for dosimetry in high flux epithermal neutron capture therapy beams," *Nucl. Instr. And Meth. A*, vol. 422, pp. 606-610, 1999.
- [7] K.M. Langen, P.J. Binns, A.J. Lennox, T.K. Kroc and P.M. DeLuca Jr., "Pileup correction of microdosimetric spectra," *Nucl. Instr. And Meth. A*, vol. 484, pp. 595-612, 2002.
- [8] V. Cesari, P. Colautti, G. Margin, L. De Nardo, W. Y. Back, B. Grosswendt, A. Alkaa, C. Khamphan, P. Ségur and G. Torielli, "Nanodosimetric measurements with an avalanche confinement TEPC," *Radiat. Prot. Dosim.* vol. 99, no. 1-4, pp. 337-342, 2002.
- [9] V. Cesari, N. Iborra, L. De Nardo, R. Querini, V. Conte, P. Colautti, G. Torielli, P. Chauvel, "Microdosimetric measurements of the Nice therapeutic proton beam," *PHYSICA MEDICA*, vol. 17, Suppl. 3, pp. 76-82, 2001.
- [10] J. Burmeister, C. Kota, R.L. Maughan and A. J. Waker, "Characterization of miniature tissue-equivalent proportional counters for neutron radiotherapy applications," *Phys. Med. Biol.*, vol. 47, pp. 1633-1645, 2002.
- [11] P. Kliuga, "Measurement of single event energy deposition spectra at 5 nm to 250 nm simulated site sizes," *Radiat. Prot. Dosim.*, vol. 31, no. 1-4, pp. 119-123, 1990.

- [12] P. Kliauga, A.J. Waker and J. Barthe, "Design of tissue-equivalent proportional counters," *Radiat. Prot. Dosim.*, vol. 61, no. 4, pp. 309-322, 1995.
- [13] H. Schuhmacher, "Tissue-equivalent proportional counters in radiation protection dosimetry: Expectation and present results," *Radiat. Prot. Dosim.*, vol. 44, no. 1-4, pp. 199-206, 1992.
- [14] M. Farahmand, A.J.J. Bos, C.W.E. van Eijk, "Gas electron multiplier (GEM) operation with tissue-equivalent gases at various pressures," *Nucl. Instr. and Meth. A*, vol. 506, pp. 160-165, 2003.
- [15] D. Srdoc and S.A. Marino, "Microdosimetry of monoenergetic neutrons," *Radiat. Res.* Vol. 146, pp 466-474, 1996.
- [16] International Commission on Radiation Units and Measurements, "Microdosimetry," (ICRU report; 36). Bethesda, Maryland, 1983.
- [17] J.F. Dicello, W. Gross and U. Kraljevic, "Radiation quality of californium-252," *Phys. Med. Biol.* Vol. 17, pp 345-355, 1972.
- [18] J. Briesmeister, editor. MCNP: A general Monte Carlo N-particle transport code, version 4C. Manual LA-13709-M. Los Alamos NM, USA: Los Alamos National Laboratory, 2000.
- [19] L. De Nardo, A. Alkaa, C. Khamphan, V. Conte, P. Colautti, P. Ségur and G. Torielli, "A detector for track-nanodosimetry," *Nucl. Instr. and Meth. A*, vol. 484, pp. 312-326, 2002.
- [20] S. Gerdung, P. Pihet, J. E. Grindborg, H. Roos, U. J. Schrewe and H. Schuhmacher, "Operation and application of tissue-equivalent proportional counters," *Radiat. Prot. Dosim.*, vol. 61, no. 4, pp. 381-404, 1995.
- [21] M. Farahmand, A. J. J. Bos, L. De Nardo and C. W. E. van Eijk, "First microdosimetric measurements with a TEPC based on a GEM," accepted for publication, *Radiat. Prot. Dosim.*, (2004).

Chapter 9

Discussion and Outlook

The main result of this work is the investigation and development of an alternative approach to currently available devices used to perform microdosimetric measurements. In experimental microdosimetry, the level of effects of ionising radiation are attempted to be quantified by investigating the statistical distribution of energy deposition events at the microscopic level employing a Tissue-Equivalent Proportional Counter (TEPC). The currently used TEPCs are proportional counters with a cavity containing a central anode wire, operated with a tissue-equivalent counting gas at low pressure to simulate tissue volumes of micrometer dimensions. TEPCs are operated in pulse mode and the pulse-height spectrum is collected and converted to a stochastic quantity such as the lineal energy. The shape of a microdosimetric spectrum contains quantitative information that can be used to predict the radiobiological effectiveness of ionising radiation of a particular type and energy.

Neutrons are an important type of radiation relevant to nuclear energy. Neutrons show also up as background radiation in radiotherapy with protons and electrons in excess of 10 MeV. In addition, neutron radiotherapy is performed at various places. The microdosimetric spectra of neutrons have been calculated applying an analytical method (see chapter 4). Calculations were performed for interactions of neutrons of different energies, with tissue and tissue equivalent materials at the micrometer level. It has been shown that the contribution of different particle tracks (insiders, starters, stoppers and crossers) changes as the neutron energy or the simulated site size varies. The largest contribution to the dose distribution is originating from the crossers as long as the ranges of the secondary particles are much larger than the simulated site size. Furthermore, the contribution from insiders decreases with increasing neutron energy.

Two parameters (neutron energy and simulated site size) which have a significant influence on the shape of microdosimetric spectra are extensively discussed. Increasing the neutron energy causes the proton peak maximum to extend to higher values of lineal energy as long as the maximum range of protons is less than the site size. In the situation that the maximum range of protons is larger than the site size, increasing the neutron energy causes the proton

peak maximum to shift to lower values of lineal energy. As the neutron energy increases, the contributions from heavy particles increase, which cause more densely ionization along their paths. These heavy particles have a higher linear energy transfer (LET) and, therefore, cause more biological damage to living tissue. Increasing the simulated site size causes a shift of the microdosimetric spectrum to lower lineal energy values. However, these calculations are based on the assumption that the energy deposition in the sensitive volume crossed by a neutron-induced ion can be calculated from the Continuous Slowing Down Approximation (CSDA). The CSDA can be used to calculate energy deposition of heavy charged particles in the sensitive volume if straggling and delta ray effects are neglected. For neutron-generated protons and heavy ions of energies below 1 MeV/u in tissue-equivalent material, straggling cannot be neglected in calculations for site sizes smaller than 1 μm .

The calculations give insight into the various parameters influencing microdosimetric spectra and can be used to interpret measured microdosimetric spectra. However, in the case of measured spectra utilizing a proportional counter there are two stochastic factors which can make the shape of microdosimetric spectra somewhat different from calculated spectra: 1) Fano-fluctuations, i.e. variation in the number of ions produced per unit energy deposition and 2) multiplication statistics. Furthermore, the neutron sources are usually contaminated by γ -rays that will also have an effect on the shape of measured spectra.

Two types of high-energy neutron sources, based on the ${}^7\text{Li}(p,n){}^7\text{Be}$ reaction and the spallation process are discussed and explained. Both neutron sources are based on the release of neutrons from matter by bombardment with energetic particles. For microdosimetric measurements of high-energetic neutrons we have focused initially on the n_TOF facility at CERN, which is based on the spallation process, since this neutron source was expected to be available to use. Some possible difficulties utilising this neutron source for extracting microdosimetric data will be discussed.

The high neutron flux density of an n-TOF type of source causes the problem of pile-up which can be reduced by decreasing the counter size. A calculation has been performed to estimate the proper counter size based on kerma rate and mass stopping power from which the number of secondary charged particles can be estimated. This calculation appears to be a fast, reliable method to estimate the fluence of secondary charged particles. The Monte Carlo code FLUKA has also been used to calculate the fluence of secondary charged particles. The results of the Monte Carlo calculation and the calculation utilising kerma and mass stopping power agree well. Therefore, we can conclude that the proton fluence estimation using kerma and mass stopping power is trustworthy.

The calculations have shown that a mini TEPC, which has a sensitive volume diameter of 1 mm, is needed to reduce the pile-up effect properly. In addition, the n-TOF facility has a large neutron pulse repetition time of 14.4 s which poses the problem of not getting enough information in reasonable measuring time which is not practical. A multi-element counter has been proposed to reduce the measuring time.

There are other problems regarding performing microdosimetric measurements at the n_TOF facility (see section 5.3.5). Therefore, it is recommended to use other neutron sources than n_TOF spallation facility such as the ${}^7\text{Li}(p,n){}^7\text{Be}$ reaction neutron sources. These sources produce almost monoenergetic neutrons with any desirable energy. However, if the purpose

of microdosimetric measurements is to be used in radiation protection the variance-covariance technique is a better option compared to single event measurements when applying high fluence sources.

As mentioned above a mini multi-element TEPC is needed to perform proper microdosimetric measurements at the CERN n_TOF facility. Various types of mini TEPCs have been developed by several groups in the past few years. This is usually done by miniaturising the dimensions of all components of existing TEPCs. However, the construction of a central wire in a small cavity is extremely difficult and expensive. It becomes even more difficult if a multiple-element cavity is applied to increase the counter sensitivity. Furthermore, the present supply of counters for routine practice is hampered by technical problems in the production of reliable detectors at reasonable cost. These drawbacks justify our efforts to develop a new type of TEPC based on a Gas Electron Multiplier (GEM) instead of detectors employing a central anode wire. This new design not only simplifies the construction of mini multi-element counters but it also facilitates microdosimetry measurements (e.g. in nanodosimetry, personal and space dosimetry) in a relatively easy manner.

To investigate the possibility of using a TEPC based on a GEM, the operation of GEMs employing Tissue-Equivalent gases has been studied. The operation of two GEM structures, of pitch/outer diameter 140/80 μm and 90/60 μm , in both methane and propane based tissue-equivalent gases at various pressures has been studied. In TE-CH₄ a maximum safe gain of $1.5 \cdot 10^3$ has been obtained while in TE-C₃H₈ a maximum safe gain of $6 \cdot 10^3$ has been reached for both GEM structures. These maxima have been obtained at different pressures depending on GEM structure and gas properties. Empirical relations have been derived which can be used to predict the maximum-safe-gain variation of GEMs operating with the same gas as a function of their structure and to predict the variation for a certain GEM as a function of counting gas.

It is observed that sufficiently high gas gains, for both GEM structures and both TE gases, can be obtained for different pressure ranges. We advise the use of TE-C₃H₈ rather than TE-CH₄ because of its relatively higher gain for the whole pressure range. For the 90/60 μm GEM structure the pressure range with high gains is broader than that for 140/90 μm GEM structure. However, for applications at relatively higher pressures it is better to use the GEM with smaller holes (90/60 GEM) while for applications at relatively low pressures we recommend to use a GEM with relatively larger GEM hole (140/90 GEM). In the latter case, a GEM with a thicker insulator (presently 50 μm thick) might also be recommended. However, charge up/polarisation effects may become significant. This has to receive attention.

The charge up/polarisation effect of the GEM could be a cause of concern in some applications e.g. at not constant fluence sources. Fortunately this effect becomes stable after a while. This effect has to be investigated in more detail for microdosimetric application. However, this effect can be reduced using cylindrical shaped GEM holes instead of conically shaped holes, used in this work.

It is observed that the energy resolution becomes better by lowering the pressure. Since the counters in microdosimetry have to be operated at low pressure we will benefit of this phenomenon.

A new type of mini multi-element TEPC based on a GEM instead of a conventional TEPC employing a central anode wire is constructed which is referred to as TEPC-GEM. For this design cylindrical geometry (diameter equal to height) was chosen because of simplification of the construction. A continuous gas flow system was selected to ensure the gas purity. Furthermore, it was chosen to hold the anode at ground potential and to apply negative high voltage to the detector wall (drift cathode). A-150 conductive plastic has been applied as counter walls and Rexolite as insulator. However, the elemental composition of Rexolite is not completely tissue-equivalent in the aspects important for some dosimetry application. Rexolite may affect the measurements since the contribution of the secondary charged particles originating from Rexolite to the measurements is not small. Implications of the contributions of this non tissue-equivalent material to the absorbed dose in the sensitive volume are depending on the type of radiation used. For applications where this non tissue-equivalency should cause a problem, Rexolite can easily be replaced by a non-conductive TE material.

Calibration of TEPCs used for microdosimetry comprises the conversion of pulse height into lineal energy. The calibration method applied for the TEPC-GEM is based on the proton edge (in the case of using neutron sources) and the electron edge (in the case of using X-ray sources) of the measured spectra. In the future design an internal alpha source can be added for calibration. However, for a small cavity this could become impractical. A calibration method that is in principle suitable for a mini multi-element proportional counter relies on addition of a small amount of ^{37}Ar to the TE gas.

The microdosimetric response of this novel counter to a 14 MeV neutron source and a ^{252}Cf source are measured. The spectra have been compared with the microdosimetric spectra measured before by TEPC employing central anode wires. Excellent agreement was found. Therefore, we can conclude that the TEPC-GEM is suitable to perform microdosimetric measurements. Microdosimetric spectra have been also measured using the TEPC-GEM and X-rays, e.g. for a cylindrical counter cavity of 1.8 mm in diameter and 1.8 mm in height simulating 1.8 μm , 1.0 μm and 0.5 μm sites, depending on the gas pressure.

The TEPC-GEM has many advantages compared to the usual TEPCs such as, simple in construction, robust and stable in operation, and suitable both as mini-single and multiple-element counter, which will broaden the applications of the counter in the fields of personal and space dosimetry. Because of the relatively simple design and construction the TEPC-GEM is not only relatively cheap and easy to produce but also its components (sensitive volume, GEM and wall materials) can be modified and adapted to the needs.

From the excellent results of the TEPC-GEM obtained applying X-ray and neutron sources it is concluded that the TEPC-GEM is a promising counter to perform microdosimetric measurements for simulating micrometer site sizes. Measurements were made of a microdosimetric spectrum, applying TEPC-GEM with a cylindrical counter cavity as small as 0.5 mm in diameter. This spectrum has been compared to the spectra measured with larger counter cavity sizes (1.0 mm and 1.8 mm) simulating the same tissue site size. These spectra

correspond mutually very well which indicates the possibility of using this counter with a cavity as small as 0.5 mm in diameter. Finally, we have measured a microdosimetric spectrum using the 0.5 mm cavity simulating tissue size of 140 nm of diameter. This seems, however, not the minimum site size that can be simulated. In future work the minimum dimension has to be investigated. Note that the 0.5 mm diameter cavity has a height of 1.8 mm. In case of applying a cavity of 0.5 mm height, the counter proportionality has to be investigated.

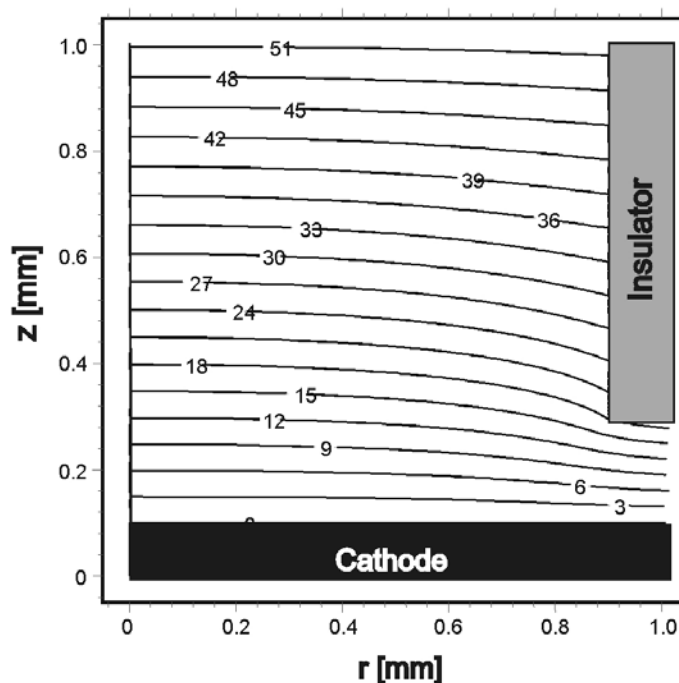


Figure 9.1: Equipotential line plots for part of the sensitive volume of TEPC-GEM close to the cathode. The cathode (lower part) is at ground potential. The insulator wall of sensitive volume is also indicated. The distance r from the centre of the sensitive volume and z from the cathode are also indicated. The voltage (V) at different positions are indicated.

More work is required to ensure even better performance of TEPC-GEM. In particular, improvement of the charge collection efficiency in the sensitive volume.

Some work has been done to find out the possibilities to improve the charge collection efficiency (see 8.5.2) in the sensitive volume of the counter. Therefore, the equipotential lines have been calculated using a two-dimensional model for the actual dimensions of 1.8 mm height and 1.8 mm diameter of the sensitive volume (see section 7.2.2 for more details of the calculation). The result for a part of the sensitive volume of TEPC-GEM close to the cathode is shown in Fig. 9.1. The lower part of the figure represents the cathode surface which is held at ground potential. The insulator wall of the sensitive volume is also indicated. It can be seen that the radial electric field component causes the electrons to move towards the insulator wall and will be absorbed to it. Furthermore, the cylindrical sensitive volume is subdivided into different rings and the charge collection efficiency of each ring is calculated. The results of the most important segments of sensitive volume are given in Table 9.1. As expected the

charge collection efficiency is worst closest to the cathode and insulator. Considering that the segment for r between 0.8 and 0.9 mm is not a small fraction of the total sensitive volume, improvements of the charge collection in this segment will lead to a better performance of the counter.

Table 9.1: The calculated charge collection efficiency for sensitive volume of 1.8 mm diameter and 1.8 mm height, at a pressure of 30 kPa TE-C₃H₈ for a uniform initial electron distribution ($E_{init} = 2$ eV) for the configuration shown in Fig. 9.1.

		r (mm)	
		0.7-0.8	0.8-0.9
		Collection efficiency (%)	
z (mm)	0-0.2	45	2
	0.2-0.4	73	9
	0.4-0.6	94	32
	0.6-0.8	99	55

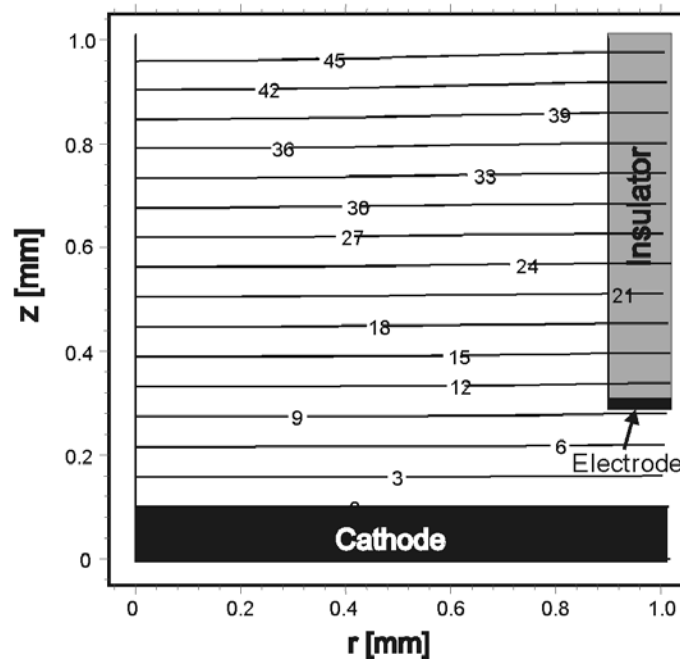


Figure 9.2: Equipotential line plots for part of the sensitive volume of a TEPC-GEM close to the cathode applying a electrode between the insulator and cathode (guard ring). The cathode (lower part) is held at ground potential and the guard ring at 10 V. The insulator wall of sensitive volume is also indicated.

It is proposed to apply an electrode, between the insulator and the cathode, biased at 10 V. The equipotential lines in this situation have been calculated for the same sensitive volume and are illustrated in Fig. 9.2. By employing this configuration, the equipotential lines close to the cathode become almost flat. The charge collection efficiency for the same segments as

above has been calculated and is shown in Table 9.2. In this situation, the efficiency at r between 0.8 and 0.9 mm is improved significantly and is less dependent on the z -position.

From these results we can conclude that using a grid at a small potential, with respect to the cathode, will improve the collection efficiency.

Table 9.2: *The calculated charge collection efficiency for sensitive volume of 1.8 mm diameter and height of 1.8 mm, at a pressure of 30 kPa TE-C₃H₈ for a uniform initial electron distribution ($E_{initial} = 2$ eV) in the case of using an electrode between the insulator and the cathode counter wall, biased at 10 V.*

		r (mm)	
		0.7-0.8	0.8-0.9
		Collection efficiency (%)	
z (mm)	0-0.2	97	61
	0.2-0.4	100	65
	0.4-0.6	100	68
	0.6-0.8	100	73

Finally, calculations are performed for different situations such as in the case of having no space (currently 0.2 mm) between the insulator and the cathode and for the case of a wall-less counter (absence of insulator). The results show the same effect as in case of applying a guard ring, although in the wall-less situation the sensitive volume is not well defined anymore.

In general, it can be concluded that this small counter cavity opens new possibilities in application for high intensity radiation fields as well as in nanodosimetry. It has to be mentioned that the present prototype TEPC-GEM is designed with seven cavities (with different dimensions) which are considered as single TEPCs in this work. In applications in which high sensitivity is important such as personal, space and aircraft dosimetry the counter cavities can easily be coupled to a multi-element TEPC.

Summary

Instruments are essential tools in science since our senses are very limited. New devices open new research possibilities for a better understanding of the laws of nature. In this work development of a new type of instrument is focused on. This device has been used to assess the impact of radiation on tissue.

Radiation is a form of energy that has always been around in nature and human beings are irradiated throughout life. To assess the impact of radiation exposure properly, it is essential to understand the mechanism of the interactions of radiation with living organisms.

Based on their primary interaction mechanisms, ionizing radiation can be classified into directly ionizing charged particles (e.g., electrons, protons, alpha, etc.) and indirectly ionizing radiation (e.g., photons and neutrons). Radiation of the indirectly ionizing type deposits its energy through the production of charged particles (so-called secondary charged particles), which are the directly ionizing type. In the case of directly ionizing interactions of charged particles with matter, the energy is lost in a large number of relatively small interactions via the Coulomb forces causing ionizations and excitations of the atoms and molecules. In a living cell, ionization and excitation of atoms and molecules initiate a complex chain of events from chemical changes in some important bio-molecules through mutations to bio-functional changes such as transformation and cell death.

A problem is that although two types of radiation may deposit the same average energy in an organ, living cells and tissues do not necessarily respond in the same way to these types of radiation. It is generally accepted that the microscopic distribution of energy deposition in volumes of cellular and sub-cellular dimensions is of critical significance for the level of biological damage caused. Therefore, measurement of radiation quantities in sites of size comparable to the cell or even the DNA cross-sections are required. In general, microdosimetry concerns the nature of the energy depositions that occur in micro-volumes of the order of cellular and sub-cellular structures. Therefore, in the early 1950s the low-pressure proportional counter has been developed which permits measurements of microdosimetric quantities at scales of the order of 1 μm . Chapter 2 describes microdosimetry and some basic principles of the main device used in microdosimetry i.e. proportional counter and the way in which the microdosimetric spectra are generally represented is explained. In addition, an introduction to the application of experimental microdosimetry is given. A few other commonly used experimental microdosimetry methods are briefly described.

Proportional counters are extensively used in experimental microdosimetry which is the study and interpretation of single-event energy deposition at microscopic sites of tissue. The equivalence to the human tissue is reached by employing Tissue-Equivalent (TE) materials. That is the reason for constructing the walls of the proportional counter out of a tissue-equivalent plastic and the use of a filling gas that has almost the same composition as human tissue. Therefore, these devices are called Tissue-Equivalent Proportional Counter (TEPC). Furthermore, the simulation of a microvolume is carried out by the reduction of the gas pressure. Currently used TEPCs are proportional counters with a cavity employing a central anode wire. TEPCs are operated in pulse mode and the pulse-height spectrum is collected and converted to the parameter extensively used in microdosimetry, i.e. lineal energy. Lineal energy is commonly presented in units of $\text{keV}\mu\text{m}^{-1}$. The shape of a microdosimetric spectrum contains quantitative information that can be used to predict the relative biological effectiveness of radiation. The TEPC and its principles are discussed in chapter 3. The gas system and electronics, to perform correct microdosimetric measurements, are also fully described. Some basic principles of the proportional counter such as gas amplification, average energy required to produce an ion pair and energy resolution are debated. The distortion of microdosimetric spectra due to wall effects and the statistical variations in microdosimetry are discussed. The calibration methods are explained. Finally, the properties of the Gas Electron Multiplier (GEM) are discussed in chapter 3.

To obtain a clear understanding of the parameters that influence neutron microdosimetric spectra, analytical calculations have been carried out. These are discussed in chapter 4. The physical principles on which these calculations are based are explained. Different particle tracks have been calculated which is useful to distinguish between insiders, starters, stoppers and crossers. Knowledge of the contributions of different types of charged particles to the total lineal energy spectrum is also useful and is discussed. Changes in the shape of the microdosimetric spectra as a result of changing neutron energy are given. Finally in chapter 4, the influence of the simulated site sizes on the shape of the microdosimetric spectra is discussed.

In chapter 5, two types high-energy neutron source are considered (i.e. quasi-monoenergetic and spallation). The neutron spallation source at CERN (European Organisation for Nuclear Research) has been planned to be used for measuring microdosimetric spectra of neutrons with energies up to 250 MeV. The problems involved in using this facility for microdosimetry, such as pile-up and not getting enough information in a reasonable period of time are discussed. Furthermore, possible solutions to these problems are given. Finally, because of the impracticability of using a conventional TEPC, a new type of TEPC based on GEM has been introduced.

Although generally considered the best available detector, the currently used TEPC has several shortcomings. These include a relatively large physical size which limits spatial resolution and increases sensitivity to pileup effects, inability to simulate smaller site sizes (nanometer), many difficulties in construction of a single and multi-element counter. Furthermore, the supply of counters for routine practice is hampered by technical problems in the production of reliable detectors with predictable characteristics at comparatively little effort and hence low cost. These drawbacks justify the efforts to develop a new type of TEPC based on a GEM instead of detectors employing a central anode wire. This new design not only simplifies the construction of mini multi-element counters but it also facilitates

microdosimetry measurements (e.g. in nanodosimetry, personal dosimetry and space dosimetry) in a relatively easy manner.

To investigate the possibility of using a TEPC based on a GEM, the operation of GEMs employing Tissue-Equivalent (TE) gases has been studied. Chapter 6 describes the operation of two GEM structures, of pitch/outer diameter 140/80 μm and 90/60 μm , in both methane and propane based TE gases at pressures varying from 0.1 to 1 atmosphere. It is observed that sufficiently high gas gains, for both GEM structures and both TE gases, can be obtained for different pressure ranges. In methane based TE gas, a maximum gas gain of $1.5 \cdot 10^3$ has been reached whereas in propane based TE gas this is $6 \cdot 10^3$. These maxima have been reached at different gas pressures depending on GEM structure and TE gas. Empirical relations have been derived, which can be used to predict the maximum-safe-gain variation of GEMs operating with the same gas as a function of their structure and to predict the variation for a certain GEM as a function of counting gas.

In chapter 7 the design and construction of the novel TEPC-GEM counter is described. The first pulse height measurements with this counter for both methane and propane based Tissue Equivalent gases are presented. These results show promising properties for application of this novel type of TEPC in microdosimetric measurements.

In chapter 8, the first microdosimetric measurements of the TEPC-GEM exposed to a 14 MeV monoenergetic neutron beam and a californium (^{252}Cf) source for a counter cavity diameter of 1.8 mm simulating 1.0 μm tissue site size are presented. The spectra have been compared with the microdosimetric spectra measured before by TEPC employing central anode wires. Excellent agreement was found. Therefore, we can conclude that the TEPC-GEM is suitable to perform microdosimetric measurements. The specific advantages of the TEPC-GEM are discussed. Furthermore, the first microdosimetric responses for low energy X-rays are presented for counter cavities of 1.8 mm, 1.0 mm and 0.5 mm diameter at various pressures, simulating tissue site sizes of 1.8 μm , 1.0 μm , 500 nm, 280 nm and 140 nm. Two independent calibration methods have been applied and are discussed.

Finally, in chapter 9, conclusions are given providing a summary of main results and suggested directions for further research.

In general, it can be concluded that this small counter cavity opens new possibilities in application for high intensity radiation fields as well as in nanodosimetry. The TEPC-GEM has many advantages compared to the usual TEPCs such as, simple in construction, robust and stable in operation, and suitable both as mini-single and multi-element counter which will broaden the applications of the counter in the fields of personal and space dosimetry. Because of the relatively simple design and construction the TEPC-GEM is not only relatively cheap and easy to produce but also its components (sensitive volume, GEM and wall materials) can be modified and adapted to the needs.

Samenvatting

Instrumenten zijn noodzakelijke hulpmiddelen voor het onderzoek naar fysische processen aangezien de mogelijkheden van onze zintuigen zeer beperkt zijn. Nieuwe instrumenten openen mogelijkheden voor een beter begrip van de natuurwetten. In dit proefschrift wordt de ontwikkeling van een nieuw type instrument beschreven. Dit instrument wordt gebruikt om een schatting te maken van de invloed van straling op weefsel.

Straling is een vorm van energie die altijd in de natuur aanwezig is en waaraan de mens gedurende zijn hele leven blootstaat. Om een goede schatting van de effecten van blootstelling aan straling te krijgen, is het essentieel om het mechanisme van wisselwerking van straling met levende organismen te begrijpen.

Op grond van de primaire wisselwerkingmechanismen met de materie kan ioniserende straling worden onderverdeeld in direct ioniserende straling (zoals elektronen, protonen, alfa, etc.) en indirect ioniserende straling (b.v. fotonen en neutronen). Indirect ioniserende straling is het gevolg van ongeladen deeltjes en van elektromagnetische straling door de vorming van geladen deeltjes (zogenaamd secundaire geladen deeltjes) in verschillende processen die ionisaties en excitaties veroorzaken. Bij direct ioniserende straling geven de geladen deeltjes hun energie direct af aan de materie waarbij de energieafgifte plaats vindt door een groot aantal wisselwerkingen via de Coulomb-interactie met weinig energieverlies per wisselwerking. Dit resulteert in ionisatie en excitatie van atomen en moleculen. In een levende cel veroorzaken ionisatie en excitatie van atomen en moleculen een gecompliceerde keten van gebeurtenissen die kunnen leiden van chemische veranderingen in sommige belangrijke bio-moleculen via bio-functionele veranderingen tot veranderingen als transformatie en celdood.

Een probleem is dat levende cellen en weefsels niet noodzakelijkerwijs hetzelfde reageren wanneer ze blootgesteld worden aan verschillende stralingssoorten die een zelfde gemiddelde energie in een orgaan afgeven. Het is algemeen aanvaard dat de microscopische verdeling van energieafgifte in volumes vergelijkbaar met cellulaire en sub-cellulaire afmetingen van groot belang zijn voor een schatting van de mate van biologisch effect. Daartoe zijn metingen van stralingsgrootheden nodig in volumes met een vergelijkbare grootte als de cel of zelfs de DNA werkzame doorsnede. In het algemeen houdt microdosimetrie zich bezig met de manier waarop de energieafgifte plaatsvindt in volumes van cellulaire en sub-cellulaire grootte. Daarvoor zijn er in begin jaren vijftig de lagedruk proportionele telbuizen ontwikkeld waarmee metingen van microdosimetrische grootheden op een schaal van een μm mogelijk zijn. Hoofdstuk 2 beschrijft microdosimetrie en enkele basisprincipes van het voornaamste

instrument dat gebruikt wordt in de microdosimetrie d.w.z. de proportionele telbuis. Tevens wordt de wijze waarop in het algemeen de microdosimetrise spectra worden weergegeven uitgelegd. Voorts is een introductie gegeven van de toepassingen van experimentele microdosimetrie. Een aantal veel gebruikte experimentele microdosimetrise methoden is beknopt beschreven.

Proportionele telbuizen worden op grote schaal gebruikt in experimentele microdosimetrie. Microdosimetrie behelst het bestuderen en interpreteren van energieafgifte middels een enkele interactie met weefsel op microscopische schaal. De equivalentie met menselijk weefsel wordt verkregen door gebruikmaking van weefselequivalente materialen. Daarom worden de wanden van de proportionele telbuizen gemaakt van weefselequivalent plastic en heeft het telgas bijna dezelfde samenstelling als menselijk weefsel. Vandaar dat deze tellers “Tissue-Equivalent Proportional Counter (TEPC)” worden genoemd. De simulatie van een microscopisch volume wordt bereikt door reductie van de gasdruk. De momenteel in gebruik zijnde TEPCs zijn proportionele telbuizen met een holte, met een centrale anode draad. Het gebruik van TEPCs geschiedt door middel van pulsen. Het pulshoogte spectrum wordt gemeten en omgezet naar de parameter die veelal in microdosimetrie wordt gebruikt, de *lineieke energie*. De lineieke energie wordt veelal uitgedrukt in de eenheid $\text{keV}\mu\text{m}^{-1}$. De vorm van een microdosimetrise spectrum bevat meetbare informatie die gebruikt kan worden om voorspellingen te doen over de relatieve biologische effectiviteit van straling. De TEPC en zijn principes worden in hoofdstuk 3 beschreven. Het gassysteem en de elektronica voor de microdosimetrise metingen zijn uitgebreid beschreven. Sommige basisprincipes van de proportionele telbuis, zoals gasversterking, de gemiddelde energie voor de vorming van een elektron-ionpaar en de energieresolutie zijn beschreven. De veranderingen in microdosimetrise spectra als gevolg van wandeffecten en de statistische variaties in microdosimetrie zijn bediscussieerd. Verder zijn ijkmethoden besproken. Tot slot zijn ook de eigenschappen van de “Gas Electron Multiplier (GEM)” beschreven in hoofdstuk 3.

Om een duidelijk begrip te verkrijgen van de parameters die invloed hebben op microdosimetrise spectra van neutronen, zijn analytische berekeningen uitgevoerd die zijn bediscussieerd in hoofdstuk 4. De fysische principes waarop deze berekeningen zijn gebaseerd zijn uitgelegd. De verschillende typen deeltjessporen die van belang zijn voor het onderscheid tussen *insiders*, *starters*, *stoppers* en *crossers* zijn berekend. De bijdrage van verschillende soorten geladen deeltjes aan het totale lineieke-energie spectrum zijn besproken, aangezien kennis daarvan erg zinvol is voor de interpretatie van deze spectra. De invloed op de microdosimetrise spectra als gevolg van neutron energieverandering zijn gegeven. Tot slot wordt in hoofdstuk 4 de invloed van de gesimuleerde diameters op de vormverandering van de microdosimetrise spectra besproken.

In hoofdstuk 5 zijn twee soorten hoge-energie neutronenbronnen beschreven (d.w.z. quasi-monoenergetisch en spallatie). De neutron spallatiebron in CERN (European Organisation for Nuclear Research) zou aanvankelijk in het huidige onderzoek worden gebruikt voor het meten van neutronen-microdosimetrise spectra met een energie tot 250 MeV. De problemen bij gebruikmaking van deze faciliteit voor microdosimetrie, zoals *pile-up* en het onvoldoende informatie verkrijgen in een redelijke periode van tijd zijn bediscussieerd. Verder worden mogelijke oplossingen voor deze problemen gegeven. Uiteindelijk wordt vanwege de onuitvoerbaarheid van het gebruik van een conventionele TEPC, een nieuw type TEPC gebaseerd op de GEM geïntroduceerd.

Hoewel de op dit moment gebruikte TEPCs in het algemeen worden beschouwd als de best beschikbare detectoren, heeft dit type telbuis een aantal nadelen: een relatief grote fysische afmeting die de ruimtelijke resolutie beperkt en de gevoeligheid voor pile-up effecten vergroot, de onmogelijkheid om kleinere diameters (nanometer) te simuleren, veel moeilijkheden bij de constructie van een enkele en een multi-element teller. Verder is de levering van dergelijke telbuizen voor routinetoepassingen beperkt door technische problemen met de productie van betrouwbare tellers met voorspelbare karakteristieken met relatief weinig inspanning en daardoor lage kosten. Deze nadelen rechtvaardigden de inspanningen voor de ontwikkeling van een nieuw type TEPC gebaseerd op een GEM, in plaats van detectoren gebruikmakend van een centrale anodedraad. Dit nieuwe ontwerp vereenvoudigt niet alleen de constructie van mini multi-element tellers, maar maakt ook microdosimetrische metingen (d.w.z. in nanodosimetrie, persoonsdosimetrie en ruimtedosimetrie) mogelijk op een makkelijkere manier.

Om de mogelijkheid te onderzoeken van een TEPC gebaseerd op de GEM, is de werking van GEMs met Tissue-Equivalent (TE) gassen bestudeerd. Hoofdstuk 6 beschrijft de werking van twee GEM structuren, namelijk: met gatcentrum tot gatcentrum afstand/buiten diameter 140/80 μm en 90/60 μm . In beide GEMs zijn methaan en propaan gebaseerde TE gassen gebruikt bij verschillende drukken, variërend van 0,1 tot 1 atmosfeer. Voor beide GEM structuren en beide TE gassen kan voldoende gasversterking worden verkregen maar in verschillende drukgebieden. Voor methaan gebaseerd TE gas, is een maximum gasversterking van $1,5 \cdot 10^3$ bereikt en voor propaan gebaseerd TE gas is dit $6 \cdot 10^3$. Een empirische relatie, die kan worden gebruikt om de maximale gasversterkingsverandering van GEMs als functie van hun structuur en als functie van telgas te kunnen voorspellen is afgeleid.

In hoofdstuk 7 is het ontwerp en de constructie van de nieuwe TEPC-GEM beschreven. De eerste pulshoogtemetingen met deze TEPC-GEM met methaan en propaan gebaseerde TE gassen zijn gepresenteerd. De resultaten zijn veelbelovend voor toepassing van dit nieuwe type TEPC voor microdosimetrische metingen.

In hoofdstuk 8 zijn de eerste microdosimetrische metingen van de nieuwe TEPC-GEM blootgesteld aan een 14 MeV mono-energetische neutronbundel en een californium (^{252}Cf) bron gepresenteerd. Bij deze experimenten was de telholte diameter 1,8 mm en de gesimuleerde afmeting 1,0 μm weefselgrote. De gemeten spectra zijn vergeleken met microdosimetrische spectra eerder gemeten met een TEPC met een centrale anodedraad. Uitstekende overeenkomsten zijn gevonden. Daarom kunnen we concluderen dat de TEPC-GEM geschikt is om microdosimetrische metingen te verrichten. De bijzondere voordelen van de TEPC-GEM zijn besproken. Verder zijn de eerste microdosimetrische metingen voor laagenergetische röntgenstraling gepresenteerd voor telholtes van 1,8 mm, 1,0 mm en 0,5 mm diameter, bij verschillende gasdrukken, met gesimuleerde weefselgrootten van 1,8 μm , 1,0 μm , 500 nm, 280 nm en 140 nm. Twee onafhankelijke ijkingmethododes zijn toegepast en bediscussieerd.

In hoofdstuk 9 zijn conclusies gegeven alsmede een samenvatting van voornaamste resultaten en suggesties voor verdere onderzoek.

In het algemeen kan geconcludeerd worden dat de kleine telholte nieuwe toepassingsmogelijkheden opent voor zowel hoge-intensiteitstralingsvelden als voor nanodosimetrie. De TEPC-GEM heeft veel voordelen in vergelijking met de conventionele TEPCs zoals: eenvoudig in constructie, robuust en stabiel in werking, en geschikt voor zowel mini-enkele als voor multi-element counter waarmee de toepassingsmogelijkheden van deze detector voor persoons- en ruimtedosimetrie worden verruimd. Vanwege het relatief eenvoudige ontwerp en constructie is de TEPC-GEM niet alleen goedkoop en makkelijk om produceren maar kunnen zijn componenten (telholte, GEM en wandmaterialen) heel makkelijk naar de behoefte worden gewijzigd en aangepast.

Dankwoord / Acknowledgement

Het werk van een wetenschapper staat niet op zichzelf, om hem heen leveren velen een bijdrage aan het onderzoek en het tot stand komen van een proefschrift. Met name de volgende personen wil ik speciaal bedanken:

Allereerst wil ik mijn promotor Carel van Eijk bedanken voor zeer nuttige vakinhoudelijke gesprekken die ertoe leidden dat ik me over de juiste dingen zorgen ging maken. Dit was trouwens hard nodig aangezien de richting van het onderzoek moest worden bijgesteld. Hans Zoetelief en Adrie Bos wil ik bedanken voor het zorgvuldig lezen van dit proefschrift en de praktische suggesties die zij leverden. Ik wil ook Jan Kaptijn, het toenmalig hoofd van de afdeling Cursorische Onderwijs, bedanken voor het mogelijk maken onderzoek te gaan doen.

I want to thank the group of Legnaro Institute (Istituto Nazionale di Fisica Nucleare), Paolo Colautti, Laura de Nardo and Valentina Cesari. You introduced me to the world of microdosimetry in an informal and pleasant way and I will never forget the time I stayed in your lab and the time we spent at the Nice therapeutic proton beam. I especially want to thank Valentina and Laura. Valentina helped me to become familiar with the experimental microdosimetry. Laura had always time to have a nice and fruitful discussion with me during my research. Even when you were busy with your own work you were ready to do one more calculation and to discuss it with me by e-mail which is not the easiest way to discuss physical problems. Persino quando ho bevuto vino, invece di una birra, mangiando una pizza, non mi hai fatto sentire... uno straniero! Sono davvero felice di aver trovato dei buoni amici durante questa mia esperienza. Grazie infinite di tutto.

De constructie van een nieuwe counter heeft expertise nodig althans als je wilt dat het zal gaan werken. Gelukkig heb ik die expertise bij het IRI in huis kunnen vinden. Van de technici wil ik met name René Gommers en Kees Langelaan bedanken voor hun voorstellen die resulteerden in de constructie van de counter. Leo Fraase-Storm wil ik bedanken voor de bouw van het gassysteem en andere bijdragen aan dit onderzoek. Hans Brouwer wil ik bedanken voor de gezellige en goede samenwerking tijdens de metingen met de neutronen generator in de bunker.

Iedereen die dit proefschrift vluchtig doorbladert, zullen de mooie foto's opgevallen zijn. Daarom wil ik Gé Brouwer bedanken voor alle foto's die hij voor mij heeft gemaakt en voor de bijdrage aan het ontwerp van de kaft. Victor Bom en Jan Jansen wil ik bedanken voor hun berekeningen die ervoor zorgden dat mijn gelijk hebben, veranderde in gelijk krijgen.

Als je intensief (aandachtig) bezig bent met research en de experimenten soms mislukken, wil je op een of andere manier je frustratie kwijt. Daarvoor heb ik sport gekozen. Ik wil daarom Aniel, Jan Sonsky, Navid, Nicolas, Aurelie en Thea bedanken voor het feit dat ze als sportmaatjes ervoor gezorgd hebben dat ik mijn frustraties kon afreageren.

Op het laatste moment heeft ook Jakob een bijdrage geleverd aan dit werk, waarvoor mijn dank.

I want to thank also Hassan, Ivan, Ibrahim and Mirko for all the nice talks and discussions and wish them good luck with their work.

Natuurlijk had ik moeten beginnen mijn vrouw Nelleke en mijn zoon Arman te bedanken voor het geduld dat ze met mij hebben gehad en de steun die ze mij gegeven hebben. Met name tijdens de spreekwoordelijke laatste loodjes, hebben zij mij die kracht gegeven om dit proefschrift af te maken.

Curriculum Vitae

Majid Farahmand was born on 25 April 1964 in the beautiful city of Isfahan, Iran. After finishing secondary school and some years of working, he moved to the Netherlands in 1988 where he started to learn Dutch and to do some education prior to university. When he was able to pronounce Utrecht in a proper way he started to study experimental physics at the University of Utrecht. He performed his graduation research at Department of Atomic and Interface Physics (Debye Institute) at the University of Utrecht. There he worked on the subject: Metastable Atom Deexcitation Spectroscopy. Because of his interest in astronomy he gained his *propaedeuse* of astronomy in 1993 at the same university. During his study he worked as student assistant for many times since he enjoys transferring his knowledge to others. After his graduation in 1997, he started to work at the Training Course Group of Interfaculty Reactor Institute (IRI), Delft University of Technology as teacher/co-ordinator.

The author started his research activities at the Radiation Technology Group at the IRI in 1999. Initially, he performed research on the construction of a neutron beam scanner based on the Micro-Gap detector. In 2000 he started to perform research on the subject of high-energy neutron microdosimetry at CERN where he finally focussed on the design and construction of a novel Tissue-Equivalent Proportional Counter based on a Gas Electron Multiplier to perform microdosimetric measurements. The results of this research are presented here. The year 2000 is also very special for him because of the birth of his son. During his research activities he was still involved in giving lectures for Radiation Protection courses Level 4 and 3. From January 2004, he is working again at the Training Course Group of the IRI.

List of Publications

- M. Farahmand, L. De Nardo, A.J.J. Bos, J.T.M. Jansen and C.W.E. van Eijk, *Microdosimetric responses of a Tissue-Equivalent Proportional Counter based on a Gas Electron Multiplier to X-ray radiation down to 140 nm simulated site sizes*, submitted for publication in IEEE Trans. Nucl. Sci. (2004).
- M. Farahmand, A.J.J. Bos, L. De Nardo and C.W.E. van Eijk, *First microdosimetric measurements with a tissue-equivalent proportional counter based on a gas electron multiplier*, accepted for publication in Radia. Prot. Dosi. (2004).
- M. Farahmand, A.J.J. Bos, J. Huizenga, L. De Nardo and C.W.E. van Eijk, *Design of a new Tissue-Equivalent Proportional Counter based on Gas Electron Multiplier*, Nucl. Instr and Meth. A **509**, (2003) 262.
- M. Farahmand A.J.J. Bos and C.W.E. van Eijk, *Gas Electron Multiplier (GEM) operation with Tissue-equivalent gases at various pressures*, Nucl. Instr and Meth. A **506**, (2003) 160.
- M. Farahmand, A.J.J. Bos, H. Zoetelief and C.W.E. van Eijk, *Experimentele Microdosimetrie*, NVS-Nieuws **2001/4** (2001) 38.

- M. Farahmand, *Neutron Microdosimetry at CERN*, internal report TUDelft, IRI, ST (2000).
- M. Farahmand, *Metastable Atom Deexcitation Spectroscopy*, internal report University Utrecht (1997).